Convection et dégazage d'un système magmatique : le cas du lac de lave l'Erebus, Antarctique.

Claudia Indira Molina Polania Molina Polania Aury

▶ **To cite this version:**

Claudia Indira Molina Polania Molina Polania Aury. Convection et dégazage d'un système magmatique : le cas du lac de lave l'Erebus, Antarctique.. Sciences de la Terre. Université d'Orléans, 2012. Français. NNT : 2012ORLE2026 . tel-00772305

HAL Id: tel-00772305

https://theses.hal.science/tel-00772305

Submitted on 10 Jan 2013

HAL is a multi-disciplinary open access archive for the deposit and dissemination of scientific research documents, whether they are published or not. The documents may come from teaching and research institutions in France or abroad, or from public or private research centers.

L'archive ouverte pluridisciplinaire **HAL**, est destinée au dépôt et à la diffusion de documents scientifiques de niveau recherche, publiés ou non, émanant des établissements d'enseignement et de recherche français ou étrangers, des laboratoires publics ou privés.

UNIVERSITÉ D'ORLÉANS

ÉCOLE DOCTORALE SCIENCES ET TECHNOLOGIES

Institut des Sciences de la Terre d'Orléans

THÈSE présentée par :

Claudia Indira MOLINA POLANIA

Soutenue le : **28 septembre 2012**

Pour obtenir le grade de : **Docteur de l'université d'Orléans**

Discipline : Structure et évolution de la Terre et des autres planètes

Convection et dégazage d'un système magmatique : le cas du lac de lave de l'Erebus, Antarctique

THÈSE dirigée par :

Alain BURGISSER	Chargé de recherche, CNRS Orléans

RAPPORTEURS :

Geneviève BRANDEIS	Physicienne-Adjointe, IPG Paris
Timothy DRUITT	Professeur, Université de Clermont-Ferrand

JURY

Jean-Louis BOURDIER	Professeur, Université d'Orléans	Président du jury
Alain BURGISSER	Chargé de recherche, CNRS Orléans	
Geneviève BRANDEIS	Physicienne-Adjointe, IPG Paris	
Timothy DRUITT	Professeur, Université de Clermont-Ferrand	
Clive OPPENHEIMER	University Reader, Cambridge University	
Marielle COLLOMBET	Enseignante Chercheuse, Université de Savoie	

Claudia Indira MOLINA POLANIA

Convection et dégazage d'un système magmatique : le cas du lac de lave de l'Erebus, Antarctique

Le phénomène de dégazage permanent observé sur le volcan Erebus s'accompagne d'une variation cyclique de la composition des gaz et du niveau de son lac de cratère que nous nous sommes proposé de modéliser en partant de l'hypothèse que ces fluctuations sont causées par l'arrivée de batch de magma naissant à faible profondeur, ascendant dans un conduit à travers duquel percole un flux continu de gaz dont l'origine est plus profonde. Nous avons tout d'abord montré par simulation numérique que la vigueur de la convection observée en surface ne pouvait être expliquée par la seule convection thermique d'un mélange liquide-cristaux. Si une alimentation continue en magma et gaz dans un système ouvert permet de simuler un comportement pulsatif de la surface, cet apport doit être suffisamment important pour que les changements de vitesse de surface ainsi générés puissent être appréciés. Le conduit doit avoir un diamètre suffisant large pour assurer la pérennité de la convection et maintenir le magma au-dessus de sa température de transition vitreuse. La présence de cristaux accélère la convection et améliore l'efficacité du transfert de chaleur entre les régions inférieures et supérieures du système magmatique ; ces cristaux se déposent dans le fond de la chambre pour former une couche de forte concentration d'une dizaine de mètres d'épaisseur. L'introduction de deux batch de magma d'origines différentes a permis de mettre en évidence combien leur composition et le comportement du lac de lave étaient sensibles à la température à laquelle ces batch sont générés. D'autre part, un batch ne contribuera au budget de dégazage dans des proportions consistantes avec les observations que si un seuil de flottabilité suffisant a été atteint. Dans le cas contraire, la migration d'une quantité de magma nécessaire à ce dégazage ne pourrait se faire que dans un conduit de très grand diamètre. Les paramètres physiques de la croute qui se forme lors du refroidissement de la surface du lac de lave, tels que son épaisseur et sa perméabilité, influent sur sa capacité à se déformer sous la pression qu'elle piège et à permettre un dégazage de type effusif. Cette pression conditionne à son tour la porosité du magma en surface et éventuellement le degré de dégazage du magma qui redescend vers la chambre magmatique. Cette étude nous a permis de mieux appréhender les mécanismes associés à une éruption de régime effusif et constitue une étape dans la compréhension de la transition à un régime explosif, préoccupation majeure des centres de surveillance volcaniques.

Mots clés : modélisation numérique, convection, dégazage, volcanologie, magma, éruption.

Convection and degassing of a magmatic system: the case of the lava lake at Erebus, Antarctica

The observed phenomenon of permanent degassing of the volcano Erebus is accompanied by a cyclic variation of gas composition and level of its crater lake that we proposed to model in the assumption that these fluctuations are caused by the arrival of batch of magma originated at shallow depth, ascending in a conduit through which percolates a continuous flow of gas whose origin is deeper. We first showed that the observed effect of convection on the surface could not be explained solely by thermal convection of a liquid-crystals mixture. If a continuous supply of magma and gas in an open system simulates a pulsating behavior of the surface, this contribution must be large enough for the changes in surface velocity thus generated can be appreciated. The conduit diameter should be sufficient large to ensure the sustainability of convection and maintain the magma above its glass transition temperature. The presence of crystals convection accelerates and improves the efficiency of heat transfer between the upper and lower regions of the magmatic system; these crystals settle at the bottom of the chamber to form a layer of high concentration of about ten meters thickness. The introduction of two batches of magma from different depths of nucleation helped to highlight how their composition and the behavior of the lava lake were sensitive to the temperature at which they are generated. On the other hand, a batch will contribute to the degassing budget in proportions consistent with the observations only if a threshold of sufficient buoyancy was achieved. Otherwise, the migration of the amount of magma required for the degassing will only occur in a conduit of very large diameter. The physical parameters of the crust forming as the surface of the lava lake cools down, such as thickness and permeability, affect its ability to deform under pressure and to allow the trapped pressure to degas under an effusive regime. This pressure in turn influences the porosity of the magma at surface and possibly the degree of degassing of the magma being recirculated toward the magma chamber. This study allowed us to better understand the mechanisms associated with an effusive eruption regime and is a step in understanding the transition to an explosive regime, a major concern for the volcanic monitoring centers.

Keywords : Numerical modeling, convection, degassing, volcanology, magma, eruption.

Institut des Sciences de la Terre d'Orléans
1A, rue de la Férollerie
45071 ORLEANS Cedex 2, France

Remerciements

La liste est longue de tous ceux qui – professeurs, collègues et amis – ont contribué à transformer l'attentif observateur de volcan que j'étais en une enthousiaste et curieuse vulcanologue.

Je voudrais d'abord et surtout remercier Dr. Alain Burgisser qui m'a guidée tout au long de cette étude avec une patience qui découle sans doute de son expertise de la turbulence. Tout en me ramenant constamment à plus de rigueur, il m'a initiée aux calculs numériques et analytiques en me donnant la liberté d'explorer des directions vers lesquelles ma curiosité me faisait dériver, qui m'ont fait découvrir des aspects entiers de la complexité des phénomènes que j'abordais. Il a ouvert une fenêtre sur un monde pour moi abstrait.

Dr. Génèvieve Brandeis et Dr. Timothy Druitt pour avoir accepté d'examiner ce travail et d'en être les rapporteurs. Leur remarques ont été d'une grande utilité lors de la préparation de la soutenance et pour de futures orientation de recherche. Un grand merci à Dr. Marielle Collombet et Dr. Jean-Louis Bourdier pour leurs critiques constructives qui contribueront également à orienter ma future démarche professionelle.

Dr Clive Oppenheimer a clarifié de multiples zones d'ombre par ses travaux et par des suggestions dont la pertinence découle d'une observation directe et d'une connaissance approfondie du volcan. Il a lui aussi apporté une précieuse contribution à la correction du style de cette étude.

Dr Hiroyuki Kumagai m'a initiée aux calculs analytiques et lourds de la volcanologie, tout en me faisant réfléchir à la relation entre sismologie et écoulement des fluides dans un volcan. Je luis dois l'apprentissage de la rigueur et de la méthodologie requise dans le traitement des données.

Je ne saurais oublier tous mes collègues et compagnons de l'ISTO (Juan Andújar, Marina Aletti, Manu LeTrong, Giada Giacomo, Caroline Martel, Michel Pichavant, Claudia Agostini, Simona Mancini, Ian Schipper, Antonio Dorado, Bruno Scaillet, Caroline Bouvet de Maisonneuve, Wimm Degruyter, David Picard, Fabrice Gaillard, Jonathan Castro, Anita

Cadoux and Rémi Champallier) qui m'ont accueillie et soutenue, tout en faisant l'effort d'essayer de me comprendre lorsque je parlais Français, Anglais ou même quand je ne parlais pas. Je remercie ma famille en Colombie et en France et mes amis dispersés dans le monde pour leurs encouragements sans faille.

Le CNRS et The European Research Council ont financé ce projet et m'ont permis de participer au congrès de l'AGU en 2009 et au congrès de l'IUGG de Melbourne en 2010.

Je dédie ce travail à ma mère qui m'a enseignée par l'exemple à ne jamais renoncer et à Francis sans qui cette aventure n'aurait jamais commencé.

Sommaire

Liste des Figures

Chapitre I. Le modèle hydrodynamique MFIX

Chapitre II. Numerical simulations of convection crystal-bearing magmas: a case study of the magmatic system at Erebus, Antarctica

Chapitre III. Numerical simulation of the effusive regime in bubbles-bearing magmas: a case study of the magmatic system at Erebus, Antarctica

Chapitre IV. Physical models addressing level fluctuations of the lava lake at Erebus, Antarctica: I. The role of degassing cycles

Chapitre V. Physical models addressing level fluctuations of the lava lake at Erebus, Antarctica: II. The role of the lake crust

Liste des tables

Chapitre I. Le modèle hydrodynamique MFIX

Chapitre II. Numerical simulations of convection crystal-bearing magmas: a case study of the magmatic system at Erebus, Antarctica

Chapitre III. Numerical simulation of the effusive regime in bubbles-bearing magmas: a case study of the magmatic system at Erebus, Antarctica

Chapitre IV. Physical models addressing level fluctuations of the lava lake at Erebus, Antarctica: I. The role of degassing cycles

Chapitre V. Physical models addressing level fluctuations of the lava lake at Erebus, Antarctica: II. The role of the lake crust

Introduction générale

Les éruptions volcaniques sont des événements parfois dévastateurs dont il convient d'anticiper les phases paroxysmales afin d'en limiter les conséquences sur les populations ; la surveillance continue s'impose comme une composante majeure de gestion des risques. L'identification rapide des événements précurseurs et la prédiction à court terme d'une manière fiable constituent un ample domaine de recherche dans le but d'améliorer les systèmes d'alerte. De nombreux travaux ont démontré l'importance de l'écoute micro-sismique comme paramètre de caractérisation des mécanismes précurseurs aux éruptions, essentiellement explosives. L'interprétation des signatures des signaux acoustiques fournit également de précieuses indications sur le caractère effusif ou explosif d'une activité en augmentation. Cependant, la compréhension des complexes procédés de mécanique des fluides qui accompagnent les éruptions représentent un troisième axe de recherche que nous proposons d'explorer ici.

Les éléments volatiles saturant le magma sont plus ou moins solubles selon les conditions de pression et de température auxquelles ils sont soumis. Lorsque les conditions d'équilibre sont rompues, l'exsolution de ces volatiles sous forme de bulles résulte en la migration du magma vers la surface. Au cours de cette ascension, la croissance des bulles s'accélère et leur solubilité diminue, entrainant une diffusion du gaz limitée essentiellement par la viscosité du liquide silicaté. Cette vitesse d'ascension dépend donc de la capacité des bulles de gaz à croître au sein du magma. L'augmentation de la flottabilité résultant de la croissance de ces bulles fournit la force motrice de l'éruption ; une énergie considérable peut s'accumuler lorsque la surface refroidie se comporte comme une barrière et piège des gaz dont la pression peut se libérer violemment.

Les magmas montant lentement vers la surface dégazent d'une manière plutôt effusive alors que les magmas rapides entrent en éruption de manière plus explosive, souvent plus dangereuse pour les populations. Au cours de cette étude, nous avons utilisé la modélisation numérique de processus de mécanique des fluides dans le but d'améliorer la compréhension

du régime effusif dont les dynamiques qui le gouverne sont encore insuffisamment connues. Le volcan Erebus, en Antarctique, présente un lac de cratère permanent dont l'activité est essentiellement effusive, accompagnée d'explosions stromboliennes de faible ampleur. Il représente donc une précieuse source de données que les scientifiques ont collectées depuis des décennies, véritable fenêtre ouverte sur le cœur d'un système magmatique.

Nous avons d'abord cherché à déterminer si la convection thermique, associée à une convection mécanique résultant de la décantation de cristaux, peut à elle seule expliquer la pérennité de l'activité. Nous avons d'abord reproduit numériquement les résultats d'une étude expérimentale portant sur la convection d'un fluide dont on augmente la densité par refroidissement d'une de ses limites. Nous avons ensuite simulé la convection magmatique dans un système idéalisé de l'Erebus. Puis nous avons alimenté notre système par un apport permanent de magma. Dans un troisième temps, nous avons introduit du gaz en quantités significatives afin de simuler l'écoulement du magma dans le conduit et en surface. Finalement, nous avons montré comment les caractéristiques de cet écoulement de surface peuvent expliquer les fluctuations cycliques de la composition des gaz relâchés à l'atmosphère et du niveau du lac de lave.

Le **chapitre I** présente la théorie de base et les concepts de base utilisés pour l'étude de l'interaction liquide silicaté-cristaux dans un contexte de lac de lave. Nous rappelons dans un premier temps les équations de transport pour un écoulement biphasique de liquide et grains sphériques de densité constante, avant de décrire comment nous avons utilisé le calcul numérique intensif appliqué à la dynamique des fluides en adaptant le code MFIX (Multiphase Flow with Interface eXchanges). Un exemple d'utilisation du code avec un écoulement monophasique clôt ce premier chapitre.

Dans le **chapitre II**, nous développons un modèle biphasique de dynamique des fluides et observons comment se comporte la convection au cours des 30 années que reproduit notre simulation lorsque nous refroidissons le lac de lave depuis sa surface. Nous étudions l'effet de la présence de cristaux sur la convection en changeant la taille du conduit et les conditions aux limites. Nous montrons que la pérennité de la convection est assurée lorsque le conduit est suffisamment large, bien que les vitesses de convection à la surface du lac calculées par notre modèle soient inférieures à celles observées in situ et nous en déduisons que la flottabilité résultant de l'exsolution des éléments volatiles ne peut être ignorée. Nous

observons la formation au fond de la chambre magmatique d'une couche d'épaisseur constante riche en cristaux et au-dessus de laquelle la fraction des cristaux en suspension augmente en présence d'une convection plus forte.

Dans le **chapitre III,** nous simulons sous des conditions non isothermes la recharge permanente d'un système de magma rempli de 2 phases distinctes : l'une dans laquelle les cristaux et le liquide silicaté font partie de la même phase liquide et l'autre dans laquelle des bulles de gaz riches en eau grandissent à la fois par diffusion et par expansion. Nous observons l'élévation d'un panache de bulles dans le conduit qui croît dès qu'il entre dans le lac de lave et se développe jusqu'en surface, où un flux de gaz peut être libéré. Il en résulte une augmentation des vitesses de convection en surface et des volatiles enrichis en eau, même si elles restent en deçà des valeurs observées. Le phénomène de pulsation se traduisant par un changement de vitesse à la surface est reproduit de manière satisfaisante.

Nous étudions dans le **chapitre IV** la variation cyclique de la composition des gaz émis en surface et du niveau du lac de lave. Notre modèle est basé sur l'hypothèse développée par *Burgisser et al*. [2008] que la température à laquelle un batch individuel de magma se trouve exposé détermine l'évolution géochimique des gaz dissouts et libres qu'il contient; l'équilibre qui en résulte conditionne la composition du gaz tout en contrôlant le processus d'exsolution et donc le comportement de ce batch de magma ascendant. Nous montrons l'influence qu'ont les températures des courants de magma ascendant et ascendant sur le comportement cyclique du niveau du lac.

Dans le **chapitre V,** nous considérons comme un milieu perméable et déformable la croûte qui se forme à la surface du lac de lave lorsqu'elle se refroidit. Nous montrons comment un mélange de gaz provenant de deux sources distinctes peut générer les fluctuations du niveau du lac observées, à condition qu'un seuil de flottabilité ou contraste de densité soit atteint entre les magmas ascendant et descendant. Nous évaluons l'influence de l'épaisseur de la croute sur l'amplitude de l'oscillation et nous déterminons qu'il existe une enveloppe de solutions pour lesquelles la porosité du magma atteignant la surface, l'épaisseur de la croûte et le diamètre du conduit permettent de reproduire les fluctuations observées.

Les chapitres suivant le chapitre 1ont été écrits sous la forme d'articles individuels dont l'un, **chapitre 2**, est sous presse. Celui-ci est coécrit avec Dr. Alain Burgisser qui, outre les directives et conseils qu'il m'a patiemment apportés, a fourni des résultats de ses propres recherches comme base de cette étude et avec Dr. Clive Oppenheimer dont nous avons cherché à reproduire les mesures faites sur site.

Mount Erebus

In Greek mythology Erebus was a primordial god of darkness and the son of Chaos (Picture taken from http://www.nhm.ac.uk/natureplus/)

Chapitre I

Le modèle hydrodynamique MFIX

Résumé

Le présent chapitre a pour objectif de présenter la théorie de base utilisée pour l'étude de l'interaction liquide silicaté-cristaux dans un contexte de lac de lave, en utilisant la dynamique des fluides, le calcul intensif et le code MFIX Ver. 2.0, 2004 (Multiphase Flow with Interface eXchanges). Nous y expliquons de manière détaillée les équations de transport pour un écoulement biphasique de liquide et grains sphériques de densité constante. Ensuite, nous mettrons en œuvre un exemple illustrant comment un utilisateur peut adapter MFIX à un écoulement monophasique et exploiter les données issues de sa simulation. Les concepts définis dans ce chapitre seront utilisés tout au long de ce travail.

1. Les équations

L'idée centrale d'une approche multiphasique est basée sur la mécanique des milieux continus. Celle-ci considère qu'un système se compose d'un nombre suffisamment important de particules pour que les discontinuités puissent être aplanies et que ses différentes propriétés puissent être traitées comme étant continues (Figure 1). Ainsi, tout système peut être divisé en petites cellules appelées volumes finis (Figure 1a), chacune d'elles étant orientée dans l'espace par rapport à chaque cellule voisine dans un système de coordonnées (Figure 1b). Tout au long de cette étude, nous adoptons un signe positif de convention : les contraintes

sont positives lorsque les forces extérieure et normale agissent dans la même direction par rapport au système de coordonnées *x*, *y* correspondant à E et vers le haut, respectivement. Chaque volume fini ou volume de référence (Figure 1c) est composé de 1 à 2 phases (Figure 1d) ; celle qui se présente sous forme de grains ou composés en petite quantité est appelée la phase dispersée ou granulaire (e.g. les cristaux) et la phase dans laquelle les grains sont dispersés est appelée la phase continue. Chaque phase granulaire est caractérisée par un diamètre et une densité uniques, et un coefficient d'élasticité.

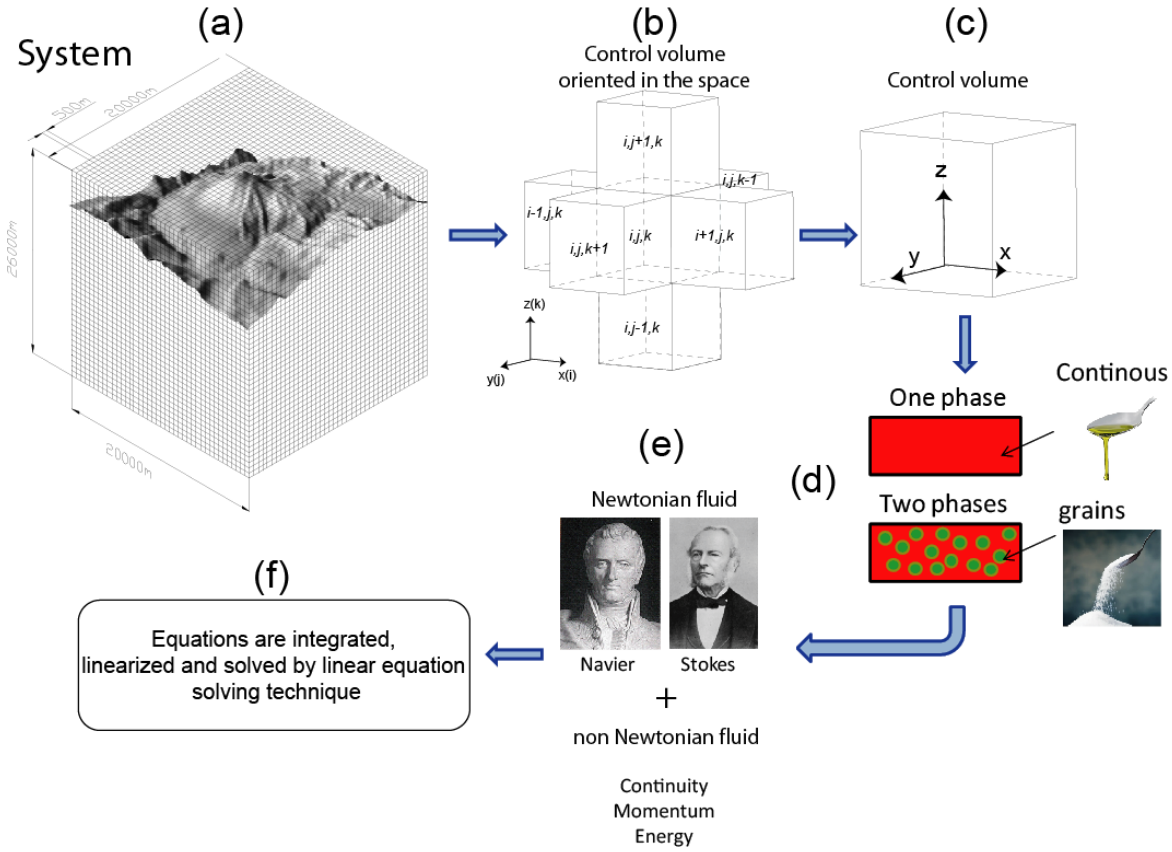

Figure 1. Représentation des principales étapes dans le calcul multiphasique.

Notre modélisation est caractéristique de modèles appelés ***continus*** dans lesquels les variables d'état d'une composante changent continuellement avec le temps (description Eulérienne) ; ceux-ci se différencient des modèles dit ***discrets*** dans lesquels les variables d'état d'une composante changent instantanément à des temps distincts (description Lagrangienne). Ces deux modèles mathématiques sont liés essentiellement à la taille de l'objet que l'on veut modéliser :

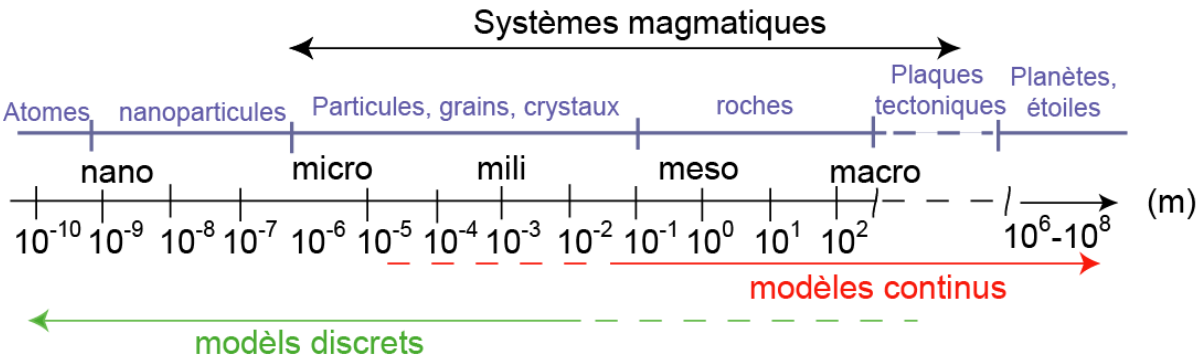

Figure 2. Représentation des principales échelles physiques et leur liaison avec les modèles mathématiques.

Dans notre étude, nous considérerons le système à deux phases dont les vitesses relatives peuvent varier. Les deux phases s'interpénètrent (selon la méthode d'Euler), occupant chacune une fraction ε dans le volume de contrôle (l'indice m se réfère à la phase liquide et l'indice s à la phase solide) ; ces fractions volumiques sont calculées en chaque point de la grille, sachant que la somme des fractions volumiques est toujours égale à 1, c'est-à-dire $\varepsilon_m + \varepsilon_s = 1$ et elles partagent le même champ de pression. L'espace occupé par une phase ne peut pas être occupé en même temps par une autre. Chaque point est défini à tout instant par un ensemble de variables microscopiques caractérisant un matériau en particulier (densité ρ, vitesse $\vec{v}$, température T, pression P, temps t). Les forces qui décrivent le mouvement de chaque phase prennent en compte la conservation de masse, de quantité de mouvement et d'énergie. Ce sont des forces non linéaires dont les dérivées partielles sont communément dénommées équations de Navier-Stokes pour décrire un fluide Newtonien ou une forme modifiée de celles-ci pour décrire les fluides non-Newtoniens (Figure 1e).

Les équations vectorielles du modèle hydrodynamique sont basées sur ces équations et sur plusieurs travaux développés depuis 1967. Pour résoudre les équations d'écoulement multiphasique, nous avons utilisé un code numérique basé sur MFIX Ver. 2.0, 2004 (Multiphase Flow with Interface eXchanges), un programme développé par le Laboratoire National Américain de Technologie Energétique du Département de l'Energie [*Syamlal et al.,* 1993 ; *Syamlal*, 1994, 1998 ; *Benyahia et al.*, 2008]. Ce programme permet de simuler la dynamique des fluides dont la complexité est telle qu'elle ne peut se résoudre à travers des méthodes numériques sans l'aide d'un ordinateur ; c'est-à-dire en utilisant la dynamique des fluides computationnelle (CFD). MFIX a la capacité de traiter jusqu'à 4 phases dispersées. Ces équations à dérivée partielle sont linéarisées et résolues à l'aide de techniques de

résolution linéaire (Figure 1f) pour l'ensemble des cellules à un temps donné. Un compte-rendu plus détaillé des équations utilisées et des méthodes de discrétisation peut être trouvé dans la section du manuel de MFIX relative à la théorie et à la technique numériques [*Syamlal*, 1993; 1994].

Nous décrivons ci-dessous les relations de transport de base incorporées dans MFIX et les relations constitutives composant ces relations de transport, que nous avons modifiées pour obtenir notre modèle. Ces équations décriront un cas non-isotherme, sans réactions chimiques entre phases, pour un système incompressible à deux phases et dont les cristaux constituent la seule phase dispersée.

1.1. Les équations de continuité ou de conservation de la masse

Les formes différentielles de l'équation de continuité ou de conservation de la masse pour les phases liquide et solide sont respectivement définies comme suit:

$$\frac{\partial}{\partial t}(\varepsilon_m \rho_m) + \nabla \cdot \left(\varepsilon_m \rho_m \vec{v}_m\right) = 0 \tag{1}$$

$$\frac{\partial}{\partial t}(\varepsilon_s \rho_s) + \nabla \cdot \left(\varepsilon_s \rho_s \vec{v}_s\right) = 0 \tag{2}$$

Où le premier et le deuxième terme de la partie gauche de l'équation spécifient l'accumulation de masse par unité de volume et le flux de masse convectif par unité de volume de référence, respectivement. La somme de ces deux termes est égale à « 0 » (le terme de droite de l'équation) car il n'y a aucune génération de masse dans les phases par réaction chimique ou transfert de masse.

La densité microscopique de la phase dispersée, ρ_s, demeure constante, alors que la densité de la phase continue, ρ_m, est modélisée comme étant celle d'un fluide dont la densité varie selon la relation:

$$\rho_m = \rho_o\left[1 - \alpha\left(T_m - T_o\right)\right] \tag{3}$$

Ou α est le coefficient d'expansion thermique du liquide – une constante, T_m est la température du magma, T_0 et ρ_o étant ses température et densité initiales.

MFIX a la capacité de à traiter des **fluides compressibles** (de densité variable) et **incompressibles** (de densité constante). Dans notre cas, la densité du fluide reste fluctue très peu ; autrement dit celui-ci est « incompressible ». Le rapport de la vitesse du fluide (~10^{-5}-10^{-6} m/s ; voir détail dans le Chapitre 2) sur la vitesse de propagation du son dans ce fluide (~10^3 m/s) donne un numéro de Mach ($Ma = \left|\vec{v}_m\right| / c$) de l'ordre de 10^{-8}-10^{-9} m/s, qui reste bien en dessous de $Ma < 0.3$, défini comme le seuil pour les écoulements incompressibles.

1.2. Les équations de bilan de la quantité de mouvement

Les bilans de quantité de mouvement de la phase continue (liquide) et de la phase solide sont respectivement définis comme suit :

$$\frac{\partial}{\partial t}\left(\varepsilon_m \rho_m \vec{v}_m\right) + \nabla \cdot \left(\varepsilon_m \rho_m \vec{v}_m \vec{v}_m\right) = \overset{(1)}{\nabla \cdot \bar{\bar{S}}_m} + \overbrace{\varepsilon_m \rho_m \vec{g}}^{(2)} - \overbrace{F_{ms}\left(\vec{v}_m - \vec{v}_s\right)}^{(3)} \tag{4}$$

$$\frac{\partial}{\partial t}\left(\varepsilon_s \rho_s \vec{v}_s\right) + \nabla \cdot \left(\varepsilon_s \rho_s \vec{v}_s \vec{v}_s\right) = \overset{(1)}{\nabla \cdot \bar{\bar{S}}_s} + \overset{(2)}{\varepsilon_s \rho_s \vec{g}} + \overbrace{F_{ms}\left(\vec{v}_m - \vec{v}_s\right)}^{(3)} \overset{(4)}{-\varepsilon_s \nabla P_m} \tag{5}$$

Ces équations impliquent que le taux d'augmentation de la quantité de mouvement et le taux de quantité de mouvement par convection par unité de volume (premier et deuxième termes de gauche des équations 4 et 5) sont égaux aux termes de droite des deux équations : (1) les forces de surface liées au tenseur de déformation qui prennent en compte l'interaction dans la phase même, (2) est la force du corps ou gravitationnelle s'exerçant sur chaque phase, c'est-à-dire son poids, (3) et (4) la force d'interaction entre les phases fluide et solide par unité de volume, c'est-à-dire la force de glissement et flottabilité, respectivement.

A noter que la flottabilité générée par la pression du fluide apparait seulement dans l'équation de quantité de mouvement pour la phase solide ; autrement dit, le bilan dynamique de la phase solide prend en compte deux aspects : (i) la pression solide (inclue dans le terme 1 de

l'équation 2) et (ii) une chute de pression en phase liquide (inclue dans le terme 4 de l'équation 2) [*Gidaspow*, 1994: Modèle A].

1.2.1. Tenseur de déformation ou de contraintes

Avant d'expliquer le premier terme de droite des équations (4) et (5), nous rappelons quelques notions de base relatives au tenseur de contraintes. La mécanique des milieux continus est le domaine de la mécanique qui s'intéresse à la déformation des solides et à l'écoulement des fluides. Ce dernier point faisant l'objet de la Mécanique des fluides (Tableau 1).

Table 1. Domaine d'étude (mis en évidence en gris)

<table>
<tr><td rowspan="4">Mécanique des milieux continus</td><td rowspan="2">Mécanique du solide</td><td colspan="2">Élasticité</td></tr>
<tr><td>Plasticité</td><td rowspan="2">Rhéologie</td></tr>
<tr><td rowspan="2">Mécanique des fluides</td><td>Fluides non-newtoniens</td></tr>
<tr><td colspan="2">Fluides newtoniens</td></tr>
</table>

La rhéologie (du grec *rheo*, couler et *logos*, étude) est l'étude de la déformation et de l'écoulement de la matière sous l'effet d'une contrainte appliquée. Ceci unit des champs d'application apparemment sans rapport, les matériaux plastiques et les fluides non newtoniens, en supposant que les deux types de matériaux sont incapables de supporter une contrainte de cisaillement en équilibre statique, ce qui fait du solide plastique un fluide. On appelle **fluide newtonien** un fluide dont la loi contrainte – vitesse de déformation est linéaire (Figure 3). La constante de proportionnalité est appelée viscosité, décrite dans un cas à une dimension (1D) comme $\tau = \mu \dot{\gamma}$ ou τ est la contrainte de cisaillement, μ est la viscosité et $\dot{\gamma}$ est le gradient de vitesse ($\dot{\gamma} = \partial v_y / \partial y$). Pour un fluide newtonien, la viscosité, par définition, ne dépend que de la température, de la pression et de sa composition chimique, non des forces agissant sur le volume de référence. Un fluide est dit **non newtonien** lorsque sa vitesse de déformation (le taux de cisaillement) n'est pas directement proportionnelle à la force qu'on lui applique. Il existe plusieurs types classiques de fluides non newtoniens : (a) dilatant, (b) pseudo-plastique et (c) Bingham (voir la légende de la Figure 3 pour plus d'explications). Ils

ne sont d'ailleurs pas exclusifs l'un de l'autre, un même fluide pouvant présenter plusieurs de ces propriétés.

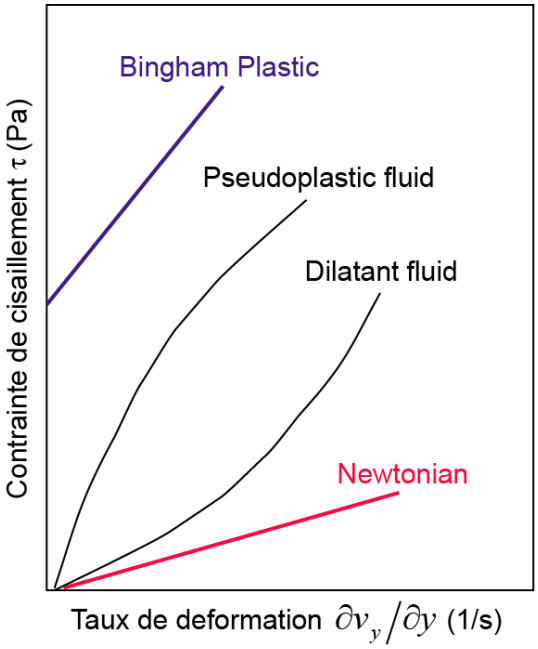

Figure 3. Comportement rhéologique d'un écoulement : Contrainte de cisaillement en fonction de la vitesse de cisaillement. La viscosité est la pente de chaque ligne. On classe le comportement rhéologique selon la manière dont varie la viscosité d'un matériel: *Newtonien* lorsque le fluide garde une viscosité constante, *Dilatant* lorsque la viscosité augmente avec le taux de cisaillement, *Pseudo-plastique* lorsque viscosité diminue en fonction du taux de cisaillement ; une matière *plastique de Bingham* se comporte comme un solide à faible contrainte mais s'écoule sous forme d'un fluide visqueux à des contraintes élevées.

Le tenseur de contraintes est un tenseur symétrique d'ordre 2 servant à décrire l'état de déformation locale résultant de contraintes ou d'efforts internes (Figure 4). L'équation constitutive qui définit n'importe quel tenseur de contraintes totales, $\overline{\overline{S}}$, est toujours composée de la somme de deux tenseurs : un tenseur sphérique $\overset{\circ}{S}$ (contrainte normale ou perpendiculaire par rapport au plan considéré) et d'un tenseur déviatorique $\overset{\circ}{\overline{\overline{S}}}$ (contrainte tangentielle par rapport au plan considéré), ainsi:

Tenseur de contrainte totale		Tenseur de contrainte normale		Tenseur de contrainte de cisaillement	
$\overline{\overline{S}}$	=	$\overset{\circ}{S}$	+	$\overset{\circ}{\overline{\overline{S}}}$	(6)

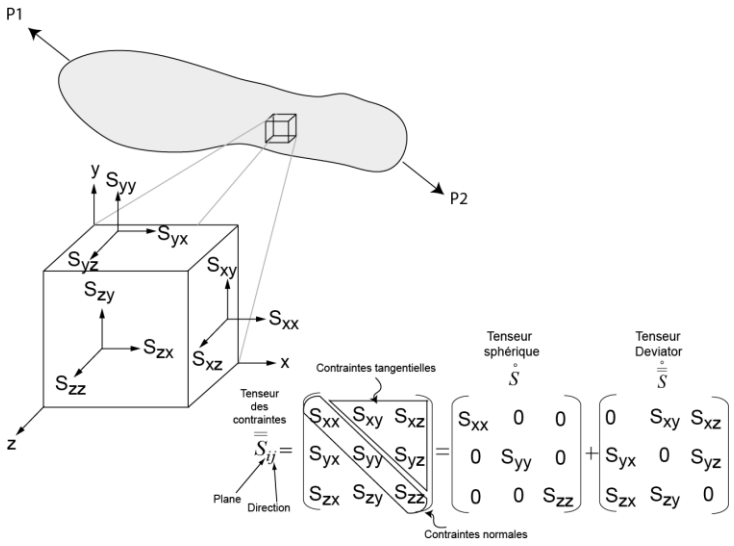

Figure 4. Représentation graphique de la tension ou des composantes du tenseur de contrainte en un point sur un corps (volume de référence). On peut remarquer que la contrainte normale s'exerce perpendiculairement au plan, alors que les contraintes de cisaillement s'exercent dans le plan.

La trace de tenseur de contraintes (voir notation tensorielle dans le Tableau A1), I_{1S}, est un invariant (i.e., une expression qui ne change pas selon la base orthogonale qu'on utilise). A partir de cette notion, on peut définir la pression hydrostatique, P, comme étant la contrainte moyenne des trois contraintes principales :

$$P = \text{la pression hydrostatique } = \frac{tr(\overline{\overline{S}})}{3} = \frac{I_{1S}}{3} = \frac{S_{kk}}{3} = \frac{S_{xx}+S_{yy}+S_{zz}}{3} \qquad (7)$$

La partie déviatorique représente la partie « cisaillement » :

$$\overset{\circ}{\overline{\overline{S}}} = \overline{\overline{S}} - \overset{\circ}{S} = \overline{\overline{S}} - P\overline{\overline{I}} = \begin{pmatrix} S_{xx} & S_{xy} & S_{xz} \\ S_{yx} & S_{yy} & S_{yz} \\ S_{zx} & S_{zy} & S_{zz} \end{pmatrix} - \begin{pmatrix} P & 0 & 0 \\ 0 & P & 0 \\ 0 & 0 & P \end{pmatrix} = \begin{pmatrix} S_{xx}-P & S_{xy} & S_{xz} \\ S_{yx} & S_{yy}-P & S_{yz} \\ S_{zx} & S_{zy} & S_{zz}-P \end{pmatrix} \qquad (8)$$

La décomposition est alors unique. On a les relations : $\begin{cases} tr(\overset{\circ}{\overline{\overline{S}}}) = 0 \\ tr(\overline{\overline{S}}) = tr(\overset{\circ}{S}) \\ \overset{\circ}{S} = tr(\overline{\overline{S}})\overline{\overline{I}} \end{cases}$ (9)

Les contraintes sont liées aux taux de déformation (i.e., tenseur de déformation), $\overline{\overline{D}}$, de manière linéaire par :

$$\overset{\circ}{S} = -P\overline{\overline{I}} + \mu^b tr(\overline{\overline{D}})\overline{\overline{I}} \qquad (10)$$

$$\overset{\circ}{\overline{\overline{S}}} = 2\mu \overset{\circ}{\overline{\overline{D}}} = 2\mu\left[\overline{\overline{D}} - \overset{\circ}{D}\right] = 2\mu\left[\overline{\overline{D}} - \frac{1}{3}tr\left(\overline{\overline{D}}\right)\overline{\overline{I}}\right] \tag{11}$$

Où μ^b est la « viscosité globale », μ est le coefficient de viscosité de cisaillement et $\overline{\overline{D}}$ est défini comme :

$$\underset{\text{taux de déformation}}{\overline{\overline{D}}} = \underset{\text{partie sphérique}}{\overset{\circ}{D}} + \underset{\text{partie deviatorique}}{\overset{\circ}{\overline{\overline{D}}}} = \overbrace{\frac{1}{3}tr\left(\overline{\overline{D}}\right)\overline{\overline{I}}}^{\text{taux de déformation volumétrique (dilatation/contraction)}} + \overbrace{\left\{\frac{1}{2}\left[\nabla\vec{v} + \left(\nabla\vec{v}\right)^{\mathrm{T}}\right] - \frac{1}{3}tr\left(\overline{\overline{D}}\right)\overline{\overline{I}}\right\}}^{\text{taux de déformation de cisaillement (distortion)}} \tag{12}$$

Ainsi, tout comme le tenseur des déformations $\overline{\overline{D}}$, le tenseur des contraintes $\overline{\overline{S}}$ ne sera déterminé que par 6 termes (Voir Annexe 1 et Figure 4). Il suffira de se donner trois contraintes normales sur la diagonale et trois contraintes tangentielles hors diagonale (tenseur symétrique).

Par souci de simplification, on réunira tous les termes liés aux viscosités sous le terme de contrainte visqueuse $\overline{\overline{\tau}}$:

$$\overline{\overline{\tau}} = \overbrace{\underset{\text{viscosité globale}}{\mu^b}\ tr\left(\overline{\overline{D}}\right)\ \underset{\text{tenseur identité}}{\overline{\overline{I}}}}^{\text{Contrainte normale visqueuse}} + \overbrace{2\ \underset{\text{visocité de cisaillement}}{\mu}\ \underset{\text{Déviateur de la vitesse de déformation}}{\overset{\circ}{\overline{\overline{D}}}}}^{\text{Contrainte visqueuse de cisaillement (trace nulle)}} \tag{13}$$

$\longleftrightarrow$

$$\overline{\overline{\tau}} = \mu^b tr\left(\overline{\overline{D}}\right)\overline{\overline{I}} + 2\mu\left(\overline{\overline{D}}_m - \frac{1}{3}tr\left(\overline{\overline{D}}\right)\overline{\overline{I}}\right) \tag{14}$$

$\longleftrightarrow$

$$\overline{\overline{\tau}} = \mu^b tr\left(\overline{\overline{D}}\right)\overline{\overline{I}} + 2\mu\overline{\overline{D}}_m - \frac{2}{3}\mu\, tr\left(\overline{\overline{D}}\right)\overline{\overline{I}} \tag{15}$$

$$\longleftrightarrow$$

$$\bar{\bar{\tau}} = \overbrace{\left(\mu^b - \frac{2}{3}\mu\right)}^{\lambda} tr\left(\bar{\bar{D}}\right)\bar{\bar{I}} + 2\mu\bar{\bar{D}}_m \tag{16}$$

Parfois les deux coefficients de viscosité : μ^b et μ sont réunis dans un seul terme appelé « deuxième coefficient de viscosité, λ »:

$$\lambda = \mu^b - \frac{2}{3}\mu \tag{17}$$

On peut donc réécrire le tenseur de contraintes visqueuses $\bar{\bar{\tau}}$ comme un tenseur qui suit une forme Newtonienne:

$$\bar{\bar{\tau}} = \lambda\, tr\left(\bar{\bar{D}}\right)\bar{\bar{I}} + 2\mu\bar{\bar{D}}_m \tag{18}$$

Il est important de retenir que tout fluide ne suivant pas cette loi est dit non-Newtonien. Ainsi le tenseur de contraintes totales est défini comme :

$$\bar{\bar{S}} = -P\bar{\bar{I}} + \bar{\bar{\tau}} \tag{19}$$

1.2.1.1. Tenseur de contrainte de la phase liquide

Ce tenseur peut s'écrire de la façon suivante :

$$\bar{\bar{S}}_m = -P_m\bar{\bar{I}} + \varepsilon_m\overbrace{\left[\lambda_m tr\left(\bar{\bar{D}}\right)\bar{\bar{I}} + 2\mu_m\bar{\bar{D}}_m\right]}^{\bar{\bar{\tau}}_m} \tag{20}$$

Où P_m est la pression du liquide qui est à son tour fonction de la densité macroscopique ρ_m du fluide (i.e. $\rho_m = \varepsilon_m\rho_m$), ε_m est la fraction volumique du liquide, μ_m est la viscosité de cisaillement (dynamique) du fluide et λ_m=-2/3μ_m. Ainsi, on obtient l'expression suivante:

$$\bar{\bar{S}}_m = -P_m\bar{\bar{I}} + 2\varepsilon_m\mu_m\bar{\bar{D}}_m - \frac{2}{3}\varepsilon_m\mu_m tr\left(\bar{\bar{D}}\right)\bar{\bar{I}} \tag{21}$$

La viscosité μ_m est définie selon le modèle « non-Arrhenian Newtonien » de *Giordano et al*. [2008] qui prend en compte le changement de viscosité du liquide en fonction de sa composition et de sa température T_m (voir détails dans le Chapitre 2). Cependant, μ_m peut aussi être défini comme constant.

1.2.1.2. Tenseur de contrainte de la phase granulaire

Nous nous sommes d'abord concentrés sur l'examen de la rhéologie globale de l'écoulement granulaire en utilisant les relations constitutives existantes dans MFIX, car elles constituent probablement l'approche la plus acceptable aujourd'hui pour modéliser les écoulements de particules [e.g., *Valentine*, 1994 ; *Patiño*, 1997 ; *Dartevelle*, 2004; *Dartevelle et al*., 2004; *Dufek and Bergantz*, 2005; *Dartevelle and Valentine*, 2007; *Ruprecht et al.*, 2008; *Dufek and Bachmann*, 2010].

Un milieu granulaire se comporte de façon très différente [*Jaeger et al*., 1996] en fonction du rapport $\varepsilon_m/\varepsilon_s$ et de la manière dont la phase dispersée transmet le mouvement à l'intérieur d'elle-même (Figure 5). Un ensemble de grains posés sur une table peut former un tas statique. Malgré des contraintes de cisaillement présentes dans le tas, le milieu reste immobile (stagnant) et se comporte donc comme un solide (Figure 5a). Les théories décrivant ce régime sont gouvernées par la mécanique des solides, spécifiquement dans le champ de « l'élasticité ». Dans ce régime, le système est dominé par les interactions de contact entre les grains. Lorsque les grains sont en mouvement, comme dans un sablier par exemple, les particules interagissent à la fois par ***collision*** et ***contacts frictionnels*** de longue durée (Figure 5b) ; lorsque les contacts entre les grains sont de type frictionnel ce régime est connu comme ***plastique***. Porté à l'extrême, si l'on secoue énergiquement un tas de billes, le milieu devient très agité avec des particules bougeant dans tous les sens, se déplaçant par translation (*cinétique*) et interagissant par collision. Dans ce régime que l'on appelle ***collisionnel***, le milieu ressemble à un gaz (Figure 5c) ; ce régime est connu comme ***visqueux***.

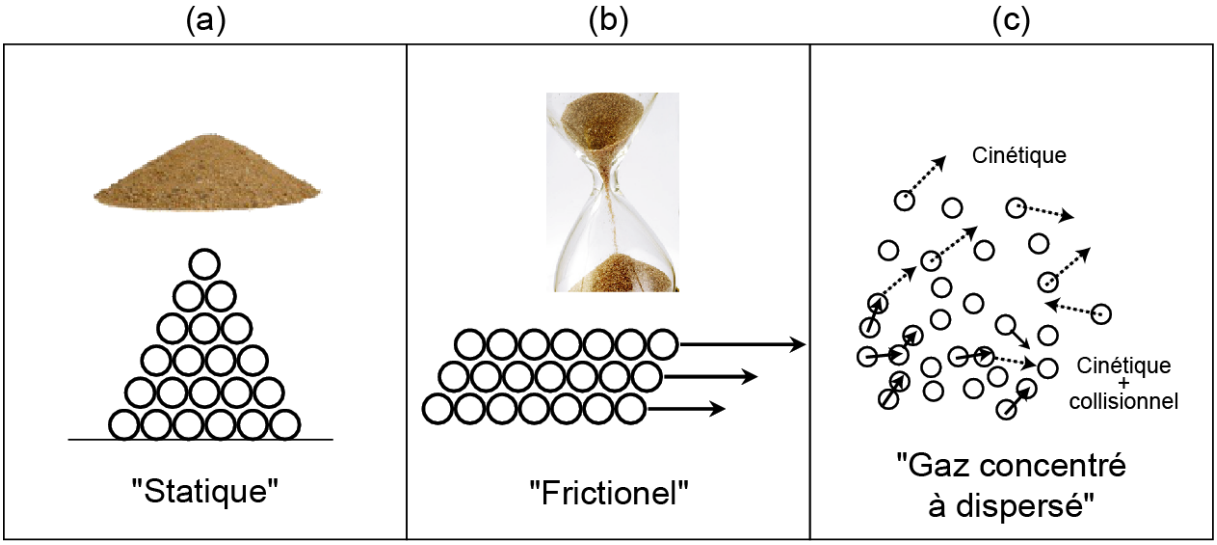

Figure 5. Le comportement rhéologique d'un milieu granulaire peut être classifié en 3 régimes principaux: (a) élastique, (b) plastique et (c) visqueux.

Une théorie de transition d'un ***régime visqueux*** à ***plastique*** a été proposée par *Johnson et Jackson* [1987] par le biais d'une fraction de vide minimale ε_m^* en conditions de compacité maximale. La combinaison des deux cas ci-dessus évite que la fraction volumique solide n'atteigne une valeur peu réaliste. MFIX a la capacité de simuler ces deux rhéologies. Voici comment MFIX traite chaque régime:

1.2.1.2.1. Tenseur Plastique/Frictionnelle

Les théories mises au point pour modéliser ce régime sont basées sur la mécanique des sols [*Schaeffer*, 1987], en spécifiant qu'à très haute concentration lorsque la fraction volumique des solides excède la fraction maximale de compactage ($1-\varepsilon_m^*$) dans le volume de référence, les grains sont sujets à des contacts qui leur font perdre leur mobilité et entraînent une dissipation par friction (plastique) et un transfert de momentum (Figure 5b).

Ce régime est valable lorsque la quantité de liquide entre les grains est minimale ($\varepsilon_m \leq \varepsilon_m^*$). Le tenseur est écrit d'une manière similaire à celle d'un fluide de type newtonien possédant à la fois une terme de pression granulaire, P_s^{P}, et un terme de contrainte visqueuse $\overline{\overline{\tau}}_s^{\text{P}}$ représentée par la contribution du deuxième coefficient de viscosité, ${}^{\text{P}}\lambda_s^b$, et de la viscosité de cisaillement (frictionnelle ou plastique) μ_s^{P} :

$$\overline{\overline{S}}_s^{\,P} = -P_s^{\,P}\,\overline{\overline{I}} + \overbrace{\lambda_s^P tr\left(\overline{\overline{D}}_s\right)\overline{\overline{I}} + 2\mu_s^P \overline{\overline{D}}_s}^{\overline{\overline{\tau}}_s^P} \tag{22}$$

Où l'exposant P définit le caractère « frictionnel ou plastique ».

Cependant, nous avons utilisé le modèle de *Schaeffer* [1987] dans lequel le deuxième coefficient de viscosité est égale à zéro ($\lambda_s^P = 0$) ; ce qui nous permet de réécrire l'équation antérieure comme suit :

$$\overline{\overline{S}}_s^{\,P} = -P_s^{\,P}\,\overline{\overline{I}} + 2\mu_s^P \overline{\overline{D}}_s \tag{23}$$

Où la pression granulaire P_s^P est définie comme l'a fait *Jenike* [1987] ; ceci donne à l'écoulement granulaire la possibilité d'une « certaine dose de compressibilité » :

$$P_s^P = 10^{24}\left(\varepsilon_m^* - \varepsilon_m\right)^{10}\varepsilon_s \tag{24}$$

La viscosité de cisaillement μ_s^P n'est plus la traditionnelle « Newtonienne », mais elle est exprimée en fonction de la quantité de grains (à travers le terme de pression granulaire) et de l'angle de friction interne ou de frottement ϕ :

$$\mu_s^P = \min\left[\frac{P_s^P \sin\phi}{2\sqrt{I_{2D}}}; \mu_s^{max}\right] \tag{25}$$

Avec $\mu_s^{max} = 100$ Pa s et I_{2D} étant le deuxième invariant du déviateur du tenseur de déformation (Tableau A1).

L'angle de frottement, ϕ, a une interprétation physique simple, étant lié à l'angle de repos, θ, représentant l'angle maximum possible que peut prendre la pente d'un tas de matière granulaire (Figure 6). Mathématiquement :

$$\theta = a\phi + b \tag{26}$$

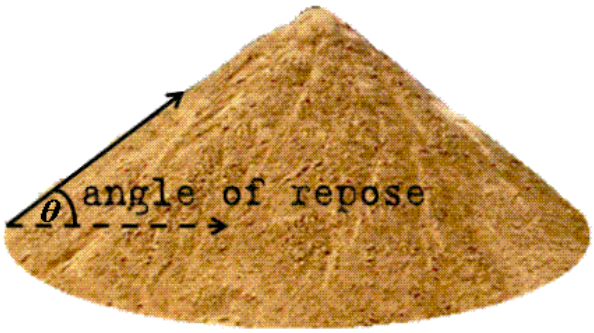

Figure 6. Tas de sable indiquant l'angle de repos.

Où θ est l'angle de repos et *a* et *b* sont des constantes liées à la cohésion et à la forme des particules. Cependant dans des matériaux non-cohérents (sans cohésion) dont les particules sont très petites, l'angle du tas au repos coïncide avec l'angle de frottement interne.

L'angle de friction interne ϕ a été testé pour le modèle final (en fixant ϕ à 0 et 24°), car si $\phi = 0$, les calculs peuvent prédire une circulation de grains non-physique dans les garnissages [*Syamlal et al*, 1993]. Nous n'avons pas trouvé de différence selon que l'on utilise $\phi = 0$ ou $\phi = 24°$ (voir détails dans le Chapitre 2).

1.2.1.2.2. Tenseur Cinétique-Collisionnel

Les équations utilisées pour traiter ce régime sont basées sur les théories d'écoulement cinétique-collisionnel, proche du comportement des gaz denses tel que l'a défini Chapman-Enskog [*Chapman et Cowling*, 1970] modifié ensuite par les travaux de *Jenkins et Savage* [1983], *Lun et al.* [1984], *Ding et Gidaspow* [1990] et *Gidaspow* [1994], qui ont pour objectif la prise en compte de la nature inélastique des collisions entre grains. Dans la partie diluée de l'écoulement (Figure 5c), les grains se déplacent au hasard par transport cinétique (déplacement de particules) lors de leur interaction avec le fluide. À concentrations supérieures (Figure 5c), les particules seront également transportées par collisions binaires de grain à grain à un temps donné.

Ce régime est valable lorsque la quantité de liquide présente entre les grains est supérieure à la fraction inter-granulaire minimale ($\varepsilon_m > \varepsilon_m^*$) et le tenseur est écrit d'une manière similaire à celle d'un fluide de type newtonien possédant à la fois une terme de pression granulaire, P_s^{v}, et un terme de contrainte visqueuse $\overline{\overline{\tau}}_s^{\mathrm{v}}$ représentée par la contribution du deuxième coefficient de viscosité, λ_s^{v}, et de la viscosité de cisaillement (visqueuse) μ_s^{v} :

$$\overline{\overline{S}}_s^{\,v} = -P_s^{\,v}\overline{\overline{I}} + \overbrace{\lambda_s^v tr\left(\overline{\overline{D}}_s\right)\overline{\overline{I}} + 2\mu_s^v \overline{\overline{D}}_s}^{\overline{\overline{\tau}}_s^{\,v}} \tag{27}$$

Où l'exposant V définit le caractère « visqueux ».

La pression granulaire, P_s^v, le deuxième coefficient de viscosité, λ_s^v, et la viscosité de cisaillement (visqueuse) μ_s^v sont définis comme suit :

$$P_s^v = K_1 \varepsilon_s^2 \Theta_s \tag{28}$$

$$\lambda_s^v = K_2 \varepsilon_s \sqrt{\Theta_s} \tag{29}$$

$$\mu_s^v = K_3 \varepsilon_s \sqrt{\Theta_s} \tag{30}$$

Où K_1, K_2 et K_3 sont des constantes de contrainte granulaire (dont les unités sont kg/m^3, kg/m^2, kg/m^2), ε_s est la fraction de cristaux, et Θ_s est la ***température granulaire*** (dont l'unité est m^2/s^2) qui à son tour dépend d'une autre constante granulaire K_4 (ayant pour unité kg/m^4). *Lun et al.* [1984] et *Syamlal* [1987] ont introduit ces constantes dans le calcul en considérant les collisions binaires et inélastiques entre grains.

Les constantes granulaires sont définies comme suit :

$$\mathrm{K}_1 = 2(1+e)\rho_s \mathrm{g}_o \tag{31}$$

$$\mathrm{K}_2 = \frac{4 d_p \rho_s (1+e)\varepsilon_s \mathrm{g}_o}{3\sqrt{\pi}} - \frac{2}{3}\mathrm{K}_3 \tag{32}$$

$$\mathrm{K}_3 = \frac{d_p \rho_s}{2}\left[\frac{\sqrt{\pi}}{3(3-e)} + \frac{2\sqrt{\pi}(1-e)(3e-1)\varepsilon_s \mathrm{g}_o}{15(3-e)} + \frac{8\varepsilon_s \mathrm{g}_o (1+e)}{5\sqrt{\pi}}\right] \tag{33}$$

$$\mathrm{K}_4 = \frac{12\left(1+e^2\right)\rho_s \mathrm{g}_o}{d_p\sqrt{\pi}} \tag{34}$$

Dans laquelle e est le ***coefficient de restitution*** donné par le rapport des vitesses avant et après l'impact grain à grain, variant de 0 à 1 (0 pour des collisions parfaitement inélastiques et

1 pour des collisions parfaitement élastiques) et g_o est ***la fonction de distribution radiale***. Nous définissons e, g_o et Θ_s à continuation :

Le ***coefficient de restitution*** est défini mathématiquement comme :

$$e = \frac{\mathrm{k}\bullet\vec{C}_{s2} - \mathrm{k}\bullet\vec{C}_{s1}}{\vec{C}^{\circ}_{s12}} \qquad (35)$$

Où k est un vecteur unitaire passant par les centres des particules 1 à 2, $\vec{C}_{s1}$ et $\vec{C}_{s2}$ sont les vitesses de chaque particule après collision et $\vec{C}^{\circ}_{s12}$ est la vitesse relative entre particules avant collision (Figure 7).

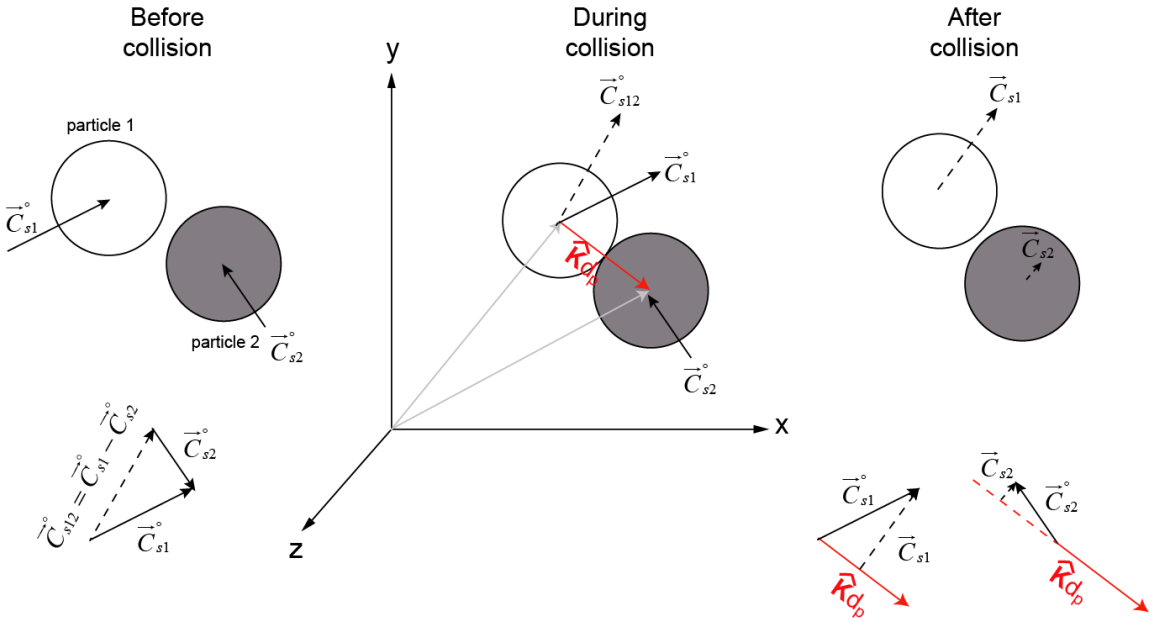

Figure 7. Configuration de deux particules en collision

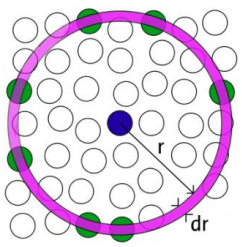

Figure 8. Calcul de g_0 en fonction de la distance pour une cellule donnée.

La ***fonction de distribution radiale au contact*** g_0 est un facteur de correction qui modifie la probabilité de collision à l'intérieur d'une phase granulaire lorsque celle-ci s'approche de la compaction, empêchant une sur-compaction des grains (Figure 8). Nous avons utilisé l'équation d'état pour des sphères solides de *Lebowitz* [1964], qui est la plus couramment utilisée et définie comme :

$$g_o = \frac{1}{\varepsilon_m} + \frac{3}{2}\frac{\varepsilon_s}{\varepsilon_m^2} \tag{36}$$

Les grains peuvent se déplacer librement et entrer éventuellement en collision avec d'autres particules, ce qui entraîne leur vibration. La vitesse instantanée d'une particule, $\vec{C}_s$, peut être décomposée en une vitesse moyenne « hydrodynamique », $\vec{v}_s$, et en une vitesse variant de manière aléatoire représentant la vibration de la particule, $\vec{\mathrm{C}}_s$. La «***température granulaire***», Θ_s, est associée à cette vitesse de fluctuation aléatoire :

$$\Theta_s = \frac{1}{3}\langle \vec{\mathrm{C}}_s \vec{\mathrm{C}}_s \rangle \tag{37}$$

Où $\vec{\mathrm{C}}_s = \vec{C}_s - \vec{v}_s$

La température granulaire est une quantité conservée qui peut être évaluée par une équation de transport de forme similaire à celle de Navier-Stokes. En négligeant les contributions de convection et de diffusion, *Syamlal* [1987] a résolu cette équation de manière algébrique comme :

$$\Theta_s = \left[\frac{-\mathrm{K}_1 \varepsilon_s tr\left(\overline{\overline{D}}_s\right) + \sqrt{\left(\mathrm{K}_1 \varepsilon_s tr\left(\overline{\overline{D}}_s\right)\right)^2 + 4\mathrm{K}_4 \varepsilon_s \left(\mathrm{K}_2 tr^2\left(\overline{\overline{D}}_s\right) + 2\mathrm{K}_3 tr^2\left(\overline{\overline{D}}_s\right)\right)}}{2\varepsilon_s \mathrm{K}_4} \right]^2 \tag{38}$$

1.2.2. Interaction entre fluide et particules

Pour conclure la description des équations qui constituent les équations de quantité de mouvement, on doit définir les ***forces de friction***, F_{ms}, causées par le déplacement relatif entre fluide et une particule sphérique solide [*Crowe et al*, 1977, p. 68] :

$$F_{ms} = 6\pi\mu_m R_p V_s = 3\pi\mu_m d_p V_s \tag{39}$$

Où d_p est le diamètre de la particule sphérique (R_p est son rayon), V_s est la vitesse de la particule dans un fluide incompressible en écoulement laminaire et de viscosité constante μ_m. Où en termes de différence de vitesse entre le liquide et la particule on a [*Crowe et al*, 1977, p. 69]:

$$\vec{F}_{ms} = 3\pi\mu_m d_p\left(\vec{v}_s - \vec{v}_m\right) = 6\pi\mu_m R_p\left(\vec{v}_s - \vec{v}_m\right) \tag{40}$$

Où $\left(\vec{v}_s - \vec{v}_m\right)$ est la vitesse de la particule par rapport au fluide qui l'entoure.

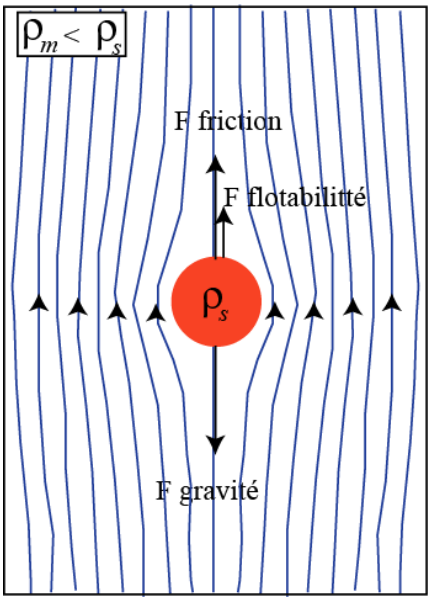

Figure 9. Ecoulement rampant d'une sphère dont la densité est inférieure à celle du liquide qui l'entoure: lignes de courant, force de flottation opposée à celle de gravité et de friction $\rho_s < \rho_m$.

Ces équations scalaire et vectorielle sont connues comme la ***force de friction de Stokes*** [Voir dérivation par exemple en *Turcotte et al*. 2002 ; p. 254-257 ; *Crowe et al* 1977 ; p. 68] qui est composée de la somme de deux forces de friction : la friction due à la pression ($2\pi\mu_m R_p V_s$) et la friction due à la viscosité ($4\pi\mu_m R_p V_s$) :

$$F_{ms} = \overbrace{2\pi\mu_m R_p V_s}^{\text{friction de pression}} + \overbrace{4\pi\mu_m R_p V_s}^{\text{friction visqueuse}} = \overbrace{6\pi\mu_m R_p V_s}^{\text{friction totale}} \tag{41}$$

La force de friction totale peut être égalisée aux forces de flottabilité et gravité en suivant la deuxième loi de Newton :

$$\overbrace{m_s \frac{dV_s}{dt}}^{\text{mass fois l'acceleration}} = \overbrace{m_s g \frac{\rho_m}{\rho_s}}^{\text{buoyancy ou flottation}} - \overbrace{m_s g}^{\text{poids}} - \overbrace{6\pi\mu_m R_p V_s}^{\text{friction totale}} \tag{42}$$

Où m_s est la masse de la particule. Ici la force nette sur la particule est égale à zéro $\left(m_s \frac{dV_s}{dt} = 0\right)$: la particule n'accélérera plus et elle atteindra le régime permanent dans lequel la ***vitesse terminale*** ou ***vitesse de Stokes***, V_s, d'une particule reste constante :

$$V_s = \frac{2}{9}\frac{(\rho_s - \rho_m) g R_p^2}{\mu_m} = \frac{1}{18}\frac{(\rho_s - \rho_m) g d_p^2}{\mu_m} \tag{43}$$

Si $\rho_s > \rho_m$ la vitesse V_s est verticalement orientée vers le bas et si $\rho_s < \rho_m$ la vitesse est orientée vers le haut.

En général, toute « ***force de friction***» peut être exprimée en termes d'un « ***coefficient de friction*** C_D» multiplié par un terme d'énergie cinétique [*Crowe et al*, 1977, p. 69] :

$$\vec{F}_{ms} = \overbrace{\frac{1}{2}\rho_m \left(\vec{v}_s - \vec{v}_m\right)\left|\vec{v}_s - \vec{v}_m\right|}^{\text{Energie cinétique}} C_D A_\perp \tag{44}$$

Où $A_\perp$ est la surface projetée de la particule dans la direction relative de la vitesse (i.e, $A_\perp = \pi R_p^2$) et $\left|\vec{v}_s - \vec{v}_m\right|$ est le module de la vitesse de la particule par rapport au fluide.

Dans le cas scalaire cette « ***force de friction***» est défini comme [*Turcotte and Schubert*, 2002 ; p. 257] :

$$F_{ms} = \frac{1}{2}\rho_m V_s^2 C_D A_\perp \tag{45}$$

En posant l'équation (40) comme étant égale à l'équation (44), ou l'équation (39) égale à l'équation (45), on obtient le « ***coefficient de friction*** C_D» dans le régime laminaire de Stokes:

$$C_D = \frac{\vec{F}_{ms}}{\frac{1}{2}\rho_m \left(\vec{v}_s - \vec{v}_m\right)\left|\vec{v}_s - \vec{v}_m\right| A_\perp} = \frac{3\pi\mu_m d_p \left(\vec{v}_s - \vec{v}_m\right)}{\frac{1}{2}\rho_m \left(\vec{v}_s - \vec{v}_m\right)\left|\vec{v}_s - \vec{v}_m\right| A_\perp} = \frac{24\mu_m}{\rho_m d_p \left|\vec{v}_s - \vec{v}_m\right|} = \frac{24}{Re_r} \tag{46}$$

Où Re_r est le nombre relatif de Reynolds basé sur la vitesse relative entre le liquide et la particule :

$$Re_r = \frac{d_p \left| \vec{v}_s - \vec{v}_m \right| \rho_m}{\mu_m} \tag{47}$$

Dans le cas scalaire, lorsqu'on égalise les équations (39) et (45), le nombre de Reynolds issu de cette opération est égal à $Re = \frac{d_p V_s \rho_m}{\mu_m}$; c'est-à-dire que la différence de vitesse exprimée dans l'équation (47) devient $\left| \vec{v}_s - \vec{v}_m \right| = V_s$. Autrement dit ce résultat s'applique lorsque le fluide reste stagnant par rapport à la particule (cas typique de Stokes). Une extension de la loi de Stokes pour une bulle avec une surface mobile a été calculée par Hadamard-Rybczynski. Nous expliquerons ce cas en détail dans le Chapitre 4.

Pour un cas 3D l'équation de mouvement définie pour le cas scalaire 1D (équation 42) peut s'écrire de la manière suivante [comme *Crowe et al*, 1997 ; p.77]:

$$m_s \frac{d\vec{v}_s}{dt} = \overbrace{\rho_m \vec{g} V_p}^{\substack{\text{force de buoyancy} \\ \text{ou force de flottation}}} - \overbrace{m_s \vec{g}}^{\substack{\text{force de corps ou} \\ \text{poids}}} - \overbrace{6\pi\mu_m R_p f \left(\vec{v}_m - \vec{v}_s \right)}^{\substack{\text{force de friction} \\ \text{totale}}} \tag{48}$$

Où V_p est le volume de la particule et f est le « ***facteur de friction*** » qui est à son tour le rapport entre le « ***coefficient de friction*** C_D » et « ***la friction de Stokes*** » ainsi :

$$f = C_D \frac{Re_r}{24} \tag{49}$$

Le coefficient de C_D défini dans les équations (46) et (49) sont seulement valide lorsque *Re* < 1. A nombre de *Re* plus grand, le coefficient C_D s'écarte de l'équation (46). On peut noter que $f = 1$ pour le cas plus simple de la friction de Stokes (Re_r < 1). Lorsque les forces d'inertie

augmentent, de la turbulence est créée dans le sillage de la particule (Figure 10) ; le nombre de Reynolds devient plus grand et le facteur de friction, f, antérieur n'est plus valable.

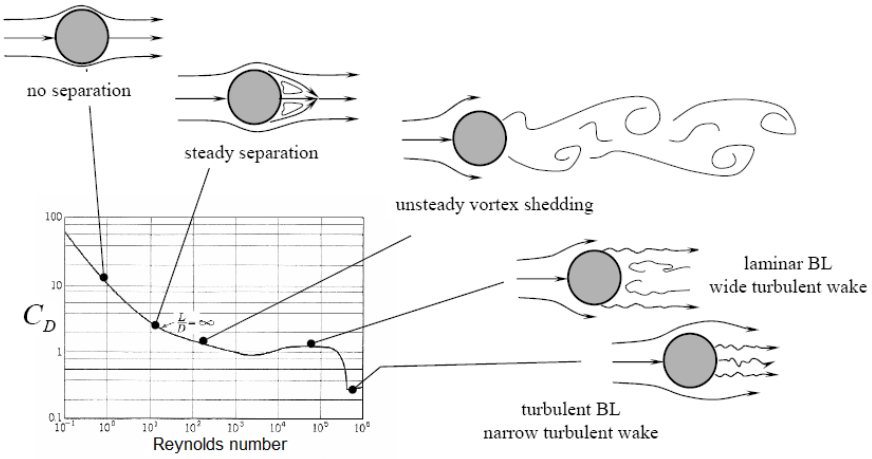

Figure 10. Variations du coefficient de friction ou de traînée, C_D, en fonction du nombre de Reynolds pour une particule sphérique.

Dans la littérature il existe plusieurs relations (à partir de données issues des expériences) pour définir f en fonction du nombre de Reynolds. Dans notre modèle MFIX, pour définir une telle friction, nous utilisons celle choisie par *Syamlal et O'Brien* [1987]. Elle s'avère appropriée pour une plage de fraction de vide de 0.5 à 0.6 et se réduit de manière correcte à une formule pour un coefficient de friction d'une particule unique, lorsque la fraction de vide s'approche de 1.0 :

$$F_{ms} = \frac{3\varepsilon_s \varepsilon_m \rho_m}{4V_r^2 d_p} \overbrace{\left(0.63 + 4.8\sqrt{V_r / Re_r}\right)}^{C_D = C_D(Re_r, \varepsilon_s)} \left|\vec{v}_s - \vec{v}_m\right| \tag{50}$$

Où le rapport de la vitesse terminale de décantation d'un système multi-particulaire à celle d'une particule unique isolée, V_r, s'écrit :

$$V_r = 0.5\left(A - 0.06Re_r + \sqrt{(0.06Re_r)^2 + 0.12Re_r(2B - A) + A^2}\right) \tag{51}$$

$$\text{Où } A = \varepsilon_m^{4.14} \text{ et } B = \begin{cases} 0.8\varepsilon_m^{1.28} & if\ \varepsilon_m \le 0.85 \\ \varepsilon_m^{2.65} & if\ \varepsilon_m \le 0.85 \end{cases} \tag{52}$$

Finalement, il existe une équation générale pour résoudre le mouvement d'une particule isolée dans un fluide non uniforme. L'équation BBO (Basset-Boussinesq-Oseen) prend en compte les effets de l'accélération et du nombre de *Re* à travers ce facteur f. Cette équation réunit alors plusieurs forces : la *force de friction* et la *force de corps* (due à la gravité) de la particule exprimée dans l'équation antérieure, la *force de flottabilité* de la particule due au *gradient de pression* et à *la contrainte de cisaillement* de la phase porteuse, *la force de masse virtuelle* [i.e. la moitié de la masse du fluide déplacé par la particule multipliée par l'accélération relative du fluide par rapport à la particule, *Crowe et al*, 1997 ; p. 83] et *la force de Basset* [*Crowe et al*, 1997 ; p. 86]. Après réarrangement du terme de pression et du tenseur de contrainte de cisaillement de la phase porteuse en fonction de l'accélération de fluide et du poids de fluide (équation typique de Navier-Stokes), l'équation BBO qui exprime l'accélération d'une particule dans un écoulement non-uniforme prend la forme suivante [*Crowe et al*, 1997 ; p. 87]:

$$\left(1+\frac{C_{vm}}{2}\frac{\rho_m}{\rho_s}\right)\frac{d\vec{v}_s}{dt}=\frac{f}{\tau_v}\left(\vec{v}_m-\vec{v}_s\right)+\left(1+\frac{C_{vm}}{2}\right)\frac{\rho_m}{\rho_s}\dot{\vec{v}}_m+C_B\sqrt{\frac{9\rho_m}{2\pi\rho_s\tau_v}}\left[\int_0^t\frac{\dot{\vec{v}}_m-\dot{\vec{v}}_s}{t-t'}dt'+\frac{\left(\vec{v}_m-\vec{v}_s\right)_0}{\sqrt{t}}\right]+\vec{g}\left(1-\frac{\rho_m}{\rho_s}\right) \quad (53)$$

Où $\tau_v=\frac{\rho_s g d_p^2}{18\mu_m}$ est le temps de réponse de la vitesse de la particule [*Crowe et al*, 1997 ; p. 71], C_{vm} [*Crowe et al*, 1997 ; p. 83] et C_B [*Crowe et al*, 1997 ; p. 86] sont des paramètres fonction de l'accélération. Cette équation, fort complète, est souvent simplifiée pour faciliter sa résolution.

Pour en terminer avec les équations de mouvement, nous ajouterons que selon les observations géologiques et expérimentales à haut température et pression, le comportement rhéologique d'un magma peut être classé en fonction de sa fraction volumique solide [*Pinotti et al*. 2010] : (i) un premier seuil rhéologique lorsque ε_s < 30 vol.%, en dessous duquel il se comporte pratiquement comme un fluide newtonien et (ii) un second seuil rhéologique lorsque 30 < ε_s < 70 vol.% en dessous duquel le magma se comporte de manière viscoplastique. (iii) Au-delà d'un troisième seuil défini pour ε_s > 70 vol.%, le magma peut se fracturer ; mais si sa vitesse de déformation est lente il peut se comporter comme un fluide

newtonien selon des processus de déformation favorisés par le liquide [i.e., *Caricchi et al*. 2007]. Par exemple, dans la vitesse de déformation lente, le magma avec une fraction importante de cristaux (ε_s > 85 vol.%) peut même se comporter comme un fluide newtonien; Cependant, à taux plus élevé de déformation avec le même pourcentage de cristaux le magma va se comporter comme un corps rigide [*Pinotti et al*. 2010].

Nous traitons dans notre modèle deux régimes de déformation : le régime visqueux si ε_s < 65 vol.% et le régime plastique si $\varepsilon_s \geq$ 65 vol.%. Ceci est une simplification qui reflète l'incertitude actuelle sur la rhéologie des magmas à forte variation de cristallinité. Quelques études récentes sur la théorie des écoulements multiphasiques ont défini des seuils rhéologiques particuliers. Par exemple, *Caricchi et al*. [2007] indique que le caractère non newtonien d'un magma prédomine lorsqu'il dépasse une cristallinité de plus de 50 vol.%; *Dufek and Bergantz* [2005] ont supprimé le régime plastique et conservé le régime visqueux pour caractériser leur modèle d'écoulement dans un conduit volcanique.

1.3. Les équations de bilan d'Energie

Les formes différentielles de l'équation d'énergie pour les phases liquide et solide sont respectivement définies comme suit:

$$\varepsilon_m \rho_m C_{pm} \left(\frac{\partial T_m}{\partial t} + \vec{v}_m \cdot \nabla T_m \right) = -\nabla \cdot \vec{q}_m + \gamma_{ms} \left(T_s - T_m \right) \tag{54}$$

$$\varepsilon_s \rho_s C_{ps} \left(\frac{\partial T_s}{\partial t} + \vec{v}_s \cdot \nabla T_s \right) = -\nabla \cdot \vec{q}_s - \gamma_{ms} \left(T_s - T_m \right) \tag{55}$$

Le terme de gauche des équations d'énergie spécifie que le taux net de variation de température à l'intérieur d'une cellule du maillage est égale à la somme du travail résultant du terme de droite : (1) la conduction de chaleur à l'intérieur de la phase et (2) le transfert de chaleur entre phases. Dans notre étude, nous négligeons la dissipation visqueuse et le travail du aux forces de friction.

La conduction thermique $\vec{q}_m$ est décrite par la loi de Fourier pour un liquide et des grains, comme respectivement :

$$\vec{q}_m = \varepsilon_m k_m \nabla T_m \tag{56}$$

$$\vec{q}_s = \varepsilon_s k_s \nabla T_s \tag{57}$$

Où k est la conductivité thermique.

Le transfert de chaleur entre phases est fonction de la différence de température entre celles-ci et du coefficient de transfert de chaleur γ_{ms} défini par *Syamlal et al* [1993] comme étant :

$$\gamma_{ms} = \frac{6 k_m \varepsilon_s Nu}{d_p^2} \tag{58}$$

Où le nombre de Nusselt défini ci-dessous est applicable pour une plage de fraction de solides $0.35 < \varepsilon_s < 1.0$:

$$Nu = \left(7 - 10_s + 5\varepsilon_m^2\right)\left(1 + 0.7 Re_s^{0.2} Pr^{1/3}\right) + \left(1.33 - 2.4\varepsilon_m + 1.2\varepsilon_m^2\right) Re_s^{0.7} Pr^{1/3} \tag{59}$$

Où le nombre de Prandtl est défini par : $Pr = \frac{C_{pm}\mu_m}{k_m}$ (60)

Dans les magmas, les cristaux ont de faibles vitesses relative par rapport au liquide, ce qui cause $Nu \cong 1$. Les équation d'énergie sont couplées entre elles en raison du transfert de chaleur entre phases et partiellement découplées avec les autres équations du système dans l'algorithme de résolution [*Syamlal et al*, 1993].

2. Conditions initiales et aux limites du système

Pour être résolues, les équations expliquées dans la section précédente ont besoin de conditions initiales (à l'intérieur d'un système) et aux limites (aux frontières). Ces conditions sont celles de vitesse $\vec{v}$, température T, pression P, géométrie, nombre et quantité de phases

présentes. Elles peuvent être groupées comme suit, en sachant qu'elles peuvent s'exclure entre elles :

(i) Conditions géométriques : celles-ci définissent les parois du système.

(ii) Conditions des phases composantes : pourcentage initial et aux parois de chaque phase (solide, gaz, liquide) qui forment un système donné.
(iii) Conditions limites cinétiques : NSW (pas de glissement aux parois), FSW (paroi avec glissement libre). En plus, FSW et NSW peuvent également être utilisées pour définir la limite de glissement dans une même phase (liquide, solide ou gaz). On peut aussi spécifier l'entrée et/ou la sortie de masse sous une condition de pression et/ou vitesse donnée.
(iv) Conditions de pression : elles peuvent être spécifiées selon le type de condition limite cinétique. Si elles ne sont pas spécifiées, la simulation commencera avec un gradient de pression hydrostatique.
(v) Conditions thermiques : les parois peuvent être non-conductrices (pas d'interaction avec le milieu qu'elles entourent) ou conductrices ; cette dernière peut être caractérisée a travers par la valeur d'un coefficient de transfert de chaleur, C_m , d'unité °C/m, comme suit:

$$\frac{\partial T_{wall_x}}{\partial n} = C_m \tag{61}$$

Où ∂/∂_n désigne la différenciation vers l'extérieur le long de la normale aux parois, et T_{wall_x} est la température de paroi en fonction de la distance.

3. Exemple d'application du modèle MFIX

Nous avons appliqué notre modèle pour reproduire une expérience analogique effectuée par *Jaupart and Brandeis* en 1986, au cours de laquelle les auteurs observent le développement de la convection dans un liquide visqueux à la suite d'un changement de température. L'analyse approfondie des résultats est présentée au Chapitre II. Nous nous focalisons ici sur la technique de mise en place d'une simulation avec MFIX. L'expérience analogique consiste à donner naissance à une convection thermique dans une cuve remplie d'huile silicone. Une caractéristique fondamentale du point de vue thermique réside dans le fait que celle-ci est refroidie par le haut et par le bas, comme l'illustre la Figure (11).

Afin de simuler des conditions de refroidissement instantané (i.e. une chute de température ΔT au temps t=0), les auteurs ont commencé leur expérience en maintenant une couche de fluide chaud et isotherme à une température T_o . Pendant ce temps, un cryostat maintenait un volume de fluide à 4°C en circuit fermé. Au temps t = 0, le fluide circulant dans le cryostat a été dévié dans le circuit incorporé aux plaques de cuivre supérieure et inférieure. Après une phase transitoire d'environ 3 minutes, la température des deux plaques avait chuté d'une valeur ΔT variant selon l'expérience (autour de 20°C). En réglant alors le cryostat à une valeur proche de cette nouvelle température, les auteurs ont réussi à stabiliser celle-ci en moins de 6 minutes à 0.1°C près. La température des limites supérieure et inférieure était donc maintenue à une valeur constante T_f après 6 minutes. Lors de l'expérience de *Jaupart et Brandeis* [1986] les conditions aux limites varient en fonction du temps (entre le moment où l'écoulement est aligné du cryostat vers la base de la cuve et celui où la température se stabilise). La vitesse de refroidissement est importante au cours des 3 premières minutes de l'expérience, jusqu'à ce que la température du cryostat soit atteinte. Elle l'est beaucoup moins pendant le reste de l'expérience, lorsque la température de la cuve est proche de celle du cryostat. Ces expériences avec différents liquides visqueux ont montré un comportement similaire : (i) la convection a commencé après environ 2 minutes, (ii) cette convection se caractérisait par la formation de plusieurs instabilités initiées dans la couche immédiatement adjacente à la plaque de cuivre supérieure, (3) ces instabilités ont atteint le fond de la cuve en 1 minute, (4) formant une couche stagnante dans le fond de la cuve.

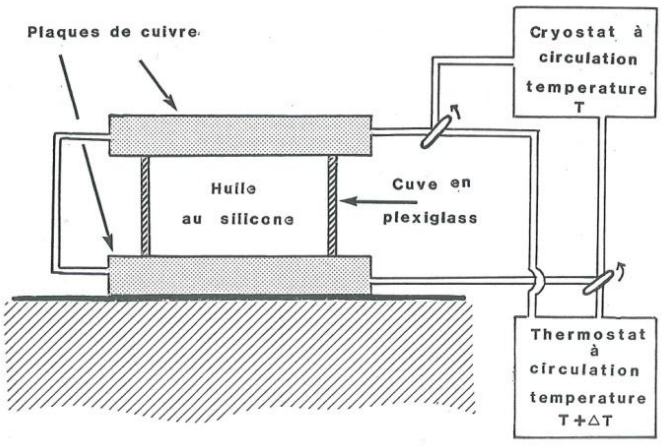

Figure 11. Description du schéma du dispositif expérimental [*Brandeis*, 1983].

3.1. Comment lancer un calcul et mettre en place l'expérience analogique avec MFIX ?

Nous donnerons ici des exemples spécifiques pour utiliser me model MFIX.

3.1.1. Le lancement d'une simulation vers le centre de calcul

Pour lancer une simulation, MFIX a besoin des informations suivantes: (i) la géométrie du système, (ii) les paramètres des caractéristiques physiques de(s) phase composante (i.e., viscosité, chaleur spécifique, densité, conductivité thermique, facteur d'expansion thermique ; Annexe 2), (iii) les conditions initiales (notées comme IC1, IC2, etc.) et aux limites du système (notées comme BC1, BC2, etc.), (iv) les paramètres permettant d'affiner le modèle numérique. Toutes ces informations vont dans un fichier nommé « mfix.dat » (Annexe 3) qui sert d'interface entre l'utilisateur et le modèle MFIX. Le modèle MFIX est composé d'environ 400 fichiers écrits en langage FORTRAN, contenant les termes qui définissent les équations de transport déterminées dans la section précédente en plus des différentes techniques de résolution numérique.

Lorsque notre modèle (fichier FORTRAN) et le fichier d'entrée (mfix.dat) sont définis, on lance le calcul sur une machine de calcul parallèle (Figure 12). Celle-ci se compose de 56 lames de calcul reparties en 4 bladecenters. 42 machines sont composées de 2 processeurs quadricoeurs et de 26Go de RAM, 14 machines sont composées de 2 processeurs hexacoeurs et de 36 Go de RAM. Le total équivaut à 504 cœurs pour une puissance de calcul de 6Tflops. La communication entre les machines se fait par l'intermédiaire de 2 réseaux: un réseau de calcul en Infiniband et un réseau d'administration en Gbit. La machine comporte un serveur frontal (Phoebus) qui assure la liaison entre les nœuds et les utilisateurs (monde extérieur) ; elle compte 2 serveurs (SYS1 et SYS2) qui assurent les services (serveur de fichiers GPFS, sauvegarde), un espace disque de 4TO et un robot d'archivage LTO4.

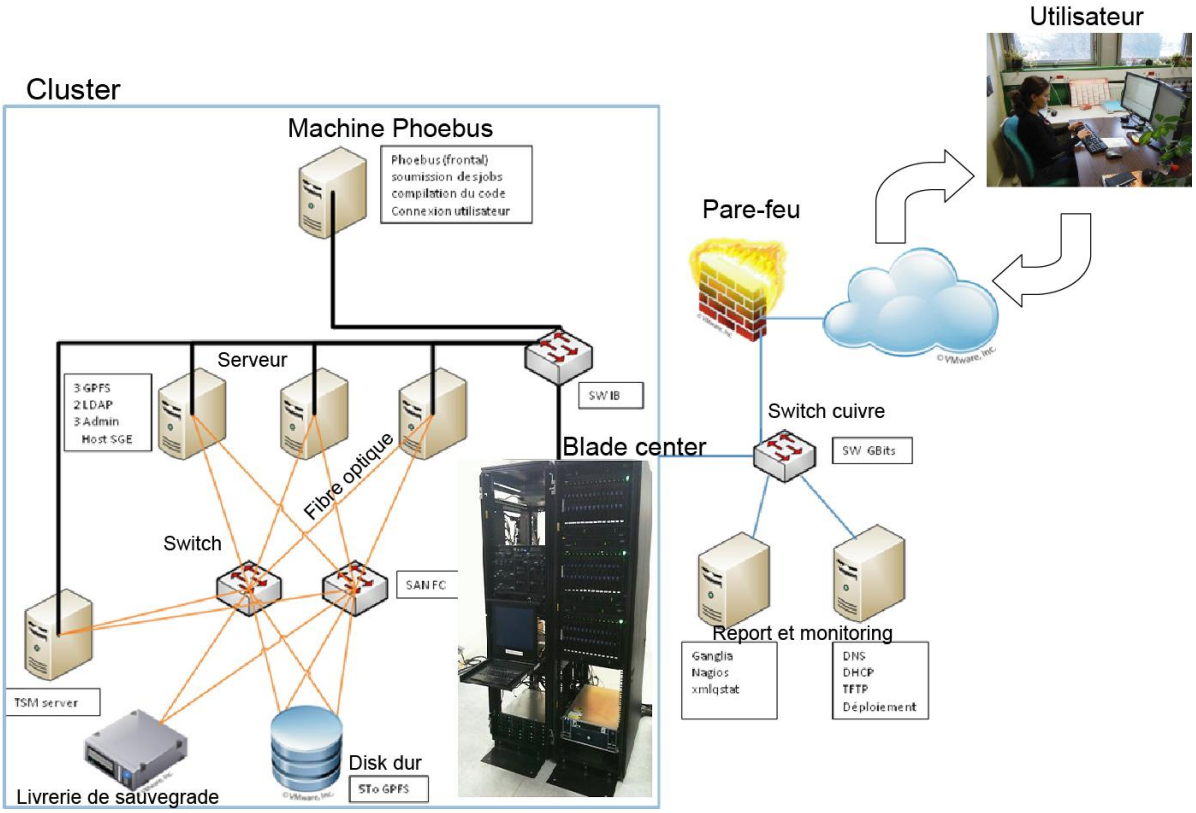

Figure 12. Centre de calcul (détails de cette machine et photo aimablement fournis par Mr. Laurent Catherine).

3.1.2 Les paramètres numériques d'affinement

Plusieurs paramètres de calcul contrôlent la convergence numérique et l'affinement d'une simulation. Ces paramètres concernent principalement la manière dont sont résolues les équations de transport et la discrétisation de notre système dans l'espace et le temps. Nous montrons ici quelques paramètres sur lesquels nous nous sommes focalisés. Dans MFIX, la progression du temps est régie par cinq paramètres: démarrage (TIME) et fin (TSTOP), pas de temps (DT), pas de temps minimum (DT_MIN) et maximum (DT_MAX). La discrétisation du domaine est contrôlée par la taille du maillage (nombre de boites). On peut considérer ce domaine comme infini dans la direction *x* (CYCLIC_X) afin de ne pas avoir de chute de pression. La solution des équations est régie par la méthode numérique utilisée (nous avons utilisé la méthode « upwinding de premier ordre »), le facteur de normalisation des équations de transport (NORM_G), le résiduel maximum acceptable des erreurs relatives aux équations de continuité et de mouvement (TOL). Parfois, pour diverses raisons, la solution peut devenir instable à moins qu'un facteur de sous-relaxation (UR_FAC) soit utilisé ; ceci permet de considérer une partie de la valeur de l'itération précédente afin de restreindre une solution et ainsi réduire les oscillations abruptes.

Obtenir une simulation satisfaisante est une opération complexe car elle requiert l'application des bonnes conditions aux limites, qui contrôlent le déroulement de la convection, tout en assurant la stabilité des paramètres numériques mentionnés ci-dessus. Nous prenons l'exemple de l'huile 47V20 (Rhodorsil® Oils référence 47V20) pour illustrer cette démarche. Nous avons testé six scenarios en variant les conditions limites et aux paramètres numériques. Les tests de sensitivité aux différentes conditions de limites et aux paramètres numériques que nous avons effectués sont résumés dans le graphique suivant. Ceux concernant les conditions aux limites seront expliquées en détail dans la section suivante.

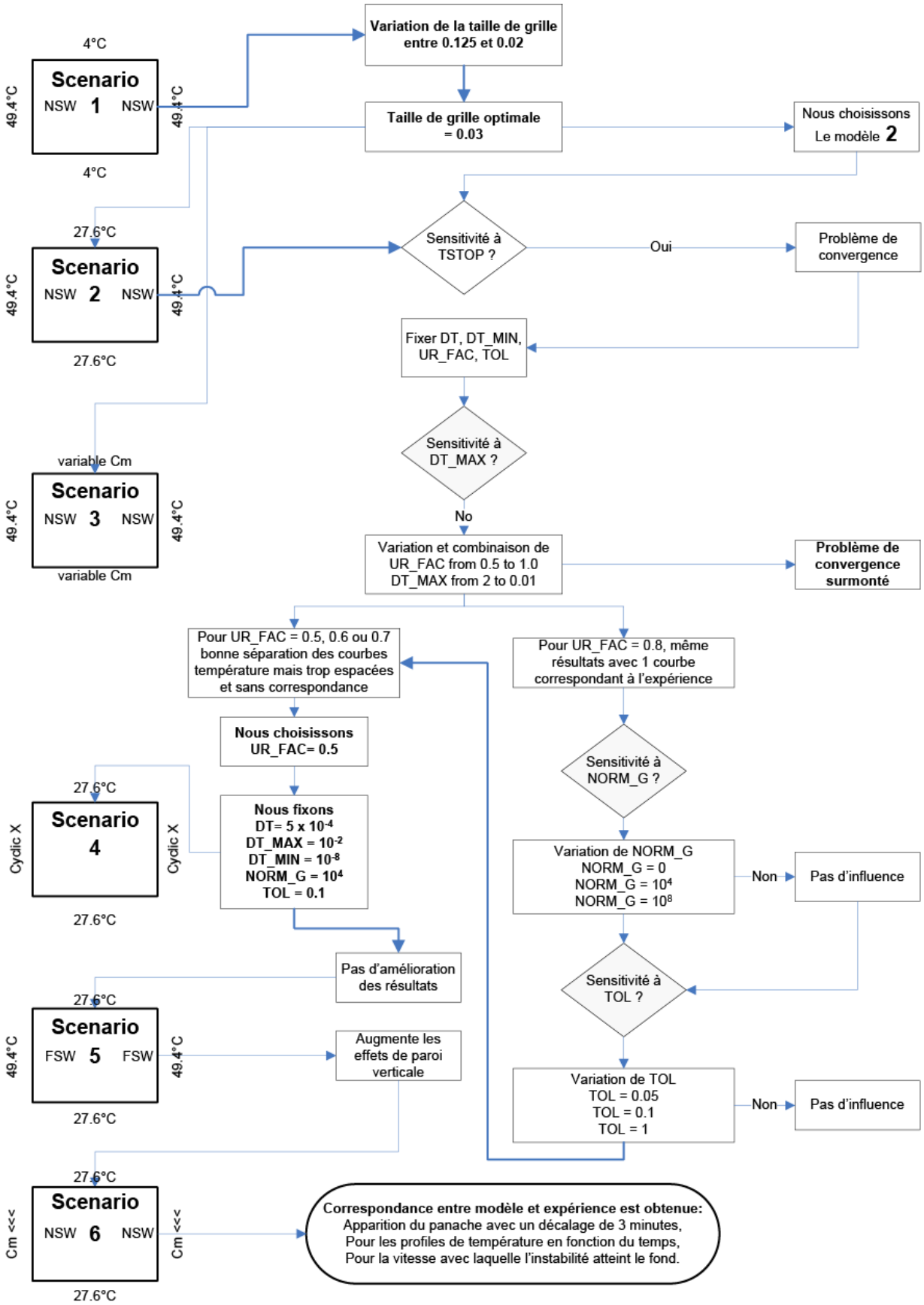

Figure 13. Logigramme des simulations (pour plus de détails sur les symboles voir *https://mfix.netl.doe.gov/documentation/Readme.pdf*)

3.1.3. Les conditions aux limites

Une fois déterminés les paramètres de calcul optimum (paramètres de raffinement numérique et conditions aux limites ; Figure 13) permettant de reproduire la convection d'une huile spécifique 47V20, nous les avons appliqués à 5 autres types d'huile (voir détails in Chapitre 2 plus Annexe 2) ; au total, nous avons donc simulé la convection de 6 huiles différentes. Nous avons utilisé les conditions aux limites suivantes:

(i) *La géométrie du système* que nous avons implémenté est en 2D et la coupe verticale représentée est en conformité avec l'expérience analogue, comme on peut le voir dans la figure suivante:

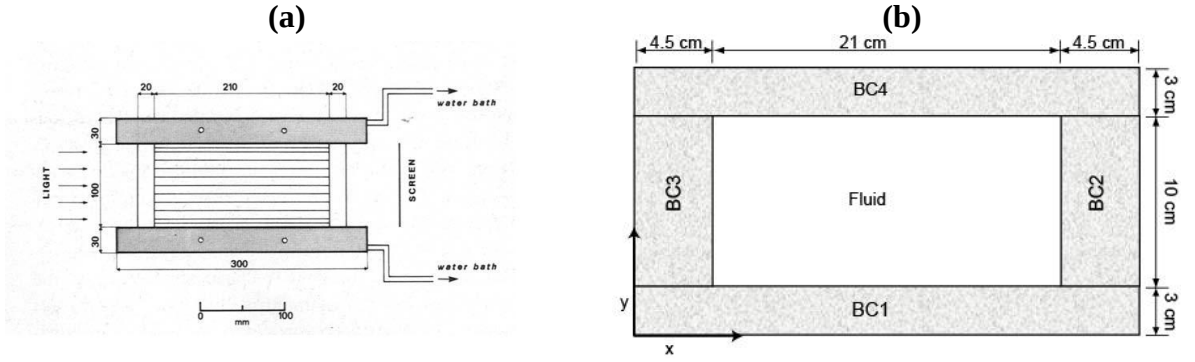

Figure 14. Détail des dimensions de la cuve de plexiglas : (a) expérience analogue [*Brandeis*, 1983]. Dans l'expérience analogique on peut noter que les parois ont 2 cm d'épaisseur, les dimensions horizontales sont de 25 x 25 cm et 10 cm de haut. Les limites supérieure et inférieure sont composées de plaques de cuivre de 3 cm d'épaisseur à travers lesquelles circule de l'eau maintenue à température constante, (b) expérience numérique. BC signifie conditions limites.

(ii) *Les paramètres physiques des huiles* sont définis pour chaque type d'huile (voir exemple en Annexe 3 pour l'huile spécifique 47V20). Ces paramètres ont un nom dans le fichier « mfix.dat » que nous indiquons ci-après entre parenthèses. Nous avons utilisé les valeurs de densité initiale ρ_o (RO_g0), viscosité dynamique (MU_g0), conductivité thermique k_m (K_g0), capacité thermique C_{pm} (C_pg0) et le coefficient de dilatation thermique thermique α, (C(2)) définis à condition de température initiale, T_o (C(1)) et répertoriées dans le manuel de Rhodorsil® Oils 47 Technical Information (Annexe 2). Ayant spécifié la valeur de la viscosité de l'huile 47V20 (MU_g0 = 0.121) dans le fichier « mfix.dat », celle-ci restera constante à chaque pas de calcul. En Annexe 4, nous présentons un fichier du modèle « calc_mu_g.f » qui calcule une viscosité variable pour un liquide silicaté; on remarque que, celle-ci ayant déjà été fixée dans le fichier « mfix.dat », sa valeur deviendra une entrée

constante de cette routine. A chaque pas de calcul, « calc_mu_g.f » entrera cette valeur (MU_g0=0.121) dans les lignes 1-2 et 22-91 de ce fichier (Annexe 4) et calculera la partie déviatorique du tenseur de contraintes. Cependant on remarque que, même si la valeur de viscosité reste constante, la densité de l'huile, ρ_m, varie en fonction de la température, T_m (voir équation 3) avec ρ_o et α qui reste constant. La densité de l'huile, ρ_m, est calculée dans un autre fichier appelé « eosg.f ».

(iii) *Les conditions thermiques et cinétiques du système* : Le scénario idéal aurait été d'introduire sous MFIX des conditions aux limites en constante évolution en fonction du temps afin de reproduire la chute de température des plaques de cuivre. Cela n'a pas été possible car cet historique de température des plaques de cuivre n'était pas disponible. Nous avons donc exécuté 6 scenarios afin de reproduire le plus fidèlement possible l'expérience de *Jaupart et Brandeis* [1986]. Ces scenarios sont les suivants :

Scénarios 1 et 2 : on a varié les températures aux limites du système afin d'apprécier l'influence de ce paramètre (Figure 15). Nous observons que le front de convection apparaît d'autant plus tôt que la différence de température entre la plaque de cuivre et l'huile silicone est importante. Cependant, nos instabilités thermiques apparaissent 2 min plus tôt que lors de l'expérience analogique.

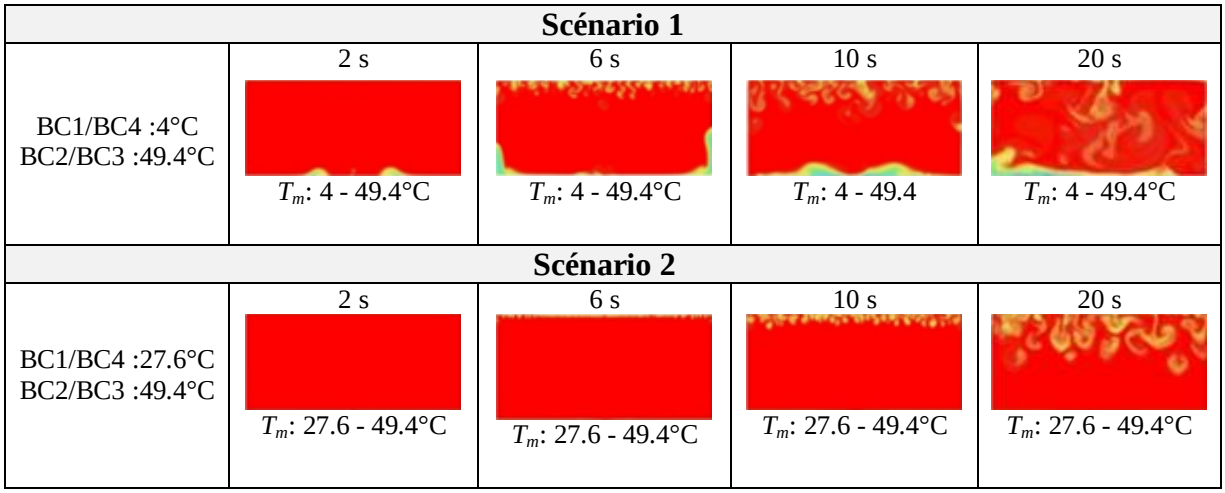

Figure 15. Cartes de températures résultant de différentes conditions appliquées aux limites: (a) Haut et bas à 4°C, (b) Haut et bas à 27.6° C. Chaque carte est accompagnée de l'échelle des températures entre les valeurs de température minimale et maximale à un temps donnée.

Scénario 3 : Comme on l'avait noté dans le scénario antérieur, le développement de la convection présente un décalage dans le temps avec le modèle analogique. En conséquence,

nous avons exécuté plusieurs nouvelles simulations numériques, changeant la valeur de la perte de chaleur au travers des plaques (C_m, équation 61). Cette valeur de C_m (dont l'unité est °C/cm) a été spécifiée en utilisant l'équation de conduction de température dans un milieu infini (Turcotte and Schubert [2002], p. 272 ; voir Chapitre 2), en prenant en compte la température aux limites : celle de la plaque de cuivre (4°C), la température de stabilisation (27.6°C) et la température ambiante (20°C). On a ainsi obtenu 4 valeurs de C_m en variant de : (a) 4°C sur une durée de 3 min (C_m = -15.13), (b) 27.6°C sur une durée de 3 min (C_m = -7.3), (c) 4°C sur une durée de 12 jours (C_m = -0.8), (d) 27.6°C sur une durée de 12 jours (C_m = -0.3). L'attribution de différentes valeurs de C_m des plaques horizontales nous permet de faire varier le délai d'apparition des instabilités. Certaines valeurs de C_m peuvent même entraîner une apparition de ces instabilités à un temps postérieur à celui de l'expérience analogique, comme on peut l'apprécier sur la Figure 16.

Scenario 3				
Temps (s)	**(a)** BC1/BC4 : C_m = -15.1 BC2/BC3 :49.4°C	**(b)** BC1/BC4 : C_m = -7.3 BC2/BC3 :49.4°C	**(c)** BC1/BC4 : C_m = -0.8 BC2/BC3 :49.4°C	**(d)** BC1/BC4 : C_m = -0.3 BC2/BC3 :49.4°C
2	 T_m : 49.1-49.4°C	 T_m : 49.3-49.4°C	 T_m : 49.4-49.4°C	 T_m : 49.3-49.4°C
20	 T_m : 48.1-49.4°C	 T_m : 48.8-49.4°C	 T_m : 48.1-49.4°C	 T_m : 49.3-49.4°C
60	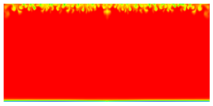 T_m : 48-49.4°C	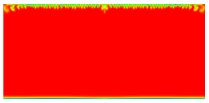 T_m : 48.5-49.4°C	 T_m : 49.3-49.4°C	 T_m : 49.3-49.4°C
180	 T_m : 47.1-49.4°C	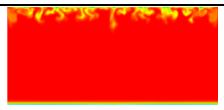 T_m : 48.3-49.4°C	 T_m : 49.3-49.4°C	 T_m : 49.3-49.4°C
300	 T_m : 47-49.4°C	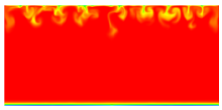 T_m : 48.2-49.4°C	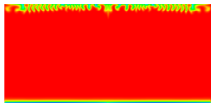 T_m : 49.3-49.4°C	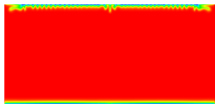 T_m : 49.3-49.4°C
420	 T_m : 48-49.4°C	 T_m : 48.1-49.4°C	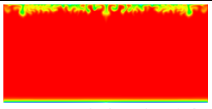 T_m : 49.3-49.4°C	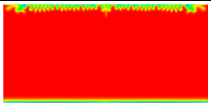 T_m : 49.3-49.4°C
480	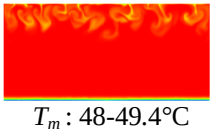 T_m : 48-49.4°C	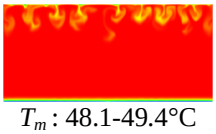 T_m : 48.1-49.4°C	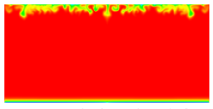 T_m : 49.3-49.4°C	 T_m : 49.3-49.4°C

Figure 16. Cartes de températures résultant de différentes conditions appliquées aux limites (voir la tête de cette figure). Chaque carte est accompagnée de l'échelle de température entre la valeur minimale et maximale des températures atteintes à un temps donné.

A la vue de ces résultats, le scenario 3c a permis de retarder l'apparition des instabilités d'un délai d'environ 2 minutes comme le montre l'expérience analogue. Cependant, l'expérience analogue indique que les instabilités arrivent au fond de la cuve en 1 minute. Le scenario 3c n'est pas complètement satisfaisant parce que les instabilités ne sont pas encore arrivées au fond de la cuve au cours des 8 minutes de la simulation. Nous en avons conclu que le modèle reproduisant de la manière la plus réaliste et la plus proche l'expérience de Jaupart et Brandeis est celui effectué à température constante, bien que les instabilités thermiques apparaissent après 6" (voir scénario 2).

Scénarios 4 et 5 : Reprenant le scénario 2, on a testé les conditions cinétiques de parois verticales du domaine. Pour cela nous avons exécuté deux simulations : une dans laquelle les parois verticales admettent l'absence de chute de pression dans la direction-*x* (condition cyclique ; voir détails dans le guide de *Syamlal et al.,* 1993) et une autre dans laquelle nous avons imposé aux parois verticales des conditions de contrainte *Free Slip Walls* (FSW). Les résultats sont les suivants :

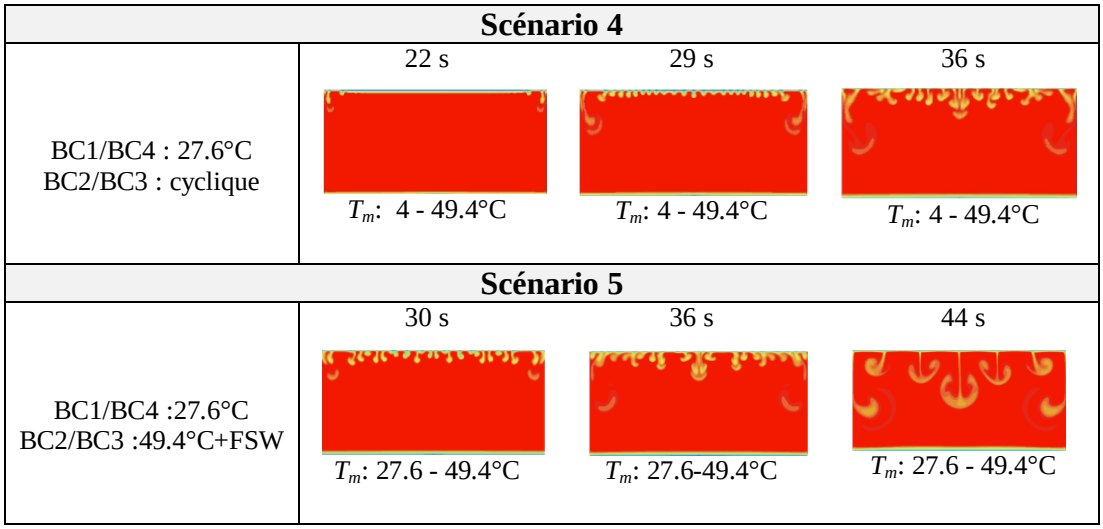

Figure 17. Cartes de températures résultant de différentes conditions appliquées aux limites (voir colonne gauche de cette figure). Chaque carte est accompagnée de l'échelle de température entre la valeur minimale et maximale des températures atteintes à un temps donnée.

A la vue de ces résultats, les instabilités thermiques apparaissent quelques secondes plus tard que celles du scénario 2 ; nous avons ainsi atteint notre objectif de retarder l'apparition des instabilités tout en gardant celles qui descendent dans la cuve dans avec un retard d'environ 1 minute. Il faut cependant noter la mise en évidence accrue des instabilités latérales, ce que nous tenterons de réduire dans le prochain scenario.

Expérience analogue BC1/BC4 : température des plaques de cuivre change de 49.4 à 4°C. BC2/BC3: isolé + NSW T_o=49.4°C	**Scenario 6** BC1/BC4 : 27.6°C+NSW BC2/BC3 : C_m = -10^{-10} T_o=49.4°C
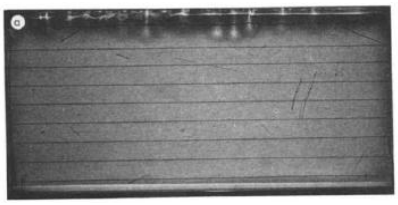 a) t_init	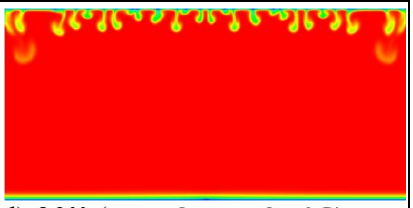 d) 30'' (T_m: 28.1 – 49.4°C)
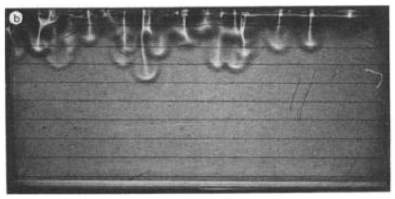 b) t_init + 7"	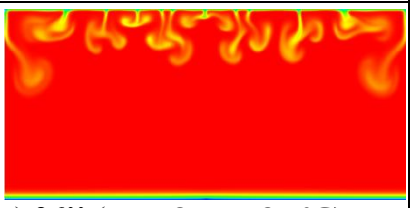 e) 36'' (T_m: 28.2 – 49.4°C)
 c) t_init + 14"	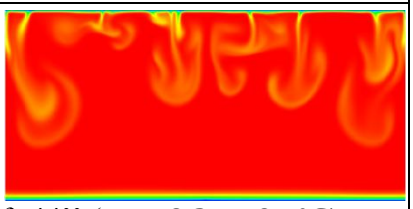 f) 44'' (T_m: 28.3 – 49.4°C)

Figure 18. Séquence d'images de la simulation numérique et d'une des expériences faites par *Jaupart et Brandeis* [1986]. Une condition initiale et deux conditions aux limites ont été prises en compte: la température initiale du cryostat, T_o, et la valeur constante T_f qui implique une chute de température d'environ 20°C pour le haut et le bas de la cuve, et l'isolation thermique des parois verticales de la cuve (C_m=-10^{-10}) (voir Tableau). Chaque carte est accompagnée de l'échelle de température entre la valeur minimale et maximale de température atteint à chaque période de la simulation.

Scenario 6 : Comme nous l'avons mentionné ci-dessus, le modèle reproduisant le plus fidèlement les résultats de Jaupart et Brandeis correspond à celui dont la température de paroi supérieure est 27.6°C ; le temps nécessaire au développement d'un front de convection est en effet plus rapide mais les instabilités atteignent le fond de la cuve en moins d'une minute. Nous avons considéré les parois verticales comme étant isolées pour voir l'influence de ce critère sur les instabilités latérales. Ceci nous a donné l'image suivante, décalée en temps par rapport à une des expériences faites par *Jaupart et Brandeis* [1986] :

On note que les instabilités latérales sont moins prononcées et moins rapides, donc on a atteint notre objectif d'en réduire l'effet. Le fait de mettre une condition cyclique ou FSW aux parois verticales (scénario 4 et 5) accélère les instabilités latérales et concentre les instabilités au centre de la cuve (Figure 17) ; ceci n'est pas observé dans l'expérience. On choisit donc le scenario 6 dont le comportement est similaire à celui de l'expérience : les températures modélisées et la vitesse de chute des instabilités sont bien en accord (voir détails in Chapitre 2). Ce scénario nous montre que subsiste encore un décalage dans le temps entre l'apparition et le développement de la convection lors de notre simulation et celui de l'expérience. Ceci est dû aux conditions initiales et aux limites. Rappelons que l'expérience analogique fait appel à 3 changements de température successifs : la température de la cuve est d'abord élevée à ~49°C, les plaques de cuivre sont ensuite refroidies à 4°C et finalement la température des limites supérieure et inférieure est maintenue à une valeur constante T_f après 6 minutes (Figure 19a). Avec MFIX, la température est abaissée à une valeur constante T_f de manière instantanée (Figure 19b). Ces ajustements expliquent le décalage du processus entre les deux types d'expérience ; cependant les températures modélisées et la vitesse de chute des instabilités dans la cuve sont bien en accord avec l'expérience (voir Chapitre 2).

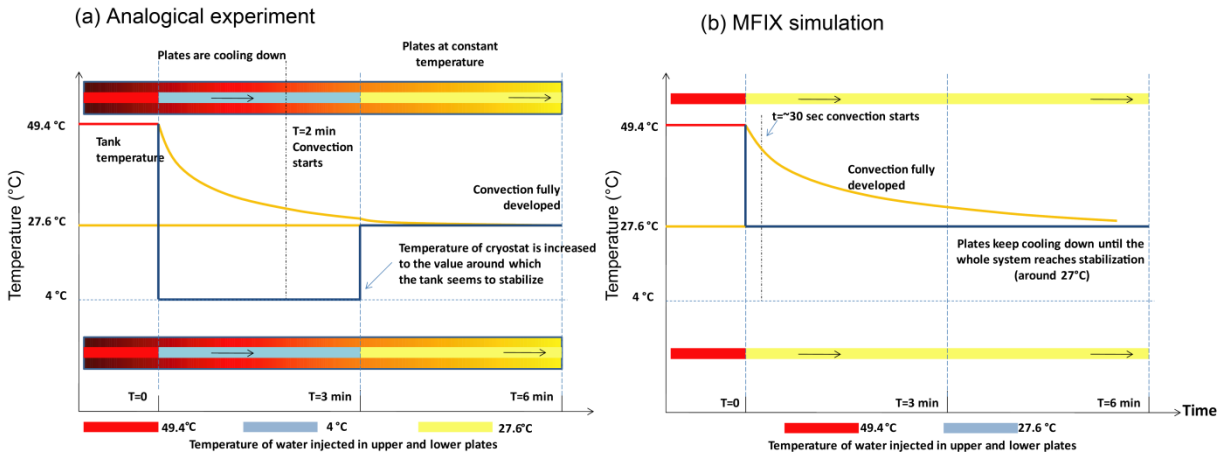

Figure 19. Traitement des conditions (e.g. l'huile 47V20) aux limites par : **a)** l'expérience analogique, **b)** la simulation MFIX.

(iv) *Les paramètres numériques d'affinement du modèle numérique* : Pour arriver au scenario 6, nous nous sommes appliqués à atteindre la stabilité du modèle. Celle-ci est extrêmement importante car nous avons voulu obtenir un modèle présentant un profil de température pratiquement stable au-delà de 310" telle que l'avaient montré *Jaupart et Brandeis* [1986].

Nous avons fait varier successivement plusieurs paramètres de calculs (e.g. Taille de maillage, Pas de calcul, Tolérance et « under-relaxation factor ») afin d'approcher au mieux l'expérience analogique (Voir figure 13).

3.2. Comment traiter les données de sortie ? Et quelques exemples d'application

Les données que fournit MFIX peuvent être traitées à l'aide d'un programme de visualisation incorporé dans MFIX (p. ex. toutes les figures montrées jusqu'ici ont été obtenues grâce à ce programme) ou de programmes disponibles en ligne (p. ex. VISIT). Les données brutes peuvent être obtenues à l'aide d'un module incorporé dans MFIX (POST) qui imprime en ASCII les résultats des variables macroscopiques dont on a besoin pour chaque nœud de la maille. En plus, l'utilisateur peut créer ses propres post-scripts en FORTRAN afin d'effectuer des calculs plus sophistiqués. Les données brutes obtenues peuvent être traitées avec un programme tel que MATLAB, EXCEL ou SURFER par exemple. Dans l'exemple d'applicabilité suivant, on a obtenu les données en utilisant simplement POST (Voir Annexe 5) et à l'aide des programmes SURFER et EXCEL, nous avons effectué les calculs qui seront détaillés par la suite.

3.2.1. Aire d'interface

L'instabilité dite de Rayleigh-Taylor (ou RT) est créée par l'instabilité de l'interface entre deux fluides de densités différentes, qui survient lorsqu'un fluide « dense » en pousse un moins dense. Afin de mieux comprendre l'instabilité de Rayleigh-Taylor, il est utile de calculer la vitesse à laquelle croit la perturbation au niveau de son interface. Considérant le fluide comme incompressible, nous avons calculé une vitesse de croissance approximative pour différents profils de densité. Nous avons calculé l'aire de l'interface englobant les instabilités avec une précision du facteur de croissance similaire à celle de la température initiale du système $T_o \pm 0.05$, $T_o \pm 0.1$ et $T_o \pm 0.2$ pour 2 expériences : l'une de faible viscosité (Tableau 1 en annexe 2) et l'autre dans laquelle la viscosité est supérieure par un facteur de 60 (Table 1 en annexe 2). Pour comprendre la différence entre les 2 simulations, pour chaque expérience, nous avons calculé une telle aire d'interface pour les instabilités qui se forment au niveau de la partie supérieure du réservoir en utilisant la formule de Simpson disponible sur le programme SURFER. Par exemple, pour une valeur de $T_o \pm 0{,}2$ le long des instabilités, nous

obtenons la Figure 20. Nous remarquons que le nombre d'instabilités diminue dans le cas de l'expérience où le fluide est le plus visqueux (comparer Figure 20a-20b). Les volutes de convection sont moins différenciées pour le fluide le plus visqueux. Dans le cas du fluide moins visqueux, les instabilités se séparent de l'instabilité initiale pour former de nouvelles instabilités en forme de bulles, atteignant plus rapidement le fond de la cuve.

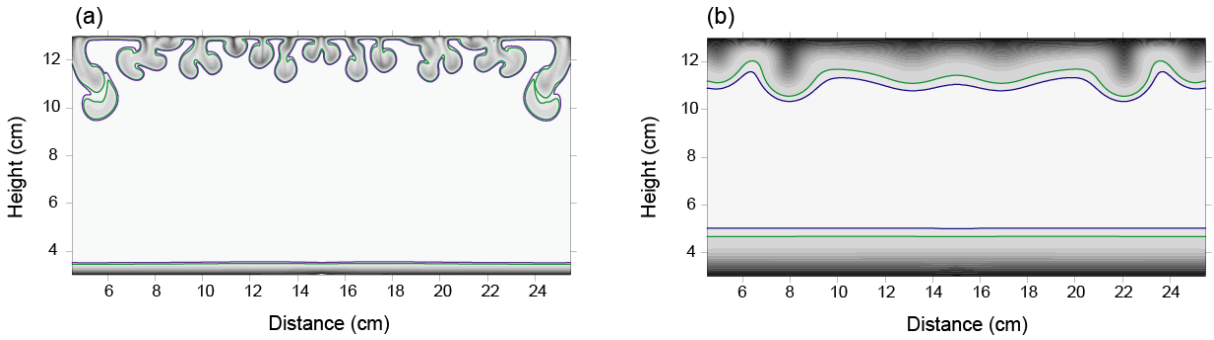

Figure 20. Représentation de l'aire de l'interface des instabilités en fonction du temps : (a) correspond à l'expérience avec l'huile 47V20 après 32 secondes, (b) correspond à l'expérience avec l'huile 47V1000 après 452 secondes. Les conditions initiales et aux limites sont à peu prés similaires pour les deux expériences (Table 1 en annexe 2). Les courbes verte et bleue indiquent l'échelle des températures aux limites à T_o ±0.2, respectivement. Cette figure et ce calcul ont été établis à l'aide du programme SURFER.

3.2.2. Influence de la viscosité (μ) sur la croissance de l'aire d'interface

Nous avons comparé la vitesse de croissance de l'interface pour les deux types d'huile (Figure 21). Nous observons qu'après un même laps de temps, l'aire de l'interface est plus petite pour une huile très visqueuse que pour une huile moins visqueuse (huile 47V20). Un modèle linéaire s'ajuste d'autant mieux qu'une huile est plus visqueuse.

Nous ne pouvions augmenter davantage la viscosité de l'huile dans notre modèle sans changer d'autres propriétés de ce dernier (densité, capacité thermique, coefficient d'expansion thermale et diffusivité thermique). Nous avons donc utilisé les paramètres de l'huile la plus visqueuse, correspondant à l'huile 47V1000 (Rhodorsil® Oils Technical Information). Cependant, si nous permettons à la viscosité de l'huile d'augmenter d'une magnitude de 10 tout en gardant constants les autres paramètres thermodynamiques (Table 1 en Annexe 1), nous observons que l'huile la plus visqueuse a tendance à « coller » au toit du réservoir et à former des instabilités de moindre aire d'interface, confirmant ainsi nos résultats antérieurs.

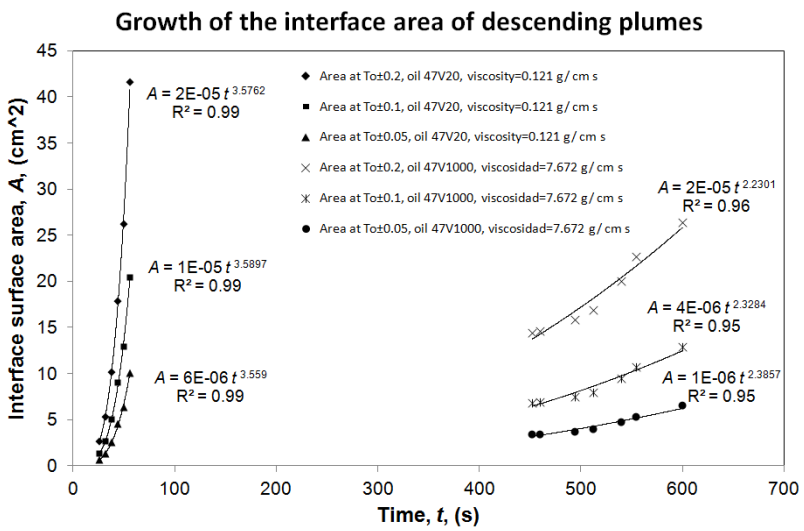

Figure 21. Évolution de l'aire d'interface des instabilités en fonction du temps : comparaison entre l'expérience avec l'huile 47V20 (moins visqueuse) et celle avec l'huile 47V1000 (plus visqueuse). Les différentes courbes (du haut vers le bas) correspondent à une précision du facteur de croissance égale à la température initiale du système T_o ±0.2, T_o±0.1 et T_o ±0.05 pour chaque expérience.

Nous comparons ici 2 simulations dans lesquels nous avons artificiellement changé la valeur de la viscosité (Figure 21), sans changer – comme nous l'avons fait dans l'exercice précédent – les autres paramètres : densité, chaleur spécifique, capacité thermique, coefficient d'expansion thermique et diffusivité thermique. Nous observons que l'huile dont la valeur de viscosité est la plus élevée (μ = 1.21 g/cm s) développe des panaches dont l'aire d'interface est plus petite que celle d'une huile de moindre viscosité (μ = 0.121 g/cm s).

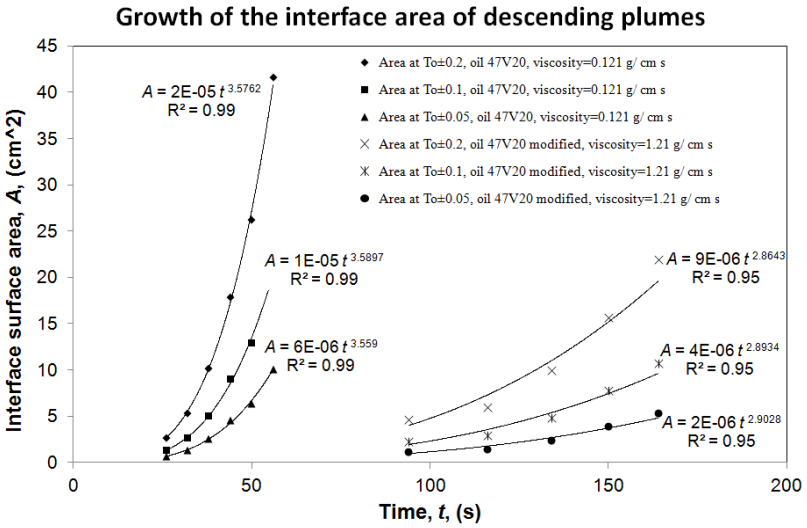

Figure 22. Comparaison de l'évolution de l'aire d'interface des instabilités en fonction du temps pour l'huile 47V20 et la même huile dont la valeur de viscosité est décuplée. Les différentes courbes (du haut vers le bas) correspondent à une précision du facteur de croissance égale à la température initiale du système T_o ±0.2, T_o ±0.1 et T_o ±0.05 pour chaque expérience.

3.2.3. Influence du coefficient d'expansion thermique (α) sur la croissance de l'aire d'interface

Nous avons exécuté deux simulations avec une « huile virtuelle » de viscosité μ = 0 g/cm s, et un coefficient d'expansion thermique de 9.45×10^{-3} K^{-1} et 9.45×10^{-4} K^{-1} (Figures 23 et 24), les autres paramètres physiques étaient les mêmes que ceux de l'huile 47V20. L'aire de l'interface augmente à tel point que les instabilités atteignent le fond plus tôt que pour une huile de coefficient de dilatation inférieur (comparer Figures 23 et 24); l'huile se refroidit et l'aire d'interface diminue à mesure que les panaches se mélangent davantage :

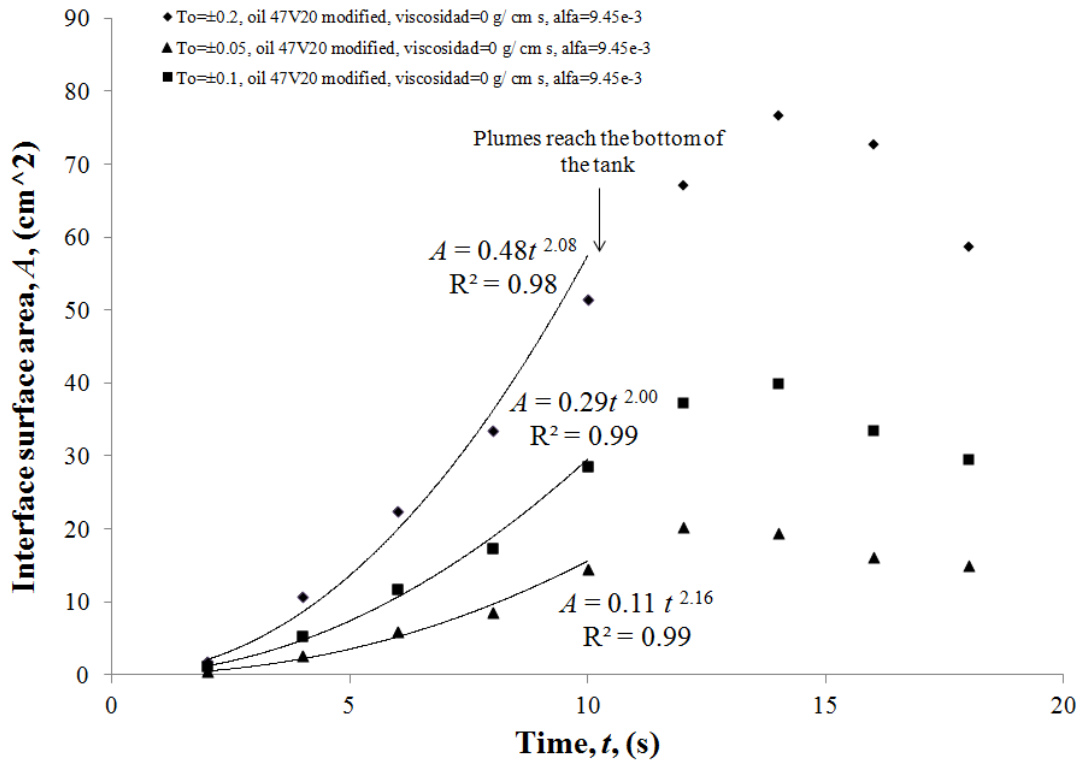

Figure 23. Evolution de l'aire d'interface des instabilités en fonction du temps pour une viscosité modifiée de l'huile silicone 47V20 avec μ = 0 g/cm s et α=9.45×10^{-3}. Les différentes courbes (du haut vers le bas) correspondent à une précision du facteur de croissance égale à la température initiale du système T_o ±0.2, T_o ±0.1 et T_o ±0.05 pour chaque expérience. Les données s'ajustent au cours des 10 premières secondes, le temps auquel les instabilités atteignent le fond de la cuve.

A mesure que le coefficient d'expansion thermique augmente, l'aire d'interface augmente. Si nous diminuons maintenant α jusqu'à des valeurs de 9.45×10^{-5} ou même à 9.45×10^{-7}, nous observons une tendance identique : l'aire de l'interface diminue lorsque le coefficient d'expansion thermique diminue. La Figure 24 illustre ce phénomène :

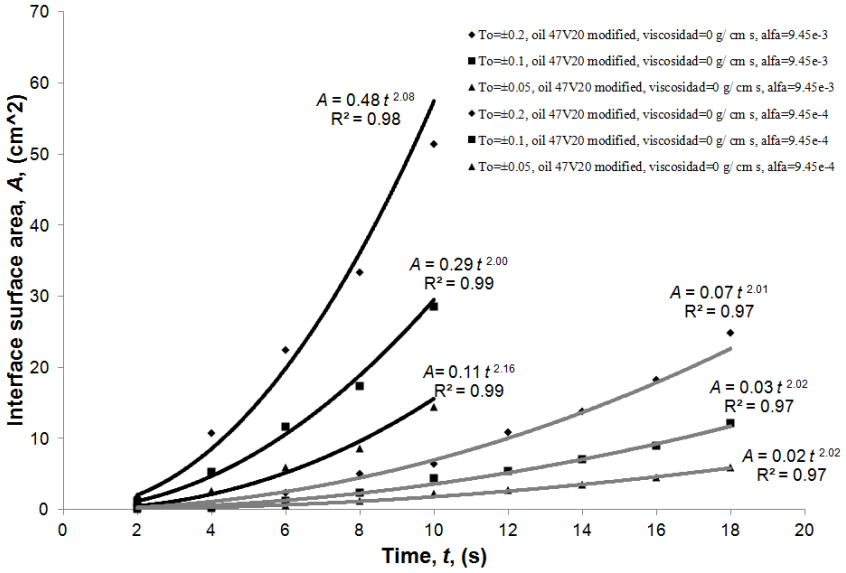

Figure 24. Évolution de l'aire d'interface des instabilités en fonction du temps : pour une huile silicone 47V20 dont la viscosité a été modifiée à μ = 0 g/cm.s et un coefficient d'expansion thermique α = 9.45x10^{-3} et α = 9.45x10^{-4}, respectivement. Les différentes courbes (du haut vers le bas) correspondent à une précision du facteur de croissance égale à la température initiale du système T_o ±0.2, T_o ±0.1 et T_o ±0.05 pour chaque expérience. Les données s'ajustent au cours des premières 10 secondes, le temps auquel les instabilités atteignent le fond de la cuve lorsque α = 9.45x10^{-3}.

3.2.4. Épaisseur théorique de la couche stagnante

La convection forme un couche plane, froide et stagnante au fond de la cuve (voir Figure 18 ou 20). Afin de calculer l'épaisseur théorique de la couche stagnante, *Jaupart et Brandeis* [1986] ont formulé l'équation suivante :

$$\frac{\delta}{d} = \sqrt{\frac{36}{13C}} Ra^{-1/6} \sqrt{\left(1+t^*\right) - \left(1+t^*\right)^{-12}} \qquad (62)$$

Où δ est le niveau supérieur de la couche stagnante, d est l'épaisseur de liquide de la cuve, Ra est le nombre Rayleigh et t^* est le temps sans dimension exprimé comme étant le rapport ($t^* = t/\tau$) entre le temps « vrai » « t » et un temps diffusif, τ, défini comme $\tau = \frac{3}{C}\frac{d^2}{\kappa} Ra^{-1/3}$, où C est une constante variant entre 0.19 et 0.23 [*Deandorff et al*, 1969] ; nous avons pris la valeur moyenne (0.21), κ est la diffusivité thermale de l'huile.

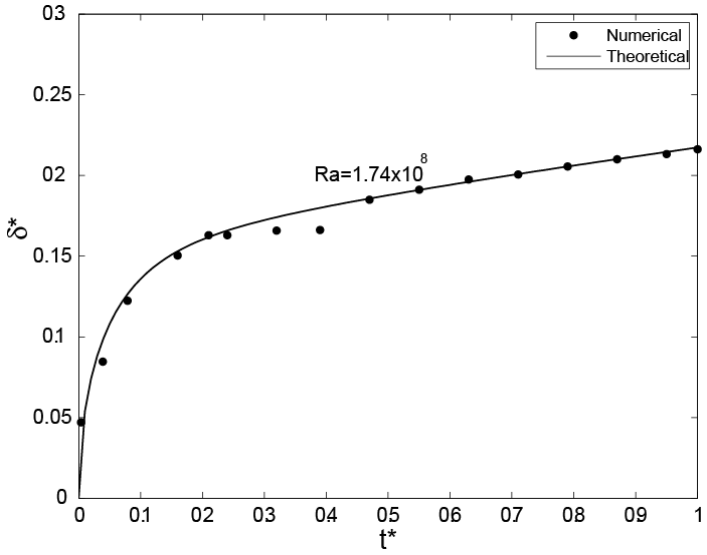

Figure 25. Épaisseur de la couche stagnante en fonction du temps adimensionnel pour des valeurs du nombre de Rayleigh élevées (l'huile 47V20). La courbe en trait plein est dérivée de l'équation (61). L'épaisseur de la couche stagnante dépend de la forme du profil de température.

Cette théorie était basée sur des expériences dans des conditions impliquant un nombre de Rayleigh modéré, pour lesquelles les forces visqueuses prévalent sur les forces de flottabilité [*Kraichnan*, 1962]. La valeur de l'épaisseur de la couche stagnante que nous avons extraite de notre simulation est très proche de la valeur théorique (Figure 25). Nous déterminons l'épaisseur de la couche stagnante en identifiant sur la courbe de température la profondeur à laquelle chaque courbe présente une déflection importante vers des températures plus froides (voir Figure 1 dans le Chapitre 2).

4. Conclusions

Ce chapitre décrit la méthodologie de modélisation numérique que nous avons mise au point et qui peut être utilisée pour d'autres types de simulation. Nous l'avons appliquée pour modéliser la convection d'un mélange composé de liquide et de cristaux et reproduire une expérience analogique ne contenant qu'un liquide. Nous avons indiqué les équations de transport et constitutives utilisées par notre modèle numérique dérivé de MFIX. Ce chapitre peut constituer un manuel pour quiconque voudrait développer, appliquer et exploiter les capacités de MFIX lors de modélisations plus complexes. Nous en donnons un exemple dans le Chapitre III. Nous avons également décrit la manière dont une particule migre en régime laminaire ($Re << 1$) au sein d'un fluide stagnant en raison d'un contraste de densité. Pour cela, nous avons utilisé le model simplifié de Stokes pour l'utiliser ensuite dans notre modélisation en Chapitre IV. Des modélisations de montée de particules plus complexes peuvent être définies en utilisant l'équation BBO (équation 53) qui peut s'avérer nécessaire lorsque le régime d'écoulement devient turbulent ($Re >> 1$).

Annexe 1.

Table A1. Formulaire de calcul tensoriel

Soient i, j des indices permettant d'identifier les composantes du vecteur $\vec{v} = \left(v_x, v_y, v_z\right)$ et du tenseur ; la convention de sommation d'Einstein est appliquée sur des indices répétés.

Tenseur identité :

$$\delta_{ij} = \begin{cases} 1 & i = j \\ 0 & i \neq j \end{cases} \rightarrow \quad \overline{\overline{I}} = \begin{pmatrix} 1 & 0 & 0 \\ 0 & 1 & 0 \\ 0 & 0 & 1 \end{pmatrix}$$

Premier invariant de tenseur de contraintes :

$$I_{1S} = \frac{1}{3}\left(S_{xx} + S_{yy} + S_{zz}\right)$$

Tenseur de vitesse de déformation (avec unités de 1/s) :

$$\overline{\overline{D}} = \overset{\circ}{D} + \overset{\circ}{\overline{\overline{D}}} = \frac{1}{2}\left[\nabla\vec{v} + \left(\nabla\vec{v}\right)^{\mathrm{T}}\right] = \frac{1}{2}\left[\frac{\partial v_i}{\partial x_j} + \frac{\partial v_j}{\partial x_i}\right] = \frac{1}{2}\begin{pmatrix} 2\frac{\partial v_x}{\partial x} & \frac{\partial v_y}{\partial x} + \frac{\partial v_x}{\partial y} & \frac{\partial v_z}{\partial x} + \frac{\partial v_x}{\partial z} \\ \frac{\partial v_x}{\partial y} + \frac{\partial v_y}{\partial x} & 2\frac{\partial v_y}{\partial y} & \frac{\partial v_z}{\partial y} + \frac{\partial v_y}{\partial z} \\ \frac{\partial v_x}{\partial z} + \frac{\partial v_z}{\partial x} & \frac{\partial v_y}{\partial z} + \frac{\partial v_z}{\partial y} & 2\frac{\partial v_z}{\partial z} \end{pmatrix}$$

Premier invariant de tenseur de vitesse de déformation (trace du tenseur ; avec unités de 1/s) :

$$I_D = tr\left(\overline{\overline{D}}\right) = \nabla\cdot\vec{v} = \frac{\partial v_i}{\partial x_i} = \left(\frac{\partial v_x}{\partial x} + \frac{\partial v_y}{\partial y} + \frac{\partial v_z}{\partial z}\right)$$

Deuxième invariant du déviateur du tenseur de vitesse de déformation (avec unités de $1/s^2$):

$$I_{2D} = \frac{1}{2}\overset{\circ}{\overline{\overline{D}}}_{ij}\overset{\circ}{\overline{\overline{D}}}_{ji} = \frac{1}{2}\left\{\left[tr\left(\overset{\circ}{\overline{\overline{D}}}\right)\right]^2 - tr\left(\overset{\circ}{\overline{\overline{D}}}^{\,2}\right)\right\}$$

$$= \frac{1}{6}\left[\left(\mathrm{D}_{11} - \mathrm{D}_{22}\right)^2 + \left(\mathrm{D}_{22} - \mathrm{D}_{33}\right)^2 + \left(\mathrm{D}_{33} - \mathrm{D}_{11}\right)^2\right] + \mathrm{D}_{12}^2 + \mathrm{D}_{23}^2 + \mathrm{D}_{31}^2$$

Déviateur de la vitesse de déformation (contrainte déviatorique ou partie déviatorique d'un tenseur symétrique) :

$$\overset{\circ}{\overline{\overline{D}}} = \overline{\overline{D}} - \overset{\circ}{D} = \overline{\overline{D}} - \frac{1}{3}I_D\overline{\overline{I}} = \overline{\overline{D}} - \frac{1}{3}\left(\nabla\cdot\vec{v}\right)\overline{\overline{I}}$$

Expression explicite (matrice) de déviateur :

$$\overset{\circ}{\overline{\overline{D}}} = \overline{\overline{D}} - \overset{\circ}{D} = \frac{1}{2}\begin{pmatrix} 2\frac{\partial v_x}{\partial x} & \frac{\partial v_y}{\partial x}+\frac{\partial v_x}{\partial y} & \frac{\partial v_z}{\partial x}+\frac{\partial v_x}{\partial z} \\ \frac{\partial v_x}{\partial y}+\frac{\partial v_y}{\partial x} & 2\frac{\partial v_y}{\partial y} & \frac{\partial v_z}{\partial y}+\frac{\partial v_y}{\partial z} \\ \frac{\partial v_x}{\partial z}+\frac{\partial v_z}{\partial x} & \frac{\partial v_y}{\partial z}+\frac{\partial v_z}{\partial y} & 2\frac{\partial v_z}{\partial z} \end{pmatrix} - \frac{1}{3}\begin{pmatrix} \frac{\partial v_x}{\partial x}+\frac{\partial v_y}{\partial y}+\frac{\partial v_z}{\partial z} & 0 & 0 \\ 0 & \frac{\partial v_x}{\partial x}+\frac{\partial v_y}{\partial y}+\frac{\partial v_z}{\partial z} & 0 \\ 0 & 0 & \frac{\partial v_x}{\partial x}+\frac{\partial v_y}{\partial y}+\frac{\partial v_z}{\partial z} \end{pmatrix}$$

Dans un cas isotrope on a: $\frac{\partial v_x}{\partial x} = \frac{\partial v_y}{\partial y} = \frac{\partial v_z}{\partial z}$

$$\overset{\circ}{\overline{\overline{D}}} = \begin{pmatrix} \frac{\partial v_x}{\partial x} & \frac{1}{2}\left(\frac{\partial v_y}{\partial x}+\frac{\partial v_x}{\partial y}\right) & \frac{1}{2}\left(\frac{\partial v_z}{\partial x}+\frac{\partial v_x}{\partial z}\right) \\ \frac{\partial v_x}{\partial y}+\frac{\partial v_y}{\partial x} & \frac{\partial v_y}{\partial y} & \frac{1}{2}\left(\frac{\partial v_z}{\partial y}+\frac{\partial v_y}{\partial z}\right) \\ \frac{1}{2}\left(\frac{\partial v_x}{\partial z}+\frac{\partial v_z}{\partial x}\right) & \frac{1}{2}\left(\frac{\partial v_y}{\partial z}+\frac{\partial v_z}{\partial y}\right) & \frac{\partial v_z}{\partial z} \end{pmatrix} - \begin{pmatrix} \frac{1}{3}3\frac{\partial v_x}{\partial x} & 0 & 0 \\ 0 & \frac{1}{3}3\frac{\partial v_y}{\partial y} & 0 \\ 0 & 0 & \frac{1}{3}3\frac{\partial v_z}{\partial z} \end{pmatrix}$$

$$= \begin{pmatrix} 0 & \frac{1}{2}\left(\frac{\partial v_y}{\partial x}+\frac{\partial v_x}{\partial y}\right) & \frac{1}{2}\left(\frac{\partial v_z}{\partial x}+\frac{\partial v_x}{\partial z}\right) \\ \frac{\partial v_x}{\partial y}+\frac{\partial v_y}{\partial x} & 0 & \frac{1}{2}\left(\frac{\partial v_z}{\partial y}+\frac{\partial v_y}{\partial z}\right) \\ \frac{1}{2}\left(\frac{\partial v_x}{\partial z}+\frac{\partial v_z}{\partial x}\right) & \frac{1}{2}\left(\frac{\partial v_y}{\partial z}+\frac{\partial v_z}{\partial y}\right) & 0 \end{pmatrix}$$

Partie sphérique d'un tenseur symétrique (contrainte moyenne):

$$\overset{\circ}{D} = \frac{1}{3} I_D \overline{\overline{I}} = \frac{1}{3}\left(\nabla \cdot \vec{v}\right)\overline{\overline{I}}$$

Annexe 2.

Table A2. List des paramètres physiques des huiles [http://www.bluestarsilicones.com/]

Variable (Unités)		**Type d'huile**			
		47V20	**47V20 [(a)]**	**47V20[(b,c)]**	**47V1000**
Température initiale (°C)	T_o	49.4	49.4	49.4	36.5
Température finale (Parois haut et bas)	T_f	27.6	27.6	27.6	21.3
Delta température	ΔT	21.8	21.8	21.8	15.2
Constantes pour calcul de densité initiale					
a		$7.34x10^{-9}$	$7.34x10^{-9}$	$7.34x10^{-9}$	$-6.18x10^{-9}$
b		$3.76x10^{-6}$	$3.76x10^{-6}$	$3.76x10^{-6}$	$3.57x10^{-6}$
c		$-1.26x10^{-3}$	$-1.26x10^{-3}$	$-1.26x10^{-3}$	$-1.21x10^{-3}$
d		$9.84x10^{-1}$	$9.84x10^{-1}$	$9.84x10^{-1}$	0.998
Densité initiale (g/cm^3)	ρ_m	0.93	0.93	0.93	0.946
Constantes pour calcul de la viscosité initiale					
Viscosité à 25° C (mm^2/s)		20	20	20	1000
Viscosité dynamique initiale (g cm/s)	μ_m	0.121	1.214	1.214	7.672
Constantes pour calcul de capacité thermique					
a		0.34708	0.34708	0.34708	0.34708
b		43	43	43	43
Capacité thermique à température initiale (cal/g C)	C_{pm}	0.3683	0.3683	0.3683	0.3683
Conductivité thermique (Cal / s K cm)		$3.4713x10^{-4}$	$3.4713x10^{-4}$	$3.4713x10^{-4}$	$3.4713x10^{-4}$
Diffusivité thermique (cm^2/s)	κ	$1.01x10^{-3}$	$1.01x10^{-3}$	$9.45x10^{-4}$	$9.96x10^{-4}$
Expansion thermale (1/C)	α	$1.07x10^{-3}$	$1.07x10^{-3}$	$9.45x10^{-3}$/$9.45x10^{-4}$	$9.45x10^{-4}$

[(a)]47V20 huile avec viscosité dynamique modifiée (10 fois plus grande que celle de 47V20).
[(b,c)] 47V20 huile avec viscosité dynamique (égal a zéro) et expansion thermale modifiée (celle de $9.45x10^{-3}$ ou $9.45x10^{-4}$).

Annexe 3.

Fichier d'entrée "mfix.dat"

```
#  Conduction and convection
#  Plexiglass tank experiment from Jaupart and Brandeis, 1986
  RUN_NAME = 'CONV1'
  DESCRIPTION = 'Convection of silicone oil type 47V20'
  RUN_TYPE = 'new'
  UNITS = 'cgs'
  ! times for calculations: they represent a real/physical time
  TIME  =0.0  TSTOP = 310   DT = 5e-4   DT_MAX = 1e-2    DT_MIN = 1e-8
  ENERGY_EQ = .TRUE.
                !MELT     !XTALS
  SPECIES_EQ =    .FALSE.   .FALSE.
  MOMENTUM_X_EQ = .TRUE.    .FALSE.
  MOMENTUM_Y_EQ = .TRUE.    .FALSE.
  MOMENTUM_Z_EQ = .FALSE.   .FALSE.
  DISCRETIZE = 7*0
# ------------------------------------------------------------------------------------------------------------------------
# Geometry Section
#
  COORDINATES = 'Cartesian'
! length of the domain (cm)      # of boxes
  XLENGTH  = 30.0             IMAX = 960    ! 0.03 cm of length each box
  YLENGTH  = 16.0             JMAX = 512    ! 0.03 cm of length each box
  CYCLIC_X = .FALSE.          ! True if it is infinite body in X direction
  NO_K     = .TRUE.

  MAX_NIT = 300
   UR_FAC = 8*0.5          ! in this way are close to the real times of unsteady state.
  LEQ_IT(6) = 15           ! nb iter in LinEq solver
  TOL_RESID  = 0.1         ! total residual p+v
  NORM_G = 1e4             ! liquid pressure scale for residuals
  NORM_S = 1e4             ! solid pressure scale for residuals
#-------------------------------------------------------------------------------------------------------------------------
#
# Melt-phase Section
#
! all what is defined as a gas corresponds to a liquid phase
  RO_g0 = 0.930            ! liquid density g/cm3 (kg/m3 * 0.001)
  MU_g0 = 0.121            ! Constant dynamic viscosity
  K_g0 = 3.4713e-04        ! liquid thermal conductivity cal/s K cm
  C_pg0 = 0.3683           ! Heat capacity of the liquid cal/g K
  C(1) = 322.55            ! liquid reference temp for thermal expansion
  C(2) = 1.07e-03          ! coefficient thermal expansion 1/K
  C_NAME = 'Reference Temp'    'Thermal Expansion'

#-------------------------------------------------------------------------------------------------------------------------
# Initial Conditions Section
#
! Total domain              x1,y1: lower left of all the domain containing the surfaces
!                           x2,y2: upper right of all the domain containing the surfaces
  IC_X_w   =  0.0
  IC_X_e   = 30.0
  IC_Y_s   =  0.0
  IC_Y_n   = 16.0

  IC_EP_g   =  1.0         ! liquid volume fraction
  IC_X_g    =  1.0         ! initial liquid fraction
```

```
 IC_U_g    = 0.0
 IC_V_g    = 0.0

 IC_T_g    = 322.55    ! liquid temp of magma (K)

#-------------------------------------------------------------------------------------------------------------------------
#  Boundary Conditions Section
#
! Coordinates of the boundaries
! x and y are positive right in upper directions, respectively
! region:                    x1,y1: lower left of the cube; x2,y2: upper right of the cube
! horizontal line:           x1,y1: left side of the plane; x2,y2: right side of the plane
! vertical line:             x1,y1: lower side of the plane; x2,y2: upper side of the plane

# BC1
! magmatic chamber  (solid region)
 BC_X_w(1)     = 0.0    !x1
 BC_X_e(1)     = 30.0   !x2
 BC_Y_s(1)     = 0.0      !y1
 BC_Y_n(1)     = 3.0    !y2

# BC2
! Left side of magmatic chamber (solid region)
 BC_X_w(2)     = 0.0
 BC_X_e(2)     = 4.5
 BC_Y_s(2)     = 3.0
 BC_Y_n(2)     = 13.0

# BC3
! Right side of magmatic chamber (solid region)
 BC_X_w(3)     = 25.5
 BC_X_e(3)     = 30.0
 BC_Y_s(3)     = 3.0
 BC_Y_n(3)     = 13.0

# BC4
! Top of magmatic chamber (solid region)
 BC_X_w(4)     = 0.0
 BC_X_e(4)     = 30.0
 BC_Y_s(4)     = 13.0
 BC_Y_n(4)     = 16.0

! Type of boundary
! NSW: non slip wall
!       BC1   BC2   BC3   BC4
BC_TYPE= 'NSW' 'NSW' 'NSW' 'NSW'

! Volume fraction of the carrier phase (liquid)
!       BC1   BC2   BC3   BC4
BC_EP_g = 1.0   1.0   1.0   1.0

! Horizontal and vertical velocities for each phase
!      BC1   BC2   BC3   BC4
BC_U_g= 0.0   0.0   0.0   0.0
BC_V_g= 0.0   0.0   0.0   0.0

! liquid temperature at wall
!
! BC_Tw_g=0 when it is considered constant flux at such boundary
!          BC1     BC2     BC3     BC4
```

```
 BC_Tw_g=   300.75  0.0  0.0  300.75

! wall heat transf coeff (1/m /100)
!
BC_hw_T_g(2) =  0.0
BC_hw_T_g(3) =  0.0
!
! wall heat flow  (K/m / 100)
! It must be 0 when the wall is at constant temperature (no heat flux)
!           BC1   BC2   BC3   BC4
BC_C_T_g =   0.0   -1e-10  -1e-10   0.0

#-----------------------------------------------------------------------------------------------------------------------
#  Output Control: visualization and writing of files
#
RES_DT = 1e20
OUT_DT = 1e20

! SP file index
! Theta_m=viscosity
!         1     2     3    4     5     6     7     8      9
       ! EP_g   P_g    U_g   U_s  ROP_s T_g   X_g  Theta_m  usr
       !        P_star V_g   V_s        T_s1  X_s
       !              W_g   W_s        T_s2
 SPX_DT =   2    2     2   1e20  1e20    2   1e20   1e20    1e20
  NLOG   = 250
  FULL_LOG = .TRUE.
  RESID_STRING = 'P0' 'V0' 'U0' 'V1' 'U1' 'T0'

#-----------------------------------------------------------------------------------------------------------------------
# DMP control

  NODESI = 1   NODESJ = 1   NODESK = 1
```

Annexe 4.

Exemple d'un fichier en FORTRAN pour calculer la viscosité dynamique du liquide.

```
 !vvvvvvvvvvvvvvvvvvvvvvvvvvvvvvvvvvvvvvvvvvvvvvvvvvvvvvvvvvvvvvvvvvvvvvvvvvvvvvvvvC
!                                                                      C
!  Module name: CALC_MU_g(IER)                                         C
!  Purpose: Calculate the effective viscosity for a turbulent flow,    C
!           which is the sum of molecular and eddy viscosities         C
!                                                                      C
!  Author: W. Sams/M. Syamlal                   Date: 18-JUL-94  C
!  Reviewer:                                 Date: dd-mmm-yy  C
!                                                                      C
!  Revision Number: 1                                                  C
!  Purpose: MFIX 2.0 mods (previous name CALC_MU_gt)                   C
!  Author:                                   Date: dd-mmm-yy  C
!  Reviewer:                                 Date: dd-mmm-yy  C
!                                                                      C
!  Revision Number: 2                                                  C
!  Purpose: allow SI unit                                              C
!  Author: S. Dartevelle                     Date: 01-Jul-02  C
!  Reviewer:                                 Date: dd-mmm-yy  C
!                                                                      C
!  Revision Number: 3                                                  C
!  Purpose: compute turbulent eddy viscosity                           C
!  Author: S. Benyahia                       Date: May-13-04  C
!  Reviewer:                                 Date: dd-mmm-yy  C
!  Literature/Document References:                                     C
!                                                                      C
!  Variables referenced:                                               C
!  Variables modified:                                                 C
!                                                                      C
!  Local variables:                                                    C
!                                                                      C
!^^^^^^^^^^^^^^^^^^^^^^^^^^^^^^^^^^^^^^^^^^^^^^^^^^^^^^^^^^^^^^^^^^^^^^^^^^^^^^^^^C
!
      SUBROUTINE CALC_MU_G(IER)
!...Translated by Pacific-Sierra Research VAST-90 2.06G5  12:17:31  12/09/98
!...Switches: -xf
!-----------------------------------------------
!  M o d u l e s
!-----------------------------------------------
      USE param
      USE param1
      USE parallel
      USE physprop
      USE geometry
      USE fldvar
      USE visc_g
      USE visc_s
      USE indices
      USE constant
      USE compar
      USE run         !S. Dartevelle
      USE sendrecv
      IMPLICIT NONE
!-----------------------------------------------
!  G l o b a l  P a r a m e t e r s
!-----------------------------------------------
!-----------------------------------------------
```

```
! D u m m y  A r g u m e n t s
!-----------------------------------------------
!-----------------------------------------------
! L o c a l  P a r a m e t e r s
!-----------------------------------------------
      DOUBLE PRECISION, PARAMETER :: F2O3 = 2./3.
!-----------------------------------------------
! L o c a l  V a r i a b l e s
!-----------------------------------------------
!                Error index
      INTEGER         IER
!                Indices
      INTEGER         I, J, K, IJK, IMJK, IPJK, IJMK, IJPK, IJKM, IJKP, &
                     IM, JM, KM
      INTEGER         IMJPK, IMJMK, IMJKP, IMJKM, IPJKM, IPJMK, IJMKP, &
                     IJMKM, IJPKM
!                Strain rate tensor components for mth solids phase
      DOUBLE PRECISION D_g(3,3)
!                U_g at the north face of the THETA cell-(i, j+1/2, k)
      DOUBLE PRECISION U_g_N
!                U_g at the south face of the THETA cell-(i, j-1/2, k)
      DOUBLE PRECISION U_g_S
!                U_g at the top face of the THETA cell-(i, j, k+1/2)
      DOUBLE PRECISION U_g_T
!                U_g at the bottom face of the THETA cell-(i, j, k-1/2)
      DOUBLE PRECISION U_g_B
!                U_g at the center of the THETA cell-(i, j, k)
!                Calculated for Cylindrical coordinates only.
      DOUBLE PRECISION U_g_C
!                V_g at the east face of the THETA cell-(i+1/2, j, k)
      DOUBLE PRECISION V_g_E
!                V_g at the west face of the THETA cell-(i-1/2, j, k)
      DOUBLE PRECISION V_g_W
!                V_g at the top face of the THETA cell-(i, j, k+1/2)
      DOUBLE PRECISION V_g_T
!                V_g at the bottom face of the THETA cell-(i, j, k-1/2)
      DOUBLE PRECISION V_g_B
!                W_g at the east face of the THETA cell-(i+1/2, j, k)
      DOUBLE PRECISION W_g_E
!                W_g at the west face of the THETA cell-(1-1/2, j, k)
      DOUBLE PRECISION W_g_W
!                W_g at the north face of the THETA cell-(i, j+1/2, k)
      DOUBLE PRECISION W_g_N
!                W_g at the south face of the THETA cell-(i, j-1/2, k)
      DOUBLE PRECISION W_g_S
!                W_g at the center of the THETA cell-(i, j, k).
!                Calculated for Cylindrical coordinates only.
      DOUBLE PRECISION W_g_C
!                Second invariant of the deviator of D_g
      DOUBLE PRECISION I2_devD_g
!                Constant in turbulent viscosity formulation
      DOUBLE PRECISION C_MU
!-----------------------------------------------
      INCLUDE 'ep_s1.inc'
      INCLUDE 'fun_avg1.inc'
      INCLUDE 'function.inc'
      INCLUDE 'ep_s2.inc'
      INCLUDE 'fun_avg2.inc'
      C_MU = 9D-02
 1. DO IJK = ijkstart3, ijkend3
```

```
 2.        IF (FLUID_AT(IJK)) THEN
 3.                IF (MU_G0 == UNDEFINED) THEN !  Molecular viscosity
 4.                        IF (T_G(IJK) .GT. 973) THEN
 5.                                MU_G(IJK) = 10**(-4.55 + 8642.3/(T_G(IJK)-319.6))
 6.                                MU_G(IJK)=MU_G(IJK)*10
 7.                         ELSE
 8.                                MU_G(IJK) = 4.74*10**9
 9.                                MU_GT(IJK) = MU_G(IJK)
10.                                LAMBDA_GT(IJK) = -F2O3*MU_GT(IJK)
11.                        ENDIF
12.                ENDIF
13.                                MU_GT(IJK) = MU_G(IJK)
14.                                LAMBDA_GT(IJK) = -F2O3*MU_GT(IJK)
15.                IF (K_Epsilon) THEN
16.                                MU_GT(IJK) = MU_G(IJK) +  RO_G(IJK)*C_mu*K_Turb_G(IJK)**2&
17.                                /(E_Turb_G(IJK)+Small_number)
18.                                MU_GT(IJK) = MIN(MU_GMAX, MU_GT(IJK))
19.                                LAMBDA_GT(IJK) = -F2O3*MU_GT(IJK)
20.                ENDIF
21.        ELSE
22.                MU_G(IJK)  = ZERO
23.                MU_GT(IJK) = ZERO
24.                LAMBDA_GT(IJK) = ZERO
25.        ENDIF
26. END DO

!!$omp parallel do &
 !!$omp$ schedule(dynamic,chunk_size) &
 !!$omp$ private(IJK, I,J,K,IM,JM,KM, &
!!$omp& IMJK,IPJK,IJMK,IJPK,IJKM,IJKP,IMJPK,IMJMK,IMJKP, &
!!$omp& IMJKM,IPJKM,IPJMK,IJMKP,IJMKM,IJPKM, &
!!$omp& U_G_N,U_G_S,U_G_T,U_G_B,V_G_E,V_G_W,V_G_T,V_G_B, &
!!$omp$ W_G_N,W_G_S,W_G_E,W_G_W,  U_G_C,W_G_C, D_G,I2_DEVD_G )
     DO IJK = ijkstart3, ijkend3
!//SP
27.      IF ( FLUID_AT(IJK) .AND. L_SCALE(IJK)/=ZERO) THEN
28.       I = I_OF(IJK)
29.       J = J_OF(IJK)
30.       K = K_OF(IJK)
31.       IM = IM1(I)
32.       JM = JM1(J)
33.        KM = KM1(K)
34.        IMJK = IM_OF(IJK)
35.        IPJK = IP_OF(IJK)
36.        IJMK = JM_OF(IJK)
37.        IJPK = JP_OF(IJK)
38.        IJKM = KM_OF(IJK)
39.        IJKP = KP_OF(IJK)
40.        IMJPK = IM_OF(IJPK)
41.        IMJMK = IM_OF(IJMK)
42.        IMJKP = IM_OF(IJKP)
43.        IMJKM = IM_OF(IJKM)
44.        IPJKM = IP_OF(IJKM)
45.        IPJMK = IP_OF(IJMK)
46.        IJMKP = JM_OF(IJKP)
47.        IJMKM = JM_OF(IJKM)
48.       IJPKM = JP_OF(IJKM)
!        Find fluid velocity values at faces of the cell
49.           U_G_N = AVG_Y(AVG_X_E(U_G(IMJK),U_G(IJK),I),AVG_X_E(U_G(IMJPK),U_G(&
50.             IJPK),I),J)                    !i, j+1/2, k
```

```
51.           U_G_S = AVG_Y(AVG_X_E(U_G(IMJMK),U_G(IJMK),I),AVG_X_E(U_G(IMJK),U_G&
52.             (IJK),I),JM)                    !i, j-1/2, k
53.           U_G_T = AVG_Z(AVG_X_E(U_G(IMJK),U_G(IJK),I),AVG_X_E(U_G(IMJKP),U_G(&
54.             IJKP),I),K)                     !i, j, k+1/2
55.           U_G_B = AVG_Z(AVG_X_E(U_G(IMJKM),U_G(IJKM),I),AVG_X_E(U_G(IMJK),U_G&
56.             (IJK),I),KM)                    !i, j, k-1/2
57.           V_G_E = AVG_X(AVG_Y_N(V_G(IJMK),V_G(IJK)),AVG_Y_N(V_G(IPJMK),V_G(&
58.             IPJK)),I)                       !i+1/2, j, k
59.           V_G_W = AVG_X(AVG_Y_N(V_G(IMJMK),V_G(IMJK)),AVG_Y_N(V_G(IJMK),V_G(&
60.             IJK)),IM)                       !i-1/2, j, k
61.           V_G_T = AVG_Z(AVG_Y_N(V_G(IJMK),V_G(IJK)),AVG_Y_N(V_G(IJMKP),V_G(&
62.             IJKP)),K)                       !i, j, k+1/2
63.           V_G_B = AVG_Z(AVG_Y_N(V_G(IJMKM),V_G(IJKM)),AVG_Y_N(V_G(IJMK),V_G(&
64.             IJK)),KM)                       !i, j, k-1/2
65.           W_G_N = AVG_Y(AVG_Z_T(W_G(IJKM),W_G(IJK)),AVG_Z_T(W_G(IJPKM),W_G(&
66.             IJPK)),J)                       !i, j+1/2, k
67.           W_G_S = AVG_Y(AVG_Z_T(W_G(IJMKM),W_G(IJMK)),AVG_Z_T(W_G(IJKM),W_G(&
68.             IJK)),JM)                       !i, j-1/2, k
69.           W_G_E = AVG_X(AVG_Z_T(W_G(IJKM),W_G(IJK)),AVG_Z_T(W_G(IPJKM),W_G(&
70.             IPJK)),I)                       !i+1/2, j, k
71.           W_G_W = AVG_X(AVG_Z_T(W_G(IMJKM),W_G(IMJK)),AVG_Z_T(W_G(IJKM),W_G(&
72.             IJK)),IM)                       !i-1/2, j, k
            IF (CYLINDRICAL) THEN
                                    !i, j, k
              U_G_C = AVG_X_E(U_G(IMJK),U_G(IJK),I)
!                       calc_mu_g.f             !i, j, k
              W_G_C = AVG_Z_T(W_G(IJKM),W_G(IJK))
            ELSE
              U_G_C = ZERO
              W_G_C = ZERO
            ENDIF
!         Find components of fluid phase strain rate
!         tensor, D_g, at center of the cell - (i, j, k)
73.           D_G(1,1) = (U_G(IJK)-U_G(IMJK))*ODX(I)
74.           D_G(1,2) = HALF*((U_G_N - U_G_S)*ODY(J)+(V_G_E-V_G_W)*ODX(I))
75.           D_G(1,3) = HALF*((W_G_E - W_G_W)*ODX(I)+(U_G_T-U_G_B)*(OX(I)*ODZ(K)&
76.             )-W_G_C*OX(I))
77.           D_G(2,1) = D_G(1,2)
78.           D_G(2,2) = (V_G(IJK)-V_G(IJMK))*ODY(J)
79.           D_G(2,3)=HALF*((V_G_T-V_G_B)*(OX(I)*ODZ(K))+(W_G_N-W_G_S)*ODY(J))
80.           D_G(3,1) = D_G(1,3)
81.           D_G(3,2) = D_G(2,3)
82.           D_G(3,3) = (W_G(IJK)-W_G(IJKM))*(OX(I)*ODZ(K)) + U_G_C*OX(I)
!         Calculate the second invariant of the deviator of D_g
83.           I2_DEVD_G = ((D_G(1,1)-D_G(2,2))**2+(D_G(2,2)-D_G(3,3))**2+(D_G(3,3&
84.             )-D_G(1,1))**2)/6. + D_G(1,2)**2 + D_G(2,3)**2 + D_G(3,1)**2
85.           MU_GT(IJK) = MIN(MU_GMAX,MU_GT(IJK)+2.0*L_SCALE(IJK)*L_SCALE(IJK)*&
86.             RO_G(IJK)*SQRT(I2_DEVD_G))
87.           LAMBDA_GT(IJK) = -F2O3*MU_GT(IJK)

88.         ENDIF
89.       END DO

90.       RETURN
91.       END SUBROUTINE CALC_MU_G
```

Annexe 5.

Exemple d'utilisation du programme POST. Celui-ci produit un fichier OUTPUT qui représente une carte de température pour chaque nœud à un temps fixe.

```
indi~/mfix/CONV/Jaupart_Brandeis_1986_b/V20_Exp8_5_f_17_mfix_corrected_isolated_verticalwalls$> post
 Enter the RUN_NAME to post_process > CONV1

 ***********************************************************

 read_res0 : code valid for running on 1 processor only

 ***********************************************************

 ****************************************************************************
  0  - Exit POST_MFIX
  1  - Examine/print data
  2  - Write .RES from data in .SPx files
  3  - Write .RES for a new grid, using old data
  4  - Calculate miscellaneous quantities
  5  - Print out variables
 ****************************************************************************
 CALL USER DEFINED SUBROUTINES:
  6  - USR_POST : getting average species mass fractions excluding bubbles
  7  - USR_POST1:
  8  - USR_POST2: getting average MELT velocity along the i-direction for
       the cells whose temperatures are below the solidus at each j-level
  9  - USR_POST3: getting average MELT velocity along the i-direction for
       the cells whose temperatures are below any temperature at each j-level
  10 - USR_POST4: getting average SOLID velocity along the i-direction for
       the cells whose temperatures are below any temperature at each j-level
  11 - USR_POST5: getting average MELT velocity along the i-direction for
       the cells whose temperatures are below any temperature at each j-level
       including all the values in k-direction
  12  - USR_POST6: getting average EP_g along the i-direction for
       the cells whose temperatures are below any temperature at each j-level
  13  - USR_POST7: getting mass blance per cell in i-direction and for each
        j-level at specific time
  14  - USR_POST8: getting mass blance per cell in i-direction for all j-level
        per time step
 ****************************************************************************
  15 - Write a new SPx file with selected records
  16 - Write new SPx files with time averaged data
  17 - Perform ORNL calculations
 ****************************************************************************

 Enter menu selection > 1

  Interactive data retrieval program. Type ? any time for help,
  or press RETURN to select default values shown in parenthesis.

 Time: (  0.000,  0.000) > 2 2
 Variable: (EP_g     ) >T_g
 I range: (  1,  1) >146 817
 Average or sum over I? (N) > N
 J range: (  1,  1) >98 417
 Average or sum over J? (N) > N
 K range: (  1,  1) >
 File: (*                    ) >x_vs_y_time2s.dat
```

OUTPUT

Z = -0.50000
Time = 2.0076

X	Y	Z	T_g
4.5156	3.0156	-0.50000	306.02
4.5469	3.0156	-0.50000	306.02
4.5781	3.0156	-0.50000	306.02
4.6094	3.0156	-0.50000	306.03
4.6406	3.0156	-0.50000	306.03
4.6719	3.0156	-0.50000	306.03
4.7031	3.0156	-0.50000	306.02
4.7344	3.0156	-0.50000	306.02
4.7656	3.0156	-0.50000	306.02
4.7969	3.0156	-0.50000	306.02
4.8281	3.0156	-0.50000	306.02
4.8594	3.0156	-0.50000	306.02
…	…	…	…
25.328	12.984	-0.50000	306.02
25.359	12.984	-0.50000	306.02
25.391	12.984	-0.50000	306.02
25.422	12.984	-0.50000	306.02
25.453	12.984	-0.50000	306.02
25.484	12.984	-0.50000	306.02

Références

Benyahia, S., Syamlal, M., O'Brien, T.J, "Summary of MFIX Equations 2005-4", From URL https://mfix.netl.doe.gov/documentation/MFIXEquations2005-4-4.pdf , August 2008.

Brandeis, G. Contribution à l'étude des couches limites dans une chambre magmatique. Thèse de Docteur Ingénieur, Université Paris 7, 1983.

Caricchi, L., L. Burlini, P. Ulmer, T. Gerya, M. Vassalli, and P. Papale (2007), Non-Newtonian rheology of crystal-bearing magmas and implications for magma ascent dynamics, *Earth Planet. Sci. Lett.*, *264*, 402–419, doi:10.1016/j.epsl.2007.09.032.

Chapman, S., and T. G. Cowling (1970), The Mathematical Theory of Non-uniform Gases, 3rd ed., 423 pp., Cambridge Univ. Press, New York.

Crowe, C., Sommerfeld, M., and Tsuji, Y., H (1997), Multiphase flows with droplets and particles, CRC Press.

Ding, J., and Gidaspow, D., 1990, "A Bubbling Fluidization Model Using Kinetic Theory of Granular Flow," AIChE J., **36**, 523-538.

Gidaspow, D. 1994, Multiphase Flow and Fluidization: Continuum and Kinetic Theory Descriptions, 467 pp., Academic, San Diego, Calif.

Dartevelle, S. (2004), Numerical modeling of geophysical granular flows: 1. A comprehensive approach to granular rheologies and geophysical multiphase flows, *Geochem. Geophys. Geosys.*, *5*(8), Q08003, doi:10.1029/2003GC000636.

Dartevelle, S., W. I. Rose, J. Stix, K. Kelfoun, and J. W. Vallance (2004), Numerical modeling of geophysical granular flows: 2. Computer simulations of plinian clouds and pyroclastic flows and surges, *Geochem. Geophys. Geosys.*, *5*(8), Q08004, doi:10.1029/2003GC000637.

Dartevelle, S., and G. A. Valentine (2007), Transient multiphase processes during the explosive eruption of basalt through a geothermal borehole (Námafjall, Iceland, 1977) and implications for natural volcanic flows, *Earth Planet. Sci. Lett.*, *262*, 363–384, doi:10.1016/j.epsl.2007.07.053.

Deardorff, J.W., Willis, G.E. and Lilly, D.K., Laboratory experiments of non-steady penetrative convection. J. Fluid Mech. 35, 7-31, 1969.

Dufek, J., and G. W. Bergantz (2005), Transient two-dimensional dynamics in the upper conduit of a rhyolitic eruption: A comparison of closure models for the granular stress, *J. Volcanol. Geotherm. Res.*, *143*, 113–132, doi:10.1016/j.jvolgeores.2004.09.013.

Dufek, J., and O. Bachmann (2010), Quantum magmatism: Magmatic compositional gaps generated by melt-crystal dynamics, *Geology*, 38(8), 687– 690, doi:10.1130/G30831.1.

Dartevelle, S. (2004), Numerical modeling of geophysical granular flows: 1. A comprehensive approach to granular rheologies and geophysical multiphase flows, *Geochem. Geophys. Geosys.*, *5*(8), Q08003, doi:10.1029/2003GC000636.

Dufek, J., and G. W. Bergantz (2005), Transient two-dimensional dynamics in the upper conduit of a rhyolitic eruption: A comparison of closure models for the granular stress, *J. Volcanol. Geotherm. Res.*, *143*, 113–132, doi:10.1016/j.jvolgeores.2004.09.013.

Gidaspow, D., *Multiphase Flow and Fluidization*, Academic Press, Inc., 1994.

Giordano, D., J. K. Russell, and D. B. Dingwell (2008), Viscosity of magmatic liquids: A model, *Earth Planet. Sci. Lett.*, *271*, 123–134, doi:10.1016/j.epsl.2008.03.038.

Jaeger, H. M., Nage, S. R. et R. P. Behringer. (1996), Granular solids, liquids and gases, Rev. Modern Phys., 68, 1259-1273.

Jaupart, C., and G. Brandeis (1986), The stagnant bottom layer of convecting magma chambers, *Earth Planet. Sci. Lett.*, *80*, 183–199, doi:10.1016/0012-821X(86)90032-4.

Jenike, A.W., 1987, "A Theory of Flow of Particulate Solids in Converging and Diverging Channels Based on a Conical Yield Function," Powder Tech., 50, 229-236.

Jenkins, J.T., and Savage, S.B., 1983, "A Theory for the Rapid Flow of Identical, Smooth, Nearly Elastic, Spherical Particles," J. Fluid Mech., *130*, 187-202.

Johnson, P. C., Nott, P. and Jackson, R. (1990), Frictional–collisional equations of motion for participate flows and their application to chutes. *Journal of Fluid Mechanics,210*, 501-535, doi:10.1017/S0022112090001380.

Kraichnan, R.H., Turbulent thermal convection at arbitrary Prandtl number, Phys. Fluids 5, 1374-1389.

Lebowitz, J.L., 1964. Exact solution of generalized Percus–Yevick equation for mixture of hard spheres. Physical Review A 133, 895– 899.

Lun, C.K.K., Savage, S.B., Jeffrey, D.J., and Chepurniy, N., 1984, "Kinetic Theories for Granular Flow: Inelastic Particles in Couette Flow and Slightly Inelastic Particles in a General Flow Field," J. Fluid Mech., *140*, 223-256.

Patiño-Palacios, G. (2007), Modélisation numérique eulérienne des écoulements gaz-solide avecplusieurs espèces de particules, Ph. D. Theses, INP-Toulose, France.

Pinotti, P., F. D'Eramo, M. Demartis, J.E. Coniglio, J.M. Tubia, Estructuras magmáticas en granitos, 2010, *Rev. Asoc. Geol. Argent*, *67*(4), pp. 562-572, ISSN 0004-4822.

Ruprecht, P., G. W. Bergantz, and J. Dufek (2008), Modeling of gas-driven magmatic overturn: Tracking of phenocryst dispersal and gathering during magma mixing, *Geochem. Geophys. Geosyst.*, *9*(7), Q07017, doi:10.1029/2008GC002022.

Schaeffer, D. G. (1987), Instability in the evolution equations describing incompressible granular flow, *J. Diff. Equations*,66, 19–50.

Syamlal, M., and O'Brien, T.J. (1987), " The Derivation of a Drag Coefficient Formula from Velocity-Voidage Correlations" pp. 20, U.S. Dep. Of Energy, Washington, D. C.

Syamlal, M., and O'Brien, T.J. (1988), "Simulation of Granular Layer Inversion in Liquid Fluidized Beds", Int. J. Multiphase Flow, 14, 473-481.

Syamlal, M. (1994), *MFIX documentation: User's manual*, *DOE/METC-95/1013, DE9500,031*, pp. 87, U.S. Dep. Of Energy, Washington, D. C.

Syamlal, M. (1998), *MFIX documentation: Numerical technique*, *DOE/MC/31346-5824, DE98002029*, pp. 80, U.S. Dep. of Energy, Washington, D. C.

Syamlal, M., W. Rogers, and T. J. O'Brien (1993), *MFIX documentation: Theory guide*, *DOE/METC-94/1004, DE9400,097*, pp. 49, U.S. Dep. of Energy, Washington, D. C.

Turcotte D. L., and G. Schubert (2002), *Geodynamics*, 2nd edition, Cambridge University Press, Cambridge.

Valentine, G. A., (1994), Multifield governing equations for magma dynamics, Geophysical & Astrophysical Fluid Dynamics, (*78*) 1-4, pp. 193-210, doi:10.1080/03091929408226578.

JOURNAL OF GEOPHYSICAL RESEARCH, VOL. 117, B07209, doi:10.1029/2011JB008760, 2012

Numerical simulations of convection in crystal-bearing magmas: A case study of the magmatic system at Erebus, Antarctica

Indira Molina,[1,2,3] Alain Burgisser,[1,2,3] and Clive Oppenheimer[1,2,4]

Received 9 August 2011; revised 27 April 2012; accepted 29 May 2012; published 21 July 2012.

[1] The sustained heat and gas output from Erebus volcano reflects a regime of magma convection that we investigate here using a bi-phase (melt and crystals), fluid dynamical model. Following validity and verification tests of the model, we carried out four single-phase and three bi-phase numerical 30-year- simulations, in an idealized 2D geometry representing a lava lake cooled from above and a reservoir heated from below that are linked by a 4-to-10–m-diameter conduit. We tested the effects of crystals on convection while changing conduit size and the system boundaries from closed to open. Neglecting crystal settling yields only a limited number of features, i.e., (i) the formation of a central instability, (ii) the average temperature evolution, and (iii) the average velocity range of the surface flow motion. Bi-phase simulations show that while crystals are quite efficiently transported by the liquid phase a small decoupling reflecting their large size (5 cm) results in settling. This leads to more complex circulation patterns and enhances the vigor of fluid motion. A sufficiently large conduit sustains convection and retains 6 and 20% of crystals in suspension, for a closed and open system, respectively. Model outputs do not yet correspond well with field observations of Erebus lava lake (e.g., real surface velocities are much faster than those modeled), suggesting that exsolved volatiles are an important source of buoyancy.

Citation: Molina, I., A. Burgisser, and C. Oppenheimer (2012), Numerical simulations of convection in crystal-bearing magmas: A case study of the magmatic system at Erebus, Antarctica, *J. Geophys. Res.*, *117*, B07209, doi:10.1029/2011JB008760.

1. Introduction

[2] Characterizing the dynamics of convection currents in magmatic plumbing systems is a challenging task, which has long been approached through experimental [e.g., *Jaupart and Brandeis*, 1986; *Weinstein et al.*, 1988; *Bazarov et al.*, 2007; *Huppert and Hallworth*, 2007] and theoretical [e.g., *Sparks et al.*, 1984; *Jaupart and Brandeis*, 1986; *Jellinek and Kerr*, 2001] studies that have considered magma as a perfectly homogeneous mixture of melt, crystals and bubbles. More recently, studies based on multiphase theory have been addressing the differential motion of these three phases, taking them in pairs [e.g., *Dartevelle*, 2004; *Dartevelle et al.*, 2004; *Dufek and Bergantz*, 2005; *Dartevelle and Valentine*, 2007; *Ruprecht et al.*, 2008; *Dufek and Bachmann*, 2010]. These studies have, among other insights, highlighted the complex relationships between convective movements, which tend to keep crystals in suspension because of high melt viscosity, and the gravitational settling of crystals, which drives melt/crystal separation. Most of these numerical and experimental studies, however, have employed highly idealized magmatic systems; only a few have focused on specific natural systems.

[3] Motivated by the fact that they provide a window into the underlying magmatic system, many field studies have been devoted to lava lakes. The nature of convection can be best understood in long-lived systems where low viscosity magmas (e.g., phonolitic, nephelinitic, basaltic andesitic, basaltic) are permanently exposed, such as Erebus volcano in Antarctica [*Oppenheimer and Kyle*, 2008, and references therein], Nyiragongo in the Democratic Republic of Congo [*Demant et al.*, 1994], Villarrica in Chile [*Witter et al.*, 2004], Erta'Ale in Ethiopia [*Bizouard et al.*, 1980], Pu' u O' in Hawaii [*Garcia et al.*, 2000], and Stromboli in Italy [e.g., *Giberti et al.*, 1992; *Laiolo and Cigolini*, 2006]. Several aspects of Erebus volcano motivated us to choose it as a subject for a numerical study of convective processes. A unique feature of its lava lake is the large size (up to ~10 cm) of crystals it contains [*Kelly et al.*, 2008]. These megacrysts represent more than 97 vol.% of the crystal cargo and beg the question as to whether their sedimentation interferes with convection or if they act as passive tracers with trajectories diagnostic of a particular convective regime. Many studies have been devoted to Erebus, providing a wealth of data on which numerical simulations can be based. They provide indications of lake and upper conduit dimensions [e.g., *Dunbar et al.*, 1994; *Aster et al.*, 2008; *Dibble et al.*, 2008; *Kyle et al.*, 1992], the current low rate of crystallization

[1]ISTO, UMR 7327, Université d'Orléans, Orléans, France.
[2]ISTO, UMR 7327, CNRS/INSU, Orléans, France.
[3]ISTO, UMR 7327, BRGM, Orléans, France.
[4]Department of Geography, University of Cambridge, Cambridge, UK.

Corresponding author: I. Molina, ISTO, UMR 7327, Université d'Orléans, FR-45071, Orléans, France. (indimolina08@gmail.com)

©2012. American Geophysical Union. All Rights Reserved.
0148-0227/12/2011JB008760

[*Dunbar et al.*, 1994; *Kelly et al.*, 2008], as well as good constraints on the magmatic properties and characteristics such as crystal content and size [e.g., *Kelly et al.*, 2008; *Dunbar et al.*, 1994], temperature [e.g., *Calkins et al.*, 2008; *Kelly et al.*, 2008; *Sweeney et al.*, 2008], viscosity [*Sweeney et al.*, 2008], crystal age [e.g., *Reagan et al.*, 1992] and steadiness of convection [e.g., *Kelly et al.*, 2008].

[4] Here, we reduce the gap in numerical studies dedicated to a given volcano by studying the behavior of the shallow magmatic system of Erebus (from reservoir to lava lake) when it is assumed to contain either a single-phase mixture of silicate melt and crystals, or a bi-phase combination of silicate melt plus crystals. Carrying out such numerical simulations involves two complementary aspects. From a modeling perspective, contrasting the convective motions generated by a simplified mixture to those generated by a bi-phase system (where crystals can settle) identifies which features of magmatic convection are best viewed using a single- or a multiphase system. This represents an important step in the development of numerical models that include the three phases (melt, crystals, and bubbles) present in magmas. The simulations also allow us to tackle technical issues concerning boundary conditions, which govern the long-term behavior of the system. More specifically, our study is relevant to understanding the behavior and stability of Erebus lava lake. A sustained activity is surprising for a lake of such small dimensions; it implies the existence of a vigorous convecting system that maintains the lake at a quasi-constant temperature. Considering the fluidal nature of molten phonolite, it is reasonable to ask whether temperature gradients alone can generate sufficient buoyancy to keep the lake from freezing, or if additional buoyancy sources, such as gas bubbles, need to be involved. The underlying driving mechanism is not unique to Erebus, and its understanding might shed light on other volcanoes.

[5] In the next section, we briefly describe the bi-phase model used and basic assumptions underlying its application to magmas. Section 3 concerns validation and verifications tests of the single-phase part of the model via reproduction of analogue experiments of transient convection, and of the bi-phase part by reproduction of the bulk behavior of a simple Poiseuille flow. In section 4 we describe the different numerical configurations tested to study the Erebus magmatic system and the results of the numerical simulations. Overall, these results suggest the existence of a minimum conduit diameter that ensures effective and lasting convection, and reveal partial settling of crystals - provided they are considered as a separate phase - leading to the formation of an enriched layer of crystals at the bottom of the magma chamber. In section 5 we compare our results with other theoretical and experimental works to draw conclusions on the suitability of using multiphase physics to simulate magma convection. We find that the extension of our results to Erebus and other magmatic systems requires consideration of bubbles.

2. Physical Model Description

[6] The dynamics of crystal-bearing magmas can be modeled as bi-phase flows (a mixture of crystals/solids/dispersed phase and fluid/continuous/carrier phase) using either a continuum (Eulerian) or a discrete-particle (Lagrangian) approach. Here, we will consider a system consisting of phases sharing the same pressure field (Eulerian-Eulerian approach) [*Dartevelle*, 2004; *Dartevelle et al.*, 2004]. We wished to limit the complexity of the model so as to capture the fundamental differences between mixture theory, where crystals and melt are considered as a single phase with modified properties, and the bi-phase formulation that considers crystals as a separate phase. This led us to make two fundamental assumptions, as follows.

[7] First, we considered Erebus magma as a bi-phase flow containing melt and crystals, thereby ignoring the presence of a gas phase. This is a shortcoming because the sustained gas emission from the lake surface and sporadic Strombolian explosions through the lake are clear indications that gas bubbles play an important role at Erebus [e.g., *Giggenbach et al.*, 1973]. Ignoring gas will lead to underestimation of the convective dynamics of the simulated system, slowing down motions because of the neglected buoyancy source. While this severely limits the applicability of our model to the real system in terms of making direct comparisons between model outputs and observed parameters, we nevertheless can simulate a magmatic system with many other realistic characteristics (complex geometry, physical parameters of the magma, timescales, etc.) and draw conclusions on the role of megacrysts in magmatic convection.

[8] Second, we treated crystals as rigid spherical particles of constant size in order to realize consistent rheological formulations for the mixed and bi-phase systems. This is a significant shape simplification because Erebus megacrysts have aspect ratios (ratio between long and short axes) of 2–3 [*Dunbar et al.*, 1994], an anisometry sufficient to affect the rheology of the suspension [e.g., *Mueller et al.*, 2010]. The works of *Caricchi et al.* [2007] and *Costa et al.* [2009] have treated magma as a homogeneous mixture of crystals and melt. They proposed effective viscosity formulations taking into account the non-sphericity of the particles through the linear dependence between the average aspect ratio and maximum packing fraction given by *Pabst et al.* [2006]. Matching such dependence with a bi-phase flow, however, is beyond the scope of the present work, mainly because drag laws and solid moment tensors for describing the behavior of non-spherical crystals are not currently available in the literature. It can nevertheless be estimated that considering our crystals as rigid spheres underestimates the viscosity of the suspension [*Picard et al.*, 2010].

[9] The numerical code that we used to solve the bi-phase flow equations is MFIX Ver. 2.0, 2004 (Multiphase Flow with Interphase eXchanges), a program developed at the Department of Energy National Energy Technology Laboratory of U.S. The software package VISIT Ver. 1.12 developed by the U.S Lawrence Livermore National Laboratory was used to visualize simulation outputs and all numerical data were post processed by script shells developed in MATLAB® and FORTRAN. MFIX is based on several works developed since 1967 [*Syamlal et al.*, 1993; *Syamlal*, 1994, 1998]. The code, based on a discretization using staggered and finite volume methods, has provided a platform by which to explore various volcanic phenomena: (i) as a closed and isothermal system to simulate magma mixing [*Ruprecht et al.*, 2008], (ii) as an open and isothermal system to explore conduit flow [*Dufek and Bergantz*,

Table 1. General Transport Equations of the Physical Model

Equation	Number
Continuity	
$\varepsilon_m + \varepsilon_s = 1$	(14)
Melt	
$\frac{\partial}{\partial t}(\varepsilon_m \rho_m) + \nabla\cdot(\varepsilon_m \rho_m \mathbf{v}_m) = 0$	(15)
Solid	
$\frac{\partial}{\partial t}(\varepsilon_s \rho_s) + \nabla\cdot(\varepsilon_s \rho_s \mathbf{v}_s) = 0$	(16)
Momentum	
Melt	
$\frac{\partial}{\partial t}(\varepsilon_m \rho_m \mathbf{v}_m) + \nabla\cdot(\varepsilon_m \rho_m \mathbf{v}_m \mathbf{v}_m) = \nabla\cdot \mathsf{S}_m + \varepsilon_m \rho_m \mathbf{g} - F_{ms}(\mathbf{v}_m - \mathbf{v}_s)$	(17)
Solid	
$\frac{\partial}{\partial t}(\varepsilon_s \rho_s \mathbf{v}_s) + \nabla\cdot(\varepsilon_s \rho_s \mathbf{v}_s \mathbf{v}_s) = \nabla\cdot \mathsf{S}_s + \varepsilon_s \rho_s \mathbf{g} + F_{ms}(\mathbf{v}_m - \mathbf{v}_s) - \varepsilon_s \nabla P_m$	(18)
Stress tensor	
Melt	
$\mathsf{S}_m = -P_m \mathsf{I} + \tau_m$	(19)
Granular	
$\mathsf{S}_s = -P_s^{\mathrm{P}} \mathsf{I} + \tau_s^{\mathrm{P}}$ *if* $\varepsilon_m \le \varepsilon_m^*$ Plastic/Frictional	(20)
$\mathsf{S}_s = -P_s^{\mathrm{v}} \mathsf{I} + \tau_s^{\mathrm{v}}$ *if* $\varepsilon_m > \varepsilon_m^*$ Kinetic - Collisional	(21)
Granular normal stress	
$P_s^{\mathrm{P}} = 10^{24}(\varepsilon_m^* - \varepsilon_m)^{10}\varepsilon_s$	(22)
$P_s^{\mathrm{v}} = 2(1+e)\rho_s g_o \varepsilon_s \Theta_s$	(23)
where $g_o = f(\varepsilon_m, \varepsilon_s)$	(24)
$\Theta_s = f(K_1, K_2, K_3, K_4, \varepsilon_s, tr(\mathsf{D}_s))$	(25)
$K_1 = f(e, g_o, \rho_s)$	(26)
$K_2 = f(e, g_o, \rho_s, d_p, \varepsilon_s, K_3)$	(27)
$K_3 = f(e, g_o, \rho_s, d_p, \varepsilon_s)$	(28)
$K_4 = f(e, g_o, \rho_s, d_p)$	(29)
Melt viscous stress	
$\tau_m = 2\varepsilon_m \mu_m \mathsf{D}_m - \frac{2}{3}\varepsilon_m \mu_m tr(\mathsf{D}_m)\mathsf{I}$	(30)
Granular viscous stress	
$\tau_s^{\mathrm{P}} = \min\left[2\mu_s^{\mathrm{P}}\mathsf{D}_s, 2\mu_s^{\max}\mathsf{D}_s\right]$ where $\mu_s^{\mathrm{P}} = \frac{P_s^{\mathrm{P}}\sin\phi}{2\sqrt{I_{2Ds}}}$ and $\mu_s^{\max} = 100$ Pas	(31)
$\tau_s^{\mathrm{v}} = 2\mu_s^{\mathrm{v}}\mathsf{D}_s + \lambda_s^{\mathrm{v}} tr(\mathsf{D}_s) I$ where $\mu_s^{\mathrm{v}} = K_3 \varepsilon_s \sqrt{\Theta_s}$	(32)
$\lambda_s^{\mathrm{v}} = K_2 \varepsilon_s \sqrt{\Theta_s}$	(33)
Momentum interface transfer coefficient	
Drag forces	
$F_{ms} = f(\varepsilon_s, \varepsilon_m, \rho_m, d_p, Re_s, V_r, \mathbf{v}_s, \mathbf{v}_m)$	(34)
Terminal velocity	
$V_r = f(\varepsilon_m, Re_s)$	(35)
Particle Reynolds Number	
$Re_s = f(d_p, \rho_m, \mu_m, \mathbf{v}_s, \mathbf{v}_m)$	(36)
Energy	
Melt	
$\varepsilon_m \rho_m C_{pm}\left(\frac{\partial T_m}{\partial t} + \mathbf{v}_m\cdot\nabla T_m\right) = -\nabla\cdot\mathbf{q}_m + \gamma_{ms}(T_s - T_m)$	(37)
Solid	
$\varepsilon_s \rho_s C_{ps}\left(\frac{\partial T_s}{\partial t} + \mathbf{v}_s\cdot\nabla T_s\right) = -\nabla\cdot\mathbf{q}_s - \gamma_{ms}(T_s - T_m)$	(38)
Heat conductivity	
Melt conductivity	
$\mathbf{q}_m = \varepsilon_m k_m \nabla T_m$	(39)
Granular conductivity	
$\mathbf{q}_s = \varepsilon_s k_s \nabla T_s$	(40)
Heat interface transfer coefficient	
$\gamma_{ms} = f(k_m, \varepsilon_s, Nu, d_p)$	(41)
Nusselt Number	
$Nu = f(\varepsilon_s, \varepsilon_m, Re_s, Pr)$	(42)
Prandtl Number	
$Pr = f(C_{pm}, \mu_m, k_m)$	(43)

2005], (iii) as an open and non-isothermal system to explore the magma chamber dynamics [*Dufek and Bachmann*, 2010] and conduit flow [*Dartevelle and Valentine*, 2007]. In this study we used MFIX to study the magmatic system feeding the lava lake at Erebus volcano as (i) closed and non-isothermal, and (ii) open non-isothermal systems. This is the first study using a closed and non-isothermal system. Since the temperature gradients in the simulated magmatic system are very large, this approach has limitations because the overall cooling causes melt contraction, which is incompatible with the finite-volume numerical scheme applied to a closed system. This issue is addressed in section 4.6.

2.1. Governing Equations

[10] MFIX uses the Navier-Stokes equations for momentum together with supplemental equations for the interphase forces, plus mass conservation and energy equations, which enable the simulation of incompressible multiphase flow with a Newtonian carrier phase. The main transport vector equations for a bi-phase system without chemical reaction between phases are reported in Table 1. The constitutive terms of each equation are explained in the text and the nomenclature is summarized in Table A1. A positive sign convention is adopted throughout this study, which means that stresses are positive when both the outward normal and force act in the same sense relative to the coordinate system x and y, or East and up, respectively.

[11] Continuity requires that the sum of the volume fractions always equals one (equation (14); equations (14)–(43) are given in Table 1). The differential form of the mass conservation equation (equations (15) and (16)) states that the accumulation of mass per unit volume plus the convective flux of mass per unit volume (first and second terms of LHS) is equal to zero (RHS). This absence of phase exchange means that there is no crystal growth or nucleation. The Navier-Stokes equations account for the rate of increase of momentum per unit volume and for the rate of momentum transferred by convection per unit volume (first and second terms of LHS in equations (17) and (18)). Thus the whole LHS term is equal to (in the RHS from left to right) (i) the interaction within the phase accounted for as the stress tensor (normal and shear stress components) per unit volume, (ii) the net gravitational body force acting on each phase, and (iii) and (iv) the interaction forces between the fluid and solid phases per unit volume (drag and buoyancy force). The term (iv) only exists in equation (18). The formulation of the stress tensor for the melt (equation (19)) follows a Newtonian form. The granular phase (equations (20) and (21)) follows the transitional theory from viscous to plastic regime proposed by *Johnson and Jackson* [1987] through the void fraction at minimum fluidization ε_m^*. Thus, at high concentrations, the grains impinge on each other, losing mobility and giving rise to a frictional (plastic) dissipation and transfer of momentum (equation (20)) [*Schaeffer*, 1987]. Otherwise (equation (21)), the grains either move randomly by kinetic transport (particle translation) or by grain-grain collisions following the Chapman-Enskog approach for dense gases [*Chapman and Cowling*, 1970]. Grains interact with the fluid through drag laws [*Jenkins and Savage*, 1983; *Lun et al.*, 1984; *Ding and Gidaspow*, 1990]. Equations (22)–(36) define the factors composing the stress tensor for the melt and granular phase,

and the drag forces [*Syamlal et al.*, 1993]. The LHS of energy equations (37) and (38) indicates that the net rate of change of temperature within a grid cell is equal to the sum of the work resulting from the RHS: (i) heat conduction within the phase and (ii) the heat transfer between phases. In this study we have neglected the viscous dissipation and the work due to drag forces. Equations (39)–(43) define the factors relevant to (i) and (ii) [*Syamlal et al.*, 1993].

[12] In simulations using two phases, crystals have a constant density and the melt has a temperature-controlled density. In single-phase simulations, the mixture phase density, $\rho_{(m+s)}$, is modeled as the weighted sum of the constant density of the dispersed phase and the thermally controlled density of the continuous phase:

$$\rho_{(m+s)} = (1 - \varepsilon_m)\rho_s + \varepsilon_m\{\rho_o[1 - \alpha(T_m - T_o)]\} \quad (1)$$

Where ε_m is the liquid fraction, ρ_s is the crystal density, T_m is the temperature of the melt, T_o is the initial temperature, ρ_o and α are the density and thermal expansion coefficient of the melt at initial temperature.

[13] The crystal content may play a fundamental role in increasing the magma bulk viscosity, $\mu_{(m+s)}$. Close to the maximum packing fraction ($1 - \varepsilon_m^*$), the effect of crystals dominates over the liquid phase, the suspension loses mobility and the bulk mixture viscosity increases significantly. Among others, *Caricchi et al.* [2007] determined that the presence of crystals causes the mixture to react as a non-Newtonian fluid. This behavior could result in visco-plastic or Bingham-plastic behavior, where the magma exhibits a finite yield strength [e.g., *Murase and McBirney*, 1973]. However, the modeling of this behavior remains uncertain and we have instead adopted the broadly accepted rheology for the mixture given by *Krieger and Dougherty* [1959]:

$$\mu_{(m+s)} = \mu_m\left(1 - \frac{\varepsilon_s}{1 - \varepsilon_m^*}\right)^{-[\eta]\left(1-\varepsilon_m^*\right)} \quad (2)$$

Where μ_m is the dynamic viscosity of the melt and ε_s is the crystal fraction. Since we consider mono-dispersed (same size) crystals as rigid spheres without attractive or repulsive forces, the Einstein coefficient was fixed at the theoretical value, $[\eta] = 2.5$. We note that the more sophisticated effective viscosity formulations proposed by *Caricchi et al.* [2007] and *Costa et al.* [2009] converge on the *Krieger and Dougherty* [1959] relationship when crystal fraction is lower than the maximum packing fraction. As mentioned in sections 3 and 4, our simulations scarcely reach such crystal fraction.

2.2. Thermal Boundary Conditions

[14] To define the heat that flows out of the computation domain, MFIX has two kinds of wall boundary conditions for the energy equations: (i) non-conducting wall (no interaction with the surrounding medium) in which the wall temperature, T_{wall}, is fixed, and (ii) boundary heat flux specified by a heat transfer coefficient C_m:

$$\frac{\partial T_{wall_x}}{\partial n} = C_m \quad (3)$$

Where ∂/∂_n denotes differentiation along the outward-drawn normal, and T_{wall_x} is the wall temperature as a function of distance.

[15] Algebraic methods can be used for the calculation of C_m across plane walls. To calculate how much heat is lost through the walls, we have used the algebraic model of *Turcotte and Schubert* [2002], which states that the temperature of the wall rock as a function of time can be obtained by solving the one-dimensional, time-dependent heat conduction equation for a semi-infinite half-space, initially at uniform temperature and suddenly brought to a new temperature that remains constant from then on. The rate of heat transfer depends on the temperature gradient and the thermal conductivity of the material as follows:

$$\frac{T_{wall_{x,t}} - T_{fwall}}{T_o - T_{fwall}} = erfc\frac{x}{2\sqrt{\kappa_{wall}t}} \quad (4)$$

Where T_o is the initial temperature of the system (the same value as that used in equation (1)), T_{fwall} is the temperature far away from the wall along the outward-drawn normal, x is the distance from the wall, t is time and κ_{wall} is the thermal diffusivity of the wall rock. At long times, the system becomes insulated because the rate of heat transfer slows down. We calculated the derivative of equation (4) to obtain C_m.

2.3. Numerical Considerations

[16] Optimal grid size can be estimated using scaling analysis. When the local Rayleigh number reaches a critical value (Ra_c) [e.g., *Sparrow et al.*, 1970; *Jaupart et al.*, 1984], a convective instability develops and the thermal boundary layer breaks down into incipient plumes. The theoretical length of the grid size of the cell that captures well the dimensions of such a plume is given by considering the Rayleigh number, Ra, at its critical value ($Ra = Ra_c$):

$$Ra = \frac{\varepsilon_m \alpha \rho_m \Delta T g dy^3}{\kappa_m \mu_m} \quad (5)$$

Where ρ_m is the melt density, ΔT is the driving temperature difference, g is the gravity, κ_m is the thermal diffusivity of the melt, μ_m is the dynamic viscosity and dy is a characteristic length (in this case cell size).

[17] Several computing parameters control numerical convergence. In MFIX, time progression is governed by three parameters: starting, maximum and minimum time steps. MFIX uses an automatic step adjustment, which can be upwards to the maximum time step or downward to the minimum time step, which ensures that convergence is obtained [*Syamlal*, 1998]. The minimum time step has a physical limit. At the sub-grid scale, in an individual computational cell, particle acceleration within a given time step should be uniform. Sub-grid crystal velocity is described by the Newtonian equation of motion:

$$V_l = v_s\left[1 - \exp\left(\frac{-\xi t}{M}\right)\right] \quad (6)$$

Where V_l is the instantaneous particle velocity, v_s is the Stokes velocity, M is the mass of the particle, ξ is a

Table 2a. Parameters of the Experiments[a]

Parameter	Symbol	Unit	47V20	47V20[b]	47V500	47V1000
Initial temperature	T_o	°C	49.4	49.4	54.4	36.5
Temperature of top and bottom walls (BC1 and BC4)	T_f	°C	27.6	27.6	27.2	21.3
Temperature contrast ($T_o - T_f$)	ΔT	°C	21.8	21.8	22.2	21.8
Density	ρ_m	kg/m^3	930	930	942	946
Dynamic viscosity	μ_m	Pa s	0.012	0.12	0.284	0.767
Heat capacity	C_{pm}	kcal/ kg °C	0.368	0.368	0.371	0.368
Thermal conductivity	k_m	W/m °C	0.145	0.145	0.144	0.145
Thermal diffusivity	κ_m	m^2/ s	1.01×10^{-7}	1.01×10^{-7}	9.87×10^{-8}	9.96×10^{-8}
Thermal expansion	α	1/°C	1.07×10^{-3}	1.07×10^{-3}	9.45×10^{-4}	9.45×10^{-4}
Rayleigh number	Ra[c]	dimensionless	1.7×10^{8}	1.7×10^{7}	6.9×10^{6}	2.5×10^{6}
Observed height of the upper thermal boundary layer	h_c	m	0.21×10^{-2}	0.48×10^{-2}	0.60×10^{-2}	0.87×10^{-2}
Theoretical height of the upper thermal boundary layer	dy[d]	m	0.21×10^{-2}	0.45×10^{-2}	0.61×10^{-2}	0.86×10^{-2}
Error % for the height of the upper thermal boundary layer			0	6	2	1
Observed wavelength of the cold crust	λ_{obs}	m	0.60×10^{-2}	1.50×10^{-2}	1.80×10^{-2}	2.70×10^{-2}
Theoretical wavelength	λ_c[e]	m	0.58×10^{-2}	1.48×10^{-2}	1.77×10^{-2}	2.57×10^{-2}
Error % for wavelength			3	6	2	5
Number of starting plumes as a function of viscosity		dimensionless	32	15	10	6
Theoretical number of starting plumes		dimensionless	34	15	12	8

[a]The data are based on *Jaupart and Brandeis* [1986] and Bluestar Silicones France SAS (http://www.bluestarsilicones.com/).
[b]47V20 oil with modified dynamic viscosity.
[c]Value calculated with equation (5) and dy is the thickness of the tank.
[d]Value calculated with equation (5) and $Ra = Ra_c = 1600$ [*Jaupart et al.*, 1984].
[e]Value calculated with equation (9) from *Odé* [1966] and *Lister and Kerr* [1989].

proportionality constant related to the drag forces exerted by the melt ($\xi = 3\pi d_p \mu_m$), which depends on the particle diameter d_p. The minimum time step so that the solid phase speed is a macroscopic property is defined as the time taken for steady motion to be reached, which is when crystal velocity equals 99.5% of its steady Stokes settling velocity, defined as $v_s = (\Delta\rho g d_p^2)/(18\mu_m)$, where $\Delta\rho$ is the density difference between particle and fluid.

3. Validation and Verification of the Physical Model

[18] When modeling convective phenomena, dynamical parameters such as cooling rate, the wavelength of instabilities that form during overturn, the velocity of the resulting plumes, and the evolution of the bulk viscosity of the mixture are key criteria to verify the numerical code. For single-phase simulations, we validated our model against an analogue experiment performed by *Jaupart and Brandeis* [1986]; this validation yielded 2D numerical solutions of fluid convection. We used this model outputs to verify that descending plumes have velocities in conformity with the formulation proposed by *Read* [1984] and *Youngs* [1984]. The wavelength of instabilities can be predicted, as suggested by *Odé* [1966] and *Lister and Kerr* [1989]. To verify our code for bi-phase simulations, we used a fully developed Poiseuille flow to retrieve a bulk viscosity that we compared to the mixture formulation proposed by *Krieger and Dougherty* [1959] in equation (2). We detail validation and verifications below.

3.1. Validation and Verification of Momentum and Heat Transfer for Single-Phase Simulations

[19] For single-phase simulations, we tested whether MFIX could reproduce data, observations and conclusions of previously reported analogue experiments of *Jaupart et al.* [1984] and *Jaupart and Brandeis* [1986] that were aimed at simulating convection in magma chambers. The analogue experiments reproduced thermal convection by imposing a thermal gradient in a tank full of various silicone oils. We focused on the experimental convection of three kinds of oil, the physical properties of which are reported in Table 2a.

[20] In order to simulate conditions of instantaneous cooling (i.e., a temperature drop ΔT at time $t = 0$), the analogue experiments started with a hot and isothermal fluid layer at $T_o = 49$°C enclosed in a Plexiglas tank capped above and below by copper plates. A cryostat maintained the cooling fluid at 4°C in closed circuit. At time $t = 0$, both copper plates surrounding the hot fluid tank were linked to the cryostat circuit. After about 3 min, the temperature of both copper plates had dropped by a certain value. By setting the temperature of the cryostat close to that new value, Jaupart and coworkers were able to stabilize the coolant temperature to within 0.1°C in less than 6 min. The temperature of both upper and lower boundaries was thus maintained at a constant value $T_f = 27.6$°C for the rest of the experiment. Results show that the cooling rate is important over the first 3 min, before the temperature of the cryostat is raised to a value close to the final temperature of the tank. The cooling rate then diminishes significantly.

[21] The fluid numerical simulation domain consists of a 2D rectangular system with x- and y- origins at the bottom left-hand corner of the tank (Figure 1a). The aspect ratio of the experimental tank was preserved, although the simulations were carried out in 2D. All the boundaries were treated as "non-slip walls" (NSW). For the simulated range of temperatures (27.6°C to 49°C), we found that the size of the cell required to resolve the time at which instabilities begin to grow is around 0.01 cm (equation (5)). We searched for the optimal computational grid size by trial and error accordingly, between 0.125 and 0.01 cm. As expected, we observed that the plumes (convective instabilities) were better defined as grid size was decreased. The resulting average temperature in the central part of the tank is constant (within ~3°C) for the three simulations with grid sizes

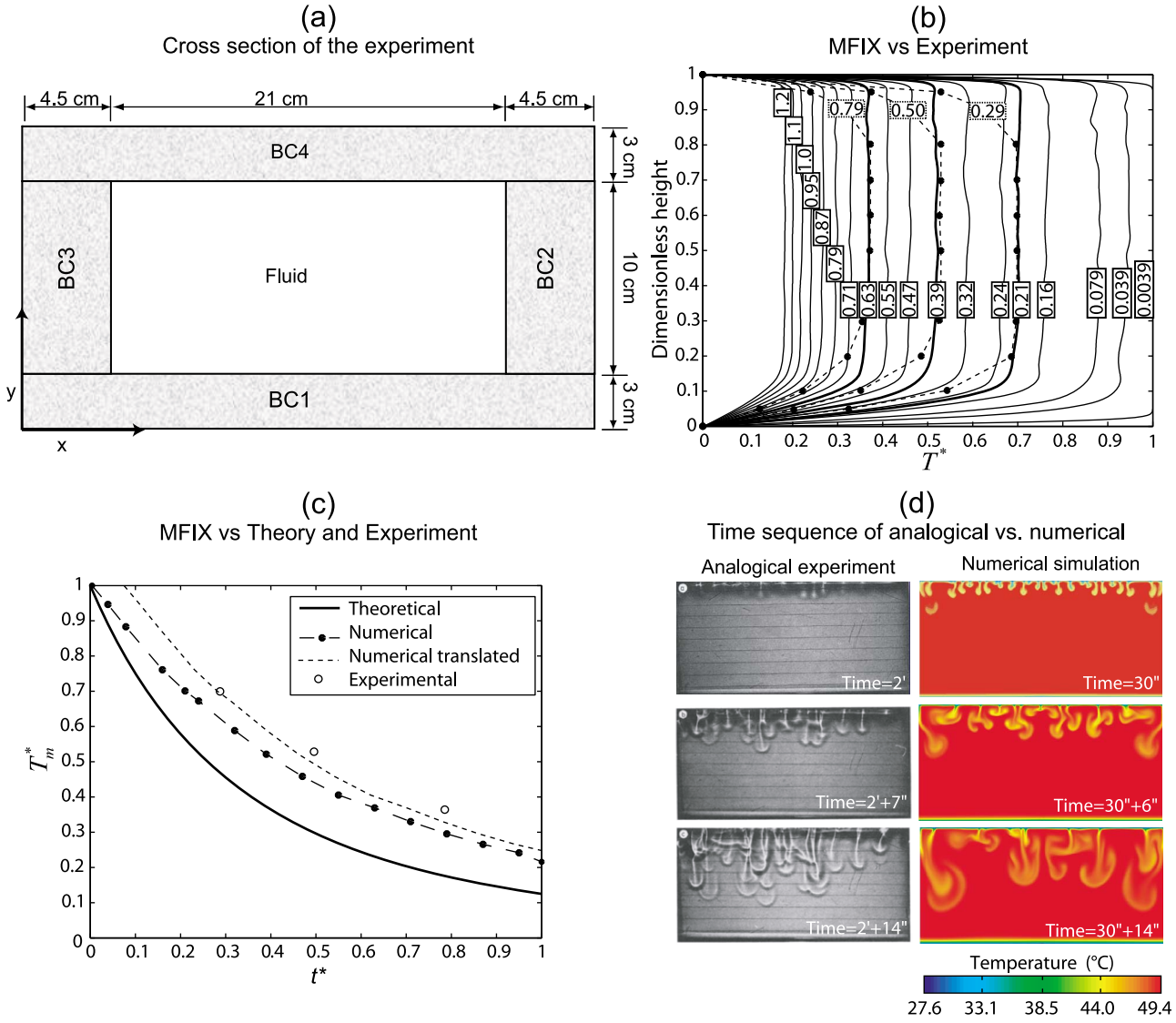

Figure 1. (a) Schematic representation of the numerical simulations based on experiments by *Jaupart and Brandeis* [1986]. The boundary conditions (BC) are as follows: BC1 and BC4 are non-slip walls with a constant and identical temperature colder than that of the fluid domain, BC2 and BC3 are non-slip walls and assumed to be insulators. (b) Time sequence of the evolution of convection. Curves are mean horizontal dimensionless temperature T^* profiles for the experiments (dashed lines) and the numerical model (plain lines). Vertical labels over the curves indicate dimensionless times for the numerical model, whereas horizontal labels show dimensionless times for the experiment. Bold lines highlight the times at which model and experiment are compared. After 30 min ($t^* \sim 0.71$), the experiment reaches near steady state conditions, which is visible on the graph as the constant height of the inflexion point marking the transition from the well-mixed central layer to the steep temperature gradient at the bottom wall. (c) Evolution of the non-dimensional temperature in the well-mixed layer, T_m^*, versus non-dimensional time t^*. The solid curve is the theoretical estimate given by *Jaupart and Brandeis* [1986]. The dashed curve is joining the numerical data and the dotted curve is obtained by translating the dashed curve along the time axis by an amount equal to the time lag of the onset of the experiment (~3 min / $\Delta t^* \sim 0.1$); dots represent the values of experimental data. (d) Time sequences of the development of convection for the experiment and numerical model at early times. Experimental shadowgraph reproduced from *Jaupart and Brandeis* [1986], copyright 1986, with permission from Elsevier.

between 0.01 and 0.03 cm. This is close to the theoretical value, and we selected a grid cell of 0.03 cm (960 × 512 computational cells) for better computational efficiency. A satisfactory match between experiments and runs will be taken as the sign that 2D simulations of a 3D tank with a square upper surface can capture important features of the convective process. These features include the vertical temperature profile, the evolution of the temperature of the well-mixed central part of the tank, the progression of the

unstable cold front, and the wavelength of the instabilities that compose it.

3.1.1. Comparison Between Numerical and Experimental Results

[22] We first describe the simulation with a tank full of oil 47V20 (Table 2a and Figure 1). The initial oil temperature was set at a uniform and constant value of 49.4°C. The tank was then cooled from above and below, which means that BC1 and BC4 were fixed at a constant temperature of 27.6°C while the vertical walls BC2 and BC3 were considered as insulators ($C_m = -10^{-8}$°C/m, Figure 1a). Following *Jaupart and Brandeis* [1986], we compare numerical runs and experiments as a function of a dimensionless time $t^* = t/\tau$, with τ as a diffusive thermal scale, and a dimensionless temperature $T^* = 1 - (T_o - T_m)/(T_o - T_f)$, which is a function of the initial fluid temperature, T_o, the horizontal average fluid temperature at a given depth, T_m, and the plates' temperature, T_f.

[23] As shown in Figure 1b, the average temperature profiles from the analogue experiments have steeper profiles at the boundaries than those of the numerical runs (especially near the top of the tank). The temperatures of the central part of the tank, in the well-mixed layer that is nearly isothermal, are, however, identical for both the model at $t^* = 0.21$, 0.39 and 0.63 and the experiment at $t^* = 0.29$, 0.5 and 0.79. These dimensionless times correspond to approximately 9, 16, and 27 min, and 12, 21, and 33 min for model and experiment, respectively. This yields an initial time shift of 3 min, which corresponds well with the time taken by the system to stabilize before the cryostat is set to the temperature of equilibrium. *Jaupart and Brandeis* [1986] calculated a theoretical dimensionless function T_m^* for the variation in temperature of the well-mixed layer (the constant flat profile for each curve in Figure 1b). This dimensionless function is plotted in Figure 1c and compared to both analogue and numerical simulations. We observe a discrepancy between the three curves. The discrepancy between theory and analogue model was already noticed by *Jaupart and Brandeis* [1986]. They report that experimental data fall on the theoretical curve when shifted in time because the theoretical curve assumes instantaneous cooling of the boundaries. The same applies to our simulation ("numerical translated" curve in Figure 1c), and explains why our simulation approaches the theoretical curve at earlier times.

[24] Rayleigh-Taylor (RT) instabilities occur in a fluid cooled from above when the surface reaches a temperature threshold that generates sufficient density contrast to induce convection. The time sequence of the development of the convection for the experiment and simulation at early times is shown in Figure 1d. The general shape and sizes of the instabilities match quite well, with a time lag varying from 3 min to 6 min at later times. The more numerous instabilities in the analogue experiments can easily be explained by the fact that, unlike our 2D simulation, the shadowgraphs capture several layers of instabilities along the line of sight. *Read* [1984] and *Youngs* [1984] found that the cold front formed by the plumes sinks into the warmer fluid as:

$$h(t) = \beta A_T g t^2 \tag{7}$$

Where $h(t)$ is the height of the plume envelope as a function of time, t, β is a constant equals to 0.05 [*Dimonte*, 1999; *Dimonte and Schneider*, 2000], g is the gravity constant (taken as 9.8 m/s^2) and A_T is the Atwood number defined as:

$$A_T = (\rho_{cold} - \rho_{hot})/(\rho_{cold} + \rho_{cold}) \tag{8}$$

Where ρ_{cold} and ρ_{hot} are the densities of the plumes and warm fluid surrounding them, respectively. We recorded in our simulations the downward progression of the dense plumes and the depth and time at which they vanish, when the density contrast becomes negligible. We found that plume velocity follows a slightly parabolic profile ($R^2 = 0.99$) (Figure A1a), which at late time approximates a straight line whose slope represents an average speed of 0.3 cm/s. We verified that this profile approaches that given by the theoretical growth predicted by equation (7) for the simple case where the Atwood number is considered constant with $\rho_{cold} = 0.95$ at $T_f = 27.6$°C and $\rho_{hot} = 0.93$ at $T_o = 49.4$°C. *Jaupart and Brandeis* [1986] report a constant plume velocity (Figure A1b) in the order of 0.5 cm/s at early times, which matches our results within experimental uncertainty. They noticed that the plumes will become slower as cooling proceeds to reach 0.3 cm/s in the region of the well-mixed layer and as they approach the lower boundary layer.

[25] We increased the viscosity of the oil 47V20 by a factor ten and ran a simulation identical to the one described above (Table 2a). We also simulated other oils (oil 47V500 and 47V1000), which led us, like *Jaupart and Brandeis* [1986], to vary the temperatures of the initial and boundary conditions BC1 and BC4. We observe that, for high viscosity values, RT instabilities look like fingers rather than ripples (compare Figure A2a with Figure A2d). The number of instabilities developing at very early times decreases as viscosity increases (Table 2a), following a logarithmic profile (Figure A2e). We conclude that, for given initial and boundary conditions, the number of developing instabilities is roughly inversely proportional to bulk viscosity. This is confirmed by measurements of the wavelength, λ_{obs}, that this conductive layer forms at the onset of the first instabilities (e.g., Figure A1f). *Odé* [1966] and *Lister and Kerr* [1989] used scaling analysis to quantify such wavelengths, λ_c:

$$\lambda_c = Q\left(\frac{\mu_{hot}}{\mu_{cold}}\right)\pi h_c \tag{9}$$

Where μ_{hot} and μ_{cold} are the viscosities of the hot and cold fluid, and h_c is the thickness of the conductive layer (e.g., Figure A1g). For $\mu_{hot} \ll \mu_{cold}$, which is always the case here, this theory defines the value of the function $Q(\mu_{hot}/\mu_{cold}) = 0.94$. The observed and theoretical values of the wavelengths match within a margin of 4% (Table 2a). Knowing the ratio between the width of our domain and λ_c, we can estimate the number of theoretical instabilities that a simulation should develop. This number is close to the one that we observe (Table 2a).

[26] From our data, we conclude that the theoretical thickness, dy, of the upper boundary layer calculated through equation (5), when $Ra = Ra_c = 1600$ [*Jaupart et al.*, 1984] yields values that match our results within a margin of 2% (Table 2a). This calculation provides anotherverification of our 2D model and confirms the accuracy of our simulations

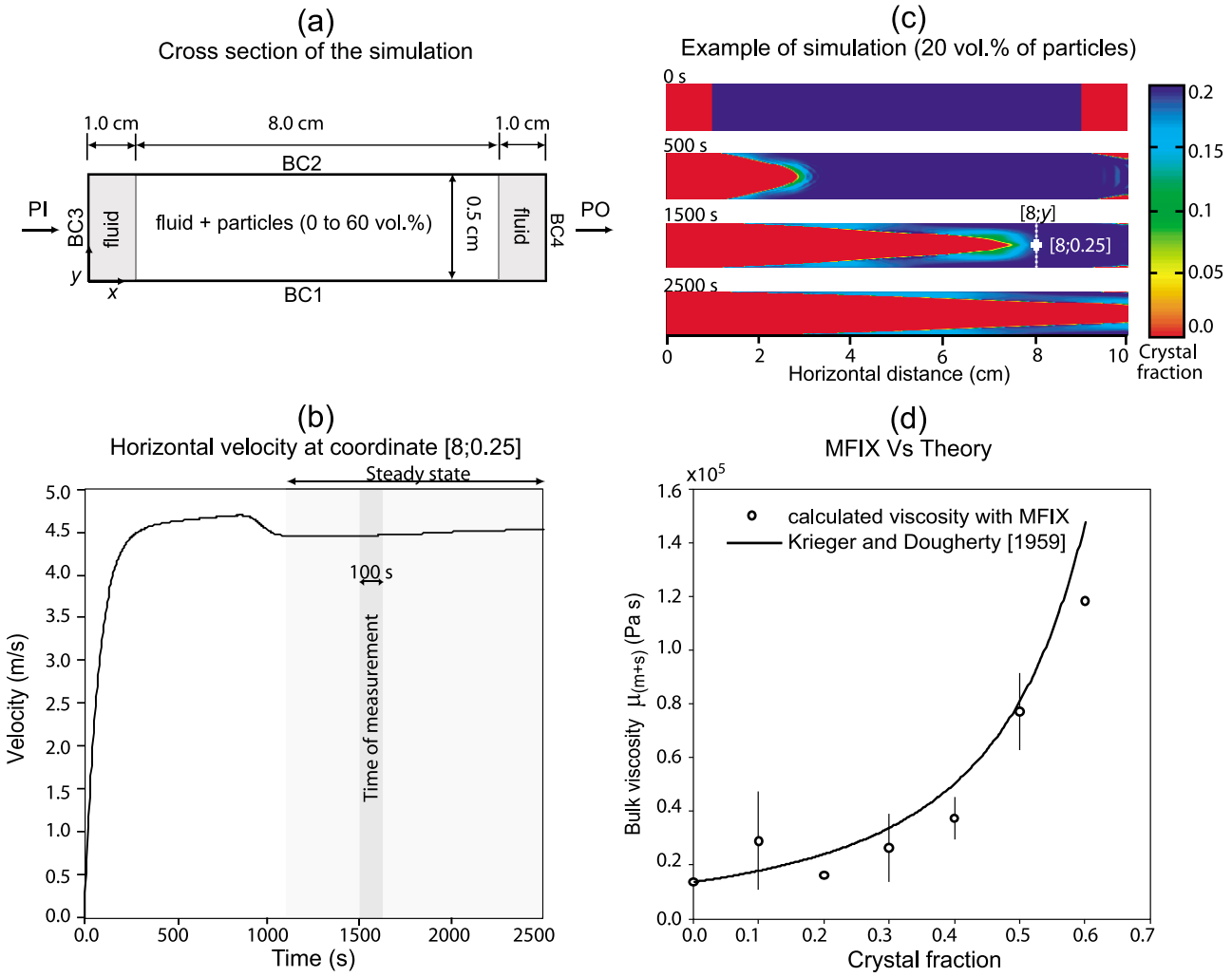

Figure 2. (a) Schematic representation of the numerical simulation of a bi-phase flow with various particle contents at the center of the bin (from 0 to 60 vol.%). BC1 and BC2 are fixed as non-slip walls, BC3 is fixed as inflow boundary with constant pressure (PI) values, and BC4 is an outflow boundary with constant pressure (PO) values. (b) Example of the horizontal flow velocity as a function of time over a computational cell located at coordinate [8; 0.25], for a simulation with 20 vol.% particles. The gray region shows the times at which steady state was reached. The dark gray region encloses the times at which we picked three measurements of bulk viscosity. (c) Time sequence of a simulation with 20 vol.% particles. The vertical dashed line at 1500 s represents the slice across which we took the measurements of bulk viscosity through equation (10). (d) Comparison between the bulk viscosities, $\mu_{(m+s)}$, retrieved from numerical simulations at specific particle content (equation (10)) and the mixture-theory viscosities provided by equation (2). Error bars represent minimum and maximum values determined over 100 s (dark gray region of Figure 2c), and data points represent the average of those values.

within the complexity of the 3D experiments and theoretical values (e.g., Ra_c).

3.2. Verification of Momentum Coupling Between Melt and Solid for Bi-phase Simulations

[27] We verified bi-phase simulations by calculating the equivalent bulk viscosity of melts carrying various amounts of particles and comparing it to the one obtained through the mixture theory of *Krieger and Dougherty* [1959]. The equivalent bulk viscosities were obtained by simulating a plane parallel Poiseuille flow with varying crystal loads.

[28] We defined a 2D horizontal domain of 10 × 0.5 cm^2 containing an arbitrary silicate melt enriched in small particles representing crystals at its center (Figure 2a). The simulations were isothermal at 900°C and the physical properties of crystals and melt are listed in Table 2b. The initial conditions were composed of a 8 × 0.5 cm^2 crystal-bearing center surrounded by two 1 × 0.5 cm^2 crystal-free regions that ensured that the solution was not perturbed by boundary conditions (Figure 2a). Null velocity was set for both phases and the entire domain was initially at hydrostatic pressure along the *y*-direction. BC1 and BC2 were set as NSW, causing the velocities of melt and crystals to approach zero on the horizontal boundaries, and BC3 and BC4 were set as fixed-pressure inlet and outlet, respectively. We

Table 2b. Parameters Used in the Plane-Parallel Poiseuille Flow With a Particle-Laden Suspension[a]

Parameter	Unit	Crystals		Melt	
		Symbol	Value	Symbol	Value
Density	kg/m^3	ρ_s	2.508×10^3	ρ_o	2.19×10^3
Dynamic viscosity	kg/m s	n/a	n/a	μ_m	1.38×10^4
Volume fraction	dimensionless	ε_s	0–0.6	ε_m	0.4–1.0
Packed bed (minimum) void fraction	dimensionless	n/a	n/a	ε_m^*	0.05
Maximum packing fraction	dimensionless	n/a	0.95	n/a	n/a
Particle diameter	m	d_p	3.74×10^{-5}	n/a	n/a
Restitution coefficient between particles	dimensionless	e	0.8	n/a	n/a
Angle of internal friction	° (degree)	ϕ	0	n/a	n/a

[a]Labels n/a mean not applicable.

defined a grid size of 0.01×0.01 cm^2 (1000×50 computational cells).

[29] We performed seven simulations where the only difference was the crystal volume fraction, which varied from 0 to 60 vol.% in steps of 10 vol.%. The simulations develop a Poiseuille flow between parallel plates in response to the pressure gradient between BC3 to BC4. For simulations containing from 0 to 30 vol.% of crystals, the inflow boundary at BC3 was set at constant pressure of 2×10^4 Pa and the outflow boundary at BC4 to 100 Pa. For the simulations containing 40 to 60% particles, decreasing the pressure gradient was necessary to reach convergence; otherwise some cells in which solids were loosely packed reached large pressure and velocity values, resulting in unstable calculations. Thus for 40, 50, and 60 vol.%, we fixed a pressure inlet of 2.5×10^3, 200, and 100 Pa, and an outlet pressure of 100, 100 and 60 Pa, respectively.

3.2.1. Comparison Between Steady State, Bi-phase Flow and Mixture Theory

[30] In steady state, the bulk behavior of the mixture can be considered because particles and fluid have nearly the same velocity. We tracked the horizontal velocity of a vertically centered cell (at coordinate 8; 0.25) to determine when our simulations reach steady state because the time evolution of velocity of this cell is constant in steady state (see the gray-shaded area in Figure 2b). In the x-direction, the governing Navier-Stokes equation for such a mixture reduces to:

$$-\frac{dP_{(m+s)}}{dx} + \mu_{(m+s)} \frac{d^2 U_{(m+s)}}{dy^2} = 0 \qquad (10)$$

Where $P_{(m+s)}$ and $U_{(m+s)}$ are, respectively, the pressure and horizontal velocity of the bi-phase flow at every cell along the y-direction. To calculate the bulk dynamic viscosity, $\mu_{(m+s)}$, we determined the pressure gradient (the first term of equation (10)) between the two consecutive faces of a range of cells at coordinates [8; y] and [8 + dx; y]. Then, we determined the double derivative of the velocity in the y-direction (the second term of equation (10)) along coordinates [8; y]. There was no single time at which the value of the bulk viscosity of the bi-phase flow could be determined for all seven simulations. We thus decided to perform this evaluation after steady conditions have been reached, but a little before the bi-phase flow leaves the bin (e.g., Figure 2c for 20 vol.% crystals). This yielded bulk viscosities at 500, 1500, 1500, 1400, 1500, 2000, 1200 s for 0, 10, 20, 30, 40, 50 and 60 vol.% of crystals, respectively. We repeated the calculations for each of the above times plus 50 and 100 s to estimate the error of our measurements. The resulting bulk viscosities are shown in Figure 2d. The error bars in Figure 2d represent the ranges of minimum and maximum values of our three measurements for a single simulation, while the data point is their average value, which we compare to the viscosity defined by *Krieger and Dougherty* [1959] (equation (2) with $\varepsilon_m^* = 0.05$). In these simulations, crystal segregation leads to significant changes in the pressure gradient and the velocity field. As a result, the bulk viscosities calculated with equation (10) only match approximately those of the perfect mixture assumed by equation (2).

4. Erebus Lava Lake Simulations

4.1. Physical Parameters of the Natural System

[31] Erebus volcano on Ross Island is the southernmost active volcano in the world (Figure 3a). The edifice has a wide base (33 km in diameter) with gentle slopes (13°) that are truncated at an elevation of approximately 3700 m by a 600-m-wide summit crater. Inside lies the 200 m diameter Inner Crater that hosts the world's only active phonolite lava lake, informally called Ray's lake in the recent literature, which has been active since at least 1972. Another small lake at the site of Werner's Vent was briefly present in 2004, while another vent called Active Vent has been the site of occasional small ash-producing explosions [*Calkins et al.*, 2008]. Our study concentrates only on the persistent Ray lava lake (Figure 3b). Examination of the surface elevations of Ray Lava Lake, Werner Vent and Active Vent indicates that they were more or less at the same altitude in December 2001 [*Csatho et al.*, 2008].

[32] An extensive series of studies have been carried out on Erebus [*Oppenheimer and Kyle*, 2008, and references therein]. Among them, geochemical and mineralogical studies were devoted to the phonolite lava. *Kelly et al.* [2008] studied lava bombs erupted between 1972 and 2004, and the lavas erupted from the summit region in the last 17 ka. They found that the mean composition of matrix glass from lava bombs is characterized by 55.35 wt.% of SiO_2, 9.04 wt.% of Na_2O, 5.64 wt.% of K_2O and 1.87 wt.% of CaO. Lava bombs and summit lava textures are similar. Phonolite lavas from summit region have ~30% of anorthoclase feldspar crystals with sizes up to ~6 cm in length, while lava bombs have 30–40 vol.% of anorthoclase crystals with sizes up to ~10 cm in length, both along with minor quantities (<3 vol.%) of other minerals (olivine, opaque

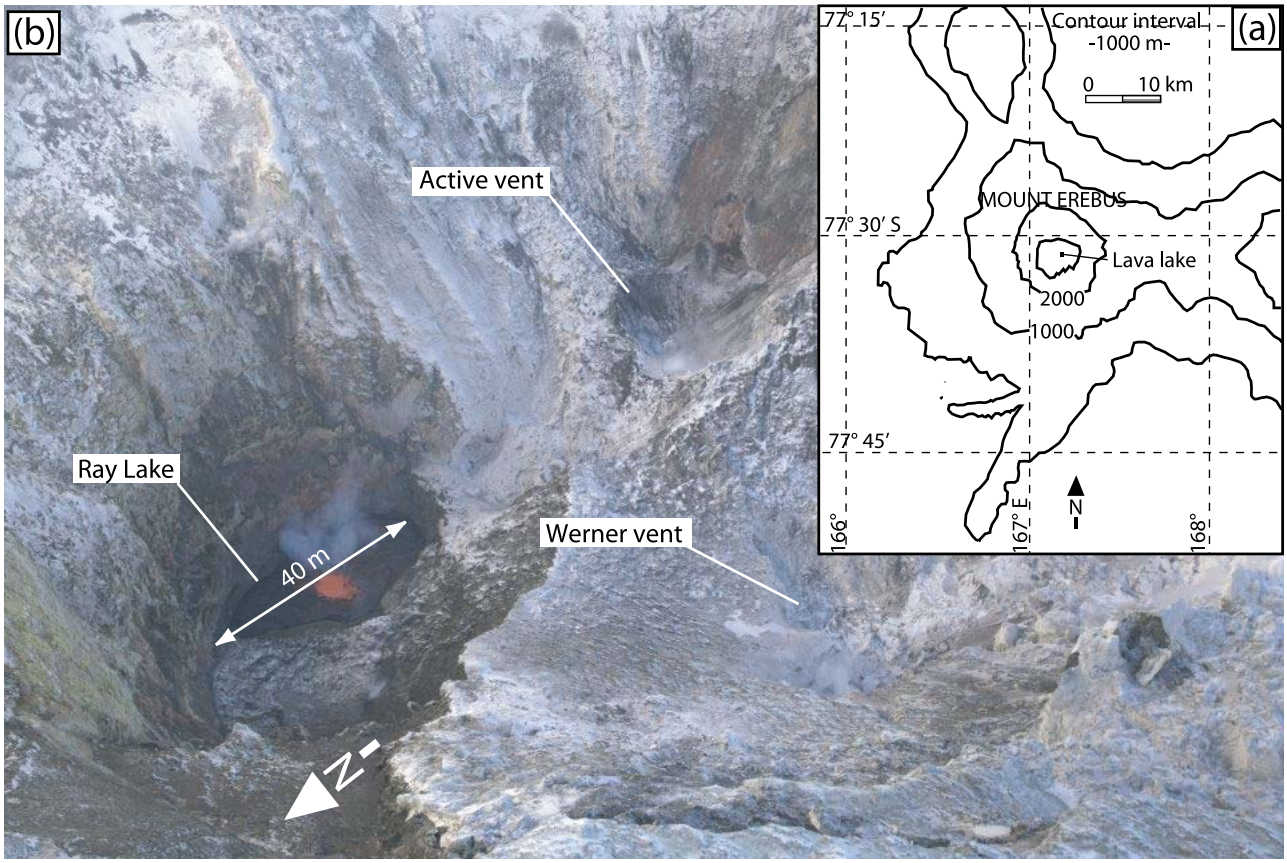

Figure 3. (a) Location of the lava lake at the Ross Island. (b) Panoramic view of Erebus caldera in December 2011, which hosts Ray, the permanent lava lake.

oxides, clinopyroxene and apatite). The mean compositional range of the anorthoclase crystals is $An_{16.2}Ab_{65.8}Or_{17.9}$ (An = Anorthite; Ab = Albite and Or = Orthoclase). No systematic study of the aspect ratios of the crystals at Erebus has been carried out; however the average length is commonly twice to 3 times the width [*Dunbar et al.*, 1994]. Melt inclusions trapped in the crystals record homogenization temperatures around 1000°C [*Dunbar et al.*, 1994]. The water contents of these anorthoclase-hosted inclusions range from 0.12 to 0.39 wt.% [*Seaman et al.*, 2006]. The Erebus phonolite density is estimated to 2400 kg/m^3 [*Eschenbacher*, 1998].

[33] Observations combined with geophysical, geochemical, and petrological studies provide some constraints on the geometry and dimensions of the magma system and convective process itself. For example, *Csatho et al.* [2008] used airborne laser scanning (lidar) and *Calkins et al.* [2008] used thermal infrared images to estimate the lake surface area as ∼770–1400 m^2 and its diameter as ∼30–40 m (Figure 3) in the period from around 2001–2004. However, the lake level does vary over time with corresponding changes in surface area [*Calkins et al.*, 2008]. In 2009, for instance, the lake area increased to 2500 m^2. Field observations and videos of the lava lake revealed that hot lava reaching the surface of the lake was rapidly cooled on contact with air, resulting in a thin crust beneath which molten lava kept convecting [*Oppenheimer et al.*, 2009]. *Kyle et al.* [1992] suggested that the continuous activity at this large alkaline phonolitic volcano implies a deep source of melt rising through a narrow vertical conduit. *Calkins et al.* [2008] based on the average temperature of the lava lake estimated that a minimum magma flux of 150 kg/s is needed to sustain the thermal output of the lake. Then by assuming a simple Poiseuille flow, they calculated that ascending magma requires a minimum conduit diameter of ∼4 m. *Dibble et al.* [2008] and *Oppenheimer et al.* [2009] reported a funnel shaped crater ∼20-m-deep after Strombolian explosion evacuated the lake, tapering to a single vent (uppermost conduit) of 5–10 m diameter. *Aster et al.* [2008] found that very long period seismic signals accompanying Strombolian explosions are related to the gas slug ascent in the conduit and are consistent with a kink in the magmatic system at around 400 m beneath and horizontally offset from the lava lake. A study focused on the melt inclusions trapped into the crystals revealed that they grew between depths as shallow as 400 m and the surface [*Dunbar et al.*, 1994], though more recent modeling of the melt inclusion CO_2 and water contents suggested entrapment depths corresponding to pressures of up to 300 MPa [*Oppenheimer et al.*, 2011]. *Sweeney et al.* [2008] found that, for a crystal content of 30 vol.%, the radiated heat flux associated to the SO_2 emission rate corresponds to a cooling of 65°C between upwelling and downwelling magma and is sufficient to drive convection. This temperature difference between magma entering and leaving the lake is consistent with that reported by *Calkins et al.* [2008] who estimate that ΔT must be inferior to 120°C to sustain convection for same crystal content.

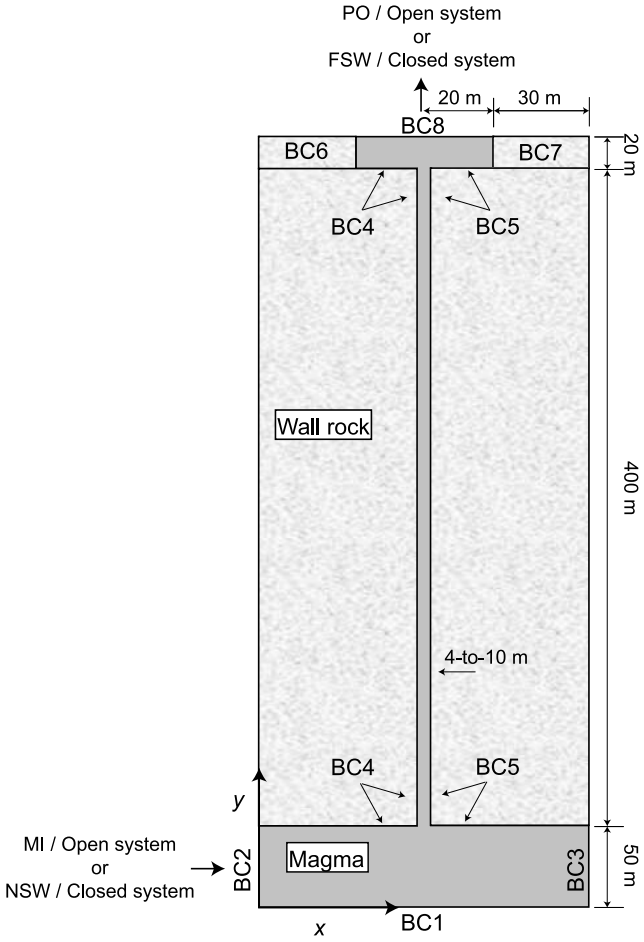

Figure 4. Schematic representation of Erebus magmatic system with a horizontal exaggeration of a factor 2. Initially, crystal content is either 30 vol.% (bi-phase flow) or 0 vol.% (single-phase flow); both crystals and melt are uniformly at 1000°C and have a null velocity. For closed-system simulations, the boundary conditions BC1 and BC8 are free-slip walls, and BC2–7 are non-slip walls. Temperatures for both crystals and/or carrier phase are of 1000°C at BC1–3, 900°C at BC4–5, and 0°C at BC8. A constant heat flux of −2°C/m is set at BC6–7. For the open-system simulations, BCs are identical, except BC2, which is an inflow boundary with constant mass influx (MI), a phasic weighted speed of 2.3×10^{-5} m/s and a magma pressure of 11 MPa, and BC8, which is an outlet pressure (PO) equal to atmospheric (0.1 MPa). The numerical grid is square and its resolution is varied as described in the text.

Sweeney et al. [2008] also estimated that, as pressure decreases, viscosity varies significantly (from 10^4–10^9 Pa s) as a function of water and above all crystal content.

[34] In addition to the studies mentioned above, mineralogical and isotopic composition of lava and tephra suggest that the Erebus magmatic system reached a steady state or is close to its equilibrium, with low to insignificant crystallization taking place. For example, *Calkins et al.* [2008] report a steady lake level over periods of weeks, constant degassing and stable mean surface temperature. *Kelly et al.* [2008] argue that, based on the exceptionally stable geochemistry of erupted lavas between 1972 and 2004, essentially constant magma temperatures must have existed without significant crystallization, magma intrusion and mixing. Indeed, they find that the mineral modes of recently erupted lava bombs are similar to those of the summit lavas erupted over the last ~17 ka. *Dunbar et al.* [1994] emphasizes that crystallization has not been considered a significant process in the last 30 years. Based on different methods such as trace element diffusion modeling and ^{238}U series geochronology, the most common age of the anorthoclase crystals is hundreds [e.g., *Sumner*, 2007] to thousands of years [*Reagan et al.*, 1992]. Isotopic studies of Sr, Nd, Hf and Pb performed by *Sims et al.* [2008] show a relative compositional uniformity that also suggests that Erebus is in a steady state and that either its source is isotopically homogeneous, or the mixing of batches of parental basanite with different isotopic compositions is extremely efficient.

4.2. Idealized Magmatic System

[35] The aforementioned geological information guided us in framing an idealized magmatic system suitable for numerical simulations. Given the evidence that the Erebus shallow magma system has reached a steady state, we conducted simulations so as to achieve steady state. The geometry of this idealized system is based on a 2D cross-section referenced in Cartesian coordinates. This setup is a compromise between computationally very intensive 3D simulations and the forced symmetry of an axisymmetric domain. We fixed the lake diameter to 40 m and its depth to 20 m. We assume a constant heat flux between the magma and the vertical walls of the lake because snow and ice on the crater walls most likely perturb the thermal stability. This heat flux was calculated using a thermal conductivity estimated through a relationship from *Zoth and Hänel* [1988] (k_{wall} = 2.90 W/m °C) for a cold volcanic country rock of intermediate composition. In the absence of information on the density and heat capacity values of the matrix rock hosting the lava lake, we used common values for basalt, respectively ρ_{wall} = 2700 kg/m^3 and $C_{pwall} \sim$ 840 J/kg °C, which yields $\kappa_{wall} = k_{wall}/(\rho_{wall}\, C_{pwall}) \sim 1.3 \times 10^{-6}$ m^2/s. The occasional Strombolian activity suggests that gas can be segregated at some level of the plumbing system. Although we do not simulate a gas phase, we use this information to derive additional knowledge about the conduit geometry. *Jaupart and Vergniolle* [1988] have argued that bubbles collect at the top of a chamber near the conduit and that collapse of the accumulated foam can generate gas slugs that rise through the conduit to burst at the surface [*Chouet et al.*, 1997]. We thus simplified the plumbing system below the lake as a single vertical conduit linked to a magma reservoir. The location of seismic signals given by *Aster et al.* [2008] plus the depth of crystal formation [*Dunbar et al.*, 1994], suggested fixing a conduit length of 400 m and a diameter from 4 to 10 m, within the range of widths reported in previous studies. Since the dimensions of the chamber are not constrained, we represented the magma reservoir as a 2-D domain in such a way that it is larger than the lava lake, 100 m wide and 50 m deep.

[36] The idealized 2D geometry (within the *x*-*y* plane) for Erebus is represented in Figure 4. The initial conditions over the whole computational domain are a uniform temperature of 1000°C and null velocity for all phases (melt, melt and crystals or mixture), and 30 vol.% of uniformly distributed

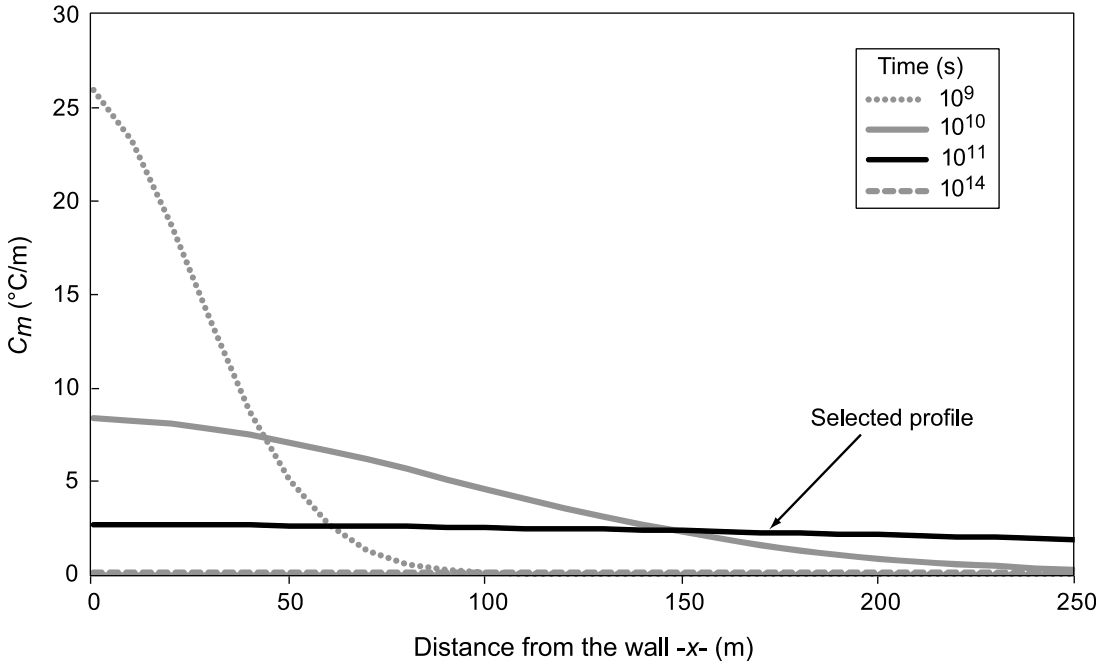

Figure 5. Derivative function of conductive temperature decay from the wall of the lava lake to the country rock as a function of time. Temperature as a function of time and space is obtained from equation (4) with initial temperature T_o = 1000°C and T_{fwall} = 0°C. Beyond 10^{11} s (3000 yr), the profile is linear; we have thus selected a C_m value at that time to represent steady state conductive heat loss.

anorthoclase crystals for bi-phase simulations. The pressure for the whole magmatic system is initially magma-static (mechanical pressure). The thermal boundary conditions (BC) were set for all phases so that the system is heated from below (BC1 = 1000°C) by a magma chamber, and cooled from above through the lava lake surface (BC8 = 0°C). All phases were kept at 1000°C on the reservoir sides (BC2 and BC3), and at 900°C along the conduit (BC4 and BC5). The vertical walls of the lava lake (BC6 and BC7) were set so that the heat flux through the walls would be of reduced intensity, $C_m = -2$°C/m. This gradient was obtained through equation (4) when the temperature gradient is established between a melt initially at 1000°C and the host rock at T_{fwall} = 0°C, which corresponds to cold country rocks in the far field (Figure 5). Even for these high initial temperature contrasts, the thermal evolution depends weakly on the initial contrast and is mostly governed by κ_{wall} and t. A series of simulations was performed in closed system, which means that no magma enters or exits the domain. In our closed system, we choose to fix the sidewall boundaries (BC2–7) as non-slip walls (NSW), while the top of the lava lake (BC8) and the bottom of the magma chamber (BC1) are free-slip walls (FSW). This last condition limits the effect that the arbitrary thickness has on the thermal evolution of the system. While this is a fair approximation for perfect mixtures of melt and crystals because of the absence of settling, the bottom boundary will cause crystal to accumulate for bi-phase simulations. The velocities for all phases approach zero on the sidewall boundaries, while the velocity gradients approach zero on the horizontal boundaries. One simulation was performed in open system, for which BCs are identical to those for the closed system, except that BC2 and BC8 were set as inlet and outlet boundaries, respectively (Figure 4). At the inlet, the bi-phase flow had a pressure of 11 MPa, a solid volumetric concentration of 30 vol.%, a phase-weighted horizontal speed of 2.3×10^{-5} m/s; at the outlet, the pressure was constant and equal to atmospheric (0.1 MPa).

[37] The size distribution and shape of crystals was also simplified. We calculated that a spherical crystal of 5 cm in diameter would have the same volume as a crystal of $6 \times 3 \times 3$ cm. The spherical shape is a necessary assumption in order to compare the behavior of the bulk viscosity of the mixture with the bi-phase simulation in a consistent manner (see sections 2 and 2.1). We took anorthoclase properties such as density from the literature, and estimated other properties such as thermal conductivity and heat capacity based on the end-member composition of the anorthoclase crystals (albite). Table 3 summarizes all the physical properties for the crystals and the phonolite melt used in the simulations. The angle of internal friction between particles has, to our knowledge, never been determined in such viscous suspensions. After trying values of 0° and 24° without obtaining noticeable changes in average temperature and velocity patterns, we set this parameter to 0° so as to decrease calculation time. We chose an intermediate value for the particle restitution coefficient, e, of 0.8 (between cork, 0.6, and glass, 0.9). We neglected crystallization given the estimates of crystal ages in the literature and the limited evidence for its significance in the real system (see section 4.1). Should it occur, the crystallization process would continuously grow existing crystals or nucleate new ones, which would eventually contribute to changes in the physical and kinetic properties of the magma (viscosity, density and drag). The validity of this assumption should be assessed in the future by comparing simulation results to the

Table 3. Parameters Used in Physical Modeling of Erebus

Parameter	Unit	Crystals			Melt		
		Symbol	Value	Reference	Symbol	Value	Reference
Density	kg/m^3	ρ_s	2.59×10^3	*Anthony et al.* [1995]	ρ_o	2.455×10^3	Output from Conflow[a]
Thermal conductivity	W/m °C	k_s	2.0	*Clauser and Huenges* [1995]	k_m	1.53	*Clauser and Huenges* [1995]
Heat Capacity	J/kg °C	C_{ps}	2218.8	*Navrosty* [1995]	C_{pm}	1367	Output from Conflow[a]
Thermal diffusivity	m^2/s	n/a	3.5×10^{-7}[b]		κ_m[b]	4.56×10^{-7}	
Thermal expansion coefficient	1/°C	n/a	n/a		α	8.054×10^{-5}	Output from Conflow[a]
Volume fraction	Dimensionless	ε_s	0.3	*Kelly et al.* [2008]	ε_m	0.7	
Packed bed void fraction	dimensionless	n/a	n/a		ε_m^*	0.35	
Maximum packing fraction	dimensionless	n/a	0.65	*Costa* [2005]	n/a	n/a	
Particle diameter	m	d_p	5×10^{-2}		n/a	n/a	
Restitution coefficient between particles	dimensionless	e	0.8		n/a	n/a	
Angle of internal friction	° (degree)	ϕ	0		n/a	n/a	

[a] *Mastin and Ghiorso* [2000].
[b] Calculated value.

equilibrium conditions given by petrologic data for Erebus phonolite; such equilibrium conditions have not been published yet. We tested values for the minimum void fraction of a packed bed of crystals of 0.35 (as in *Costa* [2005]) and 0.37 [*McGeary*, 1961] without obtaining noticeable differences and we used a packed bed void fraction, ε_m^*, of 0.35 as discussed later.

[38] We calculated the initial density ρ_o, the thermal expansion α and the heat capacity C_{pm} of the melt with Conflow [*Mastin and Ghiorso*, 2000], using the following parameters: a melt composition of anhydrous whole-rock of phonolite lavas given by *Kelly et al.* [2008], 0.26 wt.% of H_2O, a magma chamber pressure of 11 MPa, 30 vol.% of anorthoclase crystals, and a temperature of 1000°C. The parameters α, C_{pm} and k_m were kept constant (Table 3). The obtained value of ρ_o (2455 kg/m^3) is close to the estimation of *Eschenbacher* [1998] for Erebus phonolite. The thermal conductivity of the phonolite, k_m, was estimated through a relationship of *Zoth and Hänel* [1988] using a volcanic rock of intermediate composition at T_o = 1000°C. Melt viscosity is of particular importance because it controls the rate of transport of matter and, thus, of energy. We used the Newtonian model given by *Giordano et al.* [2008], which predicts the non-Arrhenian temperature and compositional dependence of melt dynamic viscosity, μ_m, for naturally occurring silicate melts at atmospheric pressure. This viscosity appears in the deviatoric term of the stress tensor in equation (30). Based on the mean of the major element concentrations of matrix glass separated from lava bombs [*Kelly et al.*, 2008] plus the water content of melt inclusions in anorthoclase (0.26 wt.%) measured by *Seaman et al.* [2006], we have calculated the coefficients B and C from the following relationship given by *Giordano et al.* [2008]:

$$\mu_m = 10 \exp\left(A + \frac{B}{T_m - C}\right) \tag{11}$$

Where $A = -4.55$ (coefficient independent of composition), $B = 8642.3$, $C = 319.6$ and T_m is the melt temperature in Kelvin. The equation (11) is valid over a range of viscosity values of 0.1 to 10^{14} Pa s and temperatures of 245–1580°C [*Giordano et al.*, 2008]. The typical melt viscosity for hot and cold Erebus magma in our simulations is of the order of 3.3×10^4 and 10^8 Pa s, respectively.

[39] Our simulations include the lake surface; it is thus necessary to determine the temperature at which cooling quenches the magma into a crust. Physically, this would be the glass transition temperature, T_g, which is the temperature separating the liquid (relaxed) from the glassy (unrelaxed) state. We decided to clip the value of viscosity at the temperature at which T_g occurs, so that the melt shows a strong viscosity increase that approximates sub-solidus conditions while the absolute value of viscosity still ensures numerical stability. The clipping method underestimates the viscosity that a colder glass can reach. The validity of this assumption will be discussed in section 5. Experimental and theoretical approaches suggest a range of values for T_g. *Giordano et al.* [2005] used differential scanning calorimetry and a fixed cooling/heating rate of 20°C/min to find an experimental peak-value for T_g of 670°C for a Teide phonolite. *Russell and Giordano* [2005] predicted a value of T_g for the end-member melt compositions diopside-anorthite-albite of 720°C, 857°C and 796°C, respectively. The thermodynamic model of MELTS [*Ghiorso and Sack*, 1995] yields an estimate of 600°C for the solidus temperature of our melt. The factors A, B and C from the viscosity model of equation (11) can also be used to estimate T_g [*Dingwell et al.*, 1993; *Giordano et al.*, 2008]:

$$T_g = C + \frac{B}{12 - A} \tag{12}$$

This provides an estimate of 570°C, which corresponds to a viscosity of 10^{12} Pas. This viscosity value corresponds to a relaxation timescale for macroscopic melt properties of about 15 min and to cooling rates of 10°C/min [*Giordano et al.*, 2008]. These considerations restrict the probable range for T_g between 600 and 800°C. Temperatures around 600°C correspond to viscosities of $\sim 10^{11}$ Pa s, which cause convergence failures due to a large increase of pressure and velocities for some cells in the top of the lake. We thus explored two clipping temperatures: 700°C, which is the lowest possible value that still ensures numerical stability, and 800°C, which approximates the value of 796°C given by *Russell and Giordano* [2005]. We first quantified the cooling rates of magma in the lake for simulations considering free-slip condition at the top of the lake (Figure 6a) and the respective viscosities as a function of temperature

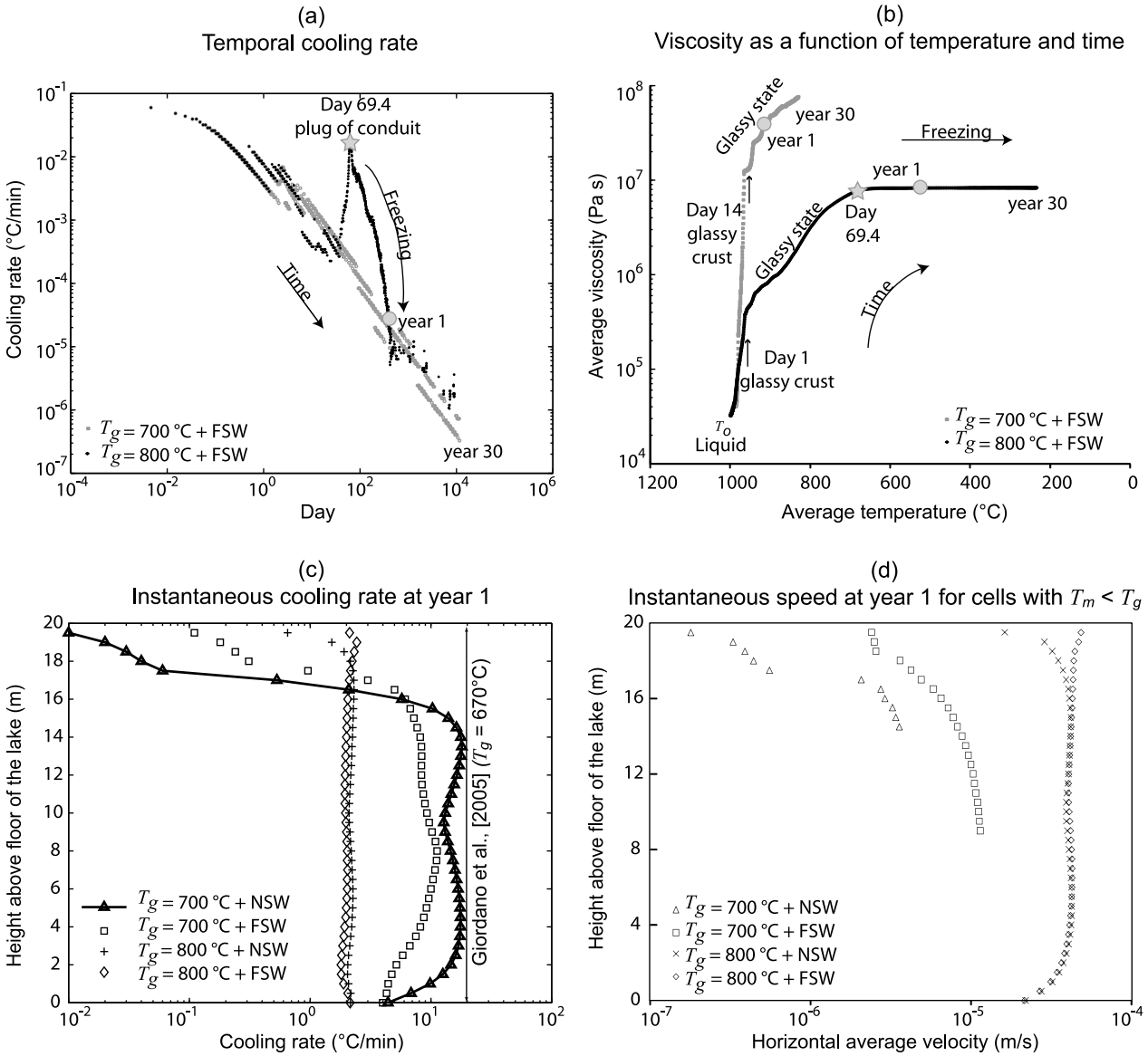

Figure 6. Comparison of four runs with 50 × 50 cm grid size and restricted to the lava lake to obtain the optimum value of glass transition temperature (T_g) for the full-scale numerical simulations. The simulated time is 30 years and the sampling rate for these simulations is 100 s. The stars in Figures 6a and 6b indicate the time at which a plug obstructs the top of the conduit and the large circles show the date at which we took the measurement of cooling rate and velocity in Figures 6c and 6d. (a) Comparison of the average cooling rate of the entire lake for two simulations differing only by the value of T_g (700 and 800°C). Cooling rate is obtained by temperature average difference between two consecutive time steps divided by the elapsed time between those time steps. (b) Average melt viscosity for the whole lake as a function of temperature for the same two simulations. T_o = 1000°C represents the initial temperature condition. Vertical arrows mark the date at which glass forms at the lake surface, which is at day 1 for T_g of 800°C and at day 14 for a T_g of 700°C. These dates mark the change of slope that mimics the change of slope from the Arrhenian melt (equilibrium state) to the non-Arrhenius behavior of the glass (disequilibrium state). (c) Instantaneous cooling rate, $cooling\ rate|_{y,t} = (T_{av}/dy)(||\mathbf{v}||_{av_m})$, at a given depth y along the x-coordinate and specific time t (year 1), when the simulations are in steady state. T_{av} and $||\mathbf{v}||_{av_m}$ are average values obtained along cells in the x-direction. For each T_g value, we varied the boundary condition at the lake surface from free-slip (FSW) to non-slip (NSW). The cooling rate given by the simulation with T_g = 700°C and NSW is close to the experimental value found by *Giordano et al.* [2005] at a cooling rate of 20°C/min. (d) Instantaneous melt velocity along the x-direction around year 1 as a function of the height above the floor of the lava lake. Only the cells with temperatures inferior to the two respective T_g values (700 and 800°C) are shown. The simulation yielding the lowest velocities is the one with T_g = 700°C and either NSW or FSW at the lake surface.

(Figure 6b). We found that cooling rates can be better compared to experimental values when the top of the lake is set to non slip (Figure 6c). We also obtained a horizontal average of melt velocity for all the cells below T_g (Figure 6d). When T_g = 700°C, melt velocity decreases from 3×10^{-5} m/s at a depth of 14 m below surface to 10^{-7} m/s just below the surface of the lava lake, because the velocities approach zero at the horizontal boundaries. In contrast, melt velocities remain almost constant above 10^{-5} m/s when T_g = 800°C. We note that changing T_g from 800°C to 700°C has a greater influence on the velocity profile than changing the slip conditions. When T_g = 800°C, a thick quenched central instability forms after 69.4 days, sinks toward the deeper part of the lake, preventing thermal exchange between lake and conduit to occur and driving the whole lake to drop below T_g (i.e., reaching a plateau average viscosity of 8×10^6 Pa s; Figure 6b). When T_g =700°C, the whole lake remains above T_g (Figure 6b). Keeping in mind that T_g is a temperature interval related to the cooling/heating rate rather than a unique temperature value, we chose a clipping temperature of 700°C because it yields the lowest velocities at the surface of the lake (Figure 6d) and it is close to the value found by *Giordano et al.* [2005] at similar instantaneous cooling rate (Figure 6c). The corresponding viscosity, 10^8 Pa s, is just below the experimental measures of 10^9–10^{13} Pa s for the glass transition of silicate melts reported by *Webb and Knoche* [1996] at cooling rates of 5°C/min and T_g temperatures spanning the wide range 400–900°C.

4.3. Overview of the Simulations and Numerical Considerations

[40] Three types of magma were simulated: (i) a pure melt, (ii) magma with crystals and melt considered as a single-phase (mixture), and (iii) magma with melt and crystals considered as bi-phase. These three types will be referred to as "pure melt," "crystals as a part of the melt," and "crystals as a separate phase."

[41] The simulations spanned 30 years. Finding an optimal time step to solve the hydrodynamic equations was thus necessary. For an individual crystal weight of 0.17 kg, and a ξ value of 1.4×10^4 kg/s, equation (6) yields a minimum time step of 6×10^{-5} s. Although such small time steps would have enabled us to follow rapid changes in the flow field and ensure greater numerical stability, we selected suitable values to optimize the computational time. We found that starting, maximum, and minimum time steps of 100, 10^9 and 1 s, respectively, gave satisfactory results for the "pure melt" configuration while 50, 100 and 2×10^{-4} s were suitable for the "crystals as a separate phase" and "crystals as a part of the melt" simulations. In all simulations the maximum number of iterations for a given time step was fixed at 300 [*Syamlal*, 1998]. We found that the length of the optimal cell for the three configurations is less than 50 cm by using equation (5) and fixing $Ra = Ra_c = 1708$, $\Delta T = 1000$°C, and considering melt viscosities at the temperatures of our boundary conditions, 900°C and 1000°C. Thus, the hydrodynamic equations were solved using square grid cells with sides of 10, 25, and 50 cm.

[42] After fixing the conduit diameter of our closed system to 4 m, we conducted sensitivity tests for the three magma configurations by reducing the tolerance (maximum residual at convergence for continuity plus momentum equations) by one order of magnitude (from 1 to 0.5 to 0.1) for a given grid size, which amounts to 12 test simulations (Table 4, simulations 1–12). Among these test simulations, we have selected one simulation per configuration (one for "pure melt," one for "crystals as a part of the melt" and one for "crystals as a separate phase") for which the general dynamics governing the simulation (e.g., temperature, number and velocity of the cold instabilities), the time step history and the tolerance had the least influence on the solution. Figure A3 shows an example of our selection based on the time history smoothness linked to a given grid size and tolerance associated to an average temperature for one of the runs (here the pure melt simulation). Specific numerical adjustments and a detailed description of the three selected simulations are presented in sections 4.4.1–4.4.3.

[43] Keeping the parameters of grid size, tolerance and time step found for every one of the above configurations, we varied the conduit diameter of our system to 10 m and ran 3 more simulations (one with "pure melt," one with "crystals as a part of the melt," and one "crystals as a separate phase"). They are described in section 4.5 (Table 4, simulations 13–15) and in section 4.6 (Table 4, simulation 15). One additional simulation was carried out as bi-phase magma with a 10–m-diameter conduit in open system and it is described in section 4.6 (Table 4, simulation 16). We thus describe in depth a total of seven numerical simulations.

4.4. Results Concerning How Melt and Crystals Are Treated in the Simulations

[44] In this section we present the results for the three selected simulations with 4–m-conduit diameter in closed system. Features of the convection in the whole system for these simulations are detailed in Figures 7a–7u and early stages of the convection in the lava lake are described in Figures 8a–8r. Details of specific numerical adjustments are detailed at the beginning of sections 4.4.1–4.4.3.

4.4.1. Pure Melt

[45] We tested numerical accuracy by keeping all the physical parameters of the pure melt configuration constant, as stated in Table 3, and varying the grid size between 50×50, 25×25, and 10×10 cm^2. Table 4 shows that the quality of the solution improves as the grid is refined, although the residuals of the norms of U_m and V_m do not evolve along the same trend. The two finer grids have the smoothest temporal evolution of both the time step history (Figures A3a–A3c) and the temperature decay (Figures A3d–A3f). The solutions with the coarsest grid show only a few instabilities surrounding a large central instability dropping from the surface of the lava lake (Figure A3a). In the smallest grid, on the other hand, there are 17 thermal plumes originating from the lake surface (Figure A3c) and 50 plumes from the top of the magma chamber (Figure A3f). The run with 10×10 cm^2 cells thus provides a better resolution of the RT instabilities and was consequently selected. It corresponds to 1000×4700 computational cells. Numerical accuracy was checked by varying the tolerance from 1 to 0.5 and 0.1. The solutions yield very similar evolutions of the temperature profiles, which indicate that the largest value of tolerance is sufficient.

[46] In section 3.1.1, we showed that the number of instabilities varies inversely with viscosity for a simulation with given BCs and initial conditions. We used *Odé* [1966]

Table 4. Residuals Average of the Main Macroscopic Variables Composing Momentum and Energy Equations, and Solution Accuracy[a]

Simulation	System	Conduit Size (m)	Magma Configuration	Grid Size (cm × cm)	TOL	NI	NI/TS	P_m	V_m	U_m	V_s	U_s	T_m
						Grid Size Study							
1	Closed	4	Pure melt	50 × 50	1.0	1675	2	7.3×10^{-3}	1.8×10^{-2}	6.3×10^{-3}	n/a	n/a	5.8×10^{-5}
2	Closed	4	Pure melt	25 × 25	1.0	1380[b]	2	4.7×10^{-4}	1.6×10^{-2c}	4.8×10^{-3c}	n/a	n/a	4.6×10^{-5}
3	**Closed**	**4**	**Pure melt**	**10 × 10**	**1.0**	**1381**	**2**	$\mathbf{3.3 \times 10^{-4c}}$	$\mathbf{3.9 \times 10^{-2}}$	$\mathbf{1.1 \times 10^{-2}}$	**n/a**	**n/a**	$\mathbf{3.0 \times 10^{-5c}}$
						Tolerance Study							
3	**Closed**	**4**	**Pure melt**	**10 × 10**	**1.0**	**1381[b]**	**2**	$\mathbf{3.3 \times 10^{-4}}$	$\mathbf{3.9 \times 10^{-2}}$	$\mathbf{1.1 \times 10^{-2}}$	**n/a**	**n/a**	$\mathbf{3.0 \times 10^{-5}}$
4	Closed	4	Pure melt	10 × 10	0.5	1432	2	1.4×10^{-4}	3.2×10^{-2}	9.7×10^{-3}	n/a	n/a	3.0×10^{-5}
5	Closed	4	Pure melt	10 × 10	0.1	2300	3	8.4×10^{-5c}	2.6×10^{-2c}	8.9×10^{-3c}	n/a	n/a	2.4×10^{-5c}
						Grid Size Study							
6	Closed	4	Mixture	50 × 50	1.0	20000025	2	5.7×10^{-6}	1.2×10^{-5c}	1.1×10^{-5}	n/a	n/a	4.1×10^{-7c}
7	**Closed**	**4**	**Mixture**	**25 × 25**	**1.0**	**14772841**	**2**	$\mathbf{1.6 \times 10^{-6c}}$	$\mathbf{1.3 \times 10^{-5}}$	$\mathbf{9.7 \times 10^{-6c}}$	**n/a**	**n/a**	$\mathbf{6.6 \times 10^{-7}}$
8	Closed	4	Mixture	10 × 10	1.0	2000165[b]	2	1.9×10^{-6}	3.9×10^{-5}	2.1×10^{-5}	n/a	n/a	4.8×10^{-6}
						Tolerance Study							
7	**Closed**	**4**	**Mixture**	**25 × 25**	**1.0**	**14772841[b]**	**2**	$\mathbf{1.6 \times 10^{-6}}$	$\mathbf{1.3 \times 10^{-5c}}$	$\mathbf{9.7 \times 10^{-6c}}$	**n/a**	**n/a**	$\mathbf{6.6 \times 10^{-7}}$
9	Closed	4	Mixture	25 × 25	0.5	14848326	2	1.5×10^{-6c}	1.4×10^{-5}	1.0×10^{-5}	n/a	n/a	6.6×10^{-7}
						Grid Size Study							
10	**Closed**	**4**	**Bi-phase**	**50 × 50**	**1.0**	**20000025**	**2**	$\mathbf{4.6 \times 10^{-4}}$	$\mathbf{1.4 \times 10^{-4}}$	$\mathbf{1.2 \times 10^{-4}}$	$\mathbf{3.8 \times 10^{-4}}$	$\mathbf{5.4 \times 10^{-4}}$	$\mathbf{8.1 \times 10^{-7}}$
11[d]	Closed	4	Bi-phase	25 × 25	1.0	n/m	n/m	n/m	n/m	n/m	n/m	n/m	n/m
						Tolerance Study							
10	**Closed**	**4**	**Bi-phase**	**50 × 50**	**1.0**	**20000025[b]**	**2**	$\mathbf{4.6 \times 10^{-4}}$	$\mathbf{1.4 \times 10^{-4}}$	$\mathbf{1.2 \times 10^{-4}}$	$\mathbf{3.8 \times 10^{-4}}$	$\mathbf{5.4 \times 10^{-4}}$	$\mathbf{8.1 \times 10^{-7c}}$
11	Closed	4	Bi-phase	50 × 50	0.5	20000084	2	2.3×10^{-4c}	7.7×10^{-5c}	6.9×10^{-5c}	2.9×10^{-4c}	4.8×10^{-4c}	8.5×10^{-7}
12	Closed	4	Bi-phase	50 × 50	0.1	20001498	2	2.6×10^{-4}	8.1×10^{-5}	7.4×10^{-5}	3.0×10^{-4}	5.0×10^{-4}	8.4×10^{-7}
						Fixed Tolerance and Grid Size							
13	**Closed**	**10**	**Pure melt**	**10 × 10**	**1.0**	**n/m**	**n/m**	**n/m**	**n/m**	**n/m**	**n/m**	**n/m**	**n/m**
14	**Closed**	**10**	**Mixture**	**25 × 25**	**1.0**	**n/m**	**n/m**	**n/m**	**n/m**	**n/m**	**n/m**	**n/m**	**n/m**
15	**Closed**	**10**	**Bi-phase**	**50 × 50**	**1.0**	**n/m**	**n/m**	**n/m**	**n/m**	**n/m**	**n/a**	**n/a**	**n/m**
16	**Open**	**10**	**Bi-phase**	**50 × 50**	**1.0**	**n/m**	**n/m**	**n/m**	**n/m**	**n/m**	**n/a**	**n/a**	**n/m**

[a]Symbols are summarized in Table A1. In bold are the selected simulations (3, 7, and 10) with 4-m-diameter conduit (details in sections 4.4.1–4.4.3) and with 10-m-diameter conduit (13–16). The simulations with 10-m-diameter conduit have been run with the same grid sizes and tolerances as the ones selected for 4-m conduit-diameter. TOL is tolerance, NI is number of iterations, NI/TS is the average number of iterations per time step, n/a is not applicable, and n/m is not measured.

[b]Least number of iteration.

[c]Least minimum value of error.

[d]Simulation was stopped after 1 year instead of 30 years.

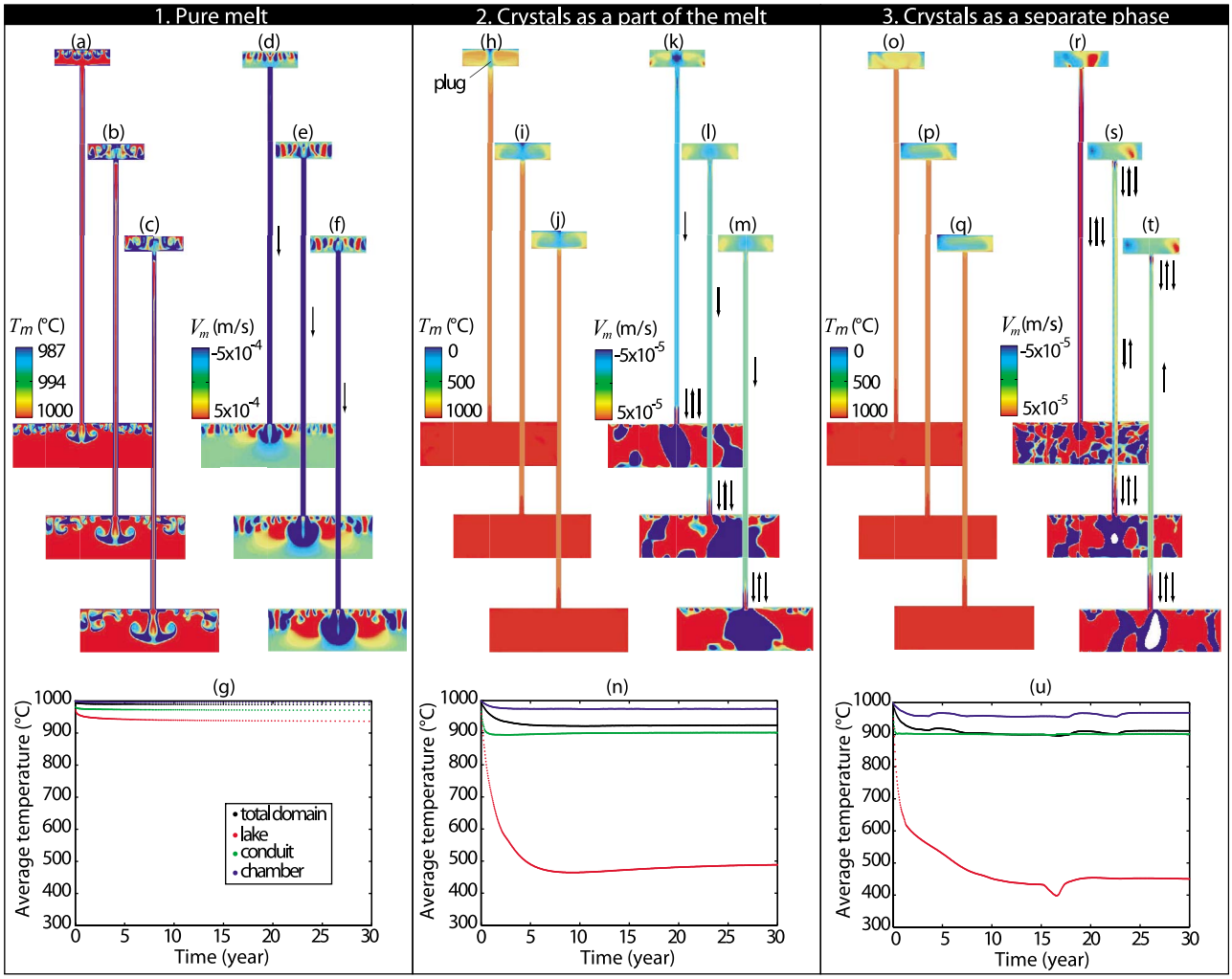

Figure 7. Maps of temperature and vertical velocity and profiles of average temperature per region of the magmatic system for the three simulations with a 4-m-diameter conduit in closed system. Simulation 1 (pure melt simulation): (a–c) Temperature (T_m) at years 1, 10, and 30, respectively; (d–f) vertical scalar velocity (V_m) at years 1, 10, and 30, respectively; and (g) average temperature as a function of time for the different regions of the magmatic system. Simulation 2 (simulation with crystals as a part of the melt): (h–j) T_m at years 1, 10, and 30, respectively; (k–m) V_m at years 1, 10, and 30, respectively; and (n) average temperature as a function of time for different regions of the magmatic system. Simulation 3 (simulation with crystals as a separate phase): (o–q) T_m at years 1, 10, and 30, respectively; (r–t) V_m at years 1, 10, and 30, respectively; and (u) average temperature as a function of time for the different regions of the magmatic system. The arrows accompanying each velocity map represent the main direction of the flow motion in the conduit. Red and blue colors in the velocity maps indicate upward (positive values) and downward (negative values) motions, respectively.

and *Lister and Kerr* [1989] to predict λ_c (equation (9)) and consequently the number of instabilities for those simulations. These theories predict that 17 and 52 instabilities should form at thermal boundary layers with thicknesses h_c of 0.8 and 0.65 m for the lake and the chamber, respectively. These values are comparable to the results of our simulations, which lead to 17 and 50 instabilities for lake and chamber, respectively. The presence of the conduit favors the merging of the instabilities at the junction between conduit and chamber. It also opens a window in the ceiling of the chamber where instabilities would otherwise have formed. This layout explains the 4% discrepancy between the theoretical values and those from our simulations.

[47] We turn next to the downward motion of the instabilities. For a melt with $\Delta T = 900°C$ and $Ra = 9.5 \times 10^9$ (lake) or $\Delta T = 100°C$ and $Ra = 1.7 \times 10^{10}$ (chamber), temperature-driven convection typically yields Rayleigh-Taylor instabilities [*Marsh*, 1988], observed as a progressive front when the downgoing cold plumes entrain more and more hot fluid with time (Figures 7a–7f and 8a–8e). Less than 15 days after the beginning of the simulation, we observe the formation of a crust atop of the lake, which is marked by the clipped viscosity that represents the glassy state. There are no rising plumes, but, with time, the cold and hot fluids inside the lake and chamber eventually mix. The RT instabilities take 4.8 years to reach the bottom of the lake,

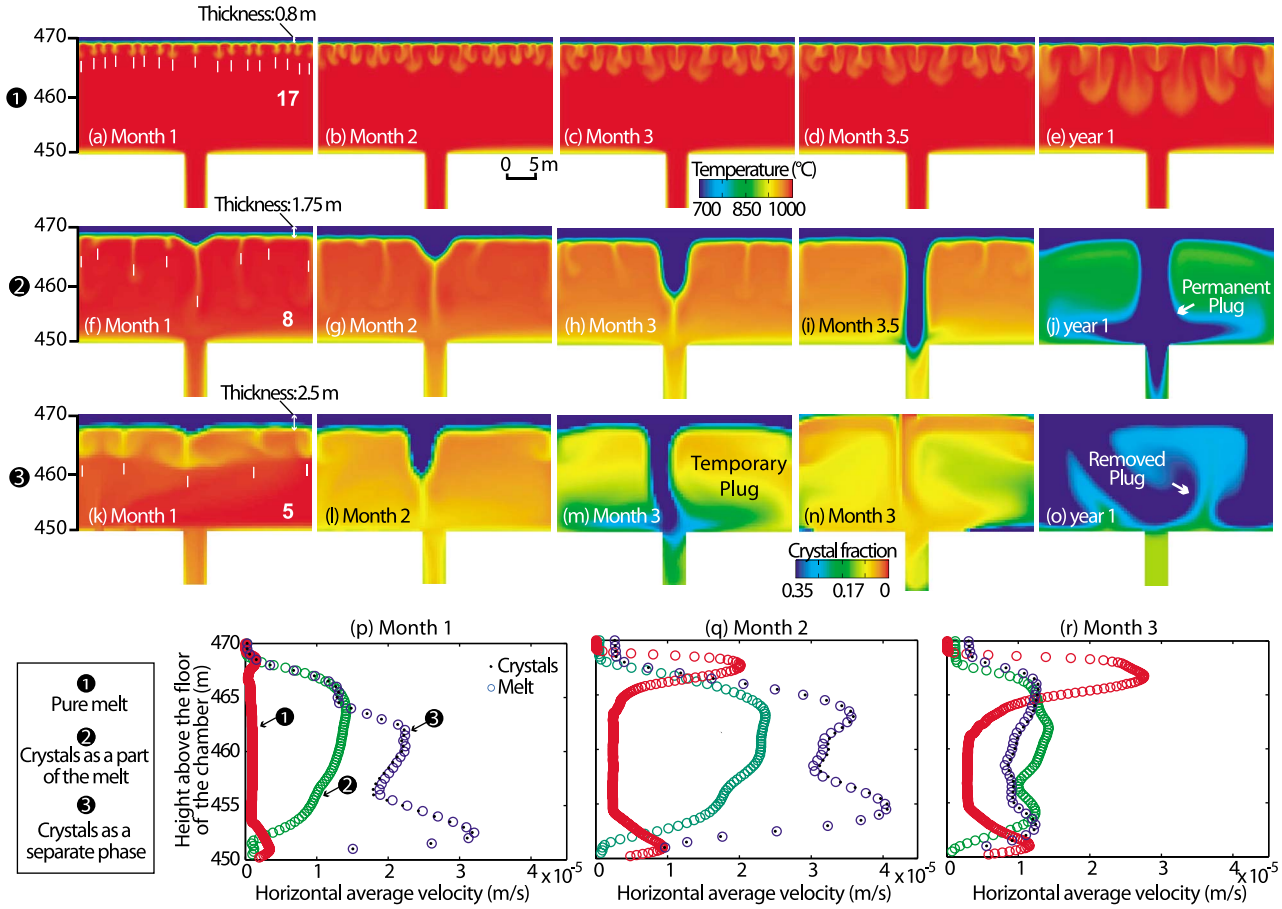

Figure 8. Lava lake dynamics for the three simulations with a 4-m-diameter conduit in closed system. (a–e) Temperature maps for the pure melt simulation at months 1, 2, 3, 3.5, and 12, respectively. (f–j) Temperature maps for the simulation with crystals as a part of the melt at months 1, 2, 3, 3.5, and 12, respectively. (k–m and o) Temperature maps for the simulation with crystals as a separated phase at months 1, 2, 3, and 12, respectively. (n) Map of crystal fraction for the simulation with crystals as a separated phase for the third month. (p–r) Cross sections of the horizontal average velocity in the lake over the first, second, and third month, respectively. The pure melt run (red circles) had a 10-cm grid size and a numerical tolerance of 1.0, the run with crystals as a part of the melt (green circles) had a 25-cm grid and a tolerance of 1.0, and the run with crystals as a separate phase (blue circle and black dots) had a 50-cm grid and a tolerance of 1.0. Labels in Figures 8a, 8f, and 8k indicate the number of instabilities of the cold crust for each simulation, which are signaled by a vertical white bar.

while the plumes forming at the top of the chamber do not reach its base within the 30 years of the simulation (Figures 7c and 7f). After the first year, the flow pattern quickly reaches a steady average temperature in the magma chamber. In the lava lake, this process slows continuously to reach a homogeneous temperature of ~950°C around year 10 (Figure 7g). The flow pattern in the conduit always shows a very gradual downward motion (Figures 7d–7f) because 30 years is not long enough to induce a significant return flow that can offset the cooling effect of the 900°C conduit walls.

4.4.2. Crystals as a Part of the Melt

[48] Based on the vertical profile of the average temperature, the simulations with different grid sizes show only slight differences in the lava lake before year 10 of the simulation; the simulation obtained with the finest grid being warmer by <10%. After 10 years, the three grid sizes converge on the same temperature range (around 500°C), which means that the lava lake completely freezes. No temperature differences are found in the magma chamber and they amount to 2% in the conduit. We selected the simulation with a grid size of 25 × 25 cm^2 and changed the tolerance from 1.0 to 0.5. Residuals are of the same order (Table 4) and vertical temperature profiles are similar, suggesting that the largest value of tolerance is sufficient. This simulation shows a cold crust of 1.75 m (Figure 8f); using this value in equation (9) yields an estimate λ_c and indicates the formation of 8 instabilities, consistent with the number of instabilities we observe (Figure 8f).

[49] The cold crust at the top of the lake develops a central instability that sinks (Figures 8f–8h) and reaches the shallower part of the conduit after 3.5 months (Figure 8i). Until then, the convection pattern is characterized by an ascending core of fluid through the central part of the conduit and

descending fluid at the sides. The extension of this flow pattern to a 3D geometry would be a core-annular flow, a terminology we use hereafter for convenience. This type of convection ceases when the central instability starts folding on itself like a periodic disturbance to create a "plug" that seals the lake at month 6. This plug (Figures 7h and 8j) leads to a continuous cooling of the lake (Figures 7i and 7j). All the heat in the system is then lost by constant cooling of the conduit, which features continuous downward motion and two independent convecting systems develop in the lake and the chamber (Figures 7k–7m). The chamber has the highest convective rates with a velocity oscillating around 7×10^{-5} m/s. The temperature of the magma chamber and the conduit remain constant around 990°C and 900°C, respectively (Figure 7n). Most of the lake reaches glass transition temperature after the first year of the simulation and after year 5 the lake reaches a temperature of about 500°C.

4.4.3. Crystals as a Separate Phase

[50] The only difference between grid sizes of 50×50 and 25×25 cm^2 is the definition of the RT instabilities at the onset of convection. With the 25×25 cm^2 grid, we counted at least five instabilities (including the central one) that are only poorly resolved by the coarser grid. Two lateral instabilities progress along the vertical walls of the lake to reach its bottom with a small delay compared to the central instability. These lateral instabilities are progressively mixed within the lake during the first year of simulation, which is characterized by highly unsteady convection at all grid size. These instabilities do appear in the grid size (50×50 cm^2) that we selected to conduct the tolerance study (Table 4). This choice was motivated by the fact that these simulations are time-consuming; one simulation with the coarse grid running on 144 processors takes 15 days to complete 30 years of simulated time. We found that the runs are almost insensitive to the tolerance values because the corresponding average temperatures differ by only ~2%. The time step history is the smoothest when tolerance equals 1.0, so we selected that run even if the residuals given by the other runs were slightly smaller (Table 4). This run shows a crust of 2.5 m (Figure 8k), from which equation (9) allows us to predict 5 instabilities. This is the number of instabilities we observe (Figure 8k).

[51] As instabilities sink deeper in the lake, they merge with each other and smear out (Figures 8k and 8l), except the central instability, which sinks toward the shallower part of the conduit (Figures 8l–8n) that it reaches after 2.5 months to form a periodic folding disturbance, the natural frequency of which can be compared with analogue models (Figure A4 and details of this in section 5). The periodic folding instability behaves differently to that observed in the simulation with crystals as part of the melt. The folding partly plugs the upward flow until year 1 before being displaced laterally by the continuous flow coming from the conduit (Figure 8o). After year 1, the fluid in the lake keeps convecting and partly chokes the conduit (Figures 7o–7q), and the convective rate decreases. The flow pattern in the conduit evolves from a core annular flow (Figure 7r) into vertically stratified flow (Figure 7s) and later into upwards-only motion (Figure 7t). The continuous cooling of the system isolates the lake and part of the conduit from the rest of the system, which then features two sustained core annular flows from chamber to the lower part of the conduit and from lake to the shallower part of the conduit, respectively (Figures 7s and 7t). As in the simulation with crystals as part of the melt, most of the lake reaches glass transition temperature after the first year of the simulation (Figure 7o) and attains a temperature of about 500°C after year 5 (Figure 7u).

4.4.4. Comparison of the Three Scenarios for Representing Phases

[52] A striking difference between the three configurations is the convection inside the conduit and the flow velocities in the lake. The bi-phase configuration shows a core-annular and a vertically stratified magma flow inside the conduit that facilitates thermal exchange between the lake and the magma chamber. When crystals are considered as a part of the melt, a similar series of patterns occurs, with an earlier shift between a single and multiple core-annular flows. In contrast, the pure melt simulation shows melt being pushed down the conduit by the front of RT instabilities descending within the lake, without generating a bi-directional flow. We surmise that a return flow would be established at much longer times. Within the time span of our simulations, however, the presence of core-annular flow along the conduit is enhanced by the presence of crystals.

[53] The velocity of the fluid is higher in the lower section of the lake during the first month (Figure 8p), and the fast-moving front progressively migrates upwards (Figures 8q and 8r) under the influence of both thermal convection and crystal settling. The presence of crystals influences the convective rate, despite the fact that particle movement is well coupled to the liquid (Figures 8p–8r). When crystals are present as a separate phase, the initial convective rate over the first 2 months is relatively high (the highest of the three) (compare Figures 8p–8r). The central instability temporally plugs the conduit at 2.5 months (Figure A4), which temporally isolates the lava lake from the conduit and decreases the convective rate (Figure 8r). In a mixture with crystals as part of the melt, it takes slightly longer (3.5 months) for the instability to reach and plug the top of the conduit (compare Figure 8i with Figure 8m). The pure melt behaves differently; after 1 month only a weak change in velocity occurs at the base of the lake (Figure 8p). The instabilities descend progressively from the top of the lake to reach only a few meters by month 3 (Figures 8a–8c and 8p–8r). The presence of crystals entrained by the central instability enhances the velocity at which the bi-phase flow sinks at the vertical of the conduit (compare Figure 8m with Figure 8h). The presence of crystals and the way they are associated with the melt have a lasting influence on the flow velocity at the surface of the lake, as discussed further in section 4.7.

4.5. The Influence of Conduit Dimensions

[54] We examine the influence of the conduit diameter while keeping the other parameters of the three different configurations constant. Figures 9a–9u show temperature and vertical velocities for the "pure melt," "crystals as a part of the melt," and "crystals as a separate phase" configurations with a 10-m diameter conduit. The comparison between Figures 7a–7g and 9a–9g suggests that increasing the conduit diameter from 4 to 10 m for a pure melt does not affect temperature nor flow velocities in the lake and chamber. The temperature remains higher in a 10 m diameter conduit, where a core annular flow develops unlike in a 4 m conduit, where we observe a downward motion. For a 4-m-

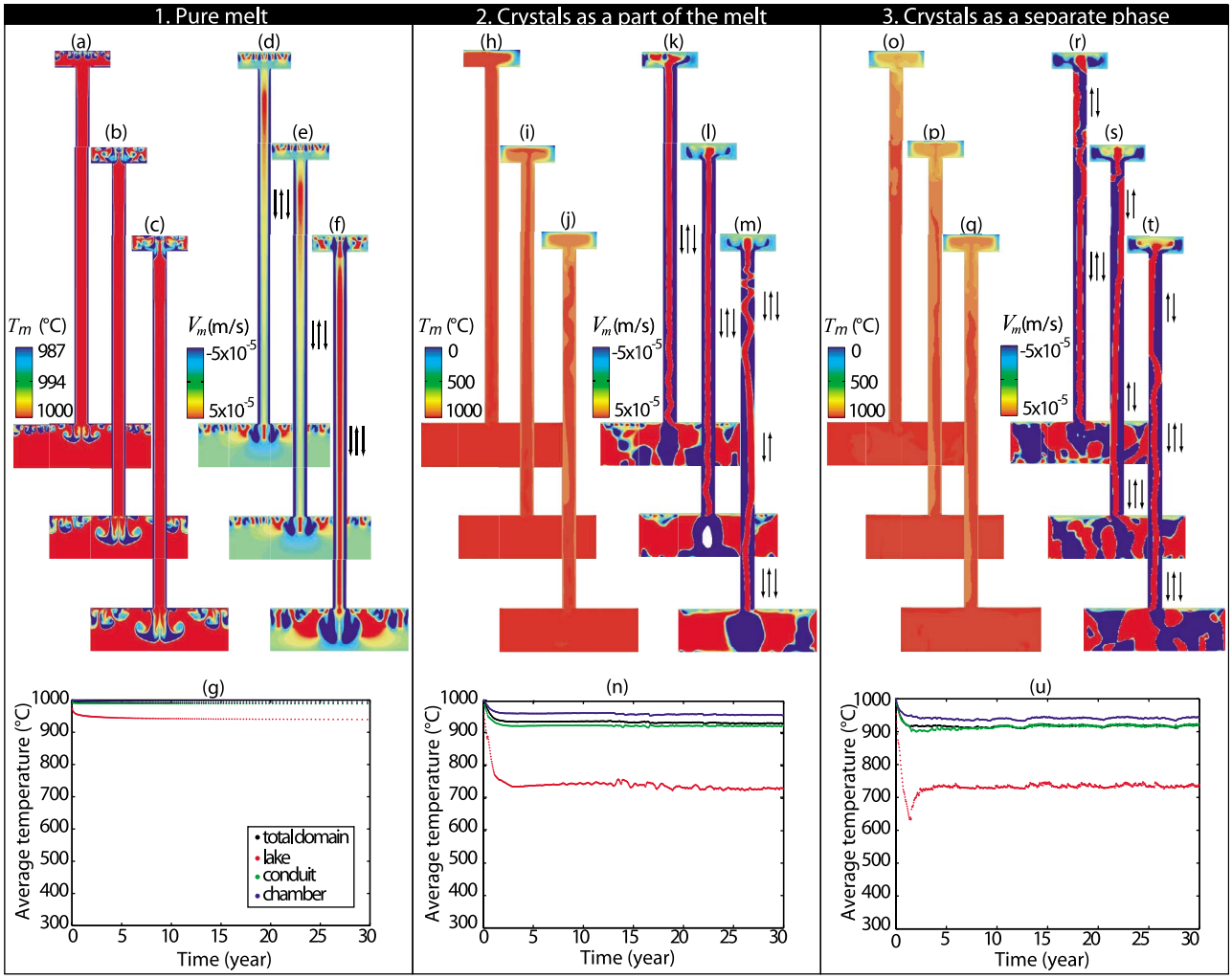

Figure 9. Maps of temperature and vertical velocity and profiles of average temperature per region of the magmatic system for the three simulations with a 10-m-diameter conduit in closed system. Simulation 1 (pure melt simulation): (a–c) Temperature (T_m) at years 1, 10, and 30, respectively; (d–f) vertical scalar velocity (V_m) at years 1, 10, and 30, respectively; and (g) average temperature as a function of time for the different regions of the magmatic system. Simulation 2 (simulation with crystals as a part of the melt): (h–j) T_m at years 1, 10, and 30, respectively; (k–m) V_m at years 1, 10, and 30, respectively; and (n) average temperature as a function of time for different regions of the magmatic system. Simulation 3 (simulation with crystals as a separate phase): (o–q) T_m at years 1, 10, and 30, respectively; (r–t) V_m at years 1, 10, and 30, respectively; and (u) average temperature as a function of time for the different regions of the magmatic system. The arrows accompanying each velocity map represent the main direction of the flow motion in the conduit. Red and blue colors in the velocity maps indicate upward (positive values) and downward (negative values) motions, respectively.

diameter conduit, crystals as a separate phase sustains the heat transfer from chamber to the lava lake for the longest period (compare Figures 7k and 7l with Figures 7r and 7s). Increasing the conduit diameter increases this period even further. The overall temperature of the system increases and remains above glass transition (compare Figure 7u with Figure 9u). The core-annular flow is maintained for all the configurations and all simulated times (compare Figures 7a–7u with Figures 9a–9u, respectively). This is mostly due to the inability of the central instability to plug such a wide conduit. A 10-m diameter conduit thus allows the full system to approach steady state convection.

4.6. Sensitivity to Boundary Conditions

[55] The numerical scheme of MFIX is based on finite volumes. When the melt cools and contracts, the imposed closed system causes mass loss. This loss is small over the 30 years of simulations (~1%). The algorithm of MFIX, however, always enforces equation (14) at the end of each iteration, which causes the small mass loss to be translated into a crystal volume fraction loss. In our bi-phase simulations, the densities of crystals and melt are close to each other. As a result, the crystal volume fraction loss becomes non negligible. We estimate that it is equal to 5% in the chamber and conduit. Up to 8 vol.% crystals are thus lost in the lake because the temperature change is higher there than

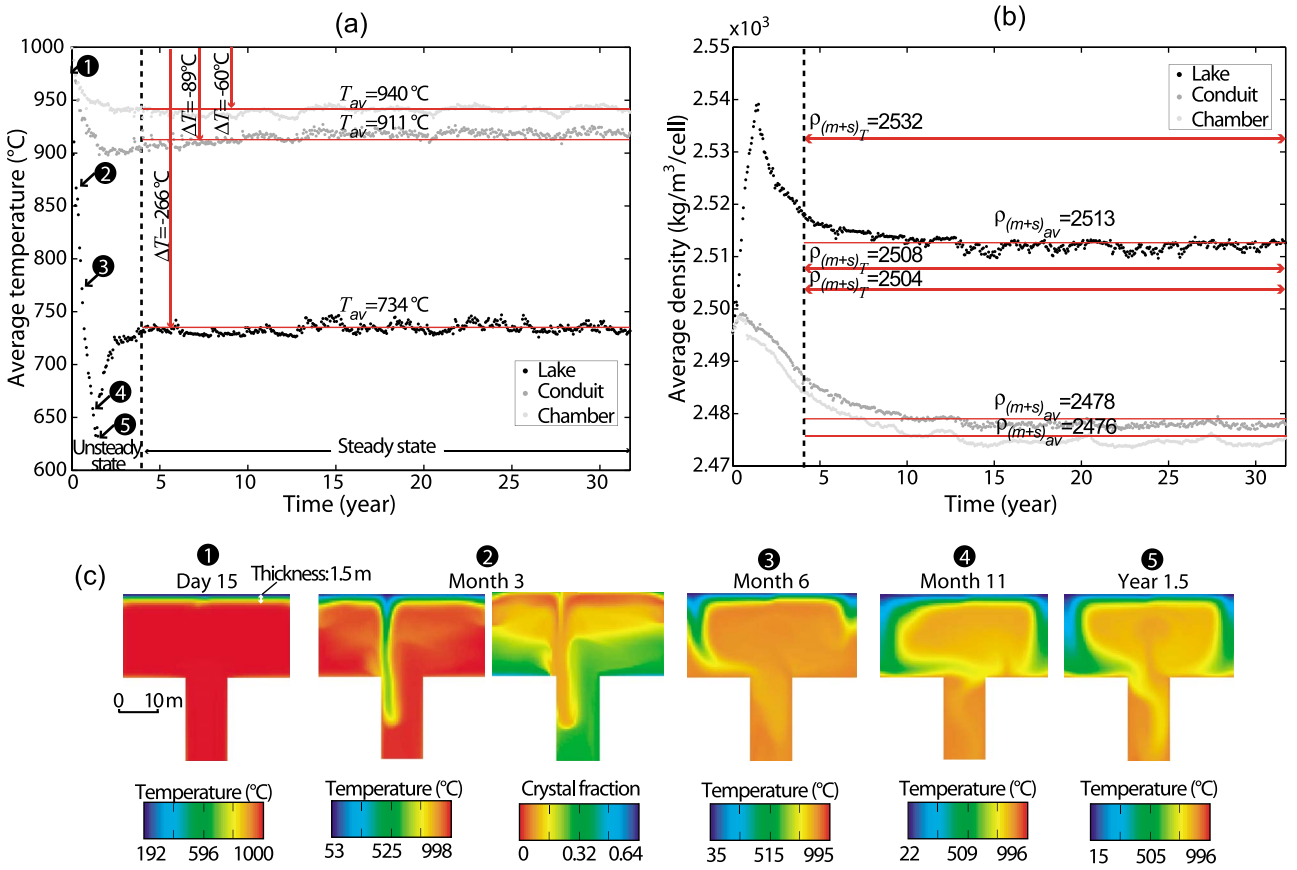

Figure 10. Results from the bi-phase simulation with a 10-m-diameter conduit in closed system. (a) Average temperature per region of the magmatic system versus time. The vertical dotted black line divides the unsteady period from the steady state period. Labels T_{av} represent the average temperatures of each region during the steady state period (marked by thin horizontal red lines). Vertical red arrows represent the difference (ΔT) between the initial 1000°C and the average temperature (T_{av}) reached by each respective region once steady state is reached. (b) Average bulk density per region of the system versus time. Red arrows represent the bulk density, $\rho_{(m+s)T}$, that is expected from the cooling of each respective region by the amount reported next to the ΔT labels in Figure 10a. Labels $\rho_{(m+s)av}$ represent the observed average bulk density of each region during the steady state period (marked by thin horizontal red lines). (c) Snapshots of the lava lake at the early stages of convection. Circular tags in Figures 10a and 10c successively refer to (1) the formation of a cold crust at the top of the lake at 15 days, (2) the cold front pushing down a crystal-poor layer at 3 months, (3) the shifting of the central instability and its merging with a lateral instability at 6 months, (4) the draping of the bottom and the sides of the lake by instabilities at 11 months, and (5) the disruption of the draped instabilities by the arrival of a hotter plume from the conduit at 1.5 years.

in the rest of the system. Simulations in open system are not subject to these mass and crystal load losses. Whether or not these losses affect convection dynamics can be assessed by comparing the bi-phase simulation with 10-m conduit diameter and in closed system with a similar simulation but in open system. We first provide a mechanical description of the closed system simulation with crystals as a separate phase and a 10-m conduit diameter before highlighting the differences introduced by the open system. Figures 10a–10c, 11a–11t, and 12a–12g highlight the effect of changing the boundaries of the system from closed to open. Figure 10 shows the evolution of temperature and bulk densities in the three regions of our closed system; the main stages of the convection and crystal settling within the lake for a 10-m-diameter conduit system are shown in Figures 11a–11e for a closed system and in Figures 11f–11j for an open system. Similarly, we compare the stages of convection for the chamber in a closed system in Figures 11k–11o to those for an open system in Figures 11p–11t. Details of the evolution of temperature variations in the three regions and crystal content inside the conduit for an open system are shown in Figure 12.

4.6.1. Crystal Settling in a Closed System (No Feeding)

[56] Over the 30 year period, the magma cools down by 266, 89 and 60°C in the lake, conduit, and chamber, respectively (Figure 10a), and one can expect its bulk density to increase. Our simulation indicates, however, a decrease of bulk density of the magma in the lake, conduit and the chamber (Figure 10b). This is a likely result of crystal settling in the system. The steady state values of the

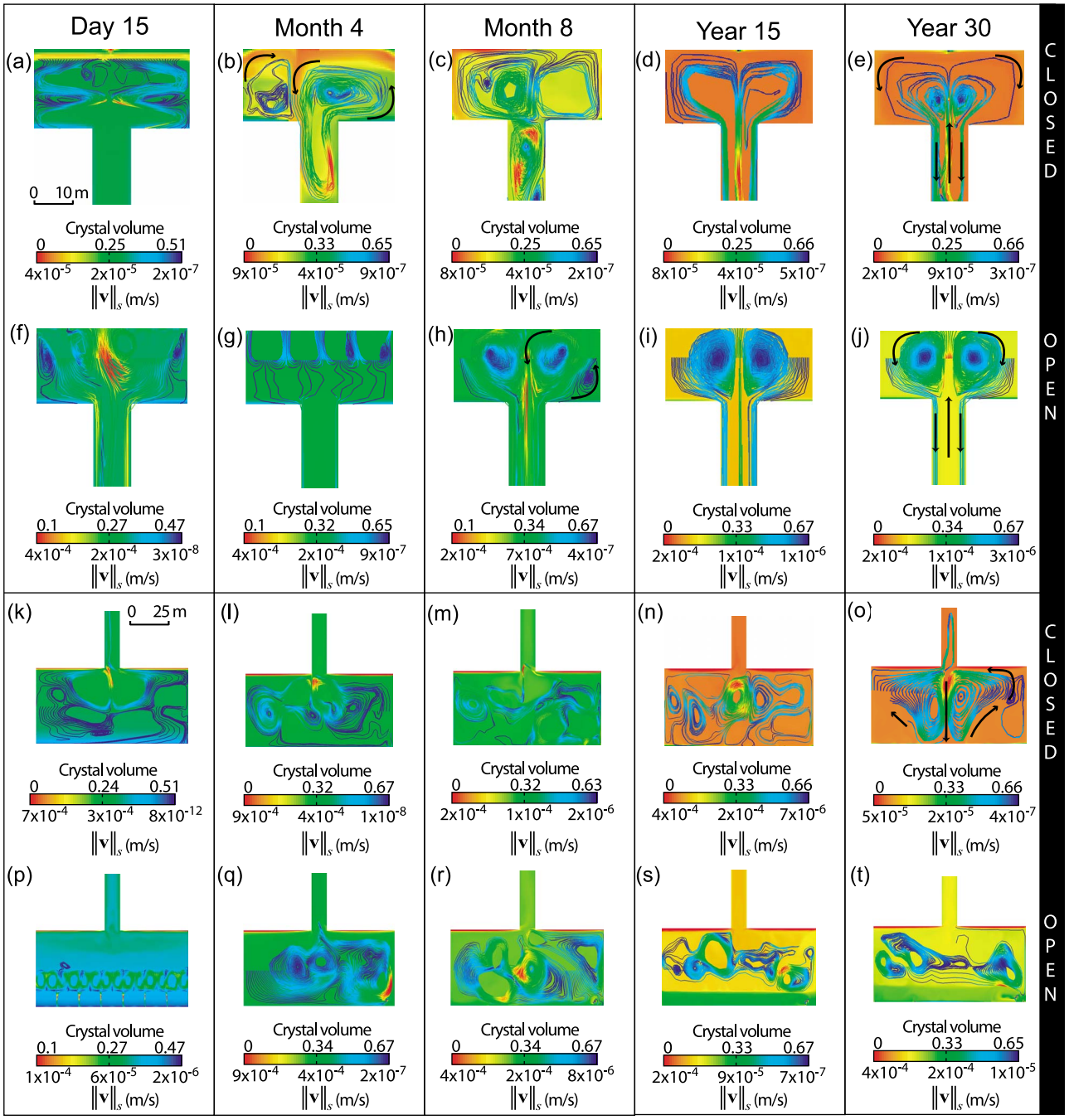

Figure 11. Comparison of lake and chamber convective patterns for the bi-phase simulations with a 10-m-diameter conduit in either closed or open system. Convection patterns are shown as individual crystal paths colored according to the magnitude velocities of crystals $||\mathbf{v}||_s$. These streamlines, which are travel paths of 25 to 100 crystals drawn with an absolute tolerance of 10^{-5} and variable time step length, are superimposed on crystal fraction maps. (a–e) Lake region of the closed-system simulation at day 15, month 4, month 8, year 15, and year 30, respectively. (f–j) Lake region of the open-system simulation at similar times. (k–o) Chamber region of the closed-system simulation at similar times. (p–t) Chamber region of the open-system simulation at similar times.

bulk density, from ~4 to 30 years, correspond to the cooling of the three domains. These results allow us to describe mechanistically the main stages of the magmatic system evolution.

[57] At the beginning of the simulation, the temperature of the vicinity of the surface of the lake decreases (Figure 10a), resulting in the formation of a thin crust of ~1.5 m and in the growth of the first instability at the center of lake after ~15 days (tag 1 in Figure 10c). Instabilities carry a few crystals enveloped by the quenched liquid (~20 vol.%) into the shallower part of the conduit (tag 2 in Figure 10c). Both crystals and the melt reach a maximum speed of 5×10^{-5} m/s.

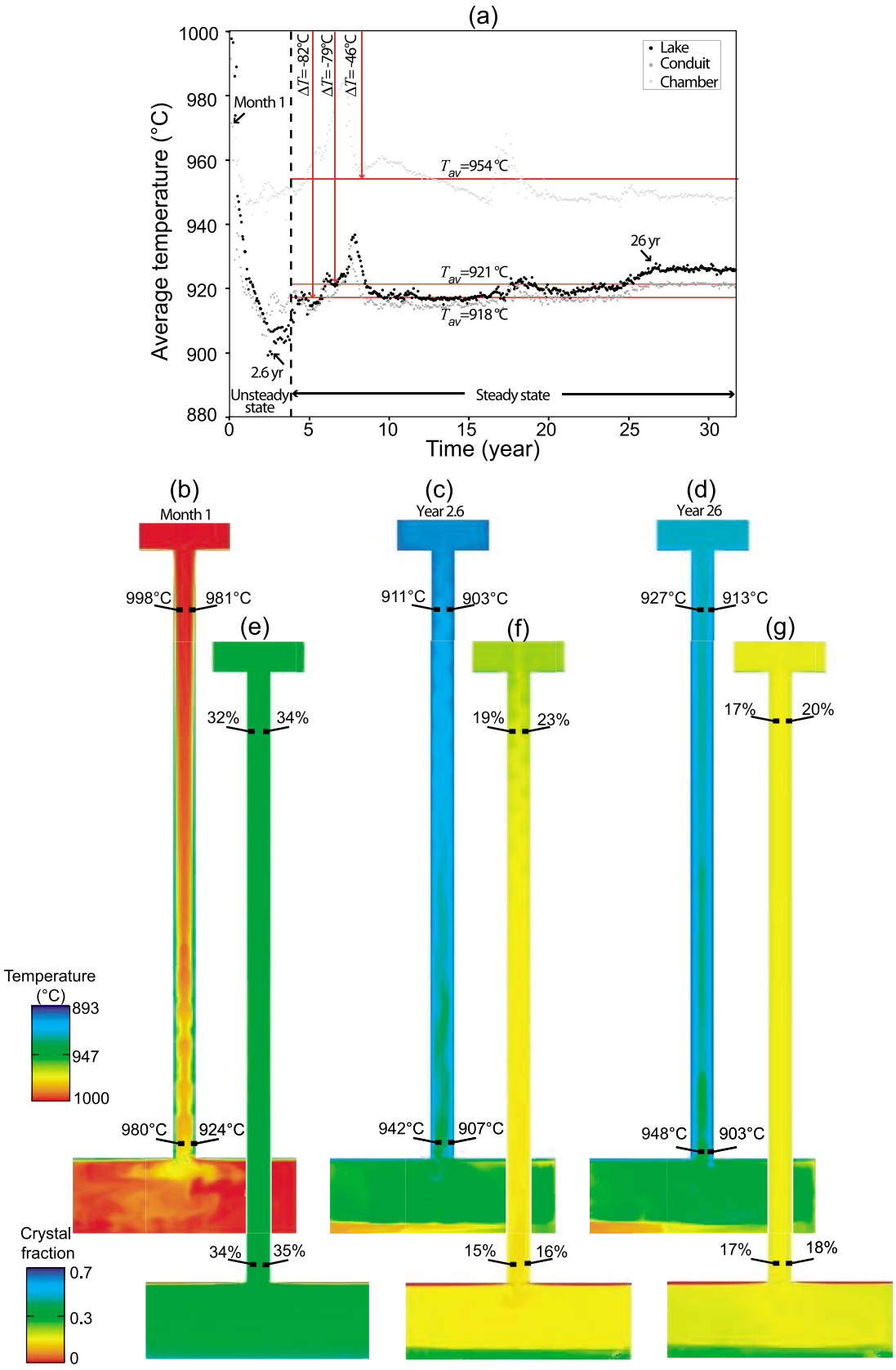
(a)
Average temperature (°C)
Time (year)
Lake
Conduit
Chamber
Month 1
ΔT=-82°C
ΔT=-79°C
ΔT=-46°C
T_av=954°C
T_av=921°C
T_av=918°C
26 yr
2.6 yr
Unsteady state
Steady state
(b)
Month 1
998°C
981°C
(c)
Year 2.6
911°C
903°C
(d)
Year 26
927°C
913°C
(e)
32%
34%
(f)
19%
23%
(g)
17%
20%
Temperature (°C)
893
947
1000
980°C
924°C
942°C
907°C
948°C
903°C
Crystal fraction
0.7
0.3
0
34%
35%
15%
16%
17%
18%

Figure 12

This strong cooling causes the bulk density of the lake to rise rapidly over the first 3 months (Figure 10b). In the conduit and the chamber, the bulk density does not increase as much as in the lake because these two domains are insulated. Unlike the 4-m conduit simulation, the plugging of the conduit-lake junction does not occur (tag 3 in Figure 10c). At month 3, the central plume shifts laterally and merges at month 6 with one of the lateral instabilities that has been simultaneously developing. This partially isolates the lake (tag 4 in Figure 10c), causing a convective pattern that keeps the volume of crystals approximately constant (~17 vol.%) inside the lake (Figures 11b and 11c). A hotter plume rises from the conduit at ~1.5 yr and progressively destroys the partial isolation of the lake by generating stronger convection in the lake (tag 5 in Figures 10a and 10c). This prevents the system from cooling further but sedimentation continues until year ~10 to stabilize at 6 vol.% of crystals in suspension (Figures 11d, 11e, 11n, and 11o). This temperature increase marks the progressive transition toward steady state at year ~4 (Figure 10a), at which point the center of the lake remains at a temperature above glass transition (734°C).

[58] The crystal content in the magma chamber never becomes homogenous during the first unsteady 4 years because cool and crystal-poor liquid keeps pouring from the conduit into the chamber. A crystal-rich (60%) layer appears at the chamber bottom when steady state is reached, but it cannot be described as "stagnant" because this layer is eventually disturbed by the convection generated by the arrival of cooler liquid from the conduit, containing less crystal. Remains of this layer can be seen in Figures 11n and 11o. The bottom layer remains enriched in crystals while the top of the magma chamber becomes almost crystal-free (Figure 11o). Some cells briefly reach ε_m^* or 1% above because of plasticity, regardless of the value of ε_m^* (35 vol.% or 37 vol.%).

[59] Taking the system as a whole, the convective pattern in steady state remains stable until the end of our 30 year simulation. Relatively crystal-rich, hot fluid reaches the lake from the conduit, sustaining the convection pattern and 6 vol.% of crystals remain suspended within the convecting magma. Should all the crystals that correspond to the 24 vol.% that are settling from the three regions accumulate at the bottom of the chamber and remain there at maximum packing fraction ($1 - \varepsilon_m^* = 65$ vol.%), the crystal-rich layer would reach 11 m in thickness. Two large and steady convective cells are observed in the lake (Figures 11d and 11e) while chamber convection does not show any characteristic pattern over time except at the end of the simulation, when two regular and symmetrical cells are established, the one on the right side circulating in an anticlockwise direction the other circulating clockwise (Figure 11o).

4.6.2. Crystal Settling in an Open System (Permanent Feeding)

[60] Based on changes in temperature profiles we differentiate two main states: unsteady behavior in which a maximum temperature drop reaches a plateau before rising again to reach steady state by year ~4. In steady state, the open-system temperatures drops by 79, 82 and 46°C in the lake, conduit, and chamber, respectively (Figure 12a). This is warmer (compare Figure 12a with Figure 10a) and more crystal-rich than the closed system (compare Figures 11f–11j with Figures 11a–11e for the lake, and Figures 11p–11t with Figures 11k–11o, for the chamber). Temperatures in both the shallow and the deep parts of the conduit decrease progressively during early stages before increasing at later times (Figures 12a–12d). This translates into a small variation of the shallow temperature contrast, from 17 to 8 to 14°C, while the contrast of deeper-seated temperatures has larger variations, from 56 to 35 to 45°C. Details of the evolution of the crystal content inside the conduit are shown in Figures 12e–12g. Ultimately, shallow and deep temperatures in the conduit increase as a consequence of a fully developed convection between the deep and hot region and the shallow and cooler region.

[61] In the chamber, several regular patterns of rolling convective cells appear at an early stage of the open system simulation (Figure 11p), before resolving into fewer cells as the mixture becomes more homogenous (Figures 11q and 11r) and as a crystal-rich layer appears at the chamber base (Figures 11s and 11t). Crystal-melt segregation at the base of the chamber is enhanced as crystals deposit, and manifests itself in the form of tiny plumes rising from a compacted region where hindered settling occurs (Figure 11p). Fluid motion generated by the convection in the chamber is practically horizontal right above the compacted region at later stages of the simulation (Figure 11t). This is in contrast to the closed system, where the much slower convection barely shows any characteristic pattern over time except at the very end of the simulation (compare Figures 11k–11n with Figures 11p–11s, respectively). Another difference with the closed system is the 10-m-thick, crystal-rich (~33 vol.%) layer that remains at the chamber bottom throughout the steady state (compare Figures 11n and 11o with Figures 11s and 11t, respectively). The cold flow pouring from the conduit sustains convection in the upper part of the chamber without disturbing this compact layer, the temperature of which remains slightly higher than the rest of the domain (Figures 12c and 12d) and causes enhanced melt extraction (Figure 11s). The thickness of accumulated crystals remains around 10 m whereas the respective fractions of melt and crystals vary due to re-entrainment of crystals in the chamber (Figure 11t). The arbitrary thickness of the chamber

Figure 12. Profiles of average temperature per region of the magmatic system for the bi-phase simulations with a 10-m-diameter conduit in open system and maps of temperature and crystal volume fractions. (a) Average temperature per region of the magmatic system versus time. The vertical dotted black line divides the unsteady period from the steady state period. Labels T_{av} represent the average temperatures of each region during the steady state period (marked by thin horizontal red lines). Vertical red arrows represent the difference (ΔT) between the initial 1000°C and the average temperature (T_{av}) reached by each respective region once steady state is reached. Arrows point out specific portions of the time series referenced as Figures 13b to 12g. (b–d) Temperature at month 1, year 2.6, and year 26, respectively. Black dots point to localized temperatures of the ascending and descending magma. The descending magma is colder than the ascending one. (e–g) Crystal fraction at month 1, year 2.6, and year 26, respectively. Black dots point to localized crystallinities of the ascending and descending magma. The descending magma is richer in crystals than the ascending one.

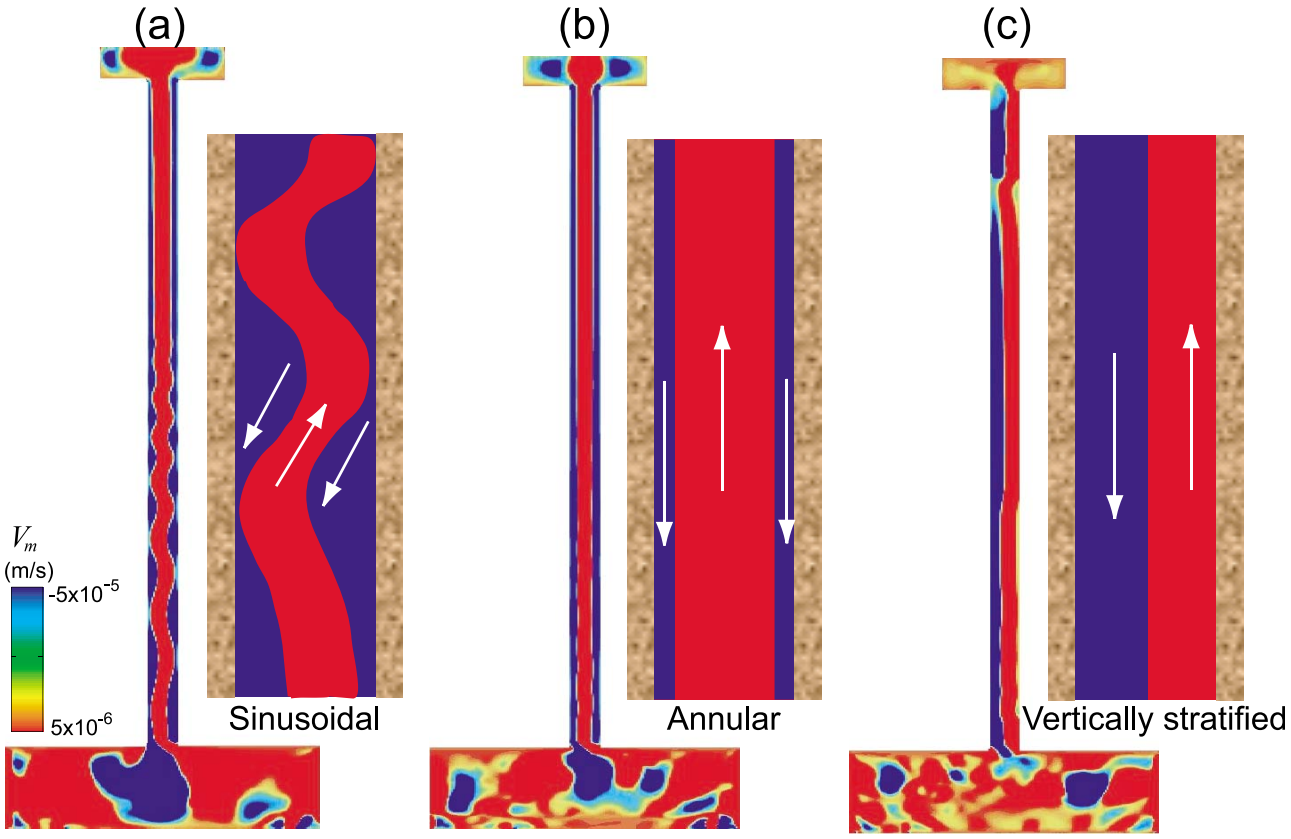

Figure 13. Examples of convective flow patterns inside a 10-m-diameter conduit for the bi-phase simulations. Red and blue colors in the vertical velocity maps indicate upward and downward motions, respectively. The positive and negative signs in the common vertical velocity scale (V_m) indicate upward and downward motions, respectively. Insets show enlarged schematics of the patterns. (a) Sinusoidal flow in the open system at year 1. (b) Core annular flow in the open system at year 30. (c) Vertically stratified flow in the closed system at year 16.

conditions the thickness of the settling horizon and the convective patterns of the chamber. Both closed and open systems display a crystal-poor layer at the top of the magma chamber on each side of the entrance to the conduit (compare Figures 11n and 11o with Figures 11s and 11t). This may suggest that the effects of the thickness of the chamber are probably limited to this level of the reservoir.

[62] In open system, a crystal-rich layer forms at the bottom of the lake on each side of the conduit (Figures 11i and 11j), mirroring that of the chamber base. Both closed and open systems result, however, in similar convection pattern in the lake. Motion is clockwise at the left side of the cell and counterclockwise on the right side of the cell (Figures 11b, 11c, and 11h), a pattern that will be reversed over time once steady state has been reached (e.g., Figures 11d, 11e, 11i, and 11j).

[63] Figure 13 describes characteristic flow patterns occurring in a 10-m conduit inside a 10-m-diameter conduit, which we call respectively sinusoidal (Figure 13a), core annular (Figure 13b) and vertical stratified flows (Figure 13c). The convective flow in a closed system presents a sinusoidal profile combined with a vertically stratified flow throughout the entire period of simulation (Figures 9r–9t and 13c). Open system causes changes in flow patterns; after several months, the conduit develops a core annular flow (Figure 11h) that evolves into a sinusoidal pattern at ~year 1 (Figures 13a). Later in the simulation (e.g., year 30), the open-system conduit features a well-established core-annular flow (Figures 11i and 11j), replacing the sinusoidal flow. We observe at year 2.6 that the sinusoidal flow is caused by the interaction of cold and hot fluids. The cold fluid (903°C) transports a magma with relatively higher crystal content (23 vol.%) and moves downward along the walls of the conduit. The hot fluid (911°C) transports a lower crystal content (19 vol.%) and ascends in the core of the conduit, from the chamber to the surface of the lake (Figures 12c and 12f). The sinusoidal regime displays a longer and longer wavelength as this instability approaches the top of the chamber (Figure 12c). It can be observed in the deeper and shallower part of the conduit that the contrast between the temperatures of ascending and descending fluids decreases to reach its lowest value at year 2.6 (Figure 12c). Then the temperature of the ascending fluid rises again (Figure 12d). The difference of crystal contents between ascending and descending fluids remains constant within 1 vol.% in the lower part of the conduit while a maximum difference of up to 4 vol.% is observed in the upper part of the conduit (Figures 12e–12g); the absolute value of crystal content increases slightly (2 vol.%) between

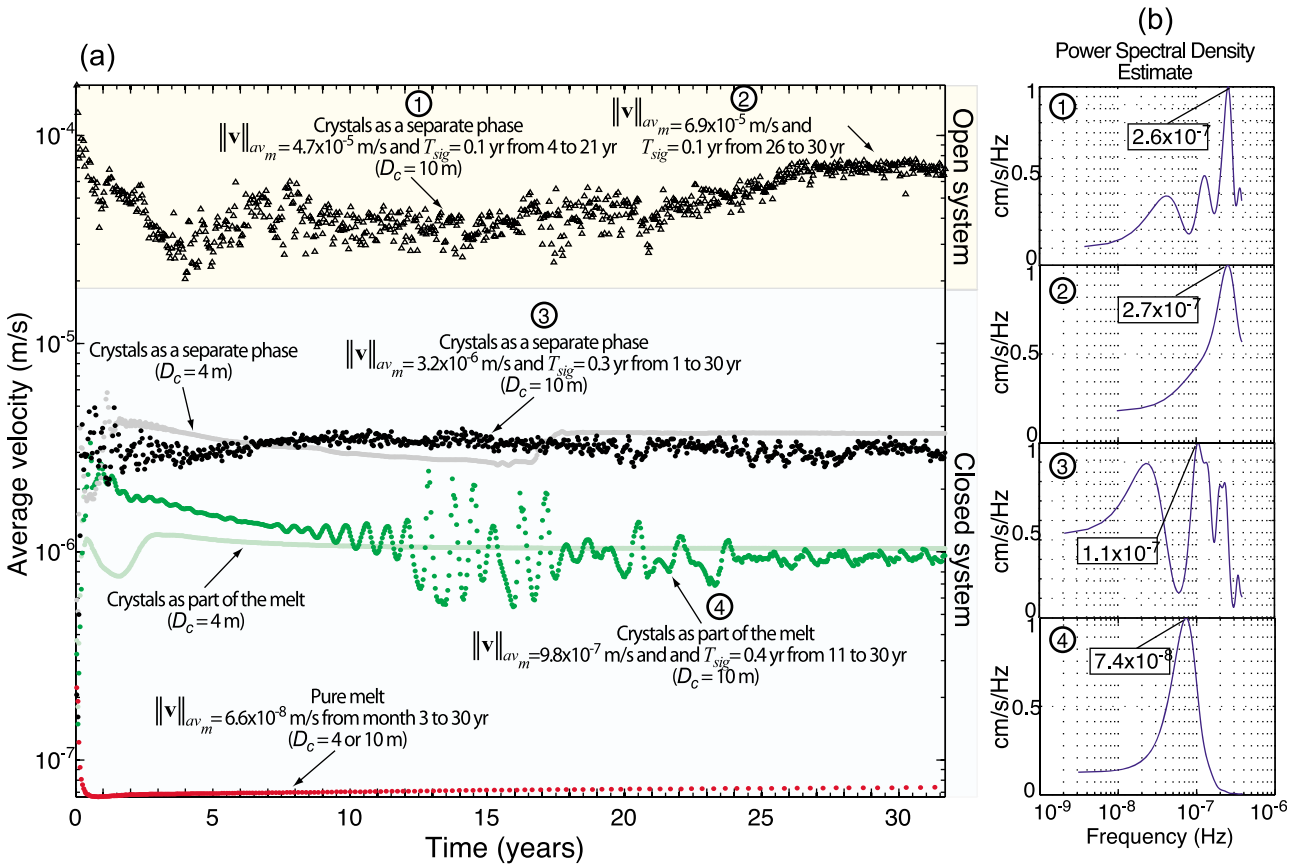

Figure 14. Characteristics of the surficial velocities at the lake surface for all seven simulations. (a) Average velocity of the uppermost meter of the lake for: runs with pure melt in closed system (red dots, 4 and 10-m conduit), runs with crystals as a part of the melt in closed system (light green and dark dots, 4 and 10-m conduit, respectively), runs with crystals as a separate phase in closed system (gray and black dots, 4 and 10-m conduit, respectively), and one run with crystals as a separate phase in open system (black triangles, 10-m conduit). The blue and yellow backgrounds highlight simulations performed in closed and in open systems, respectively. Labels have additional information with arrows pointing at specific portions of the dot/triangle series. In labels, $\|\mathbf{v}\|_{av_m}$ is the average magnitude velocity of the melt, T_{sig} is the period of the time series, and D_c is the conduit diameter. Circular labels 1–4 refer to specific portions of the time series and to Figure 14b. (b) Comparison of the Welch power spectra of the velocity average of the uppermost 1 m of the lake for the configurations shown in Figure 14a. Each spectrum, numbered for 1 to 4, refers to the corresponding circular labels in Figure 14a, which point to specific portions of the time series. Spectral amplitudes are normalized and the frequencies shown are below Nyquist frequency.

year 2.6 and 26 in the lower part of the conduit. The maximum observed contrast in temperature is 56°C (Figure 12b).

4.7. Analysis of Salient Model Outputs: Behavior of the Lake Surface

[64] We compared average surface velocities over a depth of 1 m for all seven simulations (Figure 14a). We also used the method of *Welch* [1967] to compute the Power Spectral Density (PSD) of the velocity average time series to compare the main frequency peaks. This estimate was achieved by removing the linear trend and estimating the PSD with 12 overlapping windows (50% overlap between segments) to improve the signal-to-noise ratio of the spectrum. The spectral amplitude was normalized and the main frequencies shown in Figure 14b are below Nyquist frequency, which is equal to 4×10^{-7} Hz for our sampling rate of 15 days.

[65] Overall, the trend of the average velocity is identical for both conduit sizes and the three different configurations tested to study the Erebus (Figure 14). For a closed system, the magnitude of the velocity depends more on whether the crystals are considered as part of the melt or as separate phase than on conduit diameter. The velocities of the crystals as part of the melt fall between the velocities of the bi-phase and pure melt simulations. Among all simulations, pure melt magma always shows the lower surface velocities, with an a average value of 8.6×10^{-8} m/s early on in the simulations (over the first 3 months) to reach a constant value of a 6.6×10^{-8} m/s over the rest of the period. This behavior is similar for both conduit diameters. The velocity of magma with crystals as part of the melt, in a closed system, with a 10-m conduit increases from 3.2×10^{-7} (day 15) to 3.3×10^{-6} m/s during the first half-year before dropping continuously until about year 11, when it starts to oscillate around

9.8×10^{-7} m/s. When the conduit diameter is only 4 m, this behavior is similar until month 3.5 when the velocity reaches a peak of 1.8×10^{-6} m/s before decreasing due to plugging of the conduit. It then increases again slightly (up to 1.5 yr) to reach a constant value similar to that in a 10-m conduit but without presenting any oscillating pattern. Liquid carrying crystals as a separate phase, in a closed system, with a 10-m conduit shows an increasing trend of velocity during ~1.4 yr, from 2×10^{-7} (day 15) to 4.9×10^{-6} m/s. The surface velocity reaches later an average constant value of 3.2×10^{-6} m/s. When the conduit diameter is only 4 m, the velocity behavior is similar over the first year, when it decreases from 6×10^{-6} to 2.7×10^{-6} m/s over the next 17 years. It then increases sharply to 3.7×10^{-6} m/s and remains at that value for the rest of the simulated period. In an open system with crystals as a separate phase and a 10-m conduit, the surface velocity is higher than in closed system. It sharply decreases from 1.7×10^{-4} (day 15) to 2.2×10^{-5} m/s at year 4, a value that remains approximately constant until year 21 when it increases smoothly to an average value of 6.9×10^{-5} m/s (from year 26 to 30).

[66] Whereas a pure melt features a single large initial amplitude of 10^{-7} m/s (0–3 months), the other configurations display velocity oscillations. The velocity of the mixture oscillates around $\sim 10^{-6}$ m/s with a period of 0.4 yr (over both the entire time of the simulation and from 11 to 30 yr) and that of the bi-phase in a closed system around 3.2×10^{-6} m/s with a period of ~0.3 yr (over both the entire time of the simulation and from 1 to 30 yr). For the bi-phase simulation in an open system, the surface velocity oscillates around $\sim 10^{-5}$ m/s with a period of 0.1 yr from 4 to 21 yr and over the last 4 years. Therefore, the velocity of the lake fed by 10-m-diameter conduit increases and decreases every half a period, or every 3, 2, and 1 months for a mixture in closed system, a bi-phase magma in closed system, and a bi-phase magma in open system, respectively (Figure 14b).

5. Discussion

[67] We carried out seven numerical simulations of an idealized magmatic system broadly aimed at representing the Erebus lava lake. Four simulations were single-phase and three were bi-phase, which allowed us to test the effects of crystals on convection while changing conduit size from 4 to 10 m and the system boundaries from closed to open. Our bi-phase simulations with a sufficiently large conduit (10 m) show that convective motions under steady state conditions are sufficiently vigorous to keep a proportion of the crystals in suspension and well-mixed. In particular, when the closed system reaches steady state around year 4, 65% of the initial 30 vol.% crystals have settled. The dense layer formed at the bottom of the chamber is then disturbed by convection. Complete settling is thus never achieved in any region of the system, leaving 6 vol.% crystals in suspension from year 15 until 30 and presumably for much longer. In the open system, only 34% of the initial crystal content settles, leaving about 20 vol.% in suspension in late steady state. Simulating magma by a mixture with crystals as part of the melt, on the other hand, has the major issue that crystal settling is not taken in account. Crystals, if considered as a separate phase, play a fundamental role in increasing apparent viscosity locally and creating complex circulation pattern, and in enhancing the vigor of fluid dynamics. However, the mixture theory can provide some features of the system, such as (i) the formation of a central instability, (ii) the average temperature evolution, and (iii) the average velocity range of the flow motion at the surface of the lake.

[68] Crystal size and the contrast between crystal and melt densities ($\Delta\rho = \rho_s - \rho_m$) are the two main controls on the amount of crystals remaining in suspension in the convecting magma. Using Stokes' velocity, v_s, we calculated settling velocities of 10^{-6} m/s for the closed system, a value of the same order of magnitude as the flow velocities given by our bi-phase simulations. This balance between settling and convection is in qualitative agreement with the theoretical findings of *Huppert and Sparks* [1988] and *Burgisser et al.* [2005]. Our simulations also show that some crystals come out of suspension and accumulate on the lake and chamber floors, as reported in other studies of crystal settling [*Martin and Nokes*, 1988, 1989; *Martin*, 1990; *Worster et al.*, 1990].

[69] *Lavorel and Le Bars* [2009] studied the sedimentation of spheres in a convective medium following the work of *Martin and Nokes* [1988, 1989]. They observed that the solid fraction remaining in suspension is a function of *Ra* and of the density ratio between particles and the fluid ($\Delta\rho/\rho_m$). Consequently, the number of particles N decreases as a function of time t as follows:

$$N(t) = \left(N_{t_{conv}} - N_{eq}\right) \exp\left[\frac{-v_s}{H}\left(t - t_{conv}\right)\right] + N_{eq} \qquad (13)$$

Where $N_{t_{conv}} = N(t = t_{conv})$ is the initial number of particles per cell (=38 particles/cell), t_{conv} is the time necessary to establish the temperature contrast inside the boundary layer, hence $t_{conv} = (H^2/\pi\,\kappa_m)(2Ra/Ra_c)^{2/3} \approx 10^4 s$. N_{eq} is a constant equilibrium value related to the number of particles when the statistical steady state is reached ($dN/dt = 0$), v_s is the Stokes velocity and H is the height of the system (470 m). The scaling law characterizing that equilibrium constant is written as $N_{eq} = \sigma(18\pi^2)(\kappa_m^2\nu_a\nu/H^4 g^2 d_p^2)(Ra/Ra_c)^{4/3}(\Delta\rho/\rho_m)^{-2}(S_{cell}/S_{crystal})$, where σ is a constant or "efficiency factor" of order 1, κ_m is the thermal diffusivity of the magma, ν_a is the apparent viscosity which depends on the kinematic viscosity of the mixture ν as $\nu_a \sim (Ra/Ra_c)^{0.06}\nu$, g is the gravitational constant, d_p is the crystal diameter (5×10^{-2} m), S_{cell} (0.25 m^2) and $S_{crystal}$ (2×10^{-3} m^2) are the surfaces of the cell and crystal, respectively. Thus, for $Ra/Ra_c = 6 \times 10^9$ and $\nu = 35.81$ m^2/s, $\nu_a = 137.8$ m^2/s. We applied equation (13) for a constant temperature (therefore at constant density and viscosity) and compared the results with those for our bi-phase simulation with a 10-m conduit (Figure 15a). Our data in closed system show that, after a sharp early decrease, the number of particles in suspension stabilizes around year 15 to reach a constant value of 8 particles per cell (~6 vol.%). This profile matches the theoretical prediction over the first year, after which the number of particles in suspension keeps decreasing slightly slower than for the theory where the plateau corresponds to 7 crystals per cell. This difference is partly explained by the fact that the experiments of *Lavorel and Le Bars* [2009] were conducted in a rectangular tank with set non-slip wall conditions, whereas we have set different boundary conditions. Another factor is that our geometry is more complex than a single

tank, which causes settling in the chamber and the lake to be affected by conduit circulation.

[70] Unlike the experiments of *Lavorel and Le Bars* [2009], the open system simulation has a permanent inlet/outlet of mass that limits comparison between our results and their theory. Our open-system simulation shows that most particles settle during the first 4 years to reach a plateau of 18 particles per cell from year 4 to 16 (Figure 15a). At the

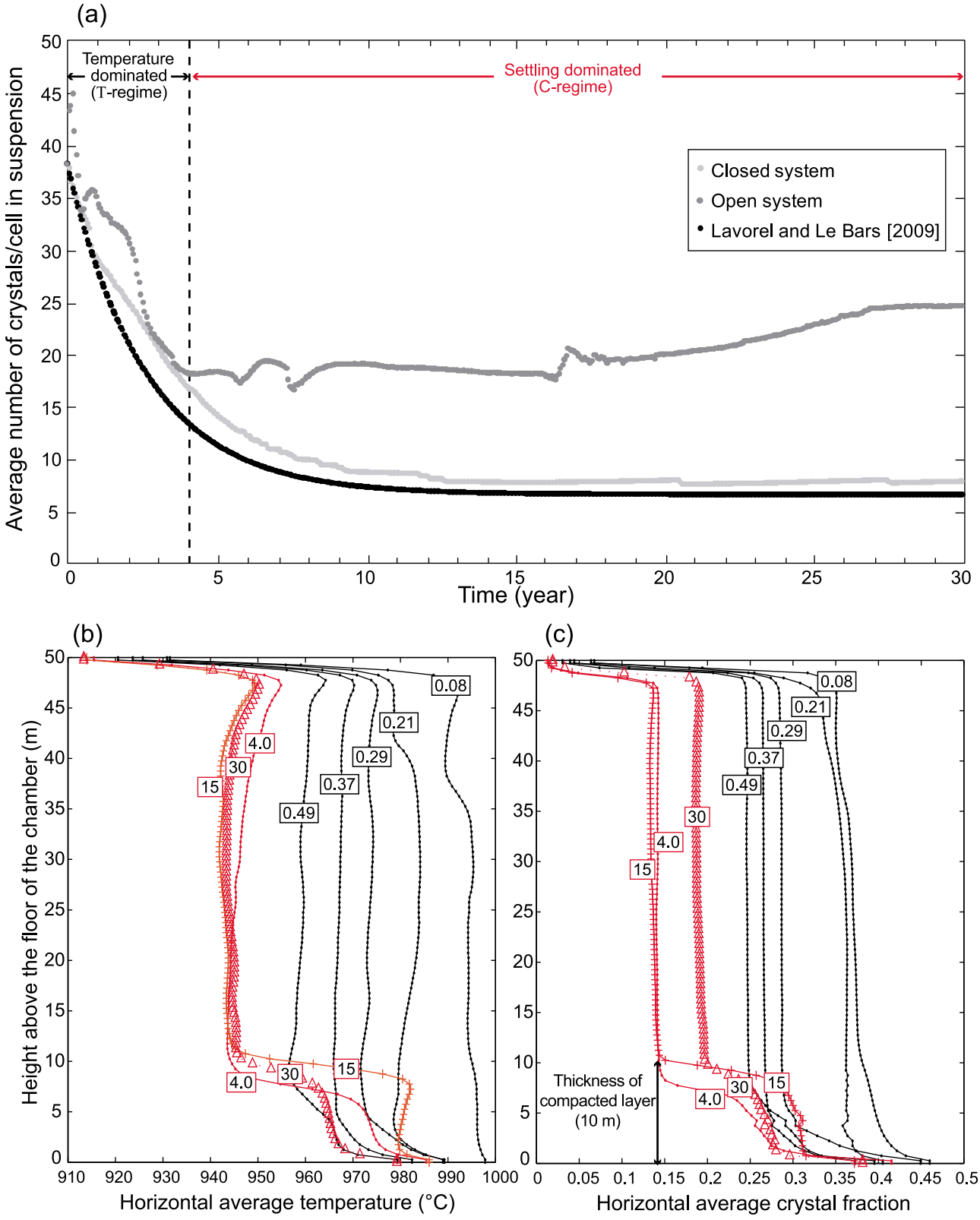

Figure 15

steady state (Figure 12a), a stepwise increase of suspended particles is noticeable after year 15 (Figure 15a). This is because a surge of temperature in the chamber around year 15 results in a delayed increase of the temperature in both the conduit and the lake until year 26, from which time it remains stable until year 30 (Figure 12a). This change in temperature is associated with a re-entrainment of suspended particles, the concentration of which increases until it reaches a new plateau at year 26 (Figure 15a). These variations, in turn, cause a velocity increase at the surface of the lake (Figure 14a).

[71] There is another way to understand crystal settling, which is mostly apparent in the open system simulation. Following the numerical study of crystals settling in convecting magma chambers by *Verhoeven and Schmalzl* [2009], and focusing on changes in temperature profiles and in particle concentrations in the chamber (Figures 15b and 15c), we differentiate two regimes of convection that affect the whole system (Figure 15a). These periods correspond to the unsteady and steady states that we determined for this simulation (Figure 12a). The thermal-dominated regime (T-regime) prevails up to year 4, a period over which crystals are mostly advected by the melt because the thermal driving force is strong enough to compete with gravitational settling forces. In this regime, the temperature and crystal content of the system decrease (Figures 12a and 15a) until particles have settled to form a ~10 m crystal-rich layer at the base of the chamber (Figures 15b and 15c). This regime then evolves into a settling-dominated regime (C-regime, from year 4 to 30), which is characterized by particle-driven convection that keeps the chamber segregated into two layers. The bottom layer is warm and mainly consists of crystals, whereas the top layer is colder and has fewer particles in suspension (Figures 15b and 15c). In the C-regime, most crystals are permanently held in suspension in the whole domain (Figure 15a). The thickness of the crystal-rich layer remains constant while the temperature sometimes displays a negative gradient across this layer (Figures 15b and 15c). This reflects the association of an increase of temperature in the crystal-rich region with an increase in crystal concentration. Such changes are similar to those described by *Verhoeven and Schmalzl* [2009].

[72] The bi-phase simulations show intricate convective patterns. Patterns change as short-lived, multicellular convection in the whole system during the initial unsteady phase that later merge progressively into two large cells, first in the lake after steady state has been reached (closed and open systems, Figures 11d, 11e, 11i, and 11j), and then in the chamber at a later stage (closed system, Figure 11o). A similar phenomenon is seen along the conduit where convective cells increase in size while decreasing in number. Crystals tend to remain with a given cell but their thermal history is likely to reflect rather complex trajectories when the number of convective cells changes. The richness of convective patterns produced by our simulations has counterparts in the literature. Our bi-phase simulations in either open or closed system reproduce the particle movement photographed by *Weinstein et al.* [1988] when steady state has been reached in the lava lake. In both studies, particle paths (streamlines) are nearly parallel at the center of the lake, traveling fastest when the flow is mostly vertical. *Weinstein et al.* [1988] have shown experimentally that, even after most particles have settled, some of them could be indefinitely retained in the laminar convecting viscous flow. Likewise, our simulations reach a steady crystal load once a balance between the carrying capacity of the convection currents and settling has been established. *Dufek and Bachmann* [2010] observed in numerical simulations that crystals accumulating on the floor of a crystallizing magmatic reservoir form a layer where melt extraction is most efficient. Unlike *Dufek and Bachmann* [2010], our open-system simulation does not take crystallization into account but shows a similar behavior, whereby small fluid-rich plumes rise through a crystal-rich layer at early times (Figure 11p) while thermal convection re-entrains crystals having reached the top of this layer (Figure 11t). In the conduit, our simulations generally show that convection is characterized by an annular or vertically stratified flow, as experimentally reproduced by *Beckett et al.* [2011]. In the early stages of the convection in open system and during most of the closed system simulation, our results show a sinusoidal pattern due to the contact between upwelling hot and less crystal-rich magma confined to the central axis of conduit and annular descending cold, denser and crystal-rich magma that partially adheres to the sidewall of the conduit. This pattern has been experimentally shown by *Huppert and Hallworth* [2007]. The convective interaction of the annular current with the magma chamber, leaking down from the lake through the conduit and returning from the chamber as a central ascending flow, was also observed in experiments with a similar geometry (two reservoirs connected by a duct) [*Bazarov et al.*, 2007]. This similarity explains why the structure of our convection currents is in good agreement with those described by *Bazarov et al.* [2007] for the overall magmatic system, except for the open-system simulation, which has a more complicated convective pattern.

[73] For a 4-m-diameter conduit and crystals as a separate phase, we observed that the tip of the central plume folds as it reaches the entrance of the conduit. Considering that the central plume has temperatures below that of glass transition and could therefore behave like a brittle solid, is this behavior realistic? Our assumption is that melt below 700°C behaves with a high (10^8 Pa s) but finite viscosity. Brittle behavior appears in a melt with such viscosity if it is strained faster than ~2 s^{-1} ($= \vartheta G/\mu_m$, with $\vartheta = 10^{-2}$ as experimental constant and shear modulus G = 25 GPa [*Webb and*

Figure 15. (a) Comparison between the theoretical evolution of the average number of crystals in suspension in a cell as a function of *Ra* (constant viscosity) at constant $\Delta\rho/\rho$ as per *Lavorel and Le Bars* [2009] and the concentration calculated by MFIX with both variable viscosity and $\Delta\rho/\rho$ in closed and open systems with 10-m-diameter conduit. The vertical dotted line separates two settling regimes. Most particles sink to the bottom of the chamber during the temperature-dominated regime, whereas during the settling-dominated regime, an approximate constant number of particles are held in suspension. (b) Horizontally averaged temperature profiles in the open-system chamber at different times (labels in years). (c) Horizontally averaged crystal fraction profiles in the open-system chamber at different times (labels in years). Black and red curves in Figures 15b and 15c enhance the thermal and settling dominated regimes, respectively.

Dingwell, 1990]). The glassy center of the instability is sheared at typical rates $\leq 10^{-6}$ s^{-1} (Figure 6d), which means that instability viscous folding is consistent with the capping of viscosity values. Glass transition occurs when strain rates exceed $\sim 10^{-6}$ s^{-1} for melt viscosities of 10^{14} Pa s, which correspond to 245°C [*Giordano et al.*, 2008]. Since such low temperatures are unlikely to be preserved very deep within a convecting lake, these considerations suggest that, to first order, our treatment of cold instabilities within the lake is realistic. *Loubet et al.* [2009] experimentally studied how a thin sheet of highly viscous corn syrup deforms when it falls vertically from a distance H through less viscous syrup onto an impermeable surface. They observed that, for a sheet/ambient viscosity ratio larger than 10 and $\Delta T > 300°$, the sheet undergoes a folding instability. For a calculated ΔT of 475° and a viscosity ratio around 10^4, MFIX reproduces this folding instability remarkably well. The corresponding scaling law for the folded sheet amplitude is $\delta = 0.41(||\mathbf{v}||_m/f)$ where f is the frequency at which the instability oscillates ($f = ||\mathbf{v}||_m/H$), and $||\mathbf{v}||_m$ is the velocity of the flow in the bent zone. Our simulation yields $||\mathbf{v}||_m = 2 \times 10^{-5}$ m/s for a lake depth of 20 m. Therefore $f = 10^{-6}$ cycles/s, which yields an instability amplitude δ of 8 m. This is the value we measured in the simulation (Figure A4).

[74] As expected, the result of some of our most restrictive assumptions, such as neglecting gas bubbles or crystallization, is to limit the range of agreement between our simulations and the natural system of Erebus. One of our motivations was to assess if thermal convection alone (without the added buoyancy of a gas phase) could prevent the lava lake from freezing. We found that a pure melt system would not freeze over 30 yr, regardless of conduit diameter. A lake containing crystals - be they treated as a separate phase or not - would see its average temperature reach the glass transition after 1 year if it is connected to the chamber by a narrow, 4-m-diameter conduit. A 10-m-diameter conduit, however, ensures that the average lake temperature remains above glass transition. Our results can be extrapolated to the natural systems qualitatively; they suggest that, given a wide enough conduit, the lake does not freeze and maintains live connection in presence of crystals. Another relevant result is that our 10-m conduit simulation in open system yields rather homogenous temperatures within the system. Such homogeneity is also observed at Erebus because the matrix glass composition, magmatic temperature (~1000°C) and oxygen fugacity are time-invariant in the lake based on geochemical analyses of matrix glass [*Kelly et al.*, 2008]. In the conduit of this simulation, the maximum temperature difference (56°C) between upwelling and downwelling magmas during the unsteady state, when there is still 30 vol.% crystals inside the conduit, is close to the value (65°C) reported by *Sweeney et al.* [2008] for the same crystal content. Our range of bulk viscosities (10^4 to 10^8 Pa s) for the shallower part of the magma system is consistent with the values reported by *Sweeney et al.* [2008] and the thickness (1.5 m) of the crust at the top of the lake given by our closed system is consistent with visual observations of a thin crust [*Oppenheimer et al.*, 2009].

[75] The velocities of the magma at the surface of the lava lake calculated by our bi-phase simulations with a 10-m-diameter conduit are on the order of 10^{-6} m/s in closed system and 10^{-5} m/s in open system, which is 10^5 and 10^4 times smaller, respectively, than surface speeds of the Erebus lava lake estimated by *Oppenheimer et al.* [2009]. The introduction of gas in our model would likely increase surface velocities by several orders of magnitude compared with the present simulations, which are controlled solely by crystal settling and thermal convection. A higher frequency of pulsation of these surface velocities can also be expected because gas motion will affect the distribution of surface temperatures, which will result in non-uniform surface velocities. The release of gas is also likely to increase the rate of crystallization; however the latent heat of crystallization would act as a buffer that would compensate the cooling induced by this release of gas to an extent that we have not quantified.

[76] We assumed that the Erebus system contained already formed crystals that are distributed homogeneously and in equilibrium with the melt at all times. Considering that the simulations started from an assumed constant crystallinity (30 vol.%), our simulations show that between 6 and 20 vol.% crystals remain in suspension, depending on whether the system is closed or open, respectively. Crystal content observed in phonolite lavas from summit (~30–40 vol.%) and lava bombs (~30 vol.%) [*Kelly et al.*, 2008] are the product of a thermal and pressure history inside the magma system. If those natural products are indicative of equilibrium conditions within the system, then our calculated values are below the observed amount of crystals and the differences are larger in closed system than in open system. This can be explained by the fact that closed system simulations compensate cooling-induced contraction by underestimating crystal content. A more quantitative assessment is difficult; one reason is that the extrapolation toward low pressures and low water content of existent phase equilibrium data on phonolitic magmas [*Andújar et al.*, 2008, 2010] is subject to caution, notably because the fluid composition (H_2O, F, Cl and Fe) may have a strong effect on the presence or absence of phases and their compositions. Crystallization may play an important role to fill the gap between our results and natural observations; however the theory developed by *Lavorel and Le Bars* [2009] and our simulation equally indicate that it will compete with particle settling and convective transport. Crystal sizes in Erebus lava suggest that crystallization at shallow levels occurs more by growth of pre-existing crystals than by addition of newly nucleated crystals. We thus anticipate that improved knowledge of low-pressure phonolite petrology and feldspar growth kinetics could bring crystallization laws that, once included in our simulations, may resolve these differences in crystal volume fraction. We nevertheless posit that the main observations and conclusions developed in this paper would remain largely unchanged for steady state simulations including crystallization.

[77] The unusually large crystal size at Erebus controls not only when convection changes from being thermally driven to being settling driven, but also how much of the crystal load remains in suspension. Crystals in other lava lakes, such as Nyiragongo [*Demant et al.*, 1994], Villarrica [*Witter et al.*, 2004] or Pu' u O' [*Garcia et al.*, 2000] are one to two orders of magnitude smaller in size. Their influence on the convective pattern is thus smaller than at Erebus. Assuming crystal sizes of 5 mm and using equation (13),

Erebus lava lake would have an initial value $N_{t_{conv}} = 3800$ but a value at equilibrium $N_{eq} = 66000$ particles/cell with an efficiency factor of one. Lowering N_{eq} to reach a solution where 100% of crystals would remain in suspension suppose a very low value of the efficiency factor ($\sigma = 10^{-2}$), far away from the order of 1 usually accepted for this constant. We instead simply suggest qualitatively that $N_{eq} > N_{t_{conv}}$ means that energy balance would be in favor of convective motions and that most 5 mm crystals would remain in suspension. We can thus infer that the convection within lava lakes bearing crystals $\ll$1 cm is quickly thermally dominated, and that crystal size is an important control of how crystal-rich the magma may remain, which, in turn, controls suspension rheology.

6. Conclusions

[78] We have studied the convective patterns beneath the surface of a lava lake by means of numerical simulations. The bi-phase, fluid dynamical model was validated by comparing the simulated structures of convective currents with those measured in the analogue experiment designed to represent cooling magma performed by *Jaupart and Brandeis* [1986]. Cooling generates Rayleigh-Taylor instabilities, the simulated motions of which are consistent to first order with those produced experimentally. The velocity at which the modeled plumes sink are in good agreement with that predicted by theoretical models and differs only within the bounds of experimental uncertainty from that seen in the experiment. At longer times, the temperature evolution in the well-mixed, central part of the tank is consistent with that observed in the experiments, though time shifted because of inevitable differences in initial conditions. The bi-phase capability of the numerical model was tested by calculating the bulk viscosity of a series of Poiseuille flow simulations with various amounts of particles. Results suggest that the model is applicable to a mixture of magmatic liquid and crystals as long as the crystal load is at or below close packing (65–67 vol.% crystals in this work).

[79] We applied the validated and verified model to an idealized Erebus magmatic system composed of a lava lake, a feeding conduit, and a magma chamber. Model parameterization was as close to the natural system as allowed by model assumptions. We tested the influence of conduit geometry, crystal load, and the nature of system boundaries on the convective regime. Overall, model outputs show that the steady state convective activity is sufficient to keep the magma above glass transition throughout a 30 yr period provided that the conduit diameter is large enough (10-m diameter), but regardless of whether the system is filled with a pure melt, a perfectly homogeneous mixture of magma with 30 vol.% crystals, or a bi-phase magma with an initial content of 30 vol.% crystals. If the conduit is narrow (4 m), the central viscous instability descending within the lake from the quenched surface chokes off the conduit and prevents hot fluid from ascending from the chamber, which slows down the whole convection rate. This phenomenon occurs at different times for the mixture and bi-phase simulations, but never for the pure melt because these simulations fail to reach steady state before the considered 30 years.

[80] Combining together crystals and melt into a virtual single-phase can reproduce some features of such systems, such as (i) the early formation of a central instability in the lake, (ii) the global temperature evolution and (iii) the order of magnitude of the average velocity range of the flow motion at the surface of the lake. The strength of the bi-phase approach, on the other hand, is to take crystal settling into account. For instance, a series of changing convective patterns are observed for bi-phase simulations throughout the simulated period. We found that conduit diameter strongly influences the circulation within the conduit itself. Overall, conduit- and system-wide patterns are in good agreement with different experiments and related numerical models. Our results show that all these emerging patterns can be gathered into a single framework. This very richness of behavior, however, poses a challenge to design numerical simulations with testable model outputs.

[81] Crystals are efficiently transported by the liquid phase but a small decoupling due to their large size (5 cm) causes settling. Compared to a crystal-free magma, their presence accelerates the convective rate and changes the convective regime, enhancing the effective heat transfer between lake and chamber. Thermal forces initially prevail and the suspended crystal content decreases following a power law until the particles accumulate in the magma chamber without being re-circulated in the whole system. A settling-driven convection then dominates, during which between 6 and 20 vol.% crystals remain in suspension, depending on whether the system is closed or open, respectively. Compared to closed-system simulations, an open system results in higher temperatures in the whole domain, higher convective rates (in both frequency and amplitude) at the surface of the lake, and a higher suspended crystal fraction, closer to the initial crystallinity. We observe a lasting crystal-rich layer of 10 m at the bottom of the chamber. Closed system simulations compensate cooling-induced contraction by underestimating crystal content. As a result, open system simulations should be more realistic than closed system ones because they correctly account for cooling-induced volume reduction.

[82] Our stringent assumptions lead to an idealized system with rich dynamics but that only poorly compares with natural observations. The average velocity at the lake surface is on the order of 10^{-6} m/s (closed system) and 10^{-5} m/s (open system). These simulated crystal loads and lake surface velocities in steady state are much lower than those observed at Erebus (30 vol.% and 10^{-1} m/s, respectively). The permanent release of gas at Erebus, unaccounted for in our simulations, is thus likely to contribute greatly in sustaining such a vigorous convection, preventing crystal settling and increasing the velocity of magma at the surface. We nevertheless estimate that the unusually large crystal size seen in Erebus phonolite controls not only when the convection changes from being thermally driven to being settling driven, but also how much of the crystal load remains in suspension. This is probably not true for other magmatic systems with much smaller crystals.

Appendix A

[83] The additional material in this appendix consists of (i) Table A1 listing the symbols used in this study, (ii) Figures A1 and A2 illustrating the evolution of the plumes height and the number of instabilities in the tank, respectively, and (iii) Figures A3 and A4 illustrating how we

Table A1. List of Subscripts, Superscripts, Latin and Greek Symbols, Operators and Abbreviations Most Commonly Used in This Work[a]

Symbol	Unit	Definition
		Subscripts[b]
av		Average
cold		Cold fluid
fwall		Far away from the wall
hot		Hot fluid
m		Melt
s		Solid
(*m*+*s*)		Melt plus solid phases or mixture
x, *y*		Coordinate along *x*(*y*)-direction
wall		Wall
		Superscripts
*		Dimensionless
max		Maximum value
p		Plastic regime
V		Viscous regime
		Latin
A, *B*, *C*	dimensionless	Compositional coefficients of viscosity (equation (11))
A_T	dimensionless	Atwood number
C_m	°C/m	Heat loss through the wall
C_p	J/kg °C	Heat capacity
D[c]	1/s	Rate-of-strain tensor
D_c	m	Conduit diameter
d_p	m	Crystal diameter
dx, *dy*	m	Cell (characteristic) length in *x*(*y*)-direction
e	dimensionless	Coefficient restitution
F_{ms}	kg/m^3 s	Drag factor between fluid and solid phases
f	s^{-1}	Frequency of folding instability
G	GPa	Shear modulus
$\mathbf{g}$	m/s^2	Gravity vector, *g* is the scalar constant
g_o	dimensionless	Radial distribution function at contact
H	m	Characteristic height of the system
h	m	Height of the plume envelope
h_c	m	Thickness of the conductive layer
I	dimensionless	Identity tensor
I_{2Ds}[d]	1/s^2	Second invariant of the deviator of the rate-of-strain tensor for solid phase; D_{s11}, D_{s22}, D_{s33}, D_{s12}, D_{s23}, D_{s31} are components of the rate-of-strain tensor for solid phase
k	J/m °C s	Thermal conductivity
M	kg	Mass of particle
N	dimensionless	Average number of crystals per cell in suspension
N_{eq}	dimensionless	Number of crystals per cell at equilibrium
$N_{t_{conv}}$	dimensionless	Number of crystals per cell when convective motions appear
Nu	dimensionless	Nusselt number
P	Pa	Pressure
Pr	dimensionless	Prandtl number
$\mathbf{q}$	J/m^2 s	Conductive heat flux vector
Ra	dimensionless	Rayleigh number, Ra_c is the critical Rayleigh number
Re	dimensionless	Reynolds number
S	Pa	Total stress tensor
S_{cell}	m^2	Cell surface
$S_{crystal}$	m^2	Crystal surface
T	°C	Thermodynamic temperature
T_o	°C	Initial thermodynamic temperature
T_f	°C	Plates' temperature in analogue experiment
T_g	°C	Glass transition temperature
T_{sig}	year	Period of a signal
t	s	Time
t_{conv}	s	Time at which convective motions appear
U, *V*	m/s	Scalar for horizontal (vertical) component velocity
V	m/s	Velocity vector, $\|\mathbf{v}\|$ is the magnitude of the velocity vector
V_l	m/s	Instantaneous particle velocity
V_r	dimensionless	The ratio of the terminal velocity of a group of particles to that of an isolated particle
v_s	m/s	Stokes velocity
x, *y*	m	Coordinate along *x*(*y*)-direction
		Greek
α	1/°C	Thermal expansion coefficient
β	dimensionless	Coefficient of growth of Rayleigh-Taylor instability
γ_{ms}	J/m^3 °C s	Heat transfer coefficient between fluid and solid phases
δ	m	Amplitude of folding instability
Δ	dimensionless	Global difference
ε	dimensionless	Volume fraction
ε^*	dimensionless	Packed-bed (minimum) void fraction
η	dimensionless	Intrinsic viscosity (reference viscosity)
Θ	m^2/s^2	Granular temperature
ϑ	dimensionless	Experimental constant
κ	m^2/s	Thermal diffusivity
K_1, K_2, K_3, K_4	kg/m^3, kg/m^2, kg/m^2, kg/m^4	Granular stress constants defined in equations (26)–(29)
λ	Pa s (kg/m s)	Second coefficient of solids viscosity
λ_c	m	Theoretical wavelength (equation (9))
λ_{obs}	m	Observed wavelength
μ	Pa s (kg/m s)	Molecular viscosity of the phase
ν	m^2/s	Kinematic viscosity of the phase
ν_a	m^2/s	Apparent viscosity of the phase
ξ	kg/s	Proportionality constant related to the drag forces exerted by the melt
ρ	kg/m^3	Macroscopic density
ρ_o	kg/m^3	Initial macroscopic density
$\rho_{(m+s)av}$	kg/m^3	Average bulk density resulting from cooling and settling
$\rho_{(m+s)_T}$	kg/m^3	Average bulk density resulting from cooling
σ	dimensionless	Constant of order 1 in equation (13)
$\boldsymbol{\tau}$	Pa	Viscous stress tensor
τ	s	Diffusive thermal scale
ϕ	degree	Angle of internal friction
		Operators
T		Transposed operation of matrices
tr[e]		Trace operation of tensor
		Abbreviations
BC[f]		Boundary condition
FSW		Free-slip wall
MI		Mass inlet
NSW		Non-slip wall
PI, PO		Pressure inlet/outlet
RT		Rayleigh-Taylor

[a]Specific values are cited in Tables 2 and 3.

[b]These subscripts can be associated to other subscripts specifying the phase.

[c]$\mathsf{D} = \frac{1}{2}\left[\nabla\mathbf{v} + (\nabla\mathbf{v})^{\mathrm{T}}\right]$.

[d]$I_{2Ds} = \frac{1}{6}\left[(D_{s11} - D_{s22})^2 + (D_{s22} - D_{s33})^2 + (D_{s33} - D_{s11})^2\right] + D_{s12}^2 + D_{s23}^2 + D_{s31}^2$.

[e]$tr(\mathsf{D}) = \nabla \cdot \mathbf{v}$.

[f]This abbreviation can be followed by a number indicating the geometrical position of a given geometrical configuration in a simulation.

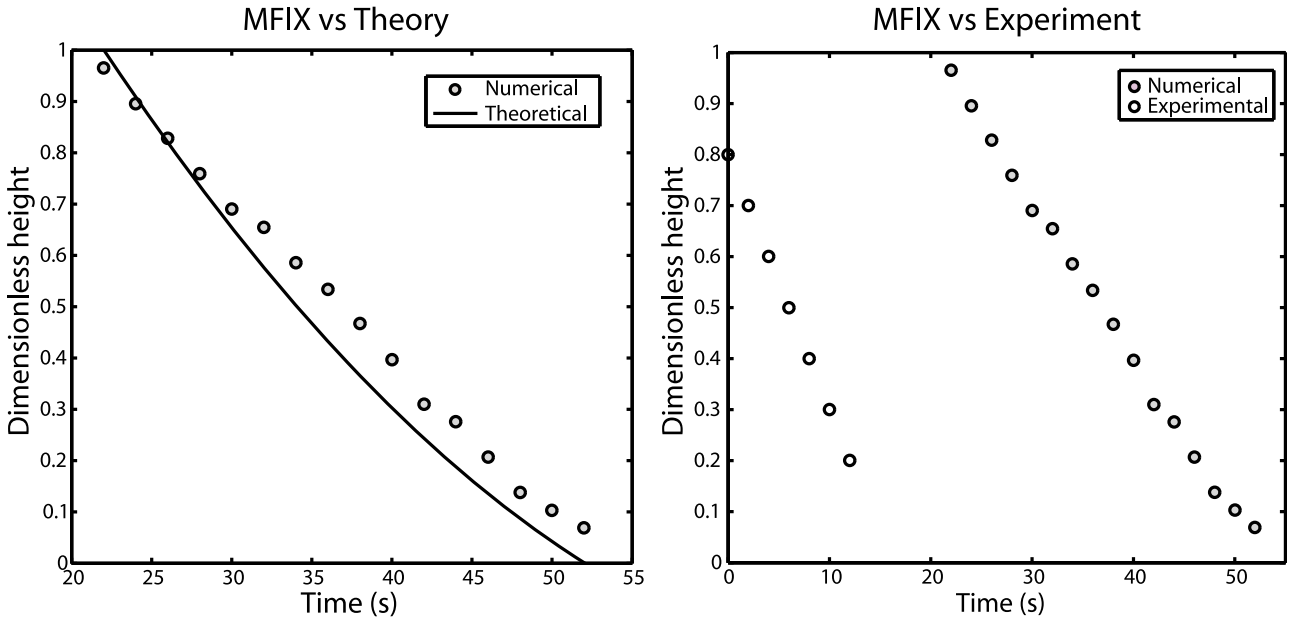

Figure A1. Dimensionless height of the plume cap versus time for the oil 47V20: (a) Gray circles represent our numerical results while the continuous black line is the theoretical curve based on *Read* [1984] and *Youngs* [1984] (equation (7)). (b) Open circles represent the results of the analogical experiment while gray circles represent our numerical results, both at early times. The height of the tank is 10 cm (1 in non-dimensional units).

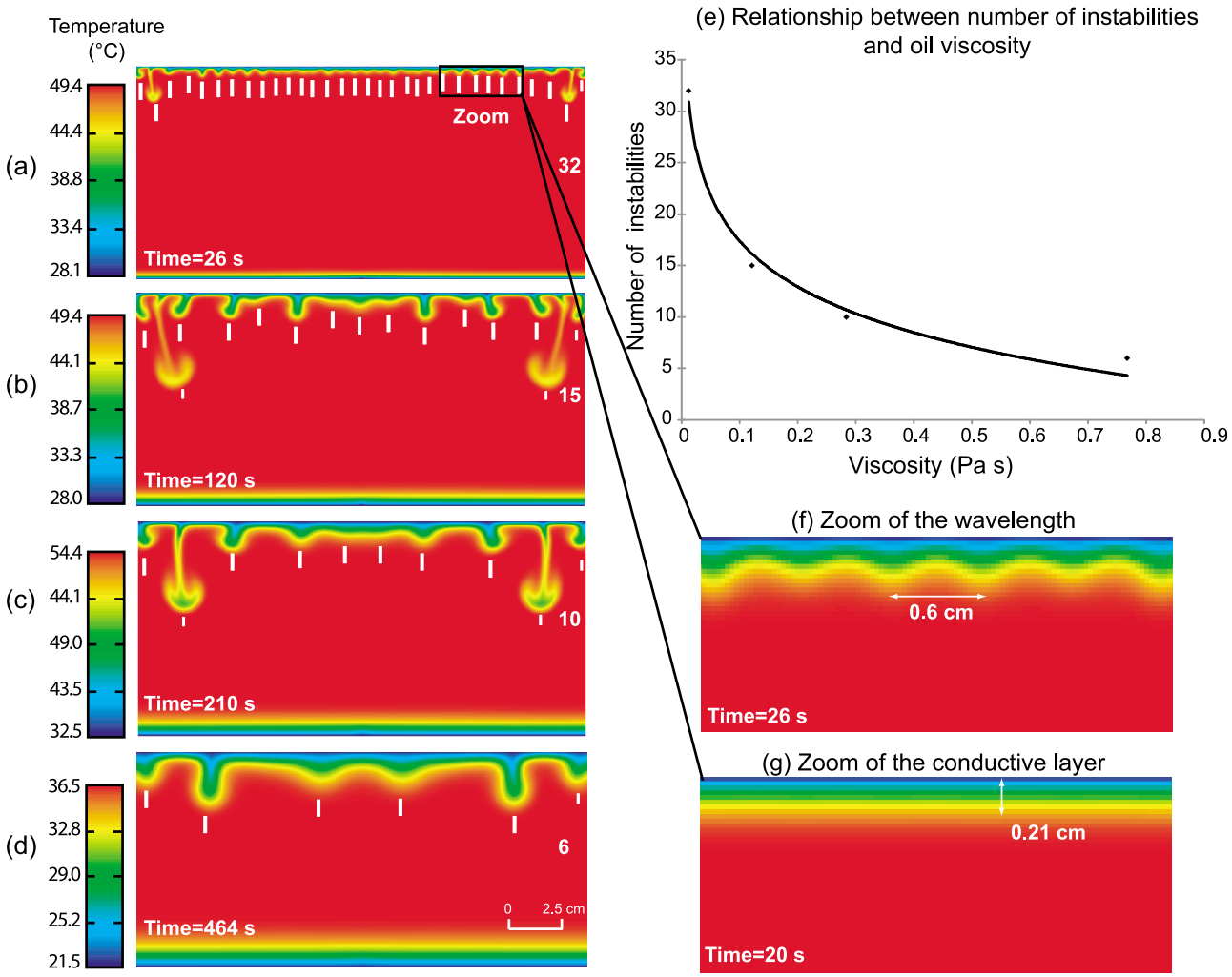

Figure A2. Temperature maps of the silicone tank simulations. Comparison of the number of instability fingers: (a and b) Experiment with oil 47V20 with a real viscosity of 0.012 and a modified viscosity of 0.12 Pa s, at times of 26 and 120 s, respectively. (c) Experiment with oil 47V500 and viscosity of 0.284 Pa s at 210 s. (d) Experiment with oil 47V1000 and viscosity of 0.767 Pa s at 464 s. (e) Relationship between number of instabilities and viscosity. (f) Magnified regions defined in a black square in Figure A2a showing the wavelength and (g) the thickness of the conductive region. The initial and boundary conditions of each experiment are indicated in Table 2a.

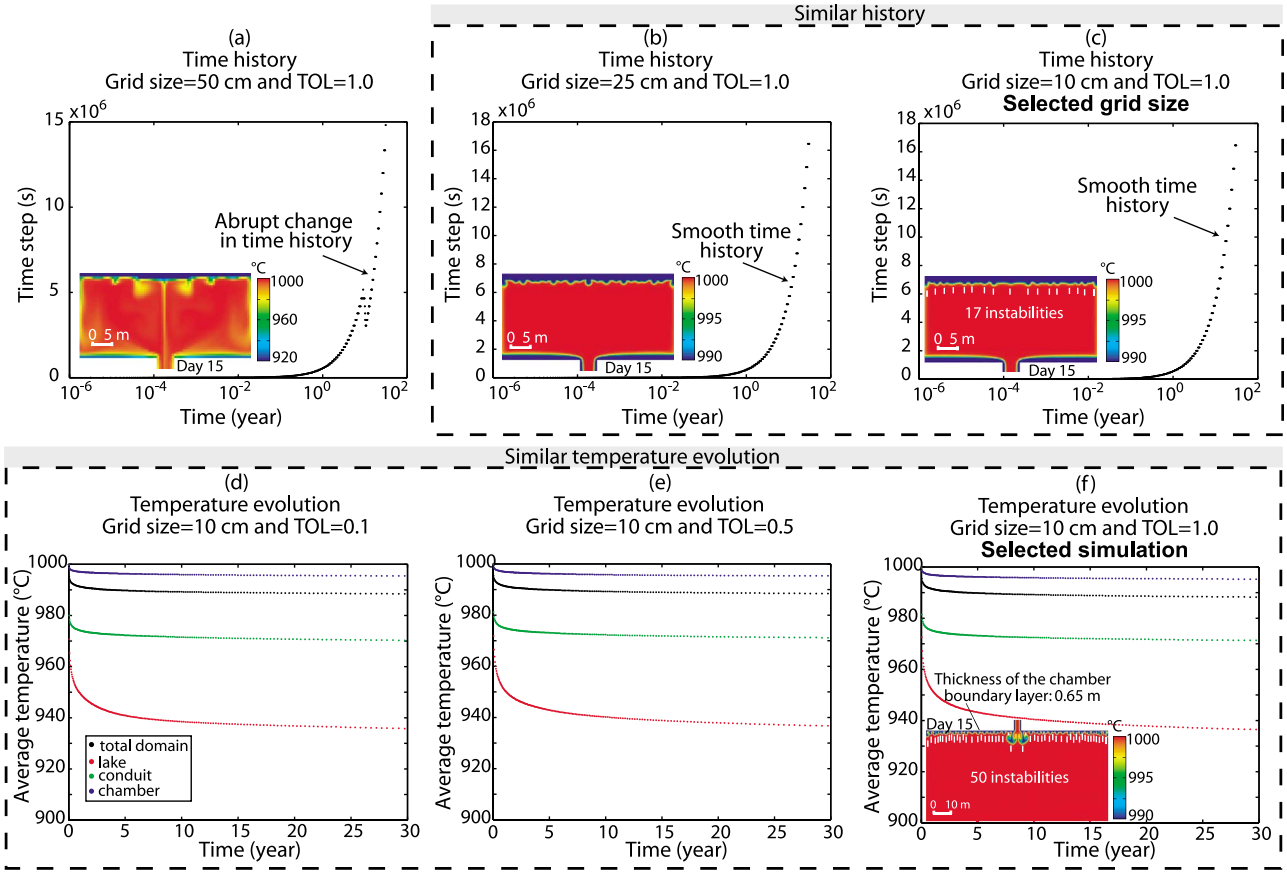

Figure A3. Evolution of the time step for simulations with pure melt in a 4-m diameter conduit for three grid sizes. (a) 50 × 50 cm^2 grid. (b) 25 × 25 cm^2 grid. (c) 10 × 10 cm^2 grid. Notice that the finer the grid size the better the Rayleigh-Taylor instabilities are defined for the lake (see the inset captions inside Figures A3a–A3c). The smooth history for grid sizes is clear for grid sizes of 25 × 25 cm^2 and 10 × 10 cm^2. (d–f) Evolution of the average temperature for 10 × 10 cm^2 grid with numerical tolerances of 0.1, 0.5 and 1.0, respectively. Inset caption in Figure A3f shows the number of instabilities for the chamber.

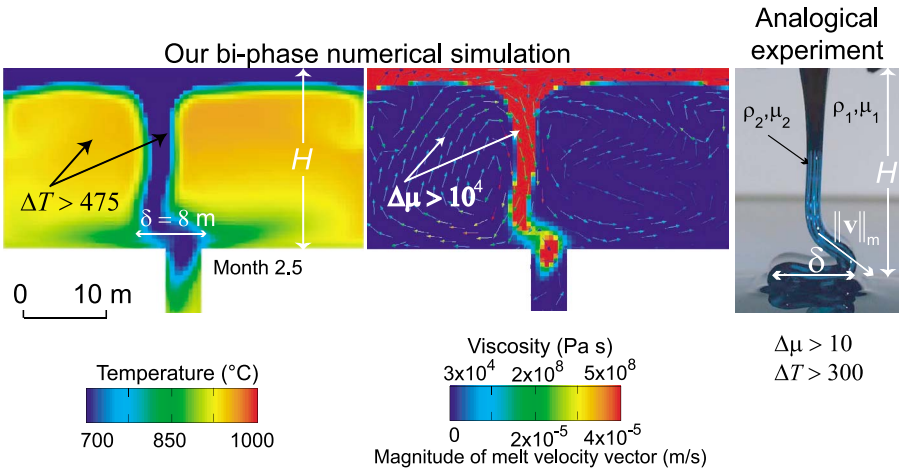

Figure A4. Illustration of our numerical simulation at month 2.5 for the simulation with crystals as a separated phase (4-m diameter conduit) and comparison with the analogue experiment of *Loubet et al.* [2009]. Notice that, both numerically and experimentally, the folding instability is produced when the contrast of temperature and viscosity is larger than 300 and 10, respectively ($\Delta T > 300$ and $\Delta\mu > 10$). H is the height at which instability falls (in our case 20 m), $||\mathbf{v}||_m$ is the downward velocity of the sheet where it enters in the folding region and δ is the amplitude of the folded instability.

selected the simulations and the comparison of instability behavior with an analogue experiment, respectively.

[84] **Acknowledgments.** This work represents part of the first author's thesis. We thank G. Brandeis and C. Jaupart for their comments on the way they conducted their experimental work and J. Andújar and M. Alletti for fruitful discussions concerning petrology. We are in debt to P. Ruprecht and two anonymous reviewers for their thorough revisions that improved the first version of the manuscript. We also thank the JGR editor, André Revil, for advice that led to further improvements of the manuscript. This work was partially funded by the ERC grant 202844 (DEMONS) under the European FP7. C. Oppenheimer additionally acknowledges support for research and monitoring of Erebus received via grants ANT-0538414, ANT-0838817 awarded by the Office of Polar Programs (National Science Foundation).

References

Andújar, J., F. Costa, J. Marti, J. A. Wolff, and M. R. Carroll (2008), Experimental constraints on pre-eruptive conditions of phonolitic magma from the caldera-forming El Abrigo eruption, Tenerife (Canary Islands), *Chem. Geol.*, *257*, 173–191, doi:10.1016/j.chemgeo.2008.08.012.

Andújar, J., F. Costa, and J. Martí (2010), Magma storage conditions of the last eruption of Teide volcano (Canary Islands, Spain), *Bull. Volcanol.*, *72*, 381–395, doi:10.1007/s00445-009-0325-3.

Anthony, J. W., R. A. Bideaux, K. W. Bladh, and M. C. Nichols (1995), Anorthoclase, in *Handbook of Mineralogy*, vol. II, *Silica, Silicates*, p. 34, Miner. Data Publ., Tucson, Ariz.

Aster, R., D. Zandomeneghi, S. Mah, S. McNamara, D. B. Henderson, H. Knox, and K. Jones (2008), Moment tensor inversion of very long period seismic signals from Strombolian eruptions of Erebus Volcano, *J. Volcanol. Geotherm. Res.*, *177*, 635–647, doi:10.1016/j.jvolgeores.2008.08.013.

Bazarov, L. S., V. I. Gordeeva, and E. I. Petrushin (2007), Specific structure of convection currents in the system layered intrusion–feeding conduit–parental magma chamber, *Russ. Geol. Geophys.*, *48*(12), 1037–1045, doi:10.1016/j.rgg.2007.11.003.

Beckett, F. M., H. M. Mader, J. C. Phillips, A. C. Rust, and F. Witham (2011), An experimental study of low-Reynolds-number exchange flow of two Newtonian fluids in a vertical pipe, *J. Fluid Mech.*, *682*, 652–670, doi:10.1017/jfm.2011.264.

Bizouard, H., F. Barberi, and J. Varet (1980), Mineralogy and petrology of Erta Ale and Boina volcanic series, Afar Rift, Ethiopia, *J. Petrol.*, *21*(2), 401–436, doi:10.1093/petrology/21.2.401.

Burgisser, A., G. W. Bergantz, and R. Breidenthal (2005), Addressing complexity in laboratory experiments: The scaling of dilute multiphase flows in magmatic systems, *J. Volcanol. Geotherm. Res.*, *141*, 245–265, doi:10.1016/j.jvolgeores.2004.11.001.

Calkins, J. A., C. Oppenheimer, and P. R. Kyle (2008), Ground-based thermal imaging of lava lakes at Mount Erebus Volcano, Antarctica in December 2004, *J. Volcanol. Geotherm. Res.*, *177*, 695–704, doi:10.1016/j.jvolgeores.2008.02.002.

Caricchi, L., L. Burlini, P. Ulmer, T. Gerya, M. Vassalli, and P. Papale (2007), Non-Newtonian rheology of crystal-bearing magmas and implications for magma ascent dynamics, *Earth Planet. Sci. Lett.*, *264*, 402–419, doi:10.1016/j.epsl.2007.09.032.

Chapman, S., and T. G. Cowling (1970), *The Mathematical Theory of Non-uniform Gases*, Cambridge Univ. Press, Cambridge, U. K.

Chouet, B., G. Saccorotti, M. Martini, P. Dawson, G. De Luca, G. Milana, and R. Scarpa (1997), Source and path effects in the wave fields of tremor and explosions at Stromboli Volcano, Italy, *J. Geophys. Res.*, *102*(B7), 15,129–15,150, doi:10.1029/97JB00953.

Clauser, C., and E. Huenges (1995), Thermal conductivity of rocks and minerals, in *Rock Physics and Phase Relations: A Handbook of Physical Constants*, *AGU Ref. Shelf Ser.*, vol. 3, edited by T. J. Ahrens, pp. 105–126, AGU, Washington, D. C., doi:10.1029/RF003p0105.

Costa, A. (2005), Viscosity of high crystal content melts: Dependence on solid fraction, *Geophys. Res. Lett.*, *32*, L22308, doi:10.1029/2005GL024303.

Costa, A., L. Caricchi, and N. Bagdassarov (2009), A model for the rheology of particle-bearing suspensions and partially molten rocks, *Geochem. Geophys. Geosyst.*, *10*, Q03010, doi:10.1029/2008GC002138.

Csatho, B., T. Schenk, P. Kyle, T. Wilson, and W. B. Krabill (2008), Airborne laser swath mapping of the summit of Erebus volcano, Antarctica: Applications to geological mapping of a volcano, *J. Volcanol. Geotherm. Res.*, *177*, 531–548, doi:10.1016/j.jvolgeores.2008.08.016.

Dartevelle, S. (2004), Numerical modeling of geophysical granular flows: 1. A comprehensive approach to granular rheologies and geophysical multiphase flows, *Geochem. Geophys. Geosyst.*, *5*, Q08003, doi:10.1029/2003GC000636.

Dartevelle, S., and G. A. Valentine (2007), Transient multiphase processes during the explosive eruption of basalt through a geothermal borehole (Námafjall, Iceland, 1977) and implications for natural volcanic flows, *Earth Planet. Sci. Lett.*, *262*, 363–384, doi:10.1016/j.epsl.2007.07.053.

Dartevelle, S., W. I. Rose, J. Stix, K. Kelfoun, and J. W. Vallance (2004), Numerical modeling of geophysical granular flows: 2. Computer simulations of plinian clouds and pyroclastic flows and surges, *Geochem. Geophys. Geosyst.*, *5*, Q08004, doi:10.1029/2003GC000637.

Demant, A., L. Patrick, T. L. Ruananza, A. B. Kampunzu, and J. Durieux (1994), Volcanological and petrological evolution of Nyiragongo volcano, Virunga volcanic field, Zaire, *Bull. Volcanol.*, *56*(1), 47–61, doi:10.1007/BF00279728.

Dibble, R. R., P. R. Kyle, and C. A. Rowe (2008), Video and seismic observations of Strombolian eruptions at Erebus volcano, Antarctica, *J. Volcanol. Geotherm. Res.*, *177*, 619–634, doi:10.1016/j.jvolgeores.2008.07.020.

Dimonte, G. (1999), Nonlinear evolution of the Rayleigh-Taylor and Richtmyer-Meshkov instabilities, *Phys. Plasmas*, *6*(5), 2009–2015, doi:10.1063/1.873491.

Dimonte, G., and M. Schneider (2000), Density ratio dependence of Rayleigh–Taylor mixing for sustained and impulsive acceleration histories, *Phys. Fluids*, *12*(2), 304–321, doi:10.1063/1.870309.

Ding, J., and D. Gidaspow (1990), A bubbling fluidization model using kinetic theory of granular flow, *AIChE J.*, *36*(4), 523–538, doi:10.1002/aic.690360404.

Dingwell, D. B., N. S. Bagdassarov, G. Y. Bussod, and S. L. Webb (1993), Magma rheology, in *Experiments at High Pressures and Application to the Earth's Mantle*, *Short Course Handb.*, vol. 21, edited by R. W. Luth, pp. 131–196, Mineral. Assoc. of Can., Nepean, Ont., Canada.

Dufek, J., and O. Bachmann (2010), Quantum magmatism: Magmatic compositional gaps generated by melt-crystal dynamics, *Geology*, *38*(8), 687–690, doi:10.1130/G30831.1.

Dufek, J., and G. W. Bergantz (2005), Transient two-dimensional dynamics in the upper conduit of a rhyolitic eruption: A comparison of closure models for the granular stress, *J. Volcanol. Geotherm. Res.*, *143*, 113–132, doi:10.1016/j.jvolgeores.2004.09.013.

Dunbar, N. W., K. V. Cashman, and R. Dupré (1994), Crystallization processes of anorthoclase phenocrysts in the Mount Erebus magmatic system: Evidence from crystal composition, crystal size distributions and volatile contents of melt inclusions, in *Volcanological and Environmental Studies of Mount Erebus, Antarctica*, edited by P. R. Kyle, *Antarct. Res. Ser.*, vol. 66, pp. 129–146, AGU, Washington, D. C., doi:10.1029/AR066p0129

Eschenbacher, A. (1998), Pre-eruptive volatile contents of fractionating, alkaline magma, Mount Erebus, Ross Island, M.S. thesis, Dep. of Earth and Environ. Sci., N. M. Inst. of Min. and Technol., Socorro.

Garcia, M. O., A. J. Pietruszka, J. M. Rhodes, and K. Swanson (2000), Magmatic processes during the prolonged Pu' u O' eruption of Kilauea Volcano, Hawaii, *J. Petrol.*, *41*(7), 967–990, doi:10.1093/petrology/41.7.967.

Ghiorso, M. S., and R. O. Sack (1995), Chemical mass transfer in magmatic processes. IV. A revised and internally consistent thermodynamic model for the interpolation and extrapolation of liquid-solid equilibria in magmatic systems at elevated temperatures and pressures, *Contrib. Mineral. Petrol.*, *119*(2–3), 197–212, doi:10.1007/BF00307281.

Giberti, G., C. Jaupart, and G. Sartoris (1992), Steady-state operation of Stromboli volcano, Italy: Constraints on the feeding system, *Bull. Volcanol.*, *54*(7), 535–541, doi:10.1007/BF00569938.

Giggenbach, W. F., P. R. Kyle, and G. L. Lyon (1973), Present volcanic activity on Mount Erebus, Ross Island, Antarctica, *Geology*, *1*(3), 135–136, doi:10.1130/0091-7613(1973)1<135:PVAOME>2.0.CO;2.

Giordano, D., A. R. L. Nichols, and D. B. Dingwell (2005), Glass transition temperatures of natural hydrous melts: A relationship with shear viscosity and implications for the welding process, *J. Volcanol. Geotherm. Res.*, *142*, 105–118, doi:10.1016/j.jvolgeores.2004.10.015.

Giordano, D., J. K. Russell, and D. B. Dingwell (2008), Viscosity of magmatic liquids: A model, *Earth Planet. Sci. Lett.*, *271*, 123–134, doi:10.1016/j.epsl.2008.03.038.

Huppert, H. E., and M. A. Hallworth (2007), Bi-directional flows in constrained systems, *J. Fluid Mech.*, *578*, 95–112, doi:10.1017/S0022112007004661.

Huppert, H. E., and R. S. J. Sparks (1988), The generation of granitic magmas by intrusion of basalt into continental crust, *J. Petrol.*, *29*(3), 599–624, doi:10.1093/petrology/29.3.599.

Jaupart, C., and G. Brandeis (1986), The stagnant bottom layer of convecting magma chambers, *Earth Planet. Sci. Lett.*, *80*, 183–199, doi:10.1016/0012-821X(86)90032-4.

Jaupart, C., and S. Vergniolle (1988), Laboratory models of Hawaiian and Strombolian eruptions, *Nature*, *331*, 58–60, doi:10.1038/331058a0.

Jaupart, C., G. Brandeis, and C. J. Allègre (1984), Stagnant layers at the bottom of convecting magma chambers, *Nature*, *308*, 535–538, doi:10.1038/308535a0.

Jellinek, A. M., and R. C. Kerr (2001), Magma dynamics, crystallization, and chemical differentiation of the 1959 Kilauea Iki lava lake, Hawaii, revisited, *J. Volcanol. Geotherm. Res.*, *110*, 235–263, doi:10.1016/S0377-0273(01)00212-8.

Jenkins, J. T., and S. B. Savage (1983), A theory for the rapid flow of identical, smooth, nearly elastic, spherical particles, *J. Fluid Mech.*, *130*, 187–202, doi:10.1017/S0022112083001044.

Johnson, P. C., and R. Jackson (1987), Frictional-collisional constitutive relations for granular materials with application to plane shearing, *J. Fluid Mech.*, *176*, 67–93, doi:10.1017/S0022112087000570.

Kelly, P. J., P. R. Kyle, N. W. Dunbar, and K. W. W. Sims (2008), Geochemistry and mineralogy of the phonolite lava lake, Erebus volcano, Antarctica: 1972–2004 and comparison with older lavas, *J. Volcanol. Geotherm. Res.*, *177*, 589–605, doi:10.1016/j.jvolgeores.2007.11.025.

Krieger, I. M., and T. J. Dougherty (1959), A mechanism for non-Newtonian flow in suspensions of rigid spheres, *Trans. Soc. Rheol.*, *3*, 137–152, doi:10.1122/1.548848.

Kyle, P. R., J. A. Moore, and M. F. Thirlwall (1992), Petrologic evolution of anorthoclase phonolite lavas at Mount Erebus, Ross Island, Antarctica, *J. Petrol.*, *33*, 849–875.

Laiolo, M., and C. Cigolini (2006), Mafic and ultramafic xenoliths in San Bartolo lava field: New insights on the ascent and storage of Stromboli magmas, *Bull. Volcanol.*, *68*(7–8), 653–670, doi:10.1007/s00445-005-0040-7.

Lavorel, G., and M. Le Bars (2009), Sedimentation of particles in vigorously convecting fluid, *Phys. Rev. E*, *80*, 046324, doi:10.1103/PhysRevE.80.046324.

Lister, J. R., and R. C. Kerr (1989), The effect of geometry on the gravitational instability of a buoyant region of viscous fluid, *J. Fluid Mech.*, *202*, 577–594, doi:10.1017/S0022112089001308.

Loubet, N., N. M. Ribe, and Y. Gamblin (2009), Deformation modes of subducted lithosphere at the core-mantle boundary: An experimental investigation, *Geochem. Geophys. Geosyst.*, *10*, Q10004, doi:10.1029/2009GC002492.

Lun, C. K. K., S. B. Savage, D. J. Jeffrey, and N. Chepurniy (1984), Kinetic theories for granular flow: Inelastic particles in Couette flow and slightly inelastic particles in a general flowfield, *J. Fluid Mech.*, *140*, 223–256, doi:10.1017/S0022112084000586.

Marsh, B. D. (1988), Crystal capture, sorting, and retention in convecting magma, *Geol. Soc. Am. Bull.*, *100*(11), 1720–1737, doi:10.1130/0016-7606(1988)100<1720:CCSARI>2.3.CO;2.

Martin, D. (1990), Crystal settling and in situ crystallization in aqueous solutions and magma chambers, *Earth Planet. Sci. Lett.*, *96*(3–4), 336–348, doi:10.1016/0012-821X(90)90011-L.

Martin, D., and R. Nokes (1988), Crystal settling in a vigorously convecting magma chamber, *Nature*, *332*, 534–536, doi:10.1038/332534a0.

Martin, D., and R. Nokes (1989), A fluid-dynamical study of crystal settling in convecting magmas, *J. Petrol.*, *30*(6), 1471–1500, doi:10.1093/petrology/30.6.1471.

Mastin, L., and M. Ghiorso (2000), A numerical program for steady-state flow of magma-gas mixtures through vertical eruptive conduits, *U.S. Geol. Surv. Open File Rep.*, *95-756*, 1–53.

McGeary, R. K. (1961), Mechanical packing of spherical particles, *J. Am. Ceram. Soc.*, *44*(10), 513–522, doi:10.1111/j.1151-2916.1961.tb13716.x.

Mueller, S., E. W. Llewellin, and H. M. Mader (2010), The rheology of suspensions of solid particles, *Proc. R. Soc. A*, *466*(2116), 1201–1228, doi:10.1098/rspa.2009.0445.

Murase, T., and A. R. McBirney (1973), Properties of some common igneous rocks and their melts at high temperature, *Geol. Soc. Am. Bull.*, *84*, 3563–3592, doi:10.1130/0016-7606(1973)84<3563:POSCIR>2.0.CO;2.

Navrosty, A. (1995), Thermodynamic properties of minerals, in *Mineral Physics and Cristallography: A Handbook of Physical Constants*, *AGU Ref. Shelf Ser.*, vol. 2, edited by T. J. Ahrens, pp. 18–28, AGU, Washington, D. C.

Odé, H. (1966), *Gravitational Instability of a Multi-Layered System of High Viscosity*, *Verh. K. Ned. Akad. Wet., Afd. Natuurkd.*, *24*, 96 pp.

Oppenheimer, C., and P. R. Kyle (2008), Volcanology of Erebus volcano, Antarctica, *J. Volcanol. Geotherm. Res.*, *177*, v–vii, doi:10.1016/j.jvolgeores.2008.10.006.

Oppenheimer, C., A. S. Lomakina, P. R. Kyle, N. G. Kingsbury, and M. Boichu (2009), Pulsatory magma supply to a phonolite lava lake, *Earth Planet. Sci. Lett.*, *284*, 392–398, doi:10.1016/j.epsl.2009.04.043.

Oppenheimer, C., R. Moretti, P. R. Kyle, A. Eschenbacher, J. B. Lowenstern, R. L. Hervig, and N. W. Dunbar (2011), Mantle to surface degassing of alkalic magmas at Erebus volcano, Antarctica, *Earth Planet. Sci. Lett.*, *306*(3–4), 261–271, doi:10.1016/j.epsl.2011.04.005.

Pabst, W., E. Gregorova, and C. Berthold (2006), Particle shape and suspension rheology of short-fiber systems, *J. Eur. Ceram. Soc.*, *26*, 149–160, doi:10.1016/j.jeurceramsoc.2004.10.016.

Picard, D., L. Arbaret, M. Pichavant, R. Champallier, and P. Launeau (2010), Rheology and microstructure of experimentally deformed plagioclase suspensions, *Geology*, *39*(8), 747–750, doi:10.1130/G32217.1.

Read, K. I. (1984), Numerical simulation of turbulent mixing by Rayleigh-Taylor instability, *Physica D*, *12*(1–3), 45–58, doi:10.1016/0167-2789(84)90513-X.

Reagan, M. K., A. M. Volpe, and K. V. Cashman (1992), ^{238}U- and ^{232}Th-series chronology of phonolite fractionation at Mount Erebus, Antarctica, *Geochim. Cosmochim. Acta*, *56*(3), 1401–1407, doi:10.1016/0016-7037(92)90071-P.

Ruprecht, P., G. W. Bergantz, and J. Dufek (2008), Modeling of gas-driven magmatic overturn: Tracking of phenocryst dispersal and gathering during magma mixing, *Geochem. Geophys. Geosyst.*, *9*, Q07017, doi:10.1029/2008GC002022.

Russell, J. K., and D. Giordano (2005), A model for silicate melt viscosity in the System $CaMgSi_2O_6$-$CaAl_2Si_2O_8$-$NaAlSi_3O_8$, *Geochim. Cosmochim. Acta*, *69*(22), 5333–5349, doi:10.1016/j.gca.2005.06.019.

Schaeffer, D. G. (1987), Instability in the evolution equations describing incompressible granular flow, *J. Differ. Equations*, *66*(1), 19–50, doi:10.1016/0022-0396(87)90038-6.

Seaman, S. J., M. D. Dyar, N. Marinkovic, and N. W. Dunbar (2006), An FTIR study of hydrogen in anorthoclase and associated melt inclusions, *Am. Mineral.*, *91*(1), 12–20, doi:10.2138/am.2006.1765.

Sims, K. W. W., J. Blichert-Toft, P. R. Kyle, S. Pichat, J. Bluzstajn, P. Kelly, L. Ball, and G. Layne (2008), A Sr, Nd, Hf, and Pb isotope perspective on the genesis and long-term evolution of alkaline magmas from Erebus volcano, Antarctica, *J. Volcanol. Geotherm. Res.*, *177*, 606–618, doi:10.1016/j.jvolgeores.2007.08.006.

Sparks, R. S. J., H. E. Huppert, and F. R. S. Turner (1984), The fluid dynamics of evolving magma chamber, *Philos. Trans. R. Soc. London, Ser. A*, *310*, 511–534, doi:10.1098/rsta.1984.0006.

Sparrow, E. M., R. B. Husar, and R. J. Goldstein (1970), Observations and other characteristics of thermals, *J. Fluid Mech.*, *41*, 793–800, doi:10.1017/S0022112070000927.

Sumner, C. L. K. (2007), Residence time estimates and controls on crystallization patterns for anothoclase phenocrysts on phonolite magma, Erebus Volcano, Antarctica, M.S. thesis, Dep. of Earth and Environ. Sci., N. M. Inst. of Min. and Technol., Socorro, N. M.

Sweeney, D., P. R. Kyle, and C. Oppenheimer (2008), Sulfur dioxide emissions and degassing behavior of Erebus volcano, Antarctica, *J. Volcanol. Geotherm. Res.*, *177*, 725–733, doi:10.1016/j.jvolgeores.2008.01.024.

Syamlal, M. (1994), MFIX documentation: User's manual, *Rep. DOE/METC-95/1013*, 87 pp., U.S. Dep. of Energy, Washington, D. C.

Syamlal, M. (1998), MFIX documentation: Numerical technique, *Rep. DOE/MC/31346-5824*, 80 pp., U.S. Dep. of Energy, Washington, D. C., doi:10.2172/656644.

Syamlal, M., W. Rogers, and T. J. O'Brien (1993), MFIX documentation: Theory guide, *Rep. DOE/METC-94/1004*, 49 pp., U.S. Dep. of Energy, Washington, D. C., doi:10.2172/10145548.

Turcotte, D. L., and G. Schubert (2002), *Geodynamics*, Cambridge Univ. Press, Cambridge, U. K.

Verhoeven, J., and J. Schmalzl (2009), A numerical method for investigating crystal settling in convecting magma chambers, *Geochem. Geophys. Geosyst.*, *10*, Q12007, doi:10.1029/2009GC002509.

Webb, S. L., and D. B. Dingwell (1990), The onset of non-Newtonian rheology of silicate melts. A fiber elongation study, *Phys. Chem. Miner.*, *17*(2), 125–132, doi:10.1007/BF00199663.

Webb, S., and R. Knoche (1996), The glass-transition, structural relaxation and shear viscosity of silicate melts, *Chem. Geol.*, *128*(1–4), 165–183, doi:10.1016/0009-2541(95)00171-9.

Weinstein, S. A., D. A. Yuen, and P. L. Olson (1988), Evolution of crystal-settling in magma-chamber convection, *Earth Planet. Sci. Lett.*, *87*, 237–248, doi:10.1016/0012-821X(88)90078-7.

Welch, P. D. (1967), The use of fast Fourier transform for the estimation of power spectra: A method based on time averaging over short, modified periodograms, *IEEE Trans. Audio Electroacoust.*, *15*(2), 70–73, doi:10.1109/TAU.1967.1161901.

Witter, J. B., V. C. Kress, P. Delmelle, and J. Stix (2004), Volatile degassing, petrology, and magma dynamics of the Villarrica Lava Lake, southern Chile, *J. Volcanol. Geotherm. Res.*, *134*, 303–337, doi:10.1016/j.jvolgeores.2004.03.002.

Worster, M. G., H. E. Huppert, and R. S. J. Sparks (1990), Convection and crystallization in magma cooled from above, *Earth Planet. Sci. Lett.*, *101*(1), 78–89, doi:10.1016/0012-821X(90)90126-I.

Youngs, D. L. (1984), Numerical simulation of turbulent mixing by Rayleigh-Taylor instability, *Physica D*, *12*(1–3), 32–44, doi:10.1016/0167-2789(84)90512-8.

Zoth, G., and R. Hänel (1988), Thermal conductivity, in *Handbook of Terrestrial Heat-Flow Density Determination*, edited by R. Hänel, L. Rybach, and L. Stegena, pp. 449–468, Kluwer Acad. Dordrecht, Netherlands, doi:10.1007/978-94-009-2847-3_10.

Chapitre III

Numerical simulation of the effusive regime in bubbles-bearing magmas: a case of the magmatic system at Erebus, Antarctica

Résumé

Le régime effusif sous lequel l'Erebus dégaze depuis des décennies n'a pas été expliqué par le biais de simulations numériques et sa compréhension représente un défi, même dans des cadres théoriques et expérimentaux. Sur l'Erebus, le régime effusif est caractérisé par une augmentation cyclique du flux de gaz, de la vitesse et du rayonnement de chaleur à la surface du lac. Dans une tentative d'explication de ce type de comportement effusif, nous avons étudié les phénomènes induits par la recharge permanente et constante d'un système de magma. Celui-ci est représenté sous la forme d'un système géométrique lac-conduit-chambre magmatique idéalisé en 2D. Notre simulation est effectuée sous des conditions non isothermes et le système de magma est rempli de deux phases distinctes: l'une dans laquelle les cristaux font partie du melt et l'autre dans laquelle des bulles de gaz riches en eau croissent à la fois par diffusion et par expansion. Le système de magma permet la libération d'un flux de gaz à travers la surface du lac.

Nos résultats montrent qu'un agglomérat de bulles s'élève à travers le conduit sous la forme d'un panache rapide composé d'une tête et d'une traîne, tandis que de minuscules bulles s'accumulent au plafond de la chambre magmatique. Lorsque la tête du panache entre dans le lac, il prend la forme d'un agglomérat de bulles en forme de nuage. Notre simulation numérique révèle que l'ascension qui s'ensuit dans le lac jusqu'à ce qu'elle atteigne finalement la surface du lac conduit à une augmentation de la vitesse et du flux d'eau. Cependant, ces valeurs de vitesse et de flux d'eau sous forme de gaz en surface sont encore 3 et 2 ordres de grandeur inférieurs aux valeurs observées.

Abstract

In an attempt to provide an explanation of the effusive behavior of the lava lake in Erebus, we investigated the phenomena induced by the permanent and constant recharge of a magma system. This one is represented through an idealized 2D geometry lake-conduit-chamber system. Our simulation is carried out under non-isothermal conditions and the magma system is filled with two distinct phases: one in which the crystals are part of the melt and the other in which water-rich gas bubbles grow both by diffusion and expansion. The magma system allows the release of a gas flux through a semi-permeable crust at the surface of the lake.

Our results show that a cluster of bubbles rises through the conduit as a rapid plume composed of a tail and a head, while tiny bubbles accumulates at the roof of chamber. When the head of the plume enters in the lake, it has the shape of cloud-like cluster of bubbles. Our numerical simulation shows that the further rise of the head through the lake until it eventually reaches the surface of the lake leads to an increase of the velocity and of the water flux. However, those values of velocity at the surface of the lake and water gas flux emitted are still 3-2 orders of magnitude, respectively smaller than the observed values.

1. Introduction

The geological deposits from Erebus show the effusive to explosive footprint of its activity [e.g., *Panter et al*., 2008; *Harpel et al*., 2008]. Since 1992, the effusive regime is characterized by a cyclic behavior producing gas emission rates that vary over minutes, hours, days and years [*Sweeney et al*. 2008]. The system is perturbed by sporadic explosions [e.g.,

Aster et al. 2008]. The effusive regime (sometimes called passive degassing) was reported to vary with a period of 10 min in 2004 and 2006 [e.g., *Sweeney et al*. 2008; *Boichu et al*. 2010; *Oppenheimer et al*. 2009, 2011;] and of 20 minutes in 2009 [*Oppenheimer et al*., in prep.] during which the lava lake level oscillates with no strombolian explosions during the period of their observations [*Oppenheimer et al*. 2009; *Boichu et al*. 2010]. The basic idea of this study is to capture the phenomenology that characterizes that effusive regime in terms of observable constrains (i.e., gas flux, surface velocities) estimated by *Oppenheimer et al*. [2009] without considering the rise of the lava lake.

The cyclic increase of gas flux, velocity and heat radiation [*Oppenheimer et al*., 2009] that seems to be coupled to the oscillating level of the lake surface [*Oppenheimer et al*., in prep.] that characterizes the effusive regime under which Erebus has been degassing for decades has not been explained by means of numerical simulations and its understanding represents a challenge. Experimental and theoretical studies performed by *Witham et al*. [2006a, 2006b] to explain the general oscillating behavior of any lake level suggest that fluctuations of the pressure at the base of the conduit are due to maximum lake height during refilling process. Their conclusions were issued assuming isothermal conditions and will not be considered herein.

Most models of conduit flows assume the magma as a single fluid (pseudo-fluid), in which the dispersed gas is perfectly coupled to the melt [e.g. *Jaupart*, 1996; *Wilson*, 1998; *Mastin and Ghiorso*, 2000], other models treat the gas as a separate phase [e.g. *Papale*, 1998; *Kozono and Koyaguchi*, 2010] but under the assumption of steady flux. Recent studies [e.g., *Llewellin et al*., 2002; *Llewellin and Manga*, 2005; *Dufek and Bergantz*, 2005; *Dartevelle and Vallentine*, 2007] have treated the gas of the magma as a separated phase under the assumption of time-dependent processes. Those models have provided ideas about specific process that link the effusive to eruptive regimes due to horizontal (through the conduit) or vertical gas loss (through the vent).

As demonstrated by *Molina et al*. [2012, under review], simulations of the Erebus system with the magma regarded as a mixture in which crystals are part of the melt retrieves similar

physical characteristics from unsteady-to-steady state (behaviour of Rayleigh-Taylor instabilities, average temperature in the lake and surface velocities, oscillating period) to the one in which magma is regarded as a bi-phase system (crystals as a separate phase) in a closed-system. In the present study, our model treats two distinct phases inside Erebus plumbing system: a mixture of magma (crystals as part of the melt) and bubbles as a separate phase that percolates through a permeable crust at the top of the lake, from which only the gas escapes (Figure 1). Our aim is to focus on the magma transient process towards the steady-state effusive regime that characterizes Erebus.

We focus on multiphase aspects not yet modeled previously and currently subject to debates in volcanology, which are abridged as follows:

(i) Is the multiphase model able to simulate the steady-state convection of a magma system regarded as a bi-phase flow composed of bubbles and magma mixture?

(ii) Are the outputs of the numerical model comparable with the real system?

(iii) Are bubbles the motor of the increase of convective rate in magma?

(iv) Are the bubbles traveling at the same velocity than the magma?

In this study, we will answer these questions as we progress in our investigation. At the moment, we are at stage (i) and started to answer the question (ii)-(iv).

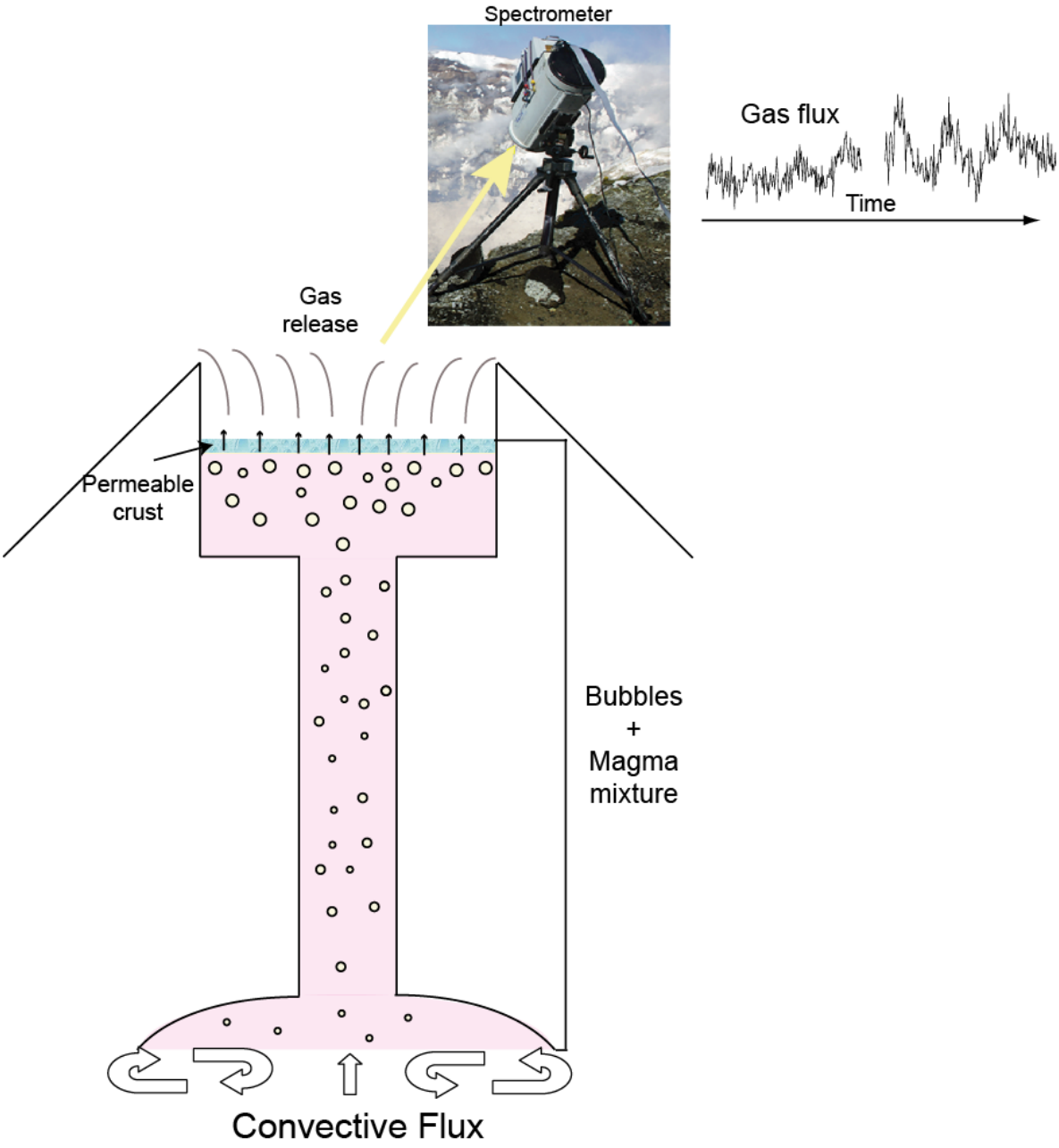

Figure 1. Sketch of the bi-phase region in Erebus: the top of the lake is a permeable crust from which only gas escapes. The released gases measured through a spectrometer show a cyclic behavior over periods of minutes [*Oppenheimer et al.*, 2009].

2. Fluid dynamical model

We used the Eulerian approach in order to model the continuous carrier phase (crystals are part of the melt) containing a dispersed phase composed of water-bearing bubbles. The carrier and dispersed phases then are treated as two interpenetrating continua so that the space occupied by one phase cannot be occupied by another at the same time. Briefly, the

hydrodynamic theory that we use is derived by the use of Reynolds Transport Theorem to principles of conservation of mass, momentum and energy to obtain the microscopic form of the conservation laws. If physical or chemical reactions are held in the system, the interphase mass transfer forms the components of the source terms in the different balance equations.

We have three fundamental assumptions for the gas phase:

(i) We neglected any form of the stress tensor within this phase.

The bubbles form an inviscid phase for which, in our model, we ignored the redistribution of momentum due to translational and binary collisions (see theory of the dense gases approach provided by *Chapman and Cowling* [1970]). This is because this theory is based on the assumption that all the particles in the system have the same diameter and the same density and collide inelastically [see the review performed by *Boyle and Massoudi*, 1989; *Gidaspow*, 1994], which is not our case. The plastic or frictional stress arising from soil mechanics theories [*Tuzun et al*., 1982; *Jackson*, 1983] was also ignored. This is because when bubbles reach a high concentration, they do not become quasi-frozen or immobile or will not try to arrange on an inclined plane under the effect of buoyancy. Furthermore, we also neglected a Newtonian form of the stress tensor of the gas phase (both the isotropic and the deviatoric components).

(ii) We assume that bubbles are composed of water.

The most common volatile content in the magma are H_2O, CO_2, S-species, F and Cl; however the dominant volatile in magmas is H_2O [*Baker et al*., 2005] and Erebus is no exception [Table 1 given by *Oppenheimer et al*., 2009]. We assume then that each bubble contains only H_2O and the surrounded melt has both dissolved water too and a fixed content of crystals (30 vol.%).

(iii) Bubble growth by expansion and diffusivity and spherical bubble shape.

Each bubble is considered a non rigid sphere that grows by diffusion under equilibrium conditions (Henry's law) and expansion; however in this study we are concentrated in studying the advection of a swarm of bubbles and therefore coalescence was ignored. In

reality, bubbles will try to coalesce if their surface tension allows. It implies that bubbles are treated as growing spheres, one assumption neglected in the case of magma chamber modeling [e.g. *Ruprecht et al*., 2008]. The spherical shape is a likely geometry for the bubbles under low capillary number [*Namiki and Manga*, 2006].

The numerical code that we used to solve the equations is MFIX Ver. 2.0, 2004 (Multiphase Flow with Interphase eXchanges) and the approach that we used to modify the equations of this model has been laid out by *Molina et al*. [2012]. The conservation equations are linearized and solved using linear equation solving techniques. A more detailed account of the equations used and discretization methods can be found in the Theory and Numerical Technique guides for MFIX [*Syamlal et al*., 1993; *Syamlal*, 1994, 1998].

2.1. Governing equations

The basic transport equations are reported in Table 1 and the nomenclature is summarized in Table A1. A positive sign convention is adopted throughout this study, which means that stresses are positive when both the outward normal and force act in the same sense relative to the coordinate system *x* and *y*, or East and up, respectively. The constitutive terms of each equation are written in terms of the local volume averaged variable for each phase, where ε, ρ, $\mathbf{v}$, *t*, *R*, *X* and *Y* pertain to the volumetric fraction, microscopic density, velocity vector, time, rate of production/consumption and mass fractions. The sub index $(m+s)$ and g characterize the mixture and gas phase, respectively. The gas phase is assumed to be contained in spherical bubbles, whose diameter varies as a function of gas volume fraction and number of bubbles in a given volume [*Gidaspow*, 1994]. We assume only one type of bubbles containing only water.

The carrier phase density $\rho_{(m+s)}$ is modeled as an incompressible flow as stated by *Molina et al*. [2012]:

$$\rho_{(m+s)} = \begin{cases} \varepsilon_s\rho_s + \varepsilon_m\left\{\rho_o\left[1-\alpha\left(T_m - T_o\right)\right]\right\} & \text{if} \quad T_m > T_g \\ \varepsilon_s\rho_s + \varepsilon_m\left\{\rho_o\left[1-\alpha\left(T_g - T_o\right)\right]\right\} & \text{if} \quad T_m < T_g \end{cases} \tag{1}$$

Where ε_m is the liquid fraction, ε_s and ρ_s are the fraction and density of the crystals (assumed to be constant), T_m is the temperature of the mixture, T_o is the initial temperature, T_g is the glass transition temperature [*Molina et al.*, 2012], ρ_o and α are the density and thermal expansion coefficient of the mixture at initial temperature.

The dispersed phase is modeled as an ideal gas:

$$\rho_g = \frac{P_g M_g}{G T_g} \tag{2}$$

Where P_g is the gas pressure, T_g is the temperature of the gas, G is the universal gas constant and M_g is the molar mass of the gas phase. In practice the gas pressure in equation (2) is the same as the ambient pressure $P_{(m+s)}$ and this constitutive relationship was set up through the scalar transport of gas volume fraction that will be explained later.

The magma is composed of two species: a dry silicate melt containing crystals as a passive tracers $Y_{(m+s)}$ and the dissolved water $X_{(m+s)}$ (Figure 2a). We have assumed a phase change from liquid to gas of the species H_2O. Bubbles are assumed spherical and non-deforming. They neither touch each other, aggregate nor coalesce, and therefore their surface forces were neglected. They contain only water as a gas and thus $X_g = 1$ because there is only one species in the gas phase. Continuity involves that the sum of the volume and species fractions in a control volume (CV) is always equals to one ($\varepsilon_{(m+s)} + \varepsilon_g = 1; X_{(m+s)} + Y_{(m+s)} = 1$). All 'T' equation numbers refer to Table 1. Thus, the left hand side (LHS) of equations (T1) and (T2) account for the rate of mass and net rate of mass outflow through the averaging volume in the CV for the mixture and gas phases, respectively. The right hand side (RHS) term accounts for the rate of mass transfer in the phase because of chemical reactions or physical process such as exsolution/dissolution of H_2O in our case (Figure 2b).

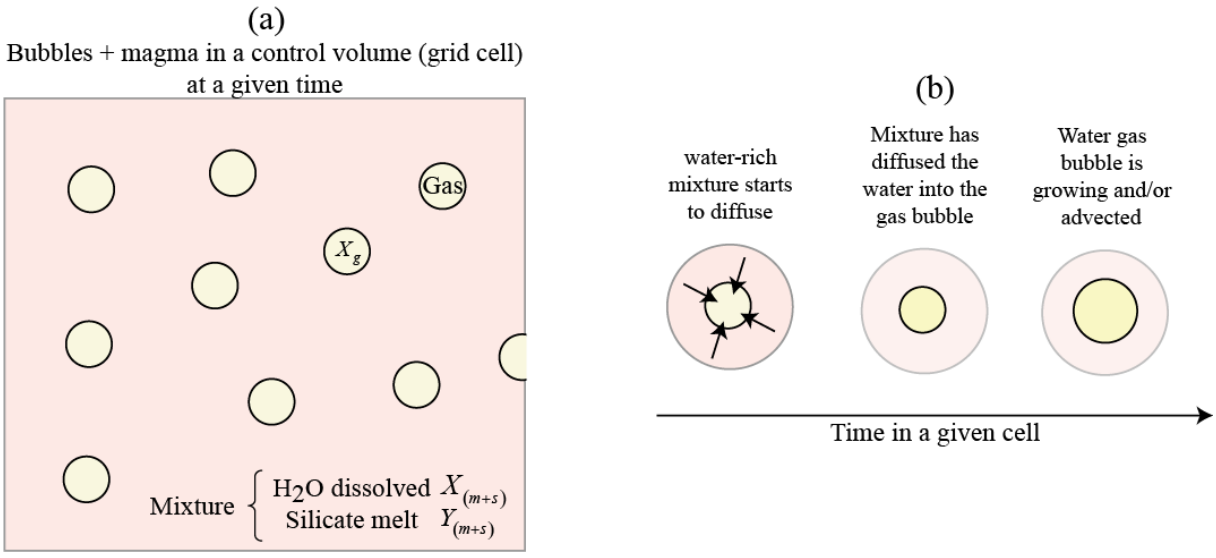

Figure 2. Schematic representation of the bi-phase flow containing a wet silicate melt and water bubbles: (a) in a control volume, (b) example of diffusion process with time in a given cell.

In the momentum equations, the first term on the LHS in equations (T3) and (T4) represents the net rate of momentum variation within a volume and the second term is the net rate of momentum transferred by convection into that volume. The RHS (from left to right) in equation (T4) accounts for: (i) the surface forces or the interaction within the phase accounted for as the stress tensor (normal and shear stress components) per unit volume, (ii) the interaction forces between the mixture and the gas phases due to drag, and (iii) the body forces are only accounted for in terms of the weight of the mixture. In equation (T4) the RHS from left to right shows that the surface forces were set to zero because bubbles do not impinge each other and do not collide, besides the deviatoric component depending on the viscosity of the gas would be negligible because the gas viscosity is 9 orders of magnitude lower than the viscosity of the magma mixture. Although the isotropic component may contribute, we didn't take it into account on this expression; thus the terms (i), (ii) are the interaction forces between the fluid and gas phases due to buoyancy (pressure gradient acting upon the bubbles) and drag forces, respectively; (iii) and (iv) are the body forces accounting for the weight of the gas and the fluid flow resistance due to porous media, respectively. This flow resistance is only for the upper part of the system as we will detail in the following section.

The formulation of the stress tensor for the mixture (equations (T5) and (T6)) follows a Newtonian form and the drag coefficient (equation (T7)) was assumed to be as *Joshi* [2001]. With this drag we have neglected the virtual mass term because bubbles have vanishing small accelerations relative to the melt. The LHS of energy equations (T8) and (T9) indicates that the net rate of change of temperature within a grid cell is equal to the sum of the work resulting from the RHS: (i) heat conduction within the phase and (ii) the heat transfer between phases. In this study we have neglected the viscous dissipation, the work due to drag forces and the rate of heat generation due to reaction. Equations (T10) to (T15) define the factors relevant to (i) and (ii). The MFIX code contains mass transfer source terms due to substraction of continuity equations from conservative form of equations (T3) and (T4) [*Benyahia et al*., 2008].

The species conservation is written in equations (T16) and (T17). The above equations consider the expansion, convection, consumption or formation of gas phase. The rate of formation of water is described below.

2.1.1. Volatile exsolution model

We incorporated in MFIX one physical process involving the mass fraction of H_2O dissolved in the melt, $X_{(m+s)}$, and the mass of H_2O exsolved from the melt –that is, the fraction found in bubbles, X_g:

$$\varepsilon_{(m+s)}\rho_{(m+s)}X_{(m+s)} \rightleftarrows \varepsilon_g \rho_g X_g \tag{4}$$

The rate of formation of H_2O, $R_{(m+s)}$, in the RHS of equations (T1), (T2), (T16) and (T17) is defined as follows:

$$R_{(m+s)} = -R_g = \varepsilon_{(m+s)}\rho_{(m+s)}\frac{\partial X_{(m+s)}}{\partial t} \tag{5}$$

Where $\frac{\partial X_{(m+s)}}{\partial t}$ is the volume fraction of water exsolved in one time step is a given cell.

The mass transfer of H_2O from the mixture to the bubbles was modeled by a sub-grid model of bubble growth solving the following equation of diffusion (Appendix 1).

$$\frac{\partial X_{(m+s)}}{\partial t} = \frac{1}{r^2}\frac{\partial}{\partial r}\left(r^2 D_{H_2O} \frac{\partial X_{(m+s)}}{\partial r} \right) \quad (6)$$

Where the water diffusivity D_{H_2O} was calculated using an expression found by *Freda et al*. [2003] as follows:

$$D_{H_2O} = \exp\left[-11.924 - 1.003 \ln\left(X_{(m+s)} \right) \right] \exp\left\{ \frac{-\exp\left[11.836 - 0.139 \ln\left(X_{(m+s)} \right) \right]}{RT_{(m+s)}} \right\} \quad (7)$$

The previous equation is based on experimental values for potassium-rich, trachytic melt at 1 GPa, 1100-1400°C and 0.25-2 wt.% H_2O.

Table 1. General transport equations of the physical model with bubbles

Continuity

Melt and crystals

$$\frac{\partial}{\partial t}\left(\varepsilon_{(m+s)}\rho_{(m+s)}\right)+\nabla\cdot\left(\varepsilon_{(m+s)}\rho_{(m+s)}\mathbf{v}_{(m+s)}\right)=R_{(m+s)} \quad \text{T1}$$

Gas

$$\frac{\partial}{\partial t}\left(\varepsilon_g\rho_g\right)+\nabla\cdot\left(\varepsilon_g\rho_g\mathbf{v}_g\right)=R_g \quad \text{T2}$$

Momentum

Melt and crystals

$$\frac{\partial}{\partial t}\left(\varepsilon_{(m+s)}\rho_{(m+s)}\mathbf{v}_{(m+s)}\right)+\nabla\cdot\left(\varepsilon_{(m+s)}\rho_{(m+s)}\mathbf{v}_{(m+s)}\mathbf{v}_{(m+s)}\right)=\nabla\cdot\mathbf{S}_{(m+s)}+F_{(m+s)g}+\varepsilon_{(m+s)}\rho_{(m+s)}\mathbf{g} \quad \text{T3}$$

Gas

$$\frac{\partial}{\partial t}\left(\varepsilon_g\rho_g\mathbf{v}_g\right)+\nabla\cdot\left(\varepsilon_g\rho_g\mathbf{v}_g\mathbf{v}_g\right)=-\varepsilon_g\nabla P_{(m+s)}-F_{(m+s)g}+\varepsilon_g\rho_g\mathbf{g}+\mathbf{f}_g \quad \text{T4}$$

Stress Tensor for the melt

$$\mathbf{S}_{(m+s)}=-P_{(m+s)}\mathbf{I}+\boldsymbol{\tau}_{(m+s)} \quad \text{T5}$$

$$\boldsymbol{\tau}_{(m+s)}=2\varepsilon_{(m+s)}\mu_{(m+s)}\mathbf{D}_{(m+s)}-\frac{2}{3}\varepsilon_{(m+s)}\mu_{(m+s)}tr\left(\mathbf{D}_{(m+s)}\right)\mathbf{I} \quad \text{T6}$$

Momentum Interface Transfer Coefficient

$$F_{(m+s)g}=\varepsilon_{(m+s)}\left(\rho_g-\rho_{(m+s)}\right)\left(1-\nabla P_{(m+s)}\right)-\varepsilon_g\rho_{(m+s)}\mathbf{D}_{(m+s)}\left|\mathbf{v}_g-\mathbf{v}_{(m+s)}\right| \quad \text{T7}$$

Energy

Melt and crystals

$$\varepsilon_{(m+s)}\rho_{(m+s)}C_{p(m+s)}\left(\frac{\partial T_{(m+s)}}{\partial t}+\mathbf{v}_{(m+s)}\cdot\nabla T_{(m+s)}\right)=-\nabla\cdot\mathbf{q}_{(m+s)}+\gamma_{(m+s)g}\left(T_g-T_{(m+s)}\right) \quad \text{T8}$$

Gas

$$\varepsilon_g\rho_gC_{pg}\left(\frac{\partial T_g}{\partial t}+\mathbf{v}_g\cdot\nabla T_g\right)=-\nabla\cdot\mathbf{q}_g-\gamma_{(m+s)g}\left(T_g-T_{(m+s)}\right) \quad \text{T9}$$

Heat conductivity

Melt conductivity

$$\mathbf{q}_{(m+s)}=\varepsilon_{(m+s)}k_{(m+s)}\nabla T_{(m+s)} \quad \text{T10}$$

Granular conductivity

$$\mathbf{q}_s=\varepsilon_gk_g\nabla T_g \quad \text{T11}$$

Heat Interface Transfer Coefficient

T12	T13	T14	T15
Coefficient	Nusselt Number	Prandtl Number	Reynolds number
$\gamma_{(m+s)g}=f\left(k_{(m+s)},\varepsilon_g,Nu,d_b\right)$	$Nu=f\left(\varepsilon_g,\varepsilon_{(m+s)},Re_g,Pr\right)$	$Pr=f\left(C_{p(m+s)},\mu_{(m+s)},k_{(m+s)}\right)$	$Re_g=f\left(d_b,\rho_{(m+s)},\mu_{(m+s)},\mathbf{v}_g,\mathbf{v}_{(m+s)}\right)$

Species balance

Dissolved water

$$\frac{\partial}{\partial t}\left(\varepsilon_{(m+s)}\rho_{(m+s)}X_{(m+s)}\right)+\nabla\cdot\left(\varepsilon_{(m+s)}\rho_{(m+s)}\mathbf{v}_{(m+s)}X_{(m+s)}\right)=R_{(m+s)} \quad \text{T16}$$

Dry melt plus crystals

$$\frac{\partial}{\partial t}\left(\varepsilon_{(m+s)}\rho_{(m+s)}Y_{(m+s)}\right)+\nabla\cdot\left(\varepsilon_{(m+s)}\rho_{(m+s)}\mathbf{v}_{(m+s)}Y_{(m+s)}\right)=0 \quad \text{T17}$$

2.1.3. Sub-grid model for the expansion of the bubbles

An example of fluid simulation domain in MFIX consists of a two-dimensional rectangular system with the origin of the *x*- and *y*- axis in the bottom left corner (Figure 3a). Every grid cell or CV contains a certain amount of bubbles (Figure 3b) whose properties (i.e., volume fraction, macroscopic bulk density, microscopic density) need to be defined in a sub-grid model (Figure 3b-c) because of the geometry of the dispersed phase (i.e., spherical) and the nature of the problem (i.e., bubbles grow by compressibility and mass diffusion).

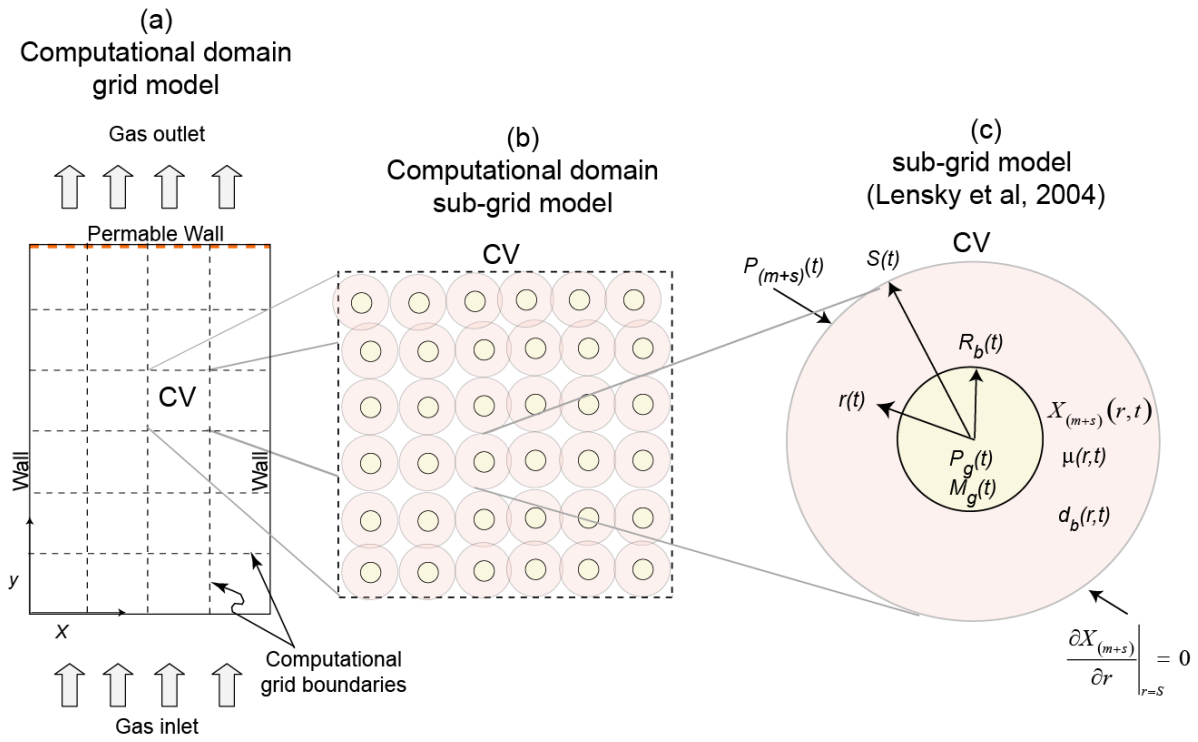

Figure 3. Sketch of grid and sub-grid models: (a) example of computational domain in which the gas inlet boundary coincide with the boundary of a computational cell. The boundary between the gas outlet and the bed is represented by a semi-permeable wall (dotted red line), (b) CV containing a magma with spherical bubbles of gas, (c) spherical bubble of gas surrounded by a spherical shell of melt (details in Appendix 2).

In equation (2), we have defined that the dispersed phase suffers density change; this density is called "microscopic", ρ_g. Since MFIX treats the density of the dispersed phase, ρ_g, as a weighted macroscopic bulk density, ρ_g, in a CV:

$$\rho_g = \varepsilon_g \rho_g \tag{8}$$

Introducing this term, ρ_g, into the first term of the LHS equation (T3) yields the following development:

$$\frac{\partial}{\partial t}\left(\rho_g\right) = \varepsilon_g \frac{\partial \rho_g}{\partial t} + \rho_g \frac{\partial \varepsilon_g}{\partial t} \tag{9}$$

As a result, the resolution implemented in MFIX cannot take into account the definition stipulated in equation (2) because ε_g and ρ_g cannot vary independently and freely with time. Our objective is to split equation (9) into two independent equations: an equation that relates the microscopic and macroscopic densities defined in equation (9), and a scalar transport equation that relates the changes in sub-grid gas volume fraction with time, $\dot{\varepsilon}_g$ and consequently the macroscopic gas volume fraction, ε_g. The transport of the amount ε_g is defined as follows:

$$\frac{\partial}{\partial t}\left(\varepsilon_g\right) + \nabla \cdot \left(\mathbf{v}_g \varepsilon_g\right) = \dot{\varepsilon}_g \tag{10}$$

We used the pre-defined scalar transport equation implemented in MFIX. This transport equation, however, was designed to advect a scalar characteristic of one of the phases. It contains the source term for the production / consumption of that phase, and the scalar is weighted by the volume fraction of that phase. Taking ϕ as a scalar advected by the gas phase, this yields (as *Syamlal* [1998]; pag. 15):

$$\frac{\partial}{\partial t}\left(\rho_g \phi\right) + \nabla \cdot \left(\rho_g \mathbf{v}_g \phi\right) = R_g + R_\phi \tag{11}$$

Where R_ϕ is the production rate of ϕ. Since we set $\phi = \varepsilon_g$ and $R_\phi = \varepsilon_g$, the resolution that was carried out was not the intended equation (10), but was:

$$\frac{\partial}{\partial t}\left(\rho_g \varepsilon_g\right) + \nabla \cdot \left(\rho_g \mathbf{v}_g \varepsilon_g\right) = R_g + \dot{\varepsilon}_g \tag{12}$$

Using (12) instead of (10) causes ε_g to increase more rapidly because of the additional source term R_g. This effect is somewhat dampered by solving the transport of ε_g^2 instead of ε_g (on the LHS of (12). The simulation presented in the results section was carried out solving (12). While its results are quantitatively incorrect, preliminary runs using (10) suggest that the sequence of degassing and convective events is qualitatively correct.

We followed the model from *Lensky et al*. [2004] in order to calculate the bubble growth by expansion, d_b, in a CV. After simplification of this model (details in Appendix 2) we have:

$$P_g = P_{(m+s)} + \frac{4\sigma}{d_b} + \frac{4\dot{d}_b}{d_b}\mu_{(m+s)}\left(1-\varepsilon_g\right) \tag{13}$$

Where $P_{(m+s)}$ is the ambient pressure, P_g the pressure inside the bubble, d_b is the diameter of the bubble, σ is the surface tension and the term $\mu_{(m+s)}\left(1-\varepsilon_g\right)$ accounts for the effective viscosity that resists bubble expansion.

Since gas density, ρ_g, is related to gas pressure, P_g, through the equation of state mentioned in equation (2), we can equate that P_g with the one obtained in the previous equation:

$$\rho_g \frac{GT}{M_g} = P_{(m+s)} + \frac{4\sigma}{d_b} + \frac{4\dot{d}_b}{d_b}\mu_{(m+s)}\left(1-\varepsilon_g\right) \tag{14}$$

In which the viscosity of the mixture $\mu_{(m+s)}$ is obtained by using the adjustable Newtonian model given by *Giordano et al*., [2008] modified with a fixed content of crystals as *Krieger and Dougherty* [1959]:

$$\mu_{(m+s)} = \begin{cases} \left[10\exp\left(A+\frac{B}{T_m-C}\right)\right]\left[1-\frac{\varepsilon_s}{1-\varepsilon_m^*}\right]^{-[\eta]\left(1-\varepsilon_m^*\right)} & if \quad T_m > T_g \\ \left[10\exp\left(A+\frac{B}{T_g-C}\right)\right]\left[1-\frac{\varepsilon_s}{1-\varepsilon_m^*}\right]^{-[\eta]\left(1-\varepsilon_m^*\right)} & if \quad T_m < T_g \end{cases} \tag{15}$$

Where ε_s is the crystal fraction, ε_m^* is the minimum void fraction at maximum packing of particles, η is the Einstein coefficient, and A, B and C are coefficients to calculate the "contribution" of the melt viscosity (details on how the coefficients B and C were calculated as a function of water content can be seen in Appendix 3). Viscosity will increase as water exsolves into the bubbles.

In order to relate gas volume fraction, ε_g, to bubble size in a cell, d_b, we define the number of bubbles per cell, per mixture, and per time step, N_b, as:

$$N_b = \frac{\varepsilon_g}{1-\varepsilon_g}\left(\frac{\pi}{6}d_b^3\right)^{-1} \tag{16}$$

Since there is neither coalescence nor nucleation, N_b is constant.

Algebraic manipulations yield expressions for bubble diameter and its derivative:

$$\dot{d}_b = \frac{1}{3}\left(\frac{\pi}{6} d_b^3\right)^{-1} \left(\frac{1-\varepsilon_g}{\varepsilon_g}\right)^{-4/3} \frac{\dot{\varepsilon}_g}{\varepsilon_g^2} \tag{17}$$

Now, we insert the above definitions of $\dot{d}_b$ and d_b, and ρ_g given equation (9) into equation (11) and after algebraic simplification we obtain:

$$\frac{\rho_g}{\varepsilon_g}\frac{GT}{M_g} = P_{(m+s)} + \frac{4\sigma}{d_b} + \frac{4}{3}\frac{\dot{\varepsilon}_g}{\varepsilon_g}\mu_{(m+s)} \tag{18}$$

And therefore we obtain the bubble growth as a function of time, $\dot{\varepsilon}_g$, as follows:

$$\dot{\varepsilon}_g = \frac{3}{4}\frac{\varepsilon_g}{\mu_{(m+s)}}\left(\frac{\rho_g}{\varepsilon_g}\frac{GT}{M_g} - P_{(m+s)} - \frac{4\sigma}{d_b}\right) \tag{19}$$

Thus we obtain the Lagrangian, sub-grid description of the evolution of the porosity that can be used in equations (10) and (12):

$$\dot{\varepsilon}_g = \frac{\partial}{\partial t}\left(\varepsilon_g\right) + \nabla \cdot \left(\varepsilon_g \mathbf{v}_g\right) = \frac{3}{4}\frac{\varepsilon_g}{\mu_{(m+s)}}\left(\frac{\rho_g}{\varepsilon_g}\frac{GT}{M_g} - P_{(m+s)} - \frac{4\sigma}{d_b}\right) \quad (20)$$

3. Erebus simulations

3.1 Physical parameters of the natural system

Erebus volcano, located in Antarctica, host one of the most active lava lake in the world informally called Ray's lake. Mineralogical studies performed by *Kelly et al.* [2008] determined its phonolitic composition based on major oxides (Table A2) and a volume of crystals of 30 vol.%. Melt inclusions trapped in the crystals record homogenization temperatures around 1000°C [*Dunbar et al*., 1994], while recent studies based on geochemistry of degassing point out that temperatures can reach between 1069 and 1085°C [*Burgisser et al*., in review]. The water contents of anorthoclase-hosted inclusions range from 0.12 to 0.39 wt.% [*Seaman et al*., 2006] and recent studies indicate that water content in those inclusions can reach values of 0.5 wt.% [*Oppenheimmer et al*., 2011]. The density of the phonolite is in the order of 2400 kg/m^3 [*Eschenbacher*, 1998].

Csatho et al. [2008] used airborne laser scanning (lidar) and *Calkins et al.* [2008] used thermal infrared images to estimate the lake surface area as ~770-1400 m^2 and its diameter as ~30-40 m in the period from around 2001–2004. However, the lake level does vary over time with corresponding changes in surface area [*Calkins et al.*, 2008]. In 2009, for instance, the lake area increased to 2500 m^2 [*Oppenheimer et al.*, 2011, in prep.]. Indeed the lake experiences cyclic changes in surface velocities (in the order of 10^{-1} m/s) that seem to be related to geochemical oscillations [*Oppenheimer et al*. 2009] and change of height [*Oppenheimer et al.*, 2011, in prep.]. Geochemical oscillations observed in 2004 show a mean period of 10 min [*Sweeney et al*. 2008; *Oppenheimer et al.*, 2009] ; these oscillations period increases up to 20 min in 2009 [*Oppenheimer et al.*, 2011, in prep.]. Representative compositions of the plume emitted by the lake indicate that H_2O and CO_2 are the main components of the gas [*Oppenheimer et al.*, 2009;*Burgisser et al*., in review]. The water flux release is in the order of 9 kg/s [Table 1 from *Oppenheimer et al*., 2009]. *Sweeney et al*. [2008] explains that open system degassing and convection is a more likely model to explain degassing variability, while *Oppenheimer et al*. [2009] suggests that those oscillations are attributed to the surging of magma flow in the uppermost conduit.

Observation reported the lake to be ~20 m deep [*Oppenheimer et al.,* 2009] and numerical studies indicate that the conduit has a diameter of at least 10 m [*Molina et al.,* 2012]. *Kyle et al.* [1992] suggested that the continuous activity at this large alkaline phonolitic volcano implies a deep source of melt rising through a narrow vertical conduit. *Aster et al.* [2008] based on the localization of seismic signals related to gas slug indicates the presence of a kink in the magmatic plumbing system at around 400 m. This depth coincides with the growth of crystals between depths as shallow as 400 m and the surface [*Dunbar et al.,* 1994]. Recent studies based on melt inclusion bearing CO_2 and water suggests entrapment depths corresponding to pressures of up to 300 MPa [*Oppenheimer et al.,* 2011]. Field observations and videos of the lava lake reveal that hot lava reaching the surface of the lake is rapidly cooled on contact with air, resulting in a thin crust beneath which molten lava keeps convecting [*Oppenheimer et al.,* 2009]. *Molina et al.* [2012] suggest that this crust reaches glass transition at temperatures of 700°C.

Since density differences between the upwelling and downwelling magma drive convection [e.g., *Kazahaya et al.,* 1994], heat flux can be used to determine temperature differences (ΔT) between the upwelling and downwelling magma. For instance, *Sweeney et al.* [2008] and *Calkins et al.* [2008] reported, for a crystal content of 30 vol.%, a minimum contrast of temperature between upwelling and downwelling magma must exist in the range of 65 to 200°C in order to sustain the heat output in the lava lake. The maximum contrast in temperature found by *Molina et al.* [2012] was of 56°C. *Sweeney et al.* [2008] take the radiative output and the total sulfur mass flux emitted by the lake to calculate ΔT, while *Calkins et al.* [2008] consider the convective and radiative heat flux, the crystallized fraction neglecting, as *Molina et al.* [2012], the contribution of bubbles.

Mineralogical and isotopical studies performed by *Kelly et al.* [2008] and *Sims et al.* [2008], respectively, indicate that Erebus is in steady-state and that either the system has been without significant crystallization, magma intrusion and mixing, or the mixing of batches of parental basanite with different isotopic compositions is extremely efficient.

3.2. Idealized magmatic system

The information given in the previous section allowed us to idealize the Erebus magma system. This is represented through an idealized 2D geometry (within the *x-y* plane) lake-

conduit-magma chamber (Figure 4). The lake has been set as being 40 m long and 20 m deep. The conduit diameter was fixed to 10-m. Based on the studies performed by *Aster et al.* [2008] plus the depth of crystal formation [*Dunbar et al.*, 1994], we fixed the magma chamber to 400 m deep. Since we do not know the dimension of this chamber, we fixed it in such a way that it is larger than the lava lake, 100 m wide and 50 m deep.

Our simulation is performed under non-isothermal and open system conditions. The magma system is filled by two phases: one phase -the carrier- in which 30 vol.% of crystals are part of the melt and another phase -the dispersed one- in which water-rich gas bubbles grow both by diffusion and expansion. The open system condition allows the release of a gas flux through a crust - semi-permeable to the gas - at the top of the lake. The flow resistance offered by this porous internal surface is calculated from the formula:

$$\mathbf{f}_g = -\frac{\mu_g}{C_1}\mathbf{v}_g \tag{21}$$

Where μ_g and $\mathbf{v}_g$ are the gas viscosity and filtration velocity of the gas through the porous boundary, respectively; C_1 is the Darcian permeability coefficient of the porous media to the gas. As it can be noticed, we have neglected the inertial permeability coefficient (see details in Chapter 4) and we consider only the vertical component of $\mathbf{v}_g$, that we call V_g. Values of μ_g, C_1 and V_g are defined in Table 2.

The initial conditions are a uniform temperature of 1000°C and null velocity for the two phases (gas and mixture). The pressure for the whole magmatic system is initially magma-static (mechanical pressure). We assumed different initial conditions (IC) for four regions of the magma system: chamber (IC1), conduit (IC2), lake (IC3) and top of the lake (IC4). The difference between those IC concerns the volume fraction of bubbles and temperature (Table 3). The mass fraction of dissolved H_2O in the mixture initially is given through the Henry's law relation:

$$X_{(m+s)} = k_H \sqrt{P_g} \quad (22)$$

Where k_H is an experimental constant based on solubility data for Erebus phonolite [*Burgisser et al. in review*] and P_g is the pressure inside the bubble, in MPa.

The thermal boundary conditions (BC) were set for all phases so that the system is heated from below (BC1 = 1000°C) by a magma chamber, and cooled from above through the lava lake surface (BC8 = 0°C) (Figure 4). All phases were kept at 1000°C on the reservoir sides (BC2 and BC3) and the vertical walls of the conduit (BC4 and BC5) and lava lake (BC6 and BC7) were set so that the heat flux through the walls would be of reduced intensity: in the case of conduit $C_m = -10^{-8}$°C/m and in the case of lava lake $C_m = -2$°C/m (details of C_m value can be seen in equation (4) from *Molina et al*. [2012]). The bottom of the magma chamber (BC1) was set as free-slip walls (FSW), while the sidewall boundary BC2 was set as inlet of a bi-phase flow with a volumetric bubble concentration of 5 vol.%, a phase-weighted horizontal speed of 2.3×10^{-5} m/s at a pressure of 11 MPa. The sidewall boundaries (BC3-7) were non-slip walls (NSW), while the top of the lava lake (BC8) is an outlet boundary with a constant pressure equal to atmospheric (0.1 MPa).

We calculated the initial density ρ_o, the thermal expansion α and the heat capacity $C_{p(m+s)}$ of the mixture with Conflow [*Mastin and Ghiorso*, 2000] and the thermal conductivity of the phonolite, k_m, using the relationship given by *Zoth and Hänel* [1988] (details of this calculation are given by *Molina et al*. [2012]). Surface tension, σ, was taken from literature for a phonolitic composition. Properties of the gas phase such as heat capacity, C_{pg}, thermal conductivity, k_g, and molar mass of water M_g were extracted from the literature (Table 2). All these parameters remain constant in our calculations. Based on the mean of the major element concentrations of matrix glass separated from lava bombs [*Kelly et al., 2008*] (Table A2) plus the water content calculated through our simulation, we have calculated the coefficients B and C (details in Appendix A3) from the viscosity relationship given by *Giordano et al*. [2008] (equation 13).

Table 2. Physical parameters

	Gas				Mixture		
Parameter	**Units**	**Symbol**	**Value**	**Reference**	**Symbol**	**Value**	**Reference**
Density	Kg/m^3	ρ_g	NA	[(a)] Output from Model	ρ_o	2455	[(b)] Output from Conflow
Thermal conductivity	W/ m °C	k_g	0.14	*Ochkov* [2009]	k_m	1.53	*Clauser and Huenges* [1995]
Heat capacity	J/kg °C	C_{pg}	0.14	*Ochkov* [2009]	$C_{p(m+s)}$	1367	[(b)] Output from Conflow
Thermal Expansion coefficient	1/ °C	NA	NA	[(a)] Output from Model	α	8.054×10^{-5}	[(b)] Output from Conflow
Molar mass of water	Kg/mol	M_g	0.018				
Surface tension	Pa m	NA	NA		σ	0.095	*Marziano et al.* [2007]
Other properties defined in a CV							
Bubble number density	$bubble/m^3$	N_b	10^{11}	*Schipper* (pers. comm.)			
Henry constant	$Kg^{1/2}\ m^{1/2}$ / s	k_H	3.8×10^{-6}	*Burgisser et al*. [in review]			
Glass transition	°C	T_g	700	*Molina et al*. [2012]			
Crystal fraction	Dimensionless	ε_s	0.3	*Kelly et al*. 2008			
Minimum void fraction	Dimensionless	ε_m^*	0.55	*Costa* [2005]			
Gas viscosity at the crust	Pa s	μ_g	10^{-5}				
Permeability of the crust	m^2	C_1	10^{-13}				
Gas velocity through the crust	m/s	V_g	1.6×10^{-6}				
Einstein coefficient	Dimensionless	η	2.5				

[(a)] This is an output from our model.
[(b)] *Mastin and Ghiorso* [2000].

Table 3. Initial conditions

Initial condition	Region of magma system	Mixture fraction	Bubble fraction	Temperature (°C)
		$\varepsilon_{(m+s)}$	ε_g	T_m
IC1	Chamber	0.999	0.001	1000
IC2	Conduit	0.950	0.050	1000
IC3	Lake	0.900	0.100	1000
IC4	Top of the lake	0.999	0.001	700

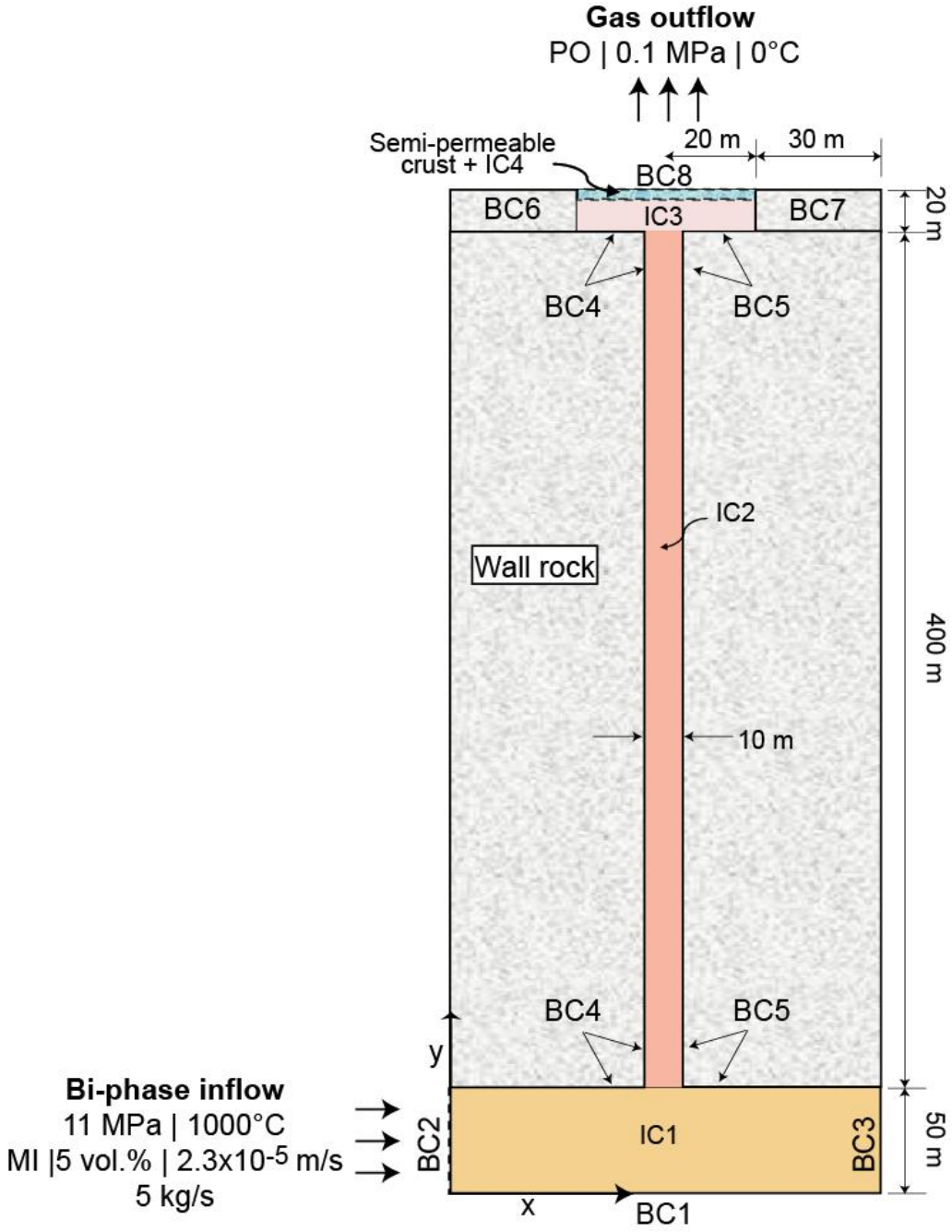

Figure 4. Schematic representation of Erebus magmatic system with a horizontal exaggeration of a factor 2. Boundary and initial conditions are referred in the text and in Table 3.

4. Results

We hereunder describe different aspects of our simulation which ran until 3150 s of simulated time:

4.1. Flow velocity

Our simulation shows that the fluid ascends from the bottom of the conduit and rapidly develops into a gas-rich continuous flow rising at ~0.1 m/s, disturbing the whole system (Figure 5a). After 500 s, we observe a discontinuity at the tail of this ascending batch in the form of a large spot of fast ascending fluid. As the former batch keeps ascending, this phenomenon repeats itself and fast-rising spots appear at regular distance of the lower extremity of the first batch. They proceed to the surface at increasing velocity, forcing the quieter fluid of the conduit to move down towards the chamber. As the upper tip of the large batch reaches the lake at 2000 s, it enhances convection even further and the fluid initially in the lake is forced down the conduit. The initial convection pattern is characterized by a fluid ascending in the central part of the conduit while the descending fluid occupies both sides. The extension of this flow pattern to a 3D geometry would be a core-annular flow, a terminology we use hereafter for convenience. The core annular flow then changes and the descending fluid occupies the center of the conduit. At 2500 s, the individual batches at the bottom of the conduit merge into a new continuous ascending flow, centered, surrounded by the descending fluid. At 3000 s, our simulation shows that motions are high in the chamber and in the lake, whereas they remain contrasted in the conduit: core annular flows are inversed in the higher and lower sections of the conduit. At 3150 s our simulation crashed because of convergence problems (i.e., due to high errors in pressure values). The likely reason is related to the semi-permeable region and the boundary conditions defined at the upper part of our system. High pressure values cannot be accommodated within the lake and chamber because the melt becomes under saturated in water, which causes ε_g to vanish and the calculations to stop.

4.2. Reaction rates

The reaction rate R_g represents the flux of water into the bubbles (Figure 5b). High values occur where bubbles grow most rapidly. Negative values, corresponding to areas were bubbles are shrinking, can be observed along the walls of the conduit at early times, whereas the reaction rate is faster in the core where ascending velocities are higher. This shrinking might result of a slight overpressure resulting from the ascending flow. Note that we imposed a maximum value to R_g (10^{-5} kg/ m^3 s) to avoid catastrophic growth ($\varepsilon_g > 0.7 – 0.8$) during the first seconds of simulation.

The reaction rates show a similar pattern over the first 500 s of the simulation: rates are comparable in the chamber, the lower part of the conduit and in the lake. They remain low in the upper two thirds of the conduit. The most "active" section of the conduit then rises along the conduit, while the reaction rate remains important in both the lake and the chamber until reaching 1000 s of simulation. The reaction rate becomes more homogeneous all along the conduit with higher intensity along its walls. The reaction rates in the lava lake are not uniform; the faster rates are distributed in a zone at the vertical of the junction of the conduit with the lake. This zone takes the form of an expanding mushroom, spreading gradually with the most reactive area at its periphery, while the rest of the lake remains less active. More "active" fluid then enters the bottom of the conduit (~1800 s) and progresses towards the lake, itself increasingly subject to higher rates. Reaction rates become maxima in the upper part of the lake, below the entire crust, and their distribution takes the form of a cup whose base would be the junction with the conduit. In the chamber reaction rates remain high without noticeable variations until the end of the simulation.

4.3. Dissolved water

Initially, the fraction of water dissolved in the mixture (Figure 5c) varies according to a gradient along the whole system as defined in Equation (22). An influx of mixture coming from the conduit reaches the lake, increasing the fraction of dissolved water, and develops as a dual panache, richer in water than the surrounding fluid already present in the lake. The variation of dissolved water fraction cannot be dissociated from the dynamics that generates a convective regime throughout the whole simulated period. Arrival of water-rich melt in the lake increases reaction rates as bubbles grow. The presence of over-saturated melt in the lake persists until the end of the simulation because the conduit feeds the lake in volatile-rich melt

at a rate faster than equilibrium bubble growth. This is due to the limit we fixed on R_g rather than a slow diffusion of water in the melt.

4.4.Gas volume fraction

Initial gas volume fraction in the chamber, conduit and lake have been set at 0.1, 5 and 10 vol.%, respectively (Figure 5d). As soon as mixture is injected in the magma chamber, slightly gas-enriched liquid (~2 vol.%), invades the bottom of the conduit and starts to rise. This inflow disturbs the homogeneity of the lake while the gas fraction remains unchanged in the conduit over the first 600 s. Gas-poor mixture keeps rising and reaches about one fourth of the length of the conduit after 1000 s. Gas fraction in the upper half of the conduit increases both due to a change in reaction rate and to gas-rich mixture (11.5 vol.%) forced down the upper section of the conduit. At 1200 s, the main part of the mixture in the lake has a lower gas fraction than at its initial conditions (down from 10 to 7 vol.%). However, gas-rich "batch" (14 vol.%) concentrates right above the junction of the conduit and inside its upper section. Gas-poor mixture keeps rising and reaches half of the length of the conduit (1500 s); the batch has now reached 20 vol.% gas fraction as its length decreases, squeezed from the top and the bottom by gas-poorer mixture. At 2000 s the batch reaches a gas fraction of 33 vol.%, surrounded in the lake by a mixture whose concentration radially decreases to 2-3 vol.% along the walls and the crust. As the rest of the mixture initially contained in the conduit reaches the lake, the gas-rich cloud (30 vol.%) expands and develops a symmetrical convecting plume that eventually mixes in the lake. At 2500 s, the gas fraction in the lake ranges between 15 and 29 vol.%, except in the far corners of the lake, less disturbed by convecting currents. At the end of the simulation, gas-rich (14 vol.%) mixture has forced back some of the gas-poor mixture down the upper part of the conduit. The lake displaces two gas-rich vortex (28 vol.%) right below the crust, while the rest of the lake is filled with a mixture whose gas fraction varies between 15-20 vol.%. During the whole simulation, the conduit remains filled up to its lower half with a mixture whose gas fraction is well below 1 vol.%.

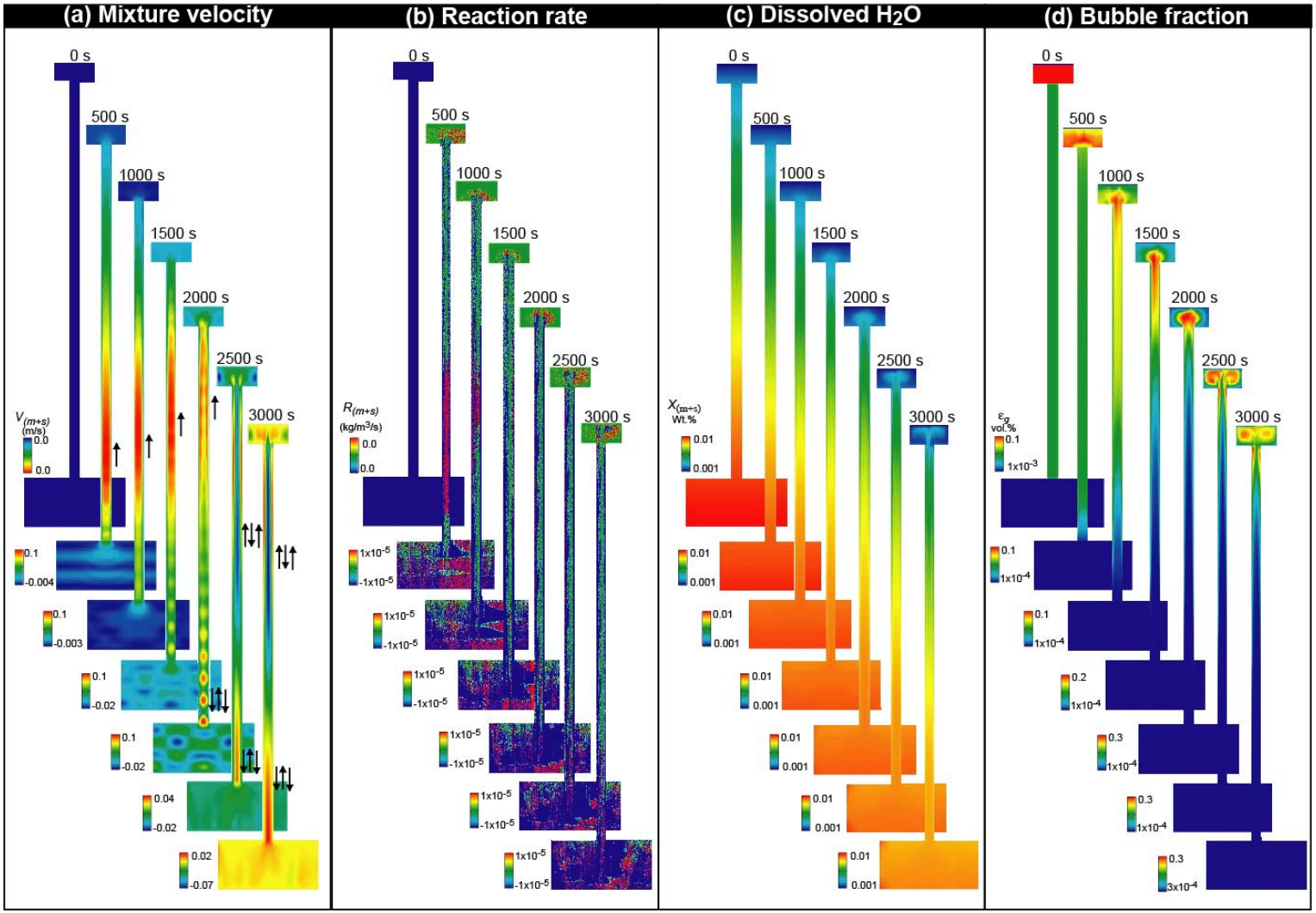

Figure 5. Results for the time span of the simulations: (a) vertical scalar velocity (V_m) map in which red and blue colors indicate upward (positive values) and downward (negative values) motions, respectively. The arrows accompanying each caption represent the main direction of the flow motion in the conduit; (b) Reaction rate ($R_{(m+s)}$) maps in which red and blue colors indicate the gain of dissolved water (positive values) and gain of water by bubbles (negative values), respectively; (c) water melt content (X_{m+s}) in which red and blue colors indicate the presence of large and small amount of water, respectively; (d) bubble fraction maps in which red and blue colors indicate the presence of large and small amount of bubbles, respectively.

4.5. Bubble diameter

Initial conditions at the chamber, conduit and lake have been set at 0.1, 5 and 10 vol.% of gas and the bubble number density is fixed at $10^{11}/m^3$. This consequently fix our initial diameter of bubbles in agreement with our definition for d_b (Figure 6). The initial bubble diameter in the lake is of 1.3×10^{-4} m, 10^{-4} m in the conduit and 3×10^{-5} m in the chamber.

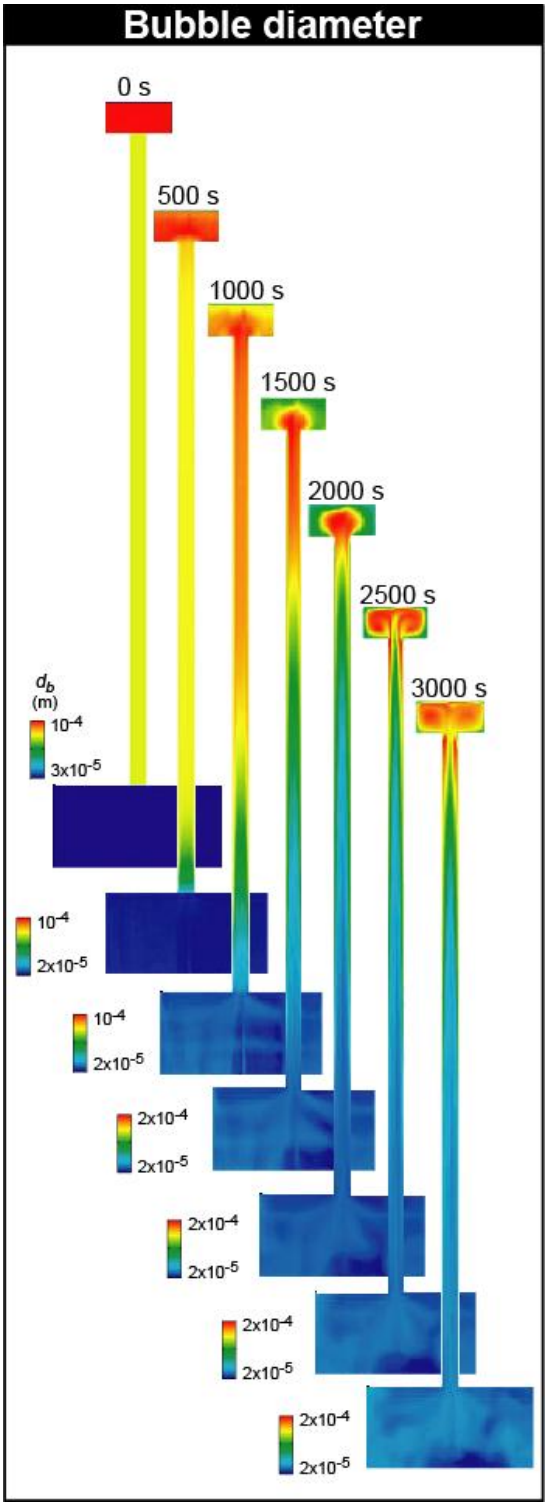

Figure 6. Results for the time span of the simulation: bubble diameter (d_b) map in which red and blue colors indicate large and small values, respectively.

As mixture enters the bottom of the conduit, the diameter of bubbles increases from its initial value of 3×10^{-5} to 7×10^{-5} m (after 500 s). The distribution of large and smaller bubbles in the lake is not uniform anymore. After 1000 s, the gradient of the bubble diameter is already well established, with 4×10^{-5} m at the bottom of the conduit and 1.3×10^{-4} m at its top. However, if most of the lake is featuring bubbles of 1.3×10^{-4} m, its upper part is showing smaller bubbles (1×10^{-4} m). As more mixture invades the conduit, large bubbles concentrate further right above the junction of the conduit with the bottom of the lake and in the upper part of the conduit, reaching 1.6×10^{-4} m in diameter after 1500 s. The rest of the lake concentrates smaller bubbles (~1×10^{-4} m). After 2100 s, the mixture that initially entered the conduit is reaching the bottom of the lake. The largest bubbles have now grown to a diameter of 2.1×10^{-4} m and largest bubbles are found right above and at the junction conduit-bottom of the lake. The rest of the lake is now filled with bubbles of 1.2×10^{-4} m in diameter, while the conduit displays a gradient from 8×10^{-5} to 10^{-4} m. The size of the bubbles in the chamber has increased as the hydrostatic pressure exerted by the mixture in

the lake and conduit has decreased. However, bubbles sizes are not evenly distributed and small ones are mostly found at the roof of the chamber. The profile of the flow of larger bubbles into the base of the conduit leads to a parabolic distribution of small bubbles on each side of the conduit. At 2500 s the largest bubbles spread in the lake with a profile of 2 symmetrical and convecting cells that eventually fade out completely after 3150 s. The lake is now filled with the mixture whose bubbles have a diameter of 2×10^{-4} m.

4.6. Water release

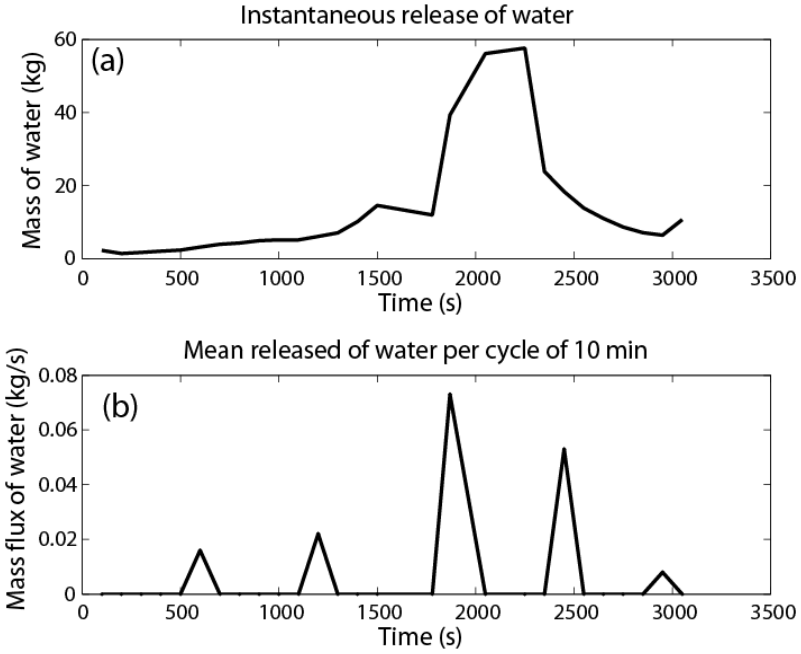

Figure 7. (a) Mass of water released through the crust per time step of the simulation; (b) average mass flux of water released every 10 minutes.

We quantified the instantaneous release of water through the lake crust (Figure 7a). It shows an increasing trend until ~2000 s and later decays until the end of the simulation. We averaged the amount of releases water over a period of 10 min (Figure 7b), which yields a maximum gas flux of 0.07 kg/s during a cycle of 10 min.

4.7. Surface velocities at the top of the lake

We measured the average of the magnitude of velocity vector of the mixture (Figure 8) at the surface of the lake and obtained a maximum velocity of 3.3×10^{-4} m/s at ~2000 s that coincides with the arrival of the batch of volatile-rich magma at the surface of the lake. The velocity decreases then during ~1000 s before increasing again sharply as a new batch of magma appears at the lower part of the conduit (Figure 5a).

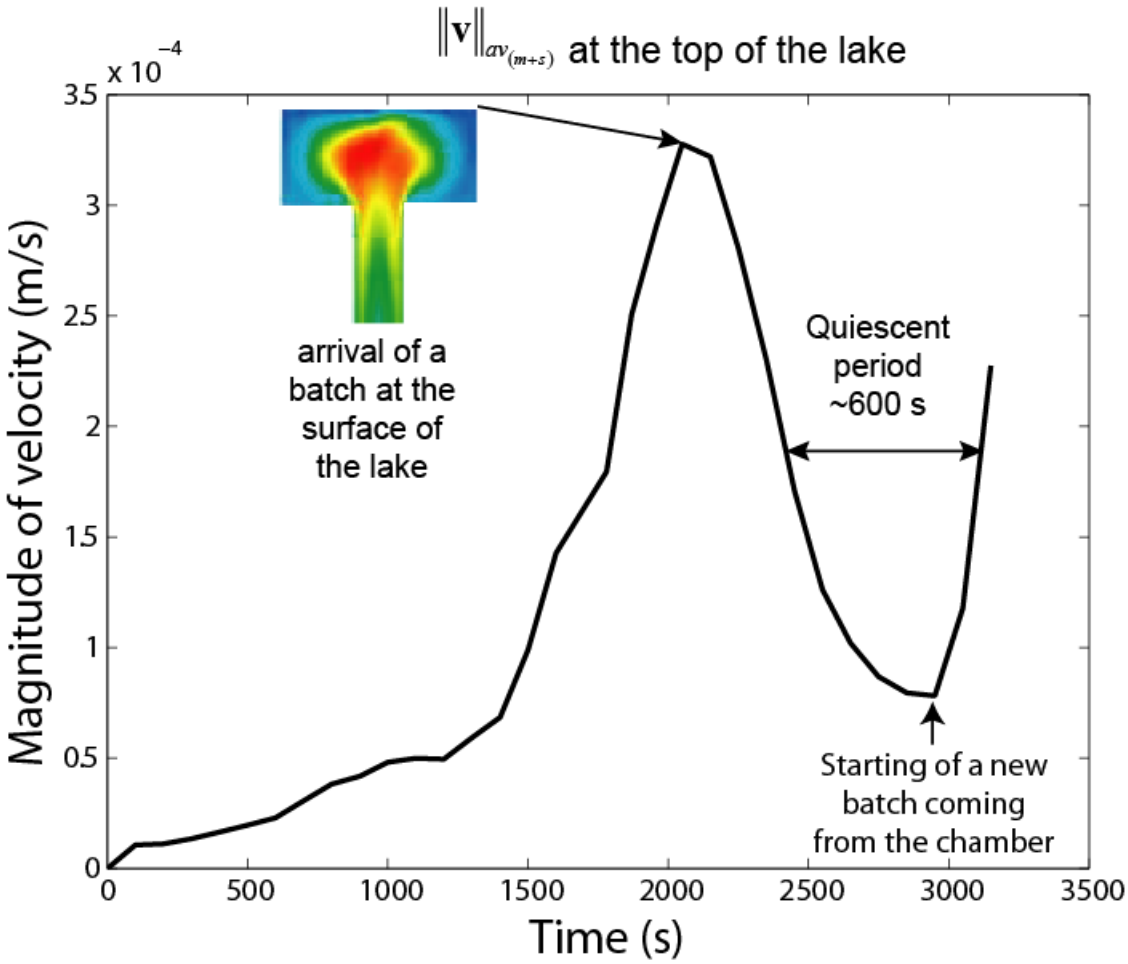

Figure 8. Characteristics of the lake surficial velocities: average values of the magnitude of velocity vector at the first meter of the lake obtained along cells in the *x*-direction average per time step (every 100 s).

4.8. Coupling of the mixture and gas velocities

We notice that mixture and bubbles travel at nearly the same velocity with minimum decoupling (Figure 9). With time, both velocities at mid-depth in the lake tend to increase to reach a value of 1.2×10^{-2} m/s after 2500 s. The velocities at the surface of the lake are in the order of 10^{-4} m/s, but they rapidly increase with depth to reach 10^{-3} m/s at only 1 m below the surface at times between 1500 and 3000 s, coincident with the arrival of the batch of magma.

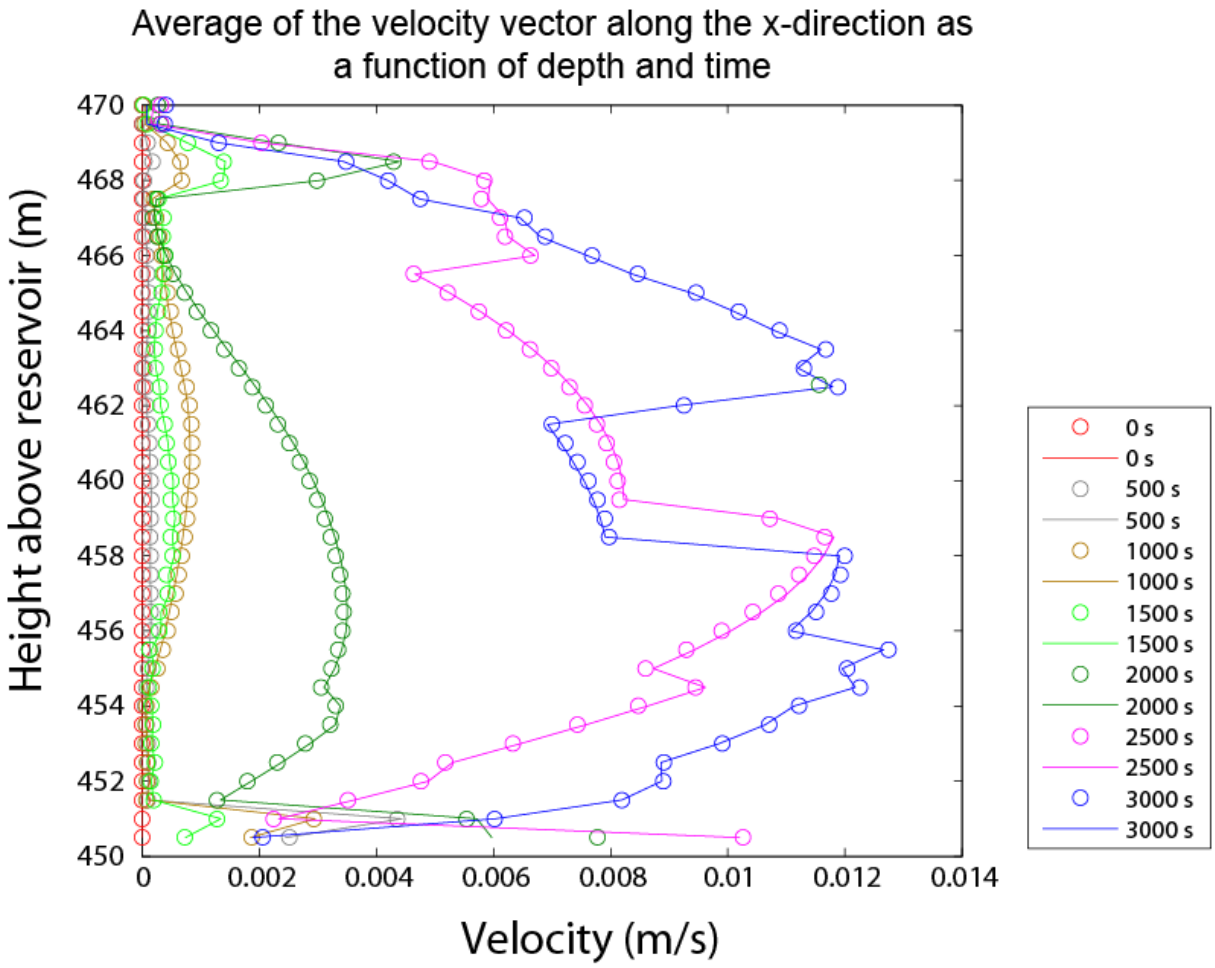

Figure 9. Horizontal velocity profile of the mixture (continuous line) and bubbles (open circles) at every time step of the simulation in the lake.

5. Interpretations and implications for the effusive regime of Erebus

We have investigated the effusive dynamics of the ascent of magma from the reservoir to the lake by means of a bi-phase model (mixture plus bubbles) in which the system receives a weighted recharge of magma (~5 kg/s) and allows a variable amount of gas to be released at atmospheric pressure. The bulk density of the mixture is temperature-controlled and laden by a fixed amount of crystals (30 vol.%). Its bulk viscosity accounts for crystal content and dissolved volatile content (H_2O). Bubbles grow by expansion and diffusion. Coalescence processes have been ignored.

Our interpretation of the numerical simulation is that the rise in the conduit of bubbles of increasing diameter results in a decrease of the pressure in the chamber due to a change in

bulk density of the mixture above. This variation enhances the process of the exsolution of water from the melt and the growth of the bubbles, which in turn result in a change of gas volume fraction. This water rich mixture reaches the upper part of the lake and takes the shape of a "cloud" that splits into two convecting cells. At this time, the fluid at the bottom of the conduit starts to rise at an increasing velocity. Unfortunately, our simulation stopped before the new batch that we observe at the bottom of the conduit could rise further up; this influx might have generated new discontinuities at regular intervals, once again merging into a single fast-rising batch that would reach surface. If this remarkable feature repeats itself, the arrival of these batches at regular intervals could correspond to the variation of flux of gas released to surface observed at Erebus and generating the oscillatory phenomena at the surface of the lake (geochemical, radiative power, velocity).

Our numerical simulation suggests that magma can rise by intermittent batches (Figure 5a). Those batches form a swarm (cluster) of bubbles in the form of a cloud such as the one observed in a geyser when a large amount of bubbles reaches the surface (Figure 10a). Studies performed by *Kieffer* [1982, 1984] and *Ingebritsen and Rojstaczer* [1993, 1996] started to look at geysers as analogs for volcanoes providing constraints and theories for multi-phase flows in hydrothermal systems.

In Chapter IV, we propose a single-phase mechanism of ascent of magma batches that causes the chemical variations of the gas released and oscillations of the lake level, when the gas of different composition is released from blobs (clusters of bubbles contained in a spherical magma batch) (Figure 10c). Briefly, those blobs would have a porosity at surface as a result of a series of assumption: (i) bubbles are well coupled with magma ascent, (ii) blob contains 770 m^3 of gas and a associated melt, (ii) the blob has a radius that can be fitted in a conduit of 10-m diameter (iii) ascending temperatures of the blob are in equilibrium with degassing and (iv) the difference between ascending and descending temperature is of 56°C (Figure 10d-10e). Thus, as those blobs reach the lake, they have a diameter of 13 m (Figure 10c-10e) and porosities varying from 10-30 vol.% to later reach a porosity of 70 vol.% at surface (Figure 10f).

In the present numerical model, the diameter of the cloud is about 15 m when it enters in the lake; as it ascends toward the shallower part of the lake, its porosity increases from 10 to 30 vol.% (Figure 10b). These results (diameter and porosity of the cloud in the middle part of the lake) are comparable to the ones found in our proposed model from Chapter IV.

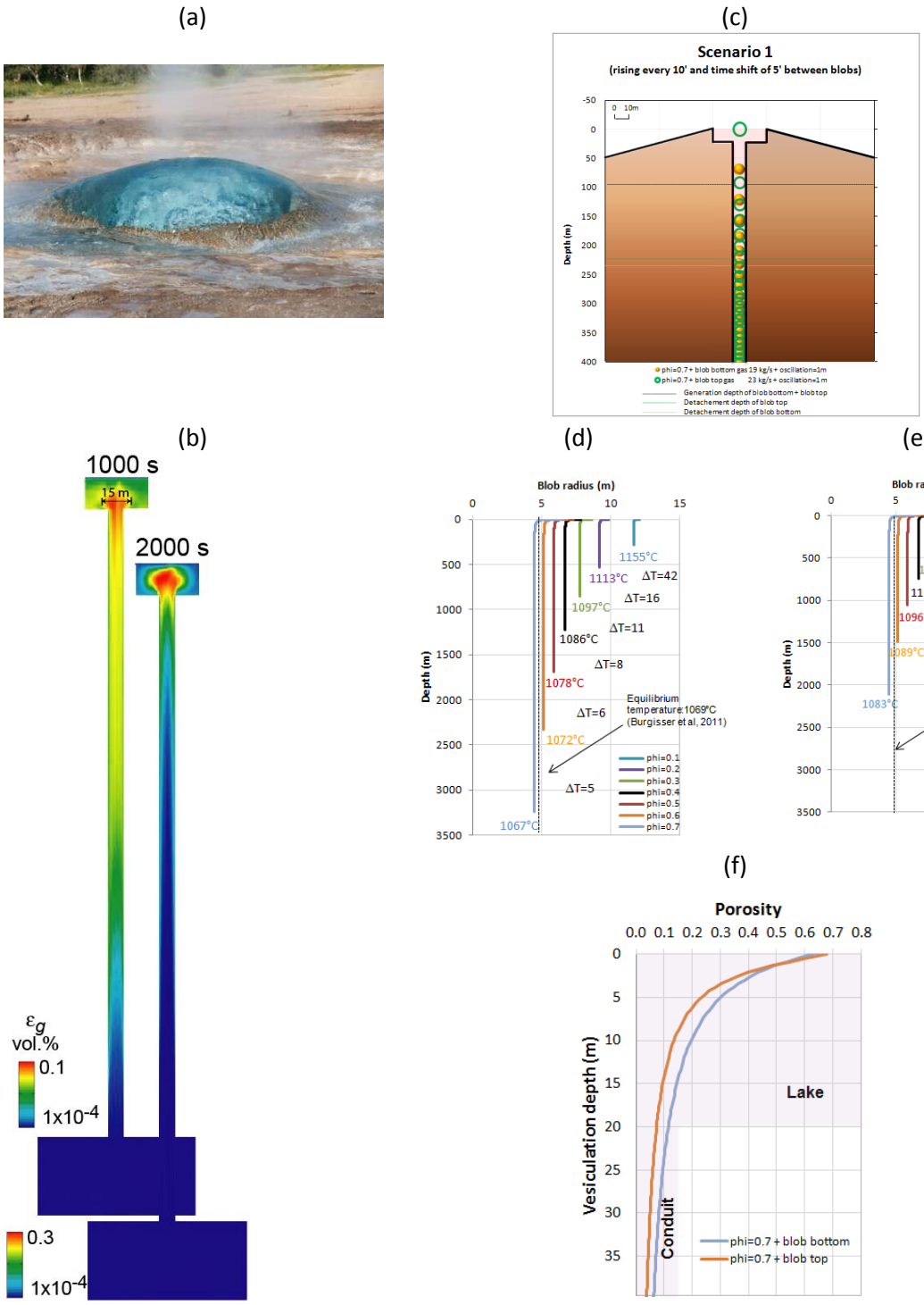

Figure 10. (a) Image of a geyser reaching surface before maximum gas release, (b) maps of porosity of our numerical simulation, (c)-(d)-(e)-(f) Scenario to explain the lava lake oscillation (see details in Chapter 4): (c)-(d)-(e) a blob entering in the lake has a diameter of ~10 m, (d)-(e) porosity evolution of the blob shows that, when it enters in the lake, it has porosities ranging between 10-30 vol.%; it is only at the last stage when blob reaches surface that its porosity reaches 70 vol.%.

The variation of gas flux of water emitted at the surface of the lake represents ~0.07 kg/s over a cycle of 10 min (Figure 7b), which is two orders of magnitude smaller than the ~7 kg/s of gas flux for the water species reported by *Oppenheimer et al*. [2009]. Resistance to flow gas through the lake crust was defined in the equation (23). We have chosen a value of permeability of 10^{-13} m^2 and a velocity of the gas flowing through this surface of 1.6×10^{-6} m/s. Should we have chosen different values for these input variables, i.e. increasing the permeability and/or decreasing the resistance to flow, the mass rate of gas would be different. To simulate a surface open to flow we could "turn off" the resistance to flow by assigning a large permeability value of say 10^{32} m^2. The fact that we ignored coalescence process also might play a role in increasing velocities; indeed, this phenomenon and its effect on decoupling bubble motion from the mixture induce complex magma ascent dynamics [e.g., *Jaupart and Vergniolle* 1989; *Gonnerman and Manga*, 2007]. However, in the time span of our simulations, we noticed that bubbles and magma are well coupled (Figure 9).

The modeled velocities at the surface of the lake during unsteady state, when crystals in magma are considered as a separate phase, are in the order of ~10^{-5} m/s (Figure 14 from *Molina et al*., 2012); the presence of the bubbles have played a role to increase the velocities to ~10^{-4} m/s (Figure 8) and much more in the middle of the lake to ~10^{-2} m/s (Figure 9), as we forecasted in our previous work [*Molina et al*., 2012]. However, this increase falls short from the value of 0.1 m/s reported by *Oppenheimer et al*. [2009]. The modeled period of relative quietness of ~500 s (Figure 8) is apparently consistent with the time interval between successive batches of magma as hypothesized in our analytical modeling (see Chapter 4) and by *Oppenheimer et al*. [2009] to explain the oscillatory phenomena of the lava lake.

The fraction of dissolved water seems to decrease in most of the lake, while gas-rich liquid concentrates right above the junction of the conduit with the bottom of the lake in a cloud-like area. This cloud reaches a gas fraction of 30 vol.% as bubbles grow in diameter and invades most of the lake, attaining an average value of 25 vol.% at the time our simulation stopped. The fastest rates of exsolution of water from the mixture correspond to the zones where the gas fraction and bubble diameters are the highest, suggesting that pressure is not evenly distributed in the lake. Indeed, fluid rising in the 10-m diameter conduit will be subjected to

decompression as it reaches the bottom of the lake. A drop in pressure favors the growth of bubbles corresponding to a larger gas volume fraction and higher reaction rate of exsolution.

In the chamber, relatively large bubbles migrate up to the base of the conduit; the size of the bubbles varies on each side of the conduit and their distribution takes a parabolic profile. Smaller bubbles seem to accumulate at the roof of the chamber, forming a thicker layer as the distance from the conduit increases (Figure 6). The velocity of this mixture is also lower than that of the mixture rising from the part of the chamber located right below the conduit. These smaller bubbles form an upper boundary layer, stagnant as a dead fluid that progressively disappears as the velocity in the system increases (Compare Figures 5a and 6). We observed a similar profile in our simulation of an open system containing crystals as a separate phase (See Figures 11s-11 from Chapter II); however in this last simulation the boundary layer is thinner than the one simulated with bubbles. Crystals sink and eventually settle while bubbles rise by buoyancy and grow; the differing behaviors of both phases may enhance the segregation process. We turned out our attention to this layer because its behaviour would provide hints about intermittent behaviour that we are looking at simulating [e.g., *Jaupart and Vergniolle* 1989] and the distribution of bubble size during that intermittent behaviour [e.g., *Vergniolle* 1996].

Finding smaller bubbles at the top of the chamber is not the distribution that we would expect (Figure 6). However, if we consider the whole system, the size of the bubbles increases as expected from tiny bubbles in the chamber to much larger bubbles in the lake (Figure 6). The mapping of the mixture velocity (Figure 5a) gives us a hint on what could be the explanation. The mixture in the central part of the chamber is put in movement much earlier than the dead fluid at the roof. As the lighter fluids progresses in the conduit, the density of the column at the vertical of the conduit decreases immediately and the bubbles contained in the magma of this zone grow faster. The fluid velocity increases. The growth of the bubbles in the upper layer will be delayed and the porosity will temporarily appear smaller than the one of the fluid entering the conduit. As bubbles grow uniformly, the whole magma is put in motion and enters the conduit; the dead layer disappears. The far corners will be the last to fade away.

After 3000 s of simulation, the average temperature of the chamber and conduit remains constant while the average temperature of the lake increases by ~3° as a result of the rise of a magma batch at the surface of the lake (Figure 11). This simulation is thus essentially isothermal, except for the thin cold crust atop the lake.

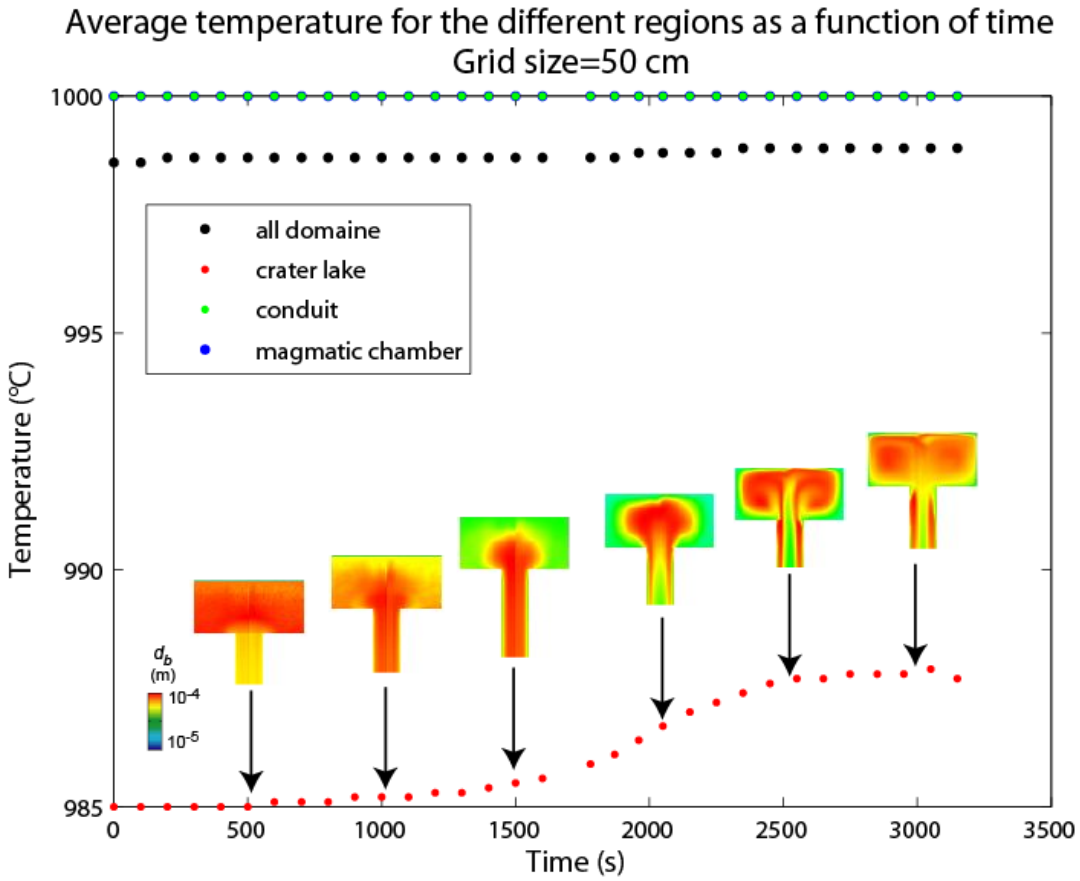

Figure 11. Evolution versus time of the average temperature per region of the magmatic system. Every inset caption corresponds to diameter of the bubbles.

6. Main conclusions and future work

The results presented in this chapter describe how successive magmatic pulses initiate and rise towards the surface of the lake. The modeled period of relative steady state quiescence of ~500 s apparently marks the building of a new batch of magma whose ascension into the conduit causes changes in velocity at the surface of the lake. This period of ~10 min is in agreement with the phase changes of velocities and geochemical ratios reported by *Oppenheimer et al*. [2009]. It seems plausible that our calculations would result in a sort of

transition toward steady flow. Our modeled velocities at the surface of the lake are in the order of 10^{-3}-10^{-4} m/s (Figures 8 and 9). These velocities are 2-3 orders of magnitude lower than those observed at Erebus (10^{-1} m/s). The gas water flux output of 0.07 kg/s (Figure 7) is 2 orders of magnitude smaller than the observed value (9 kg/s). These results need then to be reevaluated with runs using the correct transport equations for the gas volume fraction (equation (10) instead of (12)). However, we can confirm what was expected by *Molina et al*. [2012] who suggest that exsolved volatiles are an important source of buoyancy that increases the convective velocities (compare Figures 8p-8r and 14 from *Molina et al*. 2012 with the Figures 9 and 8, respectively from this work).

Overall this work has implications to provide boundary conditions for effusive regime models that use bi-phase approximations. We suggest that more work needs to be done: (i) by varying the Darcian parameters of the semi-permeable crust, (ii) by changing the rate for the continuous recharge of magma and (iii) through the refinement of the numerical parameters (e.g., tolerance, grid size and under-relaxation factors of momentum equations). All these must be addressed and refined to approximate the values of gas water flux and velocities measured by *Oppenheimer et al*. [2009].

Appendix 1. Sub-grid model for gas expansion

Lensky et al. [2004] model considers a suspension of bubbles in a viscous liquid in which bubbles are closed pack. Each bubble has a radius R_b and is surrounded by a spherical melt shell of radius S.

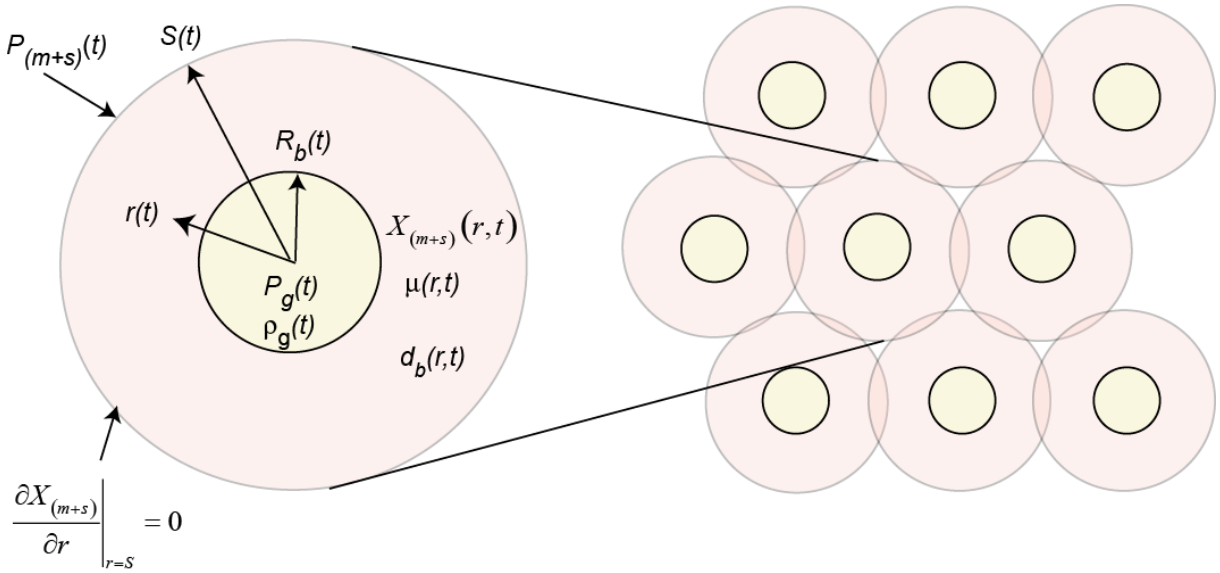

Figure A1. Sketch of the physical model taken from *Lensky et al*. [2004] (we have modified some symbols in order to use our own nomenclature). The magma is composed of spherical bubbles of radius R_b surrounded by a spherical melt shell of radius S.

Lensky et al. [2004] defined the balance of forces between pressure and viscous stresses as follows:

$$P_g = P_{amb} + \frac{2\sigma}{R_b} + \frac{4\dot{R}_b}{R_b}\mu_{eff} \qquad \text{(A1.1)}$$

Where P_{amb} is the ambient pressure, here equals $P_{(m+s)}$, P_g the pressure inside the bubble, and R_b is the radius of the bubble, σ is the surface tension and μ_{eff} is the effective viscosity that resists bubble expansion.

The effective viscosity as defined by the authors considers the finite shell size and variable viscosity; it is defined as follows:

$$\mu_{eff} = \mu_{R_b}\left(1-\frac{\mu_S}{\mu_{R_b}}\varepsilon_g + \frac{R_b^3}{\mu_{R_b}}\int_{R_b}^{S}\frac{d\mu}{dr}\frac{1}{r^3}dr\right) \quad \text{(A1.2)}$$

Where μ_{R_b} and μ_S are the viscosities at the interface between gas and melt, and at the outer part of the melt shell, respectively.

We assume $\mu_S = \mu_{R_b}$ and $\frac{d\mu}{dr} = 0$. Thus we simplify equation (A2), as follows:

$$\mu_{eff} = \mu_{R_b}\left(1-\varepsilon_g\right) \quad \text{(A1.3)}$$

In other terms, viscosity at the shell wall μ_S is the same as viscosity of the shell at the edge of the bubble μ_{R_b}, and there are not changes of viscosity inside the melt shell. We link the microscopic viscosity to the macroscopic the viscosity by $\mu_{R_b} = \mu_{(m+s)}$, then equation (A1.3) becomes:

$$\mu_{eff} = \mu_{(m+s)}\left(1-\varepsilon_g\right) \tag{A1.4}$$

Replacing the above simplification into equation A1.1 and expressing it in terms of bubble diameter yields:

$$P_g = P_{(m+s)} + \frac{4\sigma}{d_b} + \frac{4\dot{d}_b}{d_b}\mu_{(m+s)}\left(1-\varepsilon_g\right) \tag{A1.5}$$

Appendix 2. Diffusivity of dissolved water

Solving the radial concentration of water around each bubble is needed to solve the diffusion-advection equation. The equation of diffusion is a partial and linear equation, whose solution is obtained when two independent variables: time, t, and radial distance from the bubble radius outwards, r, are combined in an independent variable. The result is called similarity solution. For simplicity, we consider a 1-D situation. After ignoring the term of advection describing the motion of the bubble wall given by the 1-D advection-diffusion equation presented by *Lensky et al* [2004], and a more recent analysis of the bubble growth model by *Forestier-Coste et al*. [2012], we have:

$$\frac{\partial X_{(m+s)}}{\partial t} = \frac{1}{r^2}\frac{\partial}{\partial r}\left(r^2 D_{H_2O}\frac{\partial X_{(m+s)}}{\partial r}\right) \tag{A2.1}$$

The previous equation is solved by *Forestier-Coste et al*. [2012] using two boundary conditions. The first one considers that the gas pressure at bubble-melt interface ($r = R$) is in equilibrium with H_2O concentration through Henry's law:

$$X_{(m+s)}\left(r,t\right) = k_H\sqrt{P_g} \tag{A2.2}$$

Where k_H is an experimental constant based on solubility data for Erebus phonolite [*Burgisser et al.* in review] and P_g is the pressure inside the bubble, in MPa.

The second boundary condition establishes that there is no flux of H_2O after a radius of influence (when $r = S$):

$$\left.\frac{\partial X_{(m+s)}}{\partial r}\right|_{r=S} = 0 \qquad \text{(A2.3)}$$

The way of implementing the diffusion equation in our model is courtesy of S. Mancini and follows the method given by *Forestier-Coste et al.* [2012], in which the water concentration $X_{(m+s)}(t,r)$ is solved by splitting the equation between the advection step and diffusion step following a Lagrangian method. We neglect the advection and the discretization of that transport equation for the diffusion step part is given by the authors as:

$$r^2 \frac{\partial X_{(m+s)}}{\partial t} = \frac{1}{\Theta_D} \frac{\partial}{\partial r}\left(r^2 D_{H_2O} \frac{\partial X_{(m+s)}}{\partial r} \right) \qquad \text{(A2.4)}$$

Where Θ_D is a relaxation parameter defined as:

$$\Theta_D = \frac{R_i^2 \Delta P}{D_i P_i} \qquad \text{(A2.5)}$$

Where R_i is the initial bubble radius, D_i is the diffusion coefficient, P_i is the initial ambient pressure and ΔP is the decompression rate.

Following a standard finite volume strategy *Forestier-Coste et al.* [2012] propose the following solution for the discrete flux, F, of water between cells:

$$F_o^{n+1} = F_1^{n+1} - \frac{\Theta_D}{\Delta t^n} \frac{r_1^3 - r_o^3}{3} \left(X_{(m+s)o}{}^{n+1} - X_{(m+s)o}{}^{n} \right) \qquad \text{(A2.5)}$$

Where n is the nth node between consecutive cells and the boundary conditions given in equation (A2.2) and (A2.3) become $X_{(m+s)o}^{n} = k_H \sqrt{P_g^n}$.

Appendix 3. Viscosity model

At temperatures above their liquidus, magmas are Newtonian and their viscosity depends on temperature according to an Arrhenian law:

$$\mu_m = \mu_o \exp\left(-\frac{E_A}{GT_m}\right) \tag{A3.1}$$

where μ_o is viscosity under standard temperature conditions, E_A is the activation energy, G is the universal gas constant, and T_m is temperature.

Over the last 25 years, magma physicists have discovered that silicate melts are often non-Arrhenian, largely because of the additional impact of water on viscosity [*Dingwell*, 2006]. Water breaks chains of silica polymers in melts, and shorter polymers result in a lower viscosity. One non-Arrhenian model of viscosity is in the form of the Vogel-Fulcher-Tammann (VFT) equation:

$$\mu_m = 10 \exp\left(A + \frac{B}{T - C}\right) \tag{A3.2}$$

We use the adjustable Newtonian model given by *Giordano et al*., [2008] which predicts the non-Arrhenian temperature and compositional dependence of viscosity for naturally-occurring silicate melts at atmospheric pressure (10^5 Pa). Thus, based on the mean of the major element concentrations (SiO_2, Al_2O_3, TiO_2, FeO_{tot}, CaO, MgO, MnO, Na_2O, K_2O, P_2O_5, H_2O, F_2O_{-1}) of matrix glass separated from lava bombs erupted at Erebus volcano between December 1972 and January 2004 [*Kelly et al*., 2008], plus the water contents calculated through our model, we have calculated the coefficients B and C as linear combinations of oxide components M_s and N_s (mol%) and several multiplicative oxide cross-terms (details are given by *Giordano et al*., [2008]). These coefficients are defined in equation A3.2 as follows:

$$B = \sum_{i=1}^{7}\left[b_i M_i\right] + \sum_{j=1}^{3}\left[b_{ij}\left(M1_{1j}.M2_{1j}\right)\right]$$
$$C = \sum_{i=1}^{6}\left[c_i N_i\right] + \left[c_{11}\left(N1_{11}N2_{11}\right)\right] \quad \text{(A3.3)}$$

The coefficient A = -4.55 in equation A3.2 is independent of composition. In Table A2, we give an example of the calculation of B and C terms, by fixing the water content to 0.26 wt.% as was done by *Molina et al*. [2012]. However, note that in this work the viscosity also varies as a function of water content so that the terms *b6, b12, c6* and *c11* in Table A2 are updated at every cell and time step. This routine was included in MFIX.

Below liquidus, crystals coexist with silicate melt and bulk viscosity increases as a function of the amount of crystals. Different power laws exist to describe this behavior of crystal-bearing spherical particles [*Stickel and Power*, 2005] and we have adopted the theory of *Krieger and Dougherty* [1959] which is in agreement with most of the authors [e.g., *Caricchi et al*., 2007 ; *Costa et al*. 2009] when crystal fraction is lower than the maximum packing fraction:

$$\mu_{(m+s)} = \mu_m\left(1 - \frac{\varepsilon_s}{1-\varepsilon_m^*}\right)^{-[\eta]\left(1-\varepsilon_m^*\right)} \quad \text{(A3.4)}$$

However, it must be noticed that at higher strain rates (> 10^{-3} s) the mixture behaves as pseudo-Bingham material [e.g., *Barnes*, 1999] and therefore the effective relative viscosity of crystal-bearing magmas is function of crystal fraction and strain-rate [e.g., *Caricchi et al*. 2007 ; *Costa et al*. 2009]. In the case of the bi-phase simulations (crystals as separate phase) performed by *Molina et al*. [2012], the strain rates in Erebus are in the order of 10^{-6} s^{-1} and therefore the bulk viscosity described with equation A3.4 is a good approach.

Appendix 4. General notations and parameter of viscosity model.

Table A1. Notation, units and definitions.

	Units	**Definition**

(a) Subscripts		
amb		Ambient
eff		Effective
g		Gas
g		Glass
m		Melt
$(m+s)$		Melt plus solid phases or mixture
$shell$		Spherical shell of magma
x, y		Coordinate along x(y)-direction
Latin		
A, B, C	dimensionless	Compositional coefficients of viscosity (equation 15)
C_1	m2	Darcian permeability coefficient
C_m	°C/m	Heat loss through the wall
C_p	J/kg °C	Heat capacity
D_{H_2O}	m^2/s	Water diffusivity
$^{(b)}\mathbf{D}$	1/s	Rate-of-strain tensor
d_b	m	Bubble diameter
$\mathbf{f}_g$	N/m^3 (kg/ m2 s^2)	Flow resistance due to porous media
$F_{(m+s)g}$	kg/m^3 s	Drag factor between fluid and gas phases
$\mathbf{g}$	m/s^2	Gravity vector
$\mathbf{I}$	dimensionless	Identity tensor
$^{(c)}I_{2D}$	$1/s^2$	Second invariant of the deviator of the rate-of-strain tensor
k_H	$Kg^{1/2}$ $m^{1/2}$ / s	Henry constant
k	J/m °C s	Thermal conductivity
M_g	kg	Molar mass of gas phase
Nu	dimensionless	Nusselt number
N_b	Bubbles/m^3	Bubble number desity
P	Pa	Pressure
Pr	dimensionless	Prandtl number
$\mathbf{q}$	J/m^2 s	Conductive heat flux vector
G	J/ K mol	Universal gas constant
R	J/Kg K	Ratio if universal constant
R	Kg/m^3 s	Reaction rate
R_b	m	Radius of the bubble
Ra	dimensionless	Rayleigh number, Rac is Critical Rayleigh number
Re	dimensionless	Reynolds number
$\mathbf{S}$	Pa	Stress tensor
T	°C	Thermodynamic temperature
T_o	°C	Initial thermodynamic temperature
t	s	Time
U, V	m/s	Scalar for horizontal (vertical) component velocity
Vol	m^3	volume
$\mathbf{v}$	m/s	Velocity vector, $\|\mathbf{v}\|$ is the magnitude of the velocity vector
X	dimensionless	Weight fraction of one specie

x, y	m	Coordinate along x(y)-direction
Greek symbols		
α	1/°C	Thermal expansion coefficient
$\gamma_{(m+s)g}$	J/m^3 °C s	Heat transfer coefficient between fluid and gas phases
ε	dimensionless	Volume fraction
ε^*	dimensionless	Packed-bed (minimum) void fraction for crystals
ϕ		General scalar
η	dimensionless	Intrinsic viscosity (reference viscosity)
μ	Pa s (kg/m s)	Molecular viscosity of the phase
ρ	kg/m^3	Microscopic density
ρ	kg/m^3	Macroscopic density
σ	N/m (kg/s^2)	Surface tension
ρ_o	kg/m^3	Initial macroscopic density
$\boldsymbol{\tau}$	Pa	Deviatoric stress tensor
Operators		
T		Transposed operation of matrices
$^{(d)}tr$		Trace operation of tensor
Abbreviations		
(e) BC		Boundary condition
CV		Control volume
FSW		Free-slip wall
MI		Mass inlet
NSW		Non-slip wall
PO		Pressure inlet/outlet

(a) These subscript/sub subscripts can be associated to other subscript specifying the phase.

(b) $\mathbf{D} = \frac{1}{2}\left[\nabla\mathbf{v} + (\nabla\mathbf{v})^{\mathrm{T}}\right]$

(c) $I_{2D} = \frac{1}{6}\left[(\mathrm{D}_{11} - \mathrm{D}_{22})^2 + (\mathrm{D}_{22} - \mathrm{D}_{33})^2 + (\mathrm{D}_{33} - \mathrm{D}_{s11})^2\right] + \mathrm{D}_{12}^2 + \mathrm{D}_{23}^2 + \mathrm{D}_{31}^2$

(d) $tr(\mathbf{D}) = \nabla \cdot \mathbf{v}$

(e) This abbreviation can be followed by a number indicating the geometrical position of a given geometrical configuration in a simulation.

Table A2. Coefficients used for calculation of viscosity model in Erebus: (1) model coefficients based on the optimized model of *Giordano et al.* [2008]; (2) Computed values for obtaining *B* and *C* for the viscosity model of Erebus for a constant water content.

(1) Model Coefficients for calculation of parameters *B* and *C*						**(2) Computed values using the model coefficients**					
Oxides combination for "b" terms	"*B*" or "b" terms	b term value	Oxides combination for "c" terms	"*C*" or "c" terms	c term value	Oxides at Erebus	wt %	wt $\%_N$	mol%	*B*-terms value	*C*-terms value
SiO_2+TiO_2	b_1	159.6	SiO_2	c_1	2.75	SiO_2	55.35	55.41	61.98	*10027.05*	*170.43*
Al_2O_3	b_2	-173.3	TiO_2+Al_2O_3	c_2	15.70	TiO_2	1.01	1.01	0.85	*-2264.14*	*218.47*
FeO(T)+MnO+P_2O_5	b_3	72.1	FeO(T)+MnO+MgO	c_3	8.30	Al_2O_3	19.80	19.82	13.06	*395.30*	*55.91*
MgO	b_4	75.7	CaO	c_4	10.20	FeO(T)	5.43	5.44	5.08	*104.89*	*22.88*
CaO	b_5	-39.0	Na_2O+K_2O	c_5	-12.30	MnO	0.28	0.28	0.27	*-87.49*	*-170.24*
Na_2O+**H_20**+F_2O_{-1}	b_6	f(**H_20**)[(a)]	Ln(1+**H_2O**+F_2O_{-1})	c_6	f(**H_20**)[(a)]	MgO	0.83	0.83	1.39	*-922.52*	*-76.47*
H_20+F_2O_{-1}+ln(1+H_2O)	b_7	141.5	Al_20_3+FeO(T)+MnO+MgO+CaO-P_2O_5)*(Na_2O+K_2O+**H_2O**+F_2O_{-1})	c_{11}	f(**H_20**)[(a)]	CaO	1.87	1.87	2.24	*258.39*	*98.58*
(SiO_2+TiO_2)*(FeO(T)+MnO+MgO)	b_{11}	-2.43				Na_2O	9.04	9.05	9.81	*-1028.30*	
(SiO_2+TiO_2+Al_2O_3+P_2O_5)*(Na_2O+K_2O +**H_2O**)	b_{12}	f(**H_20**)[(a)]				K_2O	5.64	5.65	4.03	*-1023.45*	
(Al_2O_3)*(Na_2O+K_2O)	b_{13}	17.6				P_2O_5	0.28	0.28	0.13	*3182.54*	
						H_2O	0.26	0.26	0.95		
						F_2O_{-1}	0.12	0.12	0.20		

[(a)]Factor calculated as a function of water content

References

Aster, R., D. Zandomeneghi, S. Mah, S. McNamara, D. B. Henderson, H. Knox, and K. Jones (2008), Moment tensor inversion of very long period seismic signals from Strombolian eruptions of Erebus Volcano, *J. Volcanol. Geotherm. Res.*, *177*, 635–647, doi:10.1016/j.jvolgeores.2008.08.013.

Baker, D., Freda, C., Brooker, R and Scarlato, P. (2005). Volatile diffusion in silicate melts and its effects on melt inclusions. *Annals of Geophysics, 48*(4-5). doi:10.4401/ag-3227.

Barnes H (1999), The yield stress – a review or 'παντα ρει' – everything flows?, *J. Non*-479 *Newtonian Fluid Mech., 81*, 133-178.

Benyahia, S., Syamlal, M., O'Brien, T.J (2008), "*Summary of MFIX equations 2005-4" from URL https://mfix.netl.doe.giv/documentation/MFIXEquations2005-4-4.pdf"*, U.S. Dep. Of Energy, Washington, D. C.

Boichu M., Oppenheimer C., Tsanev V., Kyle P.R. (2010), High temporal resolution SO2 flux measurements at Erebus volcano, Antarctica, *J. Volcanol. Geotherm. Res*., *190*, 325–336, doi:10.1016/j.jvolgeores.2009.11.020.

Boyle, E., and M. Massoudi (1989), Kinetic theories of granular materials with applications to fluidized beds, Tech. Rep. DOE/METC—89/4088, DE89 00,977, 66 pp., U.S. Dep. Of Energy, Washington, D. C.

Burgisser, A, Oppenheimer, C., Aletti, M and Kyle, P.R. (in review), Backward tracking of gas chemistry measurements at Erebus volcano, *Geochem. Geophys. Geosyst*.

Calkins, J. A., C. Oppenheimer, and P. R. Kyle (2008), Ground-based thermal imaging of lava lakes at Mount Erebus Volcano, Antarctica in December 2004, *J. Volcanol. Geotherm. Res*., *177*, 695–704, doi:10.1016/j.jvolgeores.2008.02.002.

Caricchi, L., L. Burlini, P. Ulmer, T. Gerya, M. Vassalli, and P. Papale (2007), Non-Newtonian rheology of crystal-bearing magmas and implications for magma ascent dynamics, *Earth Planet. Sci. Lett.*, *264*, 402–419, doi:10.1016/j.epsl.2007.09.032.

Chapman, S., and T. G. Cowling (1970), The Mathematical Theory of Non-uniform Gases, 3rd ed., 423 pp., Cambridge Univ. Press, New York.

Clauser, C., and E. Huenges (1995), Thermal conductivity of rocks and minerals, in *Rock Physics and Phase Relations: A Handbook of Physical Constants*, AGU Ref. Shelf Ser., vol. 3, edited by T. J. Ahrens, pp. 105–126, AGU, Washington, D. C.

Costa, A. (2005), Viscosity of high crystal content melts: Dependence on solid fraction, *Geophys. Res. Lett.*, *32*, L22308, doi:10.1029/2005GL024303.

Costa, A., L. Caricchi, and N. Bagdassarov (2009), A model for the rheology of particle-bearing suspensions and partially molten rocks, *Geochem. Geophys. Geosyst*., *10*, Q03010, doi:10.1029/2008GC002138.

Csatho, B., T. Schenk, P. Kyle, T. Wilson, and W. B. Krabill (2008), Airborne laser swath mapping of the summit of Erebus volcano, Antarctica: Applications to geological mapping of a volcano, *J. Volcanol. Geotherm. Res.*, *177*, 531–548, doi:10.1016/j.jvolgeores.2008.08.016.

Dartevelle, S., and G. A. Valentine (2007), Transient multiphase processes during the explosive eruption of basalt through a geothermal borehole (Námafjall, Iceland, 1977) and implications for natural volcanic flows, *Earth Planet. Sci. Lett.*, *262*, 363–384, doi:10.1016/j.epsl.2007.07.053.

Dingwell, D.B. (2006), Transport Properties of Magmas: Diffusion and Rheology, Elements, *2*(5), 281-286, doi: 10.2113/gselements.2.5.281.

Dufek, J., and G. W. Bergantz (2005), Transient two-dimensional dynamics in the upper conduit of a rhyolitic eruption: A comparison of closure models for the granular stress, *J. Volcanol. Geotherm. Res.*, *143*, 113–132, doi:10.1016/j.jvolgeores.2004.09.013.

Dunbar, N. W., K. V. Cashman, and R. Dupré (1994), Crystallization processes of anorthoclase phenocrysts in the Mount Erebus magmatic system: evidence from crystal composition, crystal size distributions and volatile contents of melt inclusions, in *Volcanological and Environmental Studies of Mount Erebus, Antarctica, Antarct. Res. Ser.*, vol. 66, edited by P. R. Kyle., pp. 129–146, AGU, Washington, D. C.

Eschenbacher, A. (1998), Pre-eruptive volatile contents of fractionating, alkaline magma, Mount Erebus, Ross Island, M.S. thesis, Dep. Earth and Env. Sci. New Mexico, Institute of Mining and Technology, Socorro, New Mexico, U.S.

Forestier-Coste, L., S. Mancini, A. Burgisser and F. James (2012), Numerical resolution of a mono-disperse model of bubble growth in magmas, *Applied Mathematical Modeling*, doi:10.1016/j.apm.2012.01.031

Freda, C., D.R. Baker, C. Romano and P. Scarlato (2003), Water diffusion in natural potassic melts. *In: Volcanic Degassing (Oppenheimer, C., Pyle, D.M., and Barclay, J. eds). Geological Society, London, Special Publication*, **213**, 53-62

Gidaspow, D. (1994), Multiphase Flow and Fluidization: Continuum and Kinetic Theory Descriptions. Academic Press, 467 pp.

Gidaspow, D. (1994), Multiphase Flow and Fluidization: Continuum and Kinetic Theory Descriptions, 467 pp., Academic, San Diego, Calif.

Giordano, D., J. K. Russell, and D. B. Dingwell (2008), Viscosity of magmatic liquids: A model, *Earth Planet. Sci. Lett.*, *271*, 123–134, doi:10.1016/j.epsl.2008.03.038.

Gonnermann, H.M. and Manga, M (2007), The fluid mechanics inside a volcano, *Annual Review of Fluid Mechanics*, *39*, pp. 321-356, doi:10.1146/annurev.fluid.39.050905.110207.

Harpel, C.J., P.R. Kyle and N.W. Dunbar (2008), Englacial tephrostratigraphy of Erebus volcano, Antarctica, *J. Volcanol. Geotherm. Res.*, 177(3), 549-568, doi: 10.1016/j.jvolgeores.2008.06.001.

Iacono-Marziano, G., B. C. Schmidt, D. Dolfi (2007), Equilibrium and disequilibrium degassing of a phonolitic melt (Vesuvius AD 79 "white pumice") simulated by decompression experiments, *J. Volcanol. Geotherm. Res*., *161*(3), 151-164, doi: 10.1016/j.jvolgeores.2006.12.001.

Ingebritsen, S. E. and Rojstaczer, S. A. (1993), Controls on geyser periodicity, *Science*, *262*(5135), 889–892.

Ingebritsen, S. E. and S. A. Rojstaczer (1996), Geyser periodicity and the response of geysers to deformation, *J. Geophys. Res.*, 101(B10), 21,891–21,905, doi:10.1029/96JB02285.

Jackson, R. (1983), Some mathematical and physical aspects of continuum models for the motion of granular materials, in Theory of Dispersed Multiphase Flow, edited by R. E. Meyer, pp. 291–337, Academic, San Diego, Calif.

Jaupart, C., and Vergniolle, S (1989), The generation and collapse of a foam layer at the roof of a basaltic magma chamber, J. Fluid Mech., *203*, pp 347-380 doi:10.1017/S0022112089001497.

Jaupart, C. (1996), Physical models of volcanic eruptions, *Chem. Geol*., 128(1–4), doi: 10.1016/0009-2541(95)00175-1.

Joshi, J. B., "Computational Flow Modelling and Design of Bubble Column Reactors," *Chem. Eng. Sci.*, **56,** 5893 (2001).

Kazahaya, K., Shinohara, H., Saito, G (1994), Excessive degassing of Izu-Oshima volcano: magma convection in a conduit, *Bull. Vol*, 56, 207-216.

Kelly, P. J., P. R. Kyle, N. W. Dunbar, and K. W. W. Sims (2008), Geochemistry and mineralogy of the phonolite lava lake, Erebus volcano, Antarctica: 1972–2004 and comparison with older lavas, *J. Volcanol. Geotherm. Res*., *177*, 589–605, doi:10.1016/j.jvolgeores.2007.11.025.

Kieffer, S.W. (1982), Dynamics and thermodynamics of volcanic eruptions, *in* Morrison, D., ed., Satellites of Jupiter: Tucson, University of Arizona Press, p. 647–723.

Kieffer, S. W. (1984), Seismicity at Old Faithful Geyser: an isolated source of geothermal noise and possible analogue of volcanic seismicity, *J. Volcanol. Geotherm. Res*., 22(1–2), 59-95, doi: 10.1016/0377-0273(84)90035-0.

Kozono, T and T. Koyaguchi (2010), A simple formula for calculating porosity of magma in volcanic conduits during dome-forming eruptions, *Earth Planets Space*, *62* (5), 483-488, doi:10.5047/eps.2010.02.005.

Krieger, I. M., and T. J. Dougherty (1959), A mechanism for non-Newtonian flow in suspensions of rigid spheres, *Trans. Soc. Rheol.*, *3*, 137–152.

Kyle, P. R., J. A. Moore, and M. F. Thirlwall (1992), Petrologic evolution of anorthoclase phonolite lavas at Mount Erebus, Ross Island, Antarctica, *J. Petrol.*, *33*, 849–875.

Lensky, N.G., O. Navon, V. Lyakhovsky (2004), Bubble growth during decompression of magma: experimental and theoretical investigation, *J. Volcanol. Geotherm. Res.*, *129*(1–3), 15, 7-22, doi : 10.1016/S0377-0273(03)00229-4.

Llewellin, E. W., H. M. Mader, and S. D. R. Wilson (2002), The constitutive equation and flow dynamics of bubbly magmas, *Geophys. Res. Lett.*, *29*(24), 2170, doi:10.1029/2002GL015697.

Llewellin, E.W. and M. Manga (2005), Bubble suspension rheology and implications for conduit flow, *J. Volcanol. Geotherm. Res.*, *143*(1–3), 205-217, doi:10.1016/j.jvolgeores.2004.09.018.

Lun, C. K. K., S. B. Savage, D .J. Jeffrey and N. Chepuniy (1984), Kinetic theories for granular flow: inelastic particles in Couette flow and slighty inelastic particles in a general flow field, *J. Fluid Mech.*, *140*, 223– 256.

Oppenheimer, C., R. Moretti, P. R. Kyle, A. Eschenbacher, J. B. Lowenstern, R. L. Hervig, and N. W. Dunbar (2011), Mantle to surface degassing of alkalic magmas at Erebus volcano, Antarctica, *Earth Planet. Sci. Lett.*, *306* (3–4), 261-271, doi:10.1016/j.epsl.2011.04.005.

Mastin, L., and M. Ghiorso (2000), A numerical program for steady-state flow of magma-gas mixtures through vertical eruptive conduits, *U.S. Geological Survey Open-File Rep. 95-756*, pp. 1–53, Denver, Colorado.

Molina , I., A. Burgisser and C. Oppenheimer (2012), Numerical simulations of convection in crystal-bearing magmas: A case study of the magmatic system at Erebus, Antarctica, *J. Geophys. Res.*, doi:10.1029/2011JB008760, in press.

Namiki, A., and M. Manga (2006), Influence of decompression rate on the expansion velocity and expansion style of bubbly fluids, J. Geophys. Res., 111, B11208, doi:10.1029/2005JB004132.

Ochkov, V (2009), Applied mathematical software and a web-based interactive handbook for thermal engineering: Problems and solutions, Thermal Engineering, MAIK Nauka/Interperiodica, 53(6), pp. 485-492, http://twt.mpei.ac.ru/ochkov/WspIn/Enindex.html.

Oppenheimer, C., A. S. Lomakina, P. R. Kyle, N. G. Kingsbury and M. Boichu (2009), Pulsatory magma supply to a phonolite lava lake, *Earth Planet. Sci. Lett.*, *284*, 392–398, doi:10.1016/j.epsl.2009.04.043.

Oppenheimer, C., R. Moretti, P. R. Kyle, A. Eschenbacher, J. B. Lowenstern, R. L. Hervig, and N. W. Dunbar (2011), Mantle to surface degassing of alkalic magmas at Erebus volcano, Antarctica, *Earth Planet. Sci. Lett.*, *306* (3–4), 261-271, doi:10.1016/j.epsl.2011.04.005.

Oppenheimer, C. et al, in prep, Pulse of a volcano measured by lava lake pressure gauge!

Panter, K.S., B. Winter (2008), Geology of the side crater of the Erebus volcano, Antarctica, *J. Volcanol. Geotherm. Res*, 177 (3), 578-588, doi:10.1016/j.jvolgeores.2008.04.019.

Papale, P (1998), Volcanic conduit dynamics. In: Freundt, A., Rosi, M. (Eds.), From magma to tephra—modelling physical processes of explosive volcanic eruptions. Elsevier, Amsterdam, pp. 55–89.

Ruprecht, P., G. W. Bergantz, and J. Dufek (2008), Modeling of gas-driven magmatic overturn: Tracking of phenocryst dispersal and gathering during magma mixing, *Geochem. Geophys. Geosyst.*, *9*(7), Q07017, doi:10.1029/2008GC002022.

Seaman, S. J., M. D. Dyar, N. Marinkovic, and N. W. Dunbar (2006), An FTIR study of hydrogen in anorthoclase and associated melt inclusions, *Am. Mineral*, *91*(1), 12–20, doi:10.2138/am.2006.1765.

Stickel, J. and R. L. Power (2005), Fluid mechanics and rheology of dense suspensions, Annu. Rev. Fluid Mech, *37*, 129–49, doi: 10.1146/annurev.fluid.36.050802.122132.

Sweeney, D., P. R. Kyle, and C. Oppenheimer (2008), Sulfur dioxide emissions and degassing behavior of Erebus volcano, Antarctica, *J. Volcanol. Geotherm. Res.*, *177*, 725–733, doi:10.1016/j.jvolgeores.2008.01.024.

Sims, K. W. W., J. Blichert-Toft, P. R. Kyle., S. Pichat, J. Bluzstajn, P. Kelly, L. Ball, and G. Layne (2008), A Sr, Nd, Hf, and Pb isotope perspective on the genesis and long-term evolution of alkaline magmas from Erebus volcano, Antarctica, *J. Volcanol. Geotherm. Res.*, *177*, 606–618, doi:10.1016/j.jvolgeores.2007.08.006.

Syamlal, M. (1987), A review of granular stress constitutive relations. Technical Report: DOE/MC/21353-2372, Department of Energy, Springfield, VA.

Syamlal, M., W. Rogers, and T. J. O'Brien (1993), *MFIX documentation: Theory guide, DOE/METC-94/1004, DE9400,097*, pp. 49, U.S. Dep. of Energy, Washington, D. C.

Syamlal, M. (1994), *MFIX documentation: User's manual*, *DOE/METC-95/1013, DE9500,031*, pp. 87, U.S. Dep. Of Energy, Washington, D. C.

Syamlal, M. (1998), *MFIX documentation: Numerical technique*, *DOE/MC/31346-5824, DE98002029*, pp. 80, U.S. Dep. of Energy, Washington, D. C.

Tüzün, U., G. T. Houlsby, R. M. Nedderman, and S. B. Savage (1982), The flow of granular materials-II. Velocity distributions in slow flow, *Chem. Eng. Sci*., 37, 1691–1709.

Vergniolle, S (1996), bubble size distribution in magma chambers and dynamics of basaltic eruptions, *Earth Planet. Sci. Lett.*, *40*(1-4), 269-279, doi: 10.1016/0012-821X(96)00042-8.

Wilson, S.D.R. (1998), A mechanism for the lateral transport of gas bubbles in silicic lava rising in a vertical conduit, *Earth Planet. Sci. Lett*., 156(1–2), 13-18, doi:10.1016/S0012-821X(98)00019-3.

Witham, F., Woods, A.W., Gladstone, C., (2006a), An analogue experiment model of depth fluctuations in lava lakes, *Bull. Volcanol*., *69*, 51-56.

Witham, F., Llewellin, F., (2006b), Stability of lava lakes, *J. Volcanol. Geotherm. Res.*, *158*, 321-332.

Zoth, G., and Hänel, R. (1988), Thermal conductivity, in *Handbook of Terrestrial Heat-Flow Density Determination*, Kluwer Academic Publishers, edited by R. Hänel, L. Rybach, L. Stegena, pp. 449–453, Dordrecht.

Chapitre IV

Physical models addressing level fluctuations of the lava lake at Erebus, Antarctica: I. The role of degassing cycles

Résumé

Le volcan Erebus, en Antarctique, se caractérise par des variations de la composition géochimique des gaz émis en surface et une fluctuation du niveau du lac de lave. Modeler physiquement les oscillations du lac représente un défi, même dans des conditions de laboratoire relativement simples et précises [e.g., *Witham et al*., 2006] ou d'un cadre théorique. [e.g., *Witham et Llewellin,* 2006].]. En dépit d'une dynamique complexe, nous nous sommes penchés sur ce problème par le biais d'une analyse quantitative basée sur la convection liée à l'évolution géochimique des gaz relâchés en fonction de la profondeur. Notre modèle est basé sur l'hypothèse qu'un batch de magma dont le volume de liquide et cristaux est déterminé monte et dégaze en équilibre avec les températures alentour telles que les a déterminées *Burgisser et al*. [in review]. On a considéré que ces batch se comportent comme des sphères discrétisées obéissant aux lois physiques telles que les a définies Stokes. Des batch individuels de porosité 50-70 %vol. atteignant la surface produisent la variation de

hauteur et les variations chimiques du flux relâché telles que les a observées *Oppenheimmer et al*. [2009]. Notre modèle fournit un aperçu en profondeur de combien sont critiques les températures des courants de magma ascendant et descendant pour expliquer le comportement cyclique du niveau du lac.

Abstract

Erebus Volcano, Antarctica, presents periodical fluctuations at surface of both geochemical and physical level. The physical model of lake oscillation presents a challenge, even under relatively simple and clear laboratory circumstances [e.g., *Witham et al*., 2006] or theoretical framework [e.g., *Witham and Llewellin*, 2006]. Despite complex dynamics, we have focused on the problem through a quantitative analysis based on convection linked to the geochemistry evolution of the released gases as a function of depth. Our model is based on the assumption that a batch of magma of a fixed volume of melt ascends and degasses in equilibrium with the surrounding temperatures found by *Burgisser et al*. [in review]. Those batches were regarded as discretized spheres that obey the physics behind "Stokes-type" behavior. Individual batches with porosities of 70 vol.% reaching the surface produce the height oscillation and the chemistry variations of the released flux as observed by *Oppenheimmer et al*. [2009]. Overall our model provides deep insight that the temperatures of ascending and descending magma currents are the key parameter explaining the cyclic behaviour of the lake.

1. Introduction

The lava lake in the crater of the Erebus volcano has been continuously emitting a plume of gas for the last decades. The level of the lava lake fluctuates cyclically as the volume of released gas varies. These periodic variations are remarkably in phase with changes in the respective percentages of the volatiles composing the plume, variation of the heat loss at the surface of the lake and changes of the surface velocity of the magma [*Oppenheimer et al*., 2009]. During observations made in 2004 and 2009, the durations of the cycle have been reported to lasts between ~10 and 20 min, respectively [*Oppenheimer et al.*, 2009] and probably from year to year (P. Kyle, pers. communication). The amplitude of the pulsation

produced a surface level fluctuation of 1-1.5 m, with sporadic fluctuations up to ~3 m [*Oppenheimer et al.*, 2011, in prep.]. The short term pulsation can be described as a cyclic process starting by a steady rise of the magma surface which exposes incandescent magma through widening cracks before ending with the exposition of a large incandescent area corresponding to the release of a maximum amount of gas at surface. The culmination of the process is followed by the progressive drop of the level of the lake down to its previous value. Satellite surveys (Landsat TM) suggest that the lake area changes in terms of days by a factor of 2-4 [e.g., see Tables 1 and 2 given by *Harris et al.*, 1999]. Finally, there is a yearly variation of the lake area [e.g., see Figure 5 from *Sweeney et al*. 2008]. Since 2001, the semi-elliptical surface of the lake was estimated to ~770 m^2, with a large diameter of ~30-35 m [*Oppenheimer et al.*, 2009] and to ~2500 m^2 in December 2009 [*Oppenheimer et al.*, 2011, in prep.]. Pulsations are over imposed with longer oscillations corresponding to a few hours though this could be an artifact of the method of measuring the lake height [*Oppenheimer et al.*, 2011, in prep.]. Those oscillations have been attributed to the surging of magma flow in the uppermost conduit [*Oppenheimer et al.*, 2009] and will not be considered herein.

Our objective is to construct a simple convective model explaining the pulsation with the shortest period (the one in the time scale of minutes) based on the data collected in 2004 by *Oppenheimer et al*. [2009] (height, duration of the oscillation and gas flux measurement) and on the equilibrium temperatures of the gas composition found by *Burgisser et al*. [in review]. Our model involves convection of a magma batch (Stokes and Poiseuille-types) that ascend in the conduit by buoyancy due to porosity and temperature contrast between ascending and descending currents in order to degas at the lake surface a gas flux of 19-23 kg/s. Unlike the model by *Kazahaya et al*. [2004], our model considers the increasing vesicularity due to gas decompression of ascending magma under equilibrium conditions. As *Stevenson and Blake* [1998] we investigate if the degassing-induced convection provides an efficient mechanism for gas release at shallow levels as a function of the volatile budget coming from the deeper part of the magma system. Our difference with *Stevenson and Blake* [1998] is that our gas phase is multi-component (9 species) [*Burgisser et al*. 2008; in review]; the rheological properties of the ascending and descending currents are time-space dependent and are affected by temperature along the path between the deeper region of the magma system and the lake surface.

For our model, we require knowledge of the geometry of the plumbing system and constraints of temperature and crystal content associated to convective currents. In the 1987/1988 season, after a strombolian explosion had evacuated the lava lake, *Dibble et al*. [2008] observed that the lake had a funnel-shaped floor as deeper as its width and connected to a hole (uppermost conduit) that made half initial the diameter of the lake. There are no reports of the lake area for that particular season, however in 1989, *McClelland et al*. [1989] using satellite observation (Landsat TM) reported that the lake had a surface of 300 m^2. Assuming that during 1987/1988 season the lake had 300 m^2 and a circular shape this gives a lake diameter of 20 m and consequently the conduit diameter would be of 10 m according to *Dibble et al*. [2008] observations. Previous studies conceptualized underlying structures beneath the lake and reported that this one would be at least ~20 m deep [*Aster et al*., 2003; *Oppenheimer et al*., 2009]. Numerical simulations of convection in Erebus performed by *Molina et al*. [2012] suggests that a sufficiently large conduit of at least 10-m can sustain convection between the lake and a deeper reservoir located at 400 m. Their study shows that convective currents inside the conduit have maximum differences of 4 vol.% in crystal content and 56°C in temperature, a value close to the 65°C suggested by *Sweeney et al*. [2008] from heat flux balance.

2. Calculation of the convection model

2.1. Data

2.1.1. What do we know of height oscillations?

Based on the geochemical and observation data of *Oppenheimer et al*. [2009] and *Oppenheimer et al*, in prep., we know that magma batches periodically release at surface gas fluxes of varying compositions. The modal period to produce a batch of a given flux and gas composition is about every 10 minutes (Figure 1a). We call “bottom of the cycle” the batch of lowest flux (19.22 kg/s) which is composed of a gas named “conduit gas” by *Oppenheimer et al*. [2009] and “top of the cycle” the batch with the highest flux (22.83 kg/s). The difference in gas flux between the two types of gas compositions is what *Oppenheimer et al*. [2009] call “lake gas”, which is an indirect measurement giving a flux of ~3.6 kg/s. In this view, the “top gas” (referred to as “mixed plume” by *Oppenheimer et al*. [2009]) is conjectured to result from the superposition of geochemical signals corresponding to “conduit gas” and “lake gas” compositions. In the pause of the lake activity, the “conduit gas” is the only type of gas

emitted by the lake and it releases a gas flux of 19.22 kg/s [*Oppenheimmer et al*. 2009]. We define herein the "conduit gas" as "bottom gas".

Observations made in 2004 indicate that surface velocities are correlated with the changes in the chemical composition of the gases released at surface (Figure 1a) and that these changes occur over cycles of 10 min [*Oppenheimmer et al*. 2009. Observations made in 2009 (Figure 1b) indicate that the surface of the lake, much larger than in 2004, oscillates with a mean period of 20 min, in phase with the changes in gas composition [*Oppenheimer et al*, in prep].

A period of quiescence of 2 to 10 min being observed between two pulses, a full cycle of oscillation in 2009 can be considered to last 22 to 30 min. If visual observations and measurements allow us to link the variations in gas composition and fluxes with the changes of velocity at the surface of the lake and the variation of its level, we cannot know with certainty if the former results from the inflation and deflation of the lake. However, we know that the two types of batches cause an oscillation within 1 to 1.5 m; the periods of oscillation increase by a factor of 2.2 to 3 between 2004 and 2009, while the area of the lake increased from ~770 m^2 to ~2500 m^2 (a factor of ~ 3). This suggests that the ascent rates of the batches remain relatively constant.

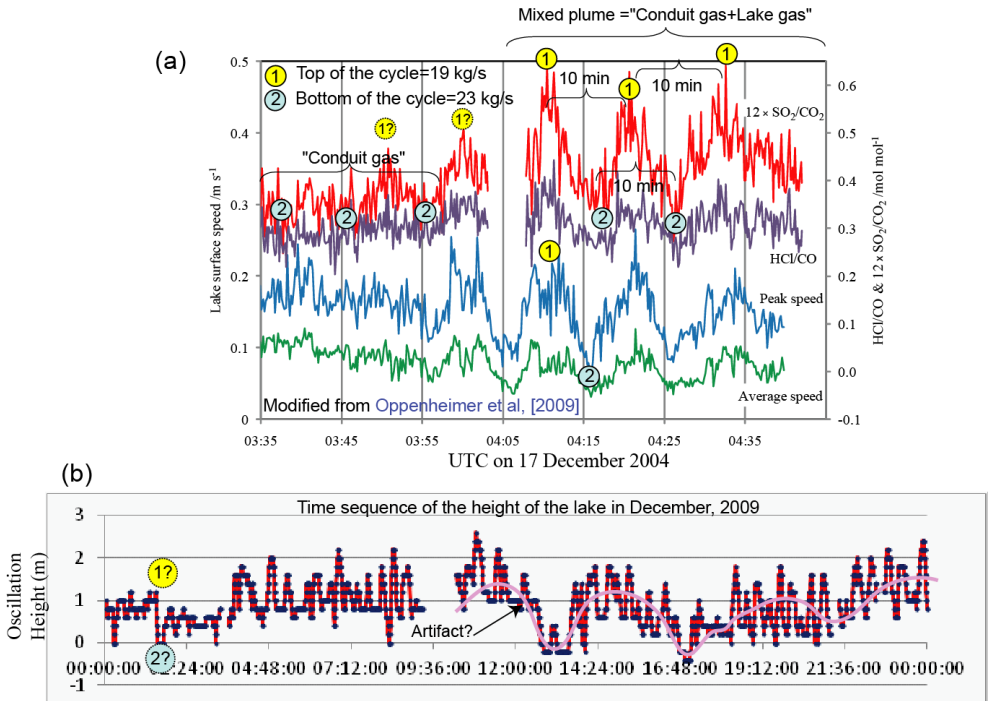

Figure 1. Time series of lake for: **(a)** geochemical and average speed data in December 2004 modified from *Oppenheimer et al*. [2009]) **(b)** time sequence of the height oscillations in 2009 modified from *Oppenheimer et al.*, in prep.

High resolution videos made in December, 2010 provide a deep insight regarding the arrival of 2 consecutive batches of magma during the lava lake level fluctuation (Figure 2a-2o). The duration of the films is limited to a maximum of 12 minutes, but the film corresponding to 2010_12_20_8111.MOV from the data base furnished by Oppenheimer provides a good sequence from which we could cross-correlate the information given by *Oppenheimer et al*. [2009] (Figure 2p-2r).

The fluctuation of the level is not regular over the whole surface of the lake. The center of the lake surges like a dome propagating a wave that spreads radially; it has about 14 m in diameter (Figure 2a). The wave is caused by the ascent of a gassy batch that reaches surface and degasses. The degassed melt resulting from the previous batch sinks at the edge of the lake (Figure 2b-2e) as the magma of the current batch spreads and overlaps the former (Figure 2f-2h); the level then seems to remain constant (Figure 2f-2i). The first wave of degassed magma reaches the edge of the lake after approximately ~5 minutes (Figure 2j). This period of 5 min corresponds exactly to the modal duration of half a cycle from 2004. Then the lake surface flattens until its center is lifted again by the arrival of a new batch which has not released any of its gas yet; it is therefore hotter, less viscous and less dense. Every batch disturbs the surface and results in its elevation with a rather similar shape and sequence than the one described above (Figure 2k); probably in the range of 1-1.5 m as suggested by *Oppenheimer et al.* (in prep). However, a sudden and localized release of gas can occur (Figure 2i) at different spots of the surface. There is a continuum between the small bubble bursting in Figure 2i and large bubbles that evacuate the lake in Strombolian explosions [e.g., *Gerst et al*., 2008].

The time scale for a magma batch arrival is reasonably congruent with the appearing of concentrical waves at the surface of the lake, which show a period of about ~5 min between consecutive batches or probably of ~10 min between batches of the same composition. We assume that two consecutive waves can be caused by the ascent of batches of gasified magma of different composition in synchrony with the level change. The image resolution and/or the size of the bubbles forming the batches could not allow us to appraise them with certainty. The cyclic radiative heat output measurement performed by *Oppenheimer et al*. [2009] (Figure 2p) and the time difference between consecutive magma batches of different composition define the modal period of 10 min for a batch of identical composition (Figure 2q) to reach surface from a specific location below surface and to be released. How those

batches can be geochemically combined or intercalated and physically conceived will be explained in the next two sections, respectively.

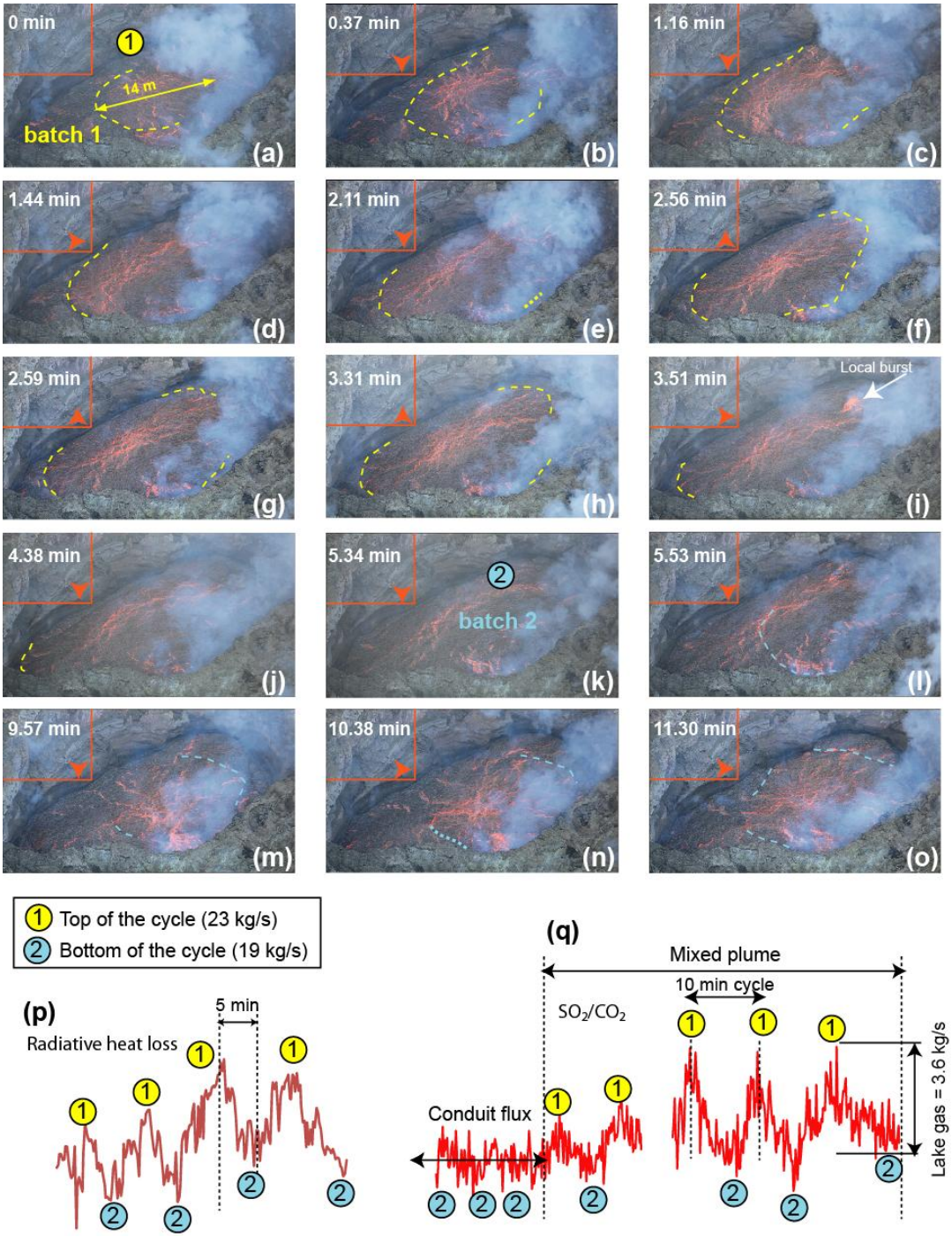

Figure 2. Summary of what we know of the lava lake oscillation: (a) to (o) sequence of lake oscillation associated to the arrival of two magma batches in December, 20th 2010. Horizontal and vertical red lines form a reference position; the red arrow indicates if the edge of the lake moves up, down, or remains still in relation with this reference. (p)-(q) pre-conceptual geochemical variations based on the data recorded in 2004 by *Oppenheimer et al*. [2009] (scale is kept).

2.1.2. Which pre-conceptual model do we have?

Burgisser et al. [2011] found through the redox state of gas compositions forming the "top and bottom of the cycles" that they result from different equilibrium temperatures. Thus "top gas" would be generated at temperature conditions at the lake surface of 1085°C, the "bottom gas" at 1069°C and the "lake gas" at 1015°C. The difference in equilibrium temperature or radiative heat loss for the 2 batches seems to be a good criteria to differentiate them (Figure 2p) even though the variation of SO_2/CO_2 between top and bottom is small (Figure 2q). This will allow us to postulate that the flux corresponding to the "top of the cycle" results of two types of gases that are simultaneously released ("top gas" plus "lake gas" or "bottom gas" plus "lake gas") or one type of gas only released at once ("top gas"). We will consider that these magma batches with a specific composition can reach the lake surface in the form of a "blob" (sphere) or a "continuous flow" (Poiseuille flow) of a given porosity (Figure 3) in order to cause the oscillation of 1-1.5 m. We will treat independently the physics behind each type of batch in the next section. Based on this information, we had to consider several constraints to be in agreement with the following parameters or criteria:

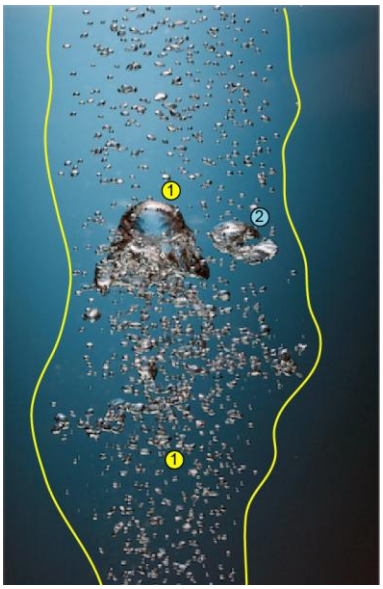

Figure 3. Ascension of simultaneous bubbly blobs within a continuous bubbly flow.

(i) The equilibrium temperatures found by *Burgisser et al.* [2011] and the ΔT found by *Molina et al.* [2012].

(ii) The geometry of the plumbing system that indicates a lake depth of ~20 m [*Aster et al.*, 2003; *Oppenheimer et al.*, 2009] and suggests that the magma should ascend through a minimum diameter of 10-m [*Molina et al.*, 2012]. We name "conduit" such an ascending diameter though it is not the physical conduit linking the magma chamber and the lake.

(iii) The emitted gas flux of 19.22 and 22.83 kg/s given by *Oppenheimer et al.* [2009].

(iv) The geochemical cyclical variations between "bottom", "top" and "lake" gas compositions.

(v) A variation of 1 or 1.5 m of the level of the lake corresponds to the release of 770 or 1155 m^3 as a direct result of the accumulation of gas below the surface.

(vi) The arrival of a magma batch with specific porosity in the form of a "blob" (sphere) and/or a "continuous flow" (Poiseuille flow).

(vii) The gas hosted in the porosity of the blob is composed of 9 chemical species (H_2O, H_2, O_2, SO_2, H_2S, S_2, CO_2, CO, and CH_4) and the melt contains dissolved H_2O, CO_2, H_2, and S_2 [*Burgisser et al*., in review]. Redox conditions during magma decompression at Erebus have been defined through geochemical modeling by *Burgisser et al*. [in review]. Thus, for a specific gas composition, the average molar mass of the gas phase M_{avg}, wt%H_2O, the total gas weight fraction W_{gT} and porosities as a function of confining pressure P are known (Table 1).

Table 1. Initial conditions at P = 0.065 MPa from *Burgisser et al*., [in review]. NA means not applicable. M_{av} is molecular average and W_{gT} is total gas weight fraction as a function of confining pressure P and porosity ϕ.

Gas Specie (mol fraction) / Parameter	**Top gas**	**Bottom gas**	**Lake gas[(a)]**
H_2O	0.730	0.555	0.859
H_2S	0.002	0.002	0.034
SO_2	0.011	0.009	0.025
H_2	0.024	0.020	0.037
O_2	7.9×10^{-11}	3.95×10^{-11}	4.12×10^{-11}
S_2	1.4×10^{-4}	1.7×10^{-4}	0.9×10^{-4}
CO	0.014	0.027	0.0025
CO_2	0.219	0.388	0.034
CH_4	9.8×10^{-6}	$1.8 \times 1\ 0^{-5}$	1.8×10^{-5}
Wt.% H_2O	0.0229	0.019	0.0256
M_{avg}(kg/mol)	0.030	0.035	0.026
W_{gT} @ ϕ=0.02	1.3×10^{-4}	NA	NA
W_{gT} @ ϕ=0.05	3.4×10^{-4}	NA	NA
W_{gT} @ ϕ=0.1	7.0×10^{-4}	9.0×10^{-4}	6.5×10^{-4}
W_{gT} @ ϕ=0.2	1.6×10^{-3}	1.9×10^{-3}	1.4×10^{-3}
W_{gT} @ ϕ=0.3	2.7×10^{-3}	3.2×10^{-3}	2.5×10^{-3}
W_{gT} @ ϕ=0.4	4.2×10^{-3}	5.0×10^{-3}	3.8×10^{-3}
W_{gT} @ ϕ=0.5	6.3×10^{-3}	7.4×10^{-3}	5.7×10^{-3}
W_{gT} @ ϕ=0.6	9.5×10^{-3}	1.1×10^{-2}	8.5×10^{-3}
W_{gT} @ ϕ=0.7	1.5×10^{-2}	1.7×10^{-2}	1.3×10^{-2}
Equilibrium temperature (°C)[(b)]	1085	1069	1015
Measured flux (kg/s)	22.83	19.22	
Deducted flux (kg/s)			3.6
Hypothetical flux (kg/s)	3.6		

[(a)] Lake gas was estimated by *Oppenheimer et al*. [2009] by differencing the component fluxes of the emitted mixed plume and conduit gas**.**

[(b)] Equilibrium temperature determined by *Burgisser et al*. [in review].

As magma batches may rise at different speeds, they can be perfectly synchronized or alternated. We consider that the geochemical variation of the cycle could be the result of 5 scenarios (i.e. cyclic behaviors):

Scenario 1: Explains the "bottom of the cycle" and "top of the cycle" by the alternating arrival of blobs reaching surface every 10 minutes and shifted in time by 5 minutes (Figure 4a). Each one will emit a gas flux of 19.22 and 22.83 kg/s and will cause an oscillation of 1 or 1.5 m when reaching surface independently.

Scenario 2: Explains the "bottom of the cycle" as the succession of blobs reaching the surface every 5 minutes. The "top of the cycle" would be caused by the addition of blobs reaching surface every 10 minutes (Figure 4b). Each one will emit a gas flux of 19.22 and 3.6 kg/s and will cause an oscillation of 1 or 1.5 m when reaching surface independently. The non-occurrence of the blob releasing 3.6 kg/s would result in the sole release of the gas associated to the "bottom of the cycle".

Scenario 3: Explains the "bottom of the cycle" as the succession of blobs reaching the surface every 5 minutes. The "top of the cycle" would be caused by the addition of blobs reaching surface every 10 minutes with "lake gas" composition (Figure 4c). Each one will emit a gas flux of 19.22 and 3.6 kg/s and will cause an oscillation of 1 or 1.5 m when reaching surface independently. The non-occurrence of the blob releasing 3.6 kg/s would result in the sole release of the gas associated to the "bottom of the cycle".

Scenario 4 and 5: Explain the "bottom of the cycle" (19.22 kg/s) as a continuous flow (Poiseuille-type) over which another blob would be superimposed (Figure 3d), with the composition of gas corresponding to a "gas top" (Figure 4b) or "lake gas" (Figure 4c) of 3.6 kg/s. They would cause an oscillation of 1 or 1.5 m independently. These specific scenarios mainly aim at explaining the flux of 23 kg/s every 10 minutes; the fluctuation is not seen as the succession of alternated blobs but can be explained by the eventual occurrence of the blob with composition "top of the cycle" or "lake gas".

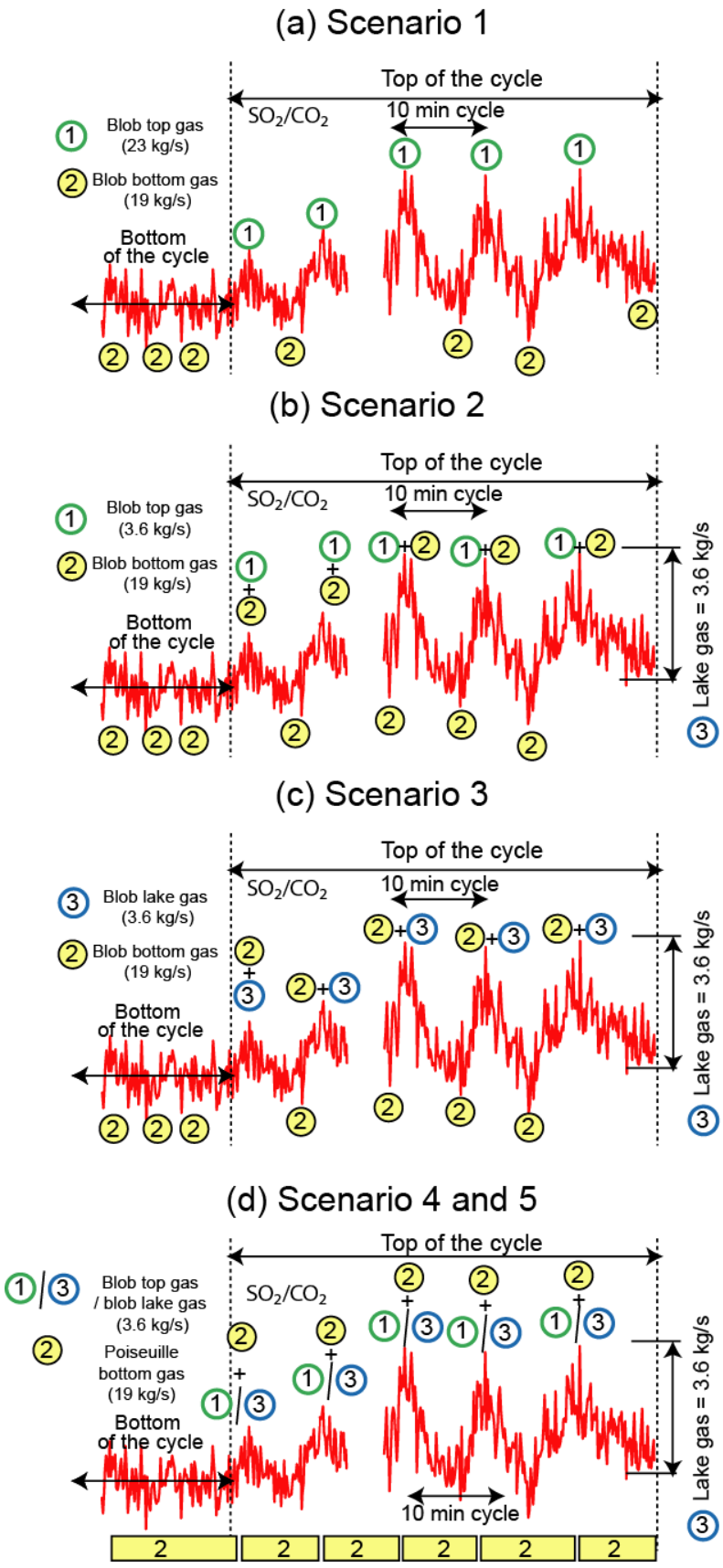

Figure 4. Sketch of the geochemical sequence for the 5 scenarios analyzed in this study.

10 cases were analyzed; they are differentiated by the type of ascending flux (Poiseuille/blob), the type of composition ("top of the cycle", "bottom of the cycle" and "lake gas"), the associated emitted gas flux (3.6, 19 or 23 kg/s) in order explain the oscillations of two different amplitudes 1 and 1.5 m (Table 2). We will test each one of the above scenarios after having described our model and evaluated which one of them better explains the lake oscillations linked to geochemical variations in Erebus.

Table 2. Compilation of the 10 cases analyzed in this study. These cases are combined among them in order to yield 5 scenarios per oscillation height.

Case Number	Gas composition	Gas flux (kg/s)	Type of batch	Oscillation height (m)
1	Bottom	19	blob	1.0
2	Top	23	blob	1.0
3	Bottom	19	blob	1.5
4	Top	23	blob	1.5
5	Top	3.6	blob	1.0
6	Top	3.6	blob	1.5
7	Lake gas	3.6	blob	1.0
8	Lake gas	3.6	blob	1.5
9	Bottom	19	Poiseuille	1.0
10	Bottom	19	Poiseuille	1.5

2.2. Theory

Volumetric magma flux by convection can be calculated thanks to two end-member fluid dynamics models: i) Stokes flow in which a sphere of non-degassed magma rises in a well-fitted manner in the core annular flow [e.g., *Kazahaya et al*., 1994]. This model is valid for viscous spheres rising within incompressible flows. ii) Poiseuille flow through double concentric pipe in which a less viscous and lighter magma ascends in the core and a more viscous, denser magma descends in the outer part along the walls. This model is only valid for incompressible flows.

2.2.1. Stokes approximation

Koyaguchi [1985] experimentally observed that magma can rise by batches. We consider that these batches include melt and gas and have a spherical geometry.

We used the derivation of Stokes' theory used by *Kazahaya et al*. [1994] to calculate the velocity of the blob and explain the gas flux repeatedly varying from 19.22 kg/s (bottom of the cycle) to 22.83 kg/s (top of the cycle) observed in Erebus by *Oppenheimer et al*. [2009]. The difference with Kazahaya's treatment is the presence of bubbles in a sphere (Figure 5).

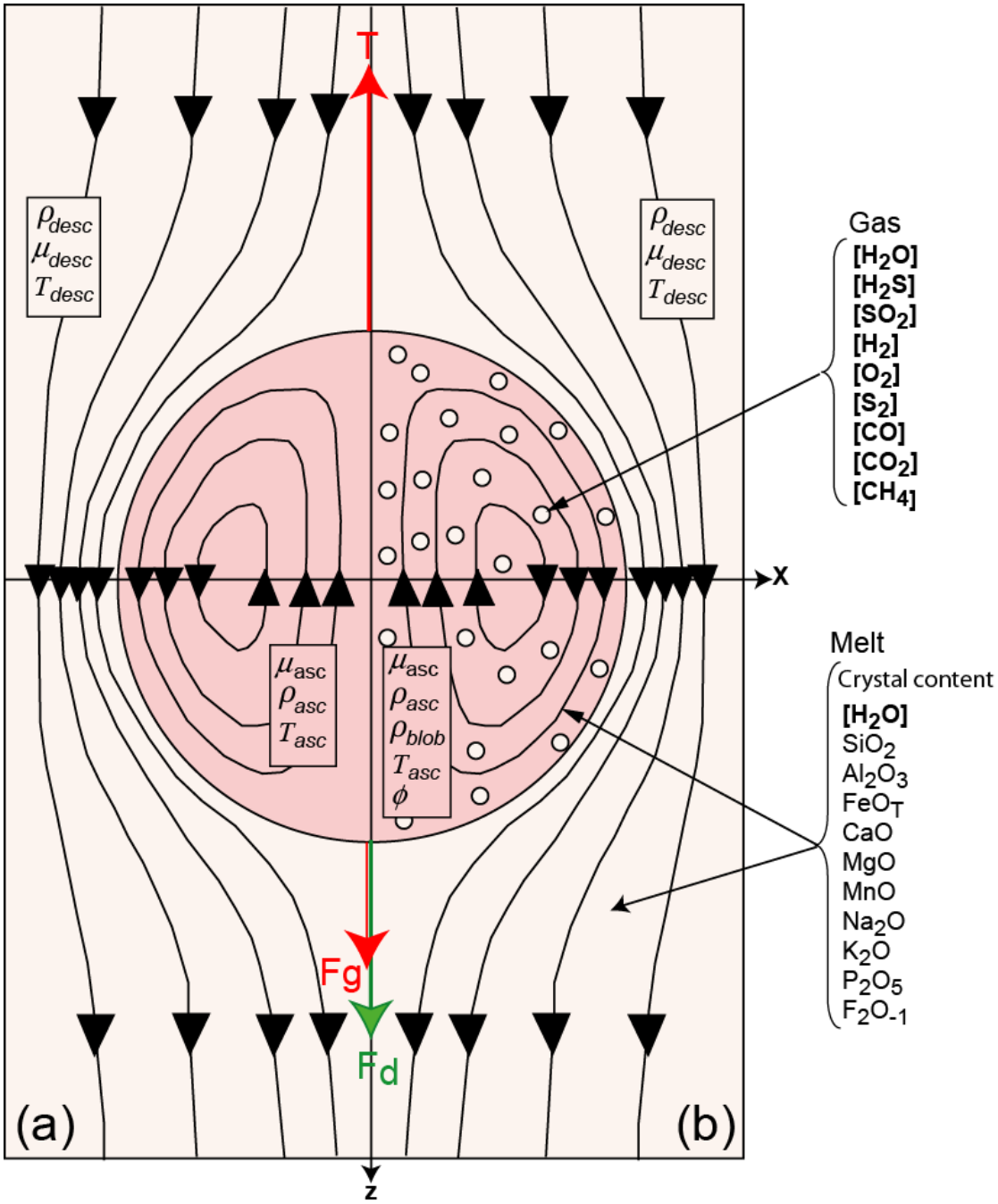

Figure 5. Streamlines in and around a viscous sphere translating through Newtonian fluid (Stokes case; redrawn from *Weinberg and Podladchikov*, [1994]): **(a)** Kazahaya's approximation takes into account the dissolved content of water for the melt part but has not bubbles, **(b)** Our approach of viscous sphere containing melt plus

bubbles in which the content of H_2O is variable for the melt part while other oxides are fixed as constant, and the content of the 9 species (Table 1) for bubbles varies as a function of depth [*Burgisser et al*, in review]. The arrows represent the main forces acting on the sphere. Red arrows are the body forces ($F_b = T - F_g$) and green arrow is the surface forces (drag forces; F_d).

A blob of density ρ_{blob}, viscosity μ_{asc}, temperature T_{asc}, porosity ϕ (made of gas of specific composition with a molecular average, M_{avg}, and weight fraction, W_{gT}), hosting a crystal bearing hydrous melt of density ρ_{asc} rises with a velocity U_{blob} within an incompressible crystal bearing anhydrous melt of density ρ_{desc}, viscosity μ_{desc} and temperature T_{desc} (Figure 5). The blob has a radius R_{blob} evolving as a function of depth, z, as the result of the expansion of the gas hosted inside itself. The fluid pressure, P, is a function of depth. We take the blob filled of melt and a bubble cluster (but without overpressure in the bubble) by analogy to that of a single bubble/sphere (e.g., Stokes model). The maximum difference in crystal content, ε_s, between the ascending and descending melts being about 4 vol.% [*Molina et al*. 2012], we assume it as constant and equal to 30 vol.%. For descending melt, we assume the magma to be completely degassed so that wt.% H_2O is fixed to 0.

We discretized our domain in space (the vertical axis 0-z is positive downwards) as follows:

$$z = \frac{P - P_{atm}}{\rho_{desc}\, g} \quad (1)$$

where z is the depth of the blob (center of the sphere), P is the hydrostatic pressure at a depth z ($P = \rho_{desc}\, g\, z + P_{atm}$) due to the melt surrounding the blob, P_{atm} is the local atmospheric pressure at 0.065 MPa, ρ_{desc} is the density of crystal bearing anhydrous melt that surrounds the blob and g is the gravity constant. ρ_{desc} is calculated through Conflow [*Mastin and Ghiorso*, 2000] by fixing the descending temperature, T_{desc}, the phonolitic melt composition (major oxides), the properties of the anorthoclase crystals with content of 30 vol.% and a water content of 0 wt.%. It is taken as a constant along the conduit (for the descending flow).

At low pressure, we can approximate the density of gas, ρ_{gas}, as a function of pressure by applying the ideal gas law:

$$\rho_{gas}(z) = \frac{P\, M_{avg}}{R\, T_{asc}} \quad (2)$$

where P is the hydrostatic pressure, M_{avg} is the average molecular weight of gas as a function of pressure, R is the universal constant gas law (8.314 J/K mol) and T_{asc} is the temperature inside the blob. Therefore we obtain the volume of gas, V_g, occupied by such a mass of gas as a function of depth, z, as follows:

$$V_g(z) = \begin{cases} V_{go}, & z = 0 \\ V_{go}\, \frac{\rho_{gas}|_{z=0}}{\rho_{gas}|_z}, & z > 0 \end{cases} \quad (3)$$

where the initial gas volume, V_{go}, is 770 or 1150 m^3, depending of the oscillation height considered (1 or 1.5 m).

Following *Burgisser et al*. [2008], the gas volume fraction, ϕ, of the ascending blob can be calculated at each pressure according to:

$$\phi(z) = \left[1 + \frac{M_{avg}\, P\, (1 - W_{gT})}{R\, T_{asc}\, \rho_{asc} W_{gT}}\right]^{-1} \quad (4)$$

where ρ_{asc} is the density of hydrous melt inside the blob calculated with Conflow [*Mastin and Ghiorso*, 2000] by fixing the ascending temperature, T_{asc}, the phonolitic melt composition (major oxides) [see the mean values reported in Table 2, pag. 594, given by *Kelly et al.* 2008], the properties of the anorthoclase crystals with content of 30 vol.% [see Table 3 from *Molina et al*., 2012] and the amount of water that contains the magma at $z = 0$ (Table 1), and taken as a constant along the ascending flow as the change in melt water content induces negligible density variations. M_{avg} and W_{gT} are the average molar mass of the gas phase and the total gas weight fraction, respectively, calculated as a function of P at each depth.

As it ascends, the blob grows by expansion of the gas it contains. The melt is taken as incompressible so that it is displaced by the expanding gas. We obtain the constant volume of melt with:

$$V_{melt} = V_{go}\left(\frac{1}{\phi|_{z=0}} - 1\right) \quad (5)$$

By combining equations (3) and (5) we calculate the total volume of the blob (melt plus gas), and derive its radius, R_{blob}:

$$R_{blob}(\mathrm{z}) = \sqrt[3]{\frac{3}{4\pi}\left[V_g(z) + V_{melt}\right)} \quad (6)$$

The relationship to calculate the effective dynamic viscosity of the magma, μ_m, was obtained by multiplying the relative contribution provided by three phases: melt, crystals and bubbles. The viscosity given by the melt part is obtained through the VFT equation from *Giordano et al*. [2008] calibrated in Erebus by *Molina et al*. [2012], in which the viscosity of the melt is a function of the major oxides including dissolved water. Since dissolved H_2O varies as a function of depth, we calculated different B and C coefficients for the VFT equation (see equation (11) given by *Molina et al*. [2012] and details about how those coefficients vary are given in Table A2 from Chapter III). Then, this equation was corrected to take into account the presence of crystals stated by *Krieger and Dougherty* [1959] (see equation (2) given by *Molina et al*. [2012]). Following *Shimozuru* [1978], the viscosity increases with the presence of gas bubbles, thus the viscosity equation was modified for the presence of bubbles, which represent the term $\left(1 + \phi(z)\right)$ under the assumption of a small Reynolds number:

$$\mu_m = \begin{cases} \mu_{asc}(\mathrm{z}) = \left[10\exp\left(A + \frac{B}{T_{asc} - C}\right)\right][1 + \phi(\mathrm{z})]\left[1 - \frac{\varepsilon_s}{1-\varepsilon_m^*}\right]^{-[\eta](1-\varepsilon_m^*)} \\ \mu_{desc} = 10\exp\left(A + \frac{B}{T_{desc} - C}\right)\left[1 - \frac{\varepsilon_s}{1-\varepsilon_m^*}\right]^{-[\eta](1-\varepsilon_m^*)} \end{cases} \quad (7)$$

where μ_{asc} and μ_{desc} are ascending and descending viscosities, A = -4.55 (coefficient independent of composition), ε_s is the crystal fraction (equal 30 vol.%), ε_m^* is the void fraction at maximum packing (equal 0.35), $[\eta]$ is the Einstein coefficient (equal 2.5), T_{asc} and T_{desc} are the temperatures for ascending and descending magma, respectively, related by a difference that we consider fixed to 56°C. For descending melt, we assume the magma to be completely degassed so that wt.% H_2O is fixed as 0 in order to calculate the descending constant melt viscosity μ_{desc}.

2.2.1.1. Terminal velocity of ascending blob

According to Archimedes, the resulting buoyancy force acting on the sphere is proportional to the difference between the weight of displaced fluid, and the weight of the sphere, F_d: $F_b \sim 4/3\ \pi R_{blob}^3(\rho_{desc} - \rho_{blob})g$ (see Chapter I). In order to take into account the internal as well as the external motion in a spherical viscous sphere, Hadamard and Rybczynski defined the drag forces as the product between the force acting on the motion of a solid sphere into stagnant fluid: $6\pi R_{blob}U_{blob}$ which is well-known as Stokes law (*Lamb* [1945], pag. 598) and the ratio of viscosities between ascending sphere and descending fluid: $6\pi R_{blob}U_{blob}\left(2\mu_{desc} + 3\mu_{asc}\right)/\left(3\mu_{desc} + 3\mu_{asc}\right)$ (*Lamb* [1945], pag. 601). Hadamard and Rybczynski's approximation neglects the surface tension and inertia force of the sphere and it is valid for a bubble with mobile surface and Reynolds number lower than 1. For increasing Reynolds number, the inertial forces become more important and Oseen also extended Stokes analysis to include the first-order inertial effects (*Crowe et al.*, [1997], pag.70; *Lamb* [1945], pag. 617). Oseen's approximation then becomes a multiplicative factor to the drag forces defined by Stokes: $6\pi R_{blob}U_{blob}(1 + 3/16\,Re)$ (*Lamb* [1945], pag. 617). This approximation is valid for Reynolds number up to 5 [*Crowe et al.*, 1997].

As *Lamb* [1945] defined the drag forces acting either in a viscous sphere or sphere in which inertial forces become important, *Kazahaya et al.* [2004] (pag. 213, equation 16) defined a more complete expression of the drag forces, F_d acting in a moving viscous sphere through an infinite Newtonian fluid: $F_d \sim 6\pi R_{blob}U_{blob}\{(2\mu_{desc} + 3\mu_{asc})/(3\mu_{desc} + 3\mu_{asc})\}(1 + 3/16\,Re)$. As the force associated to surface tension is negligible because our 2 fluids (ascending and descending) are miscible silicate melts, the total force acting on the motion of the blob in order to maintain it steady-state motion in the stream is then given by the balance:

$$\overbrace{\frac{4}{3}\pi R_{blob}^3(\rho_{desc} - \rho_{blob})g}^{\text{Excess of buoyancy of the sphere over its graviy}} - \overbrace{\overbrace{\overbrace{6\pi R_{blob}U_{blob}\mu_{desc}}^{\text{Resistance of a solid sphere}}\ \frac{2\mu_{desc}+3\mu_{asc}}{3\mu_{desc}+3\mu_{asc}}}^{\text{Resistance of a viscous sphere with internal and external motions}}\left(1 + \frac{3}{16}Re\right)}^{\text{Resistance of a viscous sphere with internal and external motions including first order inertial}} = 0 \qquad (8)$$

where U_{blob} is the terminal velocity of the blob, R_{blob} is the radius of the blob, ρ_{blob} is the blob density, ρ_{desc} is the density of descending melt, μ_{asc} and μ_{desc} are the viscosities of ascending and descending flows, and Re is the blob Reynolds number defined as:

$$Re = \frac{2R_{blob}U_{blob}\rho_{desc}}{\mu_{desc}} \quad (9)$$

Terminal velocity is defined as the steady velocity that the blob reaches when there is a balance between buoyancy and drag forces (equation 8). Stokes drag formula can be used to determine the velocity of a sphere rising buoyantly through a viscous incompressible fluid at each confining pressure P if the ascent velocity of a blob is governed by the balance of these 2 forces. We calculated the velocity of the blob, U_{blob}, based on the approach of Stokes model. This is found by solving the polynomial of second order after re-arranging equation (8) and (9) [as *Kazahaya et al*. 2004]:

$$\frac{3}{8}R_{blob}\,\rho_{desc}\,M\,U_{blob}^2 + \mu_{desc}\,M\,U_{blob} - \frac{2}{3}gR_{blob}^2(\rho_{desc} - \rho_{blob}) = 0 \quad (10)$$

In which $M = \frac{2\mu_{desc}+3\mu_{asc}}{\mu_{desc}+\mu_{asc}}$.

The positive solution of that polynomial is given by:

$$U_{blob}(\mathrm{z}) = \frac{4}{3}\frac{\sqrt{(\mu_{desc}M)^2+\rho_{desc}\,R_{blob}^3(\rho_{desc}-\rho_{blob})Mg}-\mu_{desc}M}{R_{blob}\,\rho_{desc}\,M} \quad (11)$$

where the density of the blob, ρ_{blob}, was calculated as:

$$\rho_{blob}(\mathrm{z}) = \phi\rho_{gas} + (1-\phi)\rho_{asc} \quad (12)$$

Once we know the velocity of the blob as a function of depth, we can calculate the rising time. At the instant t_{i-1} the velocity of the blob is $U_{blob\,i-1}$, at the instant t_i the velocity of the blob is $U_{blob\,i}$. The average velocity $\langle U_{blob}\rangle$ in the time interval $\Delta t_i = t_i - t_{i-1}$ is $\langle U_{blob}\rangle = [U_{blob}(z_i) + U_{blob}(z_{i-1})]/2$ and the time for a blob to ascend from z_{i-1} to z_i is given by:

$$t_i \approx \frac{z_i - z_{i-1}}{\langle U_{blob} \rangle} + t_{i-1} \quad (13)$$

Considering a cylindrical shell coincident with the circular section of the sphere, we can calculate the total gas flux reaching the surface, by removing the liquid part contained in this blob as:

$$Q_{mgas_{St}} = \pi R_{blob}^2 U_{blob} \phi \rho_{gas} \quad (14)$$

2.2.1.1. Method of solution

Our aim is to investigate how a fluid dynamics model linked to the geochemical model of *Burgisser et al*. [in Review] can explain the gas fluxes measured by *Oppenheimer et al*. [2009]. Our method of solution is to fix the initial values of V_{go} and $T_{desc} = T_{asc} - 56$. We then used the chemical model outputs as function of pressure for up to 9 values of initial gas content, W_{gT}, for each gas compositions : top, bottom and lake gas (Table 1). These initial conditions are summarized in Table 1. We then choose different blob temperatures, T_{asc}, and we get T_{desc} from the initial temperature difference, from which all the other variables were calculated. We get ρ_{gas} from equation (2), ϕ from equation (4), V_{melt} from equation (5), R_{blob} from equation (6), μ_{asc} and μ_{desc} from equation (7), ρ_{desc} and ρ_{asc} from Conflow, U_{blob} from equation (11) and ρ_{blob} from equation (12). By combing equations (2), (4), (6), (11) and (14), and after algebraic arrangement, the gas flux at the surface becomes:

$$Q_{mgas_{St}} = \frac{4}{3}\pi R_{blob} M_{avg} \frac{\left[(\mu_{desc} M)^2 + R_{blob}^3 \rho_{desc}(\rho_{desc} - \rho_{blob}) g M\right]^{1/2} - \mu_{desc} M}{\rho_{desc} M T_{asc} R} \left[\frac{M_{avg}(1 - W_{gT}) P}{\rho_{asc} T_{asc} W_{gT} R} + 1\right]^{-1} \quad (15)$$

The ascending blob temperature is thus adjusted until the calculated flux $Q_{mgas_{St}}$ matches the observed values of 3.6, 19.22 and 22.83 kg/s. This temperature is then compared to that given by the chemical model (1015, 1069 and 1085°C; Table 1). Runs with the initial gas content yielding T_{asc} closest to the relevant equilibrium temperature from the chemical model are considered as plausible, while the others are discarded.

2.2.2. Poiseuille approximation

The volumetric flow rate of magma of viscosity μ_{asc} through a straight conduit of uniform circular section is the total volume of fluid passing across any section per unit of time:

$$Q_{v_p} = \frac{\pi R_c^4}{8\mu_{asc}} \frac{dP}{dZ} \quad (16)$$

Following *Kazahaya et al*. [2004], we consider that the ascending fluid is the center part of a core annular flow. R_c is the core radius and dP/dZ is the pressure gradient that drives the magma upward. The differential buoyancy of ascending core relative to the annular descending magma is given by $dP/dZ = (\rho_{desc} - \rho_{core})g$ (*Turcotte et al*. [2002]); then we can calculate the total volume flux as *Kazahaya et al*. [2004] and the mass of gas reaching the surface as a "continuous flux" by removing the liquid part:

$$Q_{mgas_P} = \frac{\pi(\rho_{desc} - \rho_{core})gR_{core}^4}{8\mu_{asc}} \phi \rho_{gas} \quad (17)$$

where the ascending magma density and the core radius are calculated in the same fashion as for a blob ($\rho_{core} = \rho_{blob}$ and $R_{core} = R_{blob}$). As for the "Stokes approximation", we use the initial values of Table 1 and assign the temperature of ascending current T_{asc} to match Q_{mgas_P} =19.22 kg/s; we did not approach to the fluxes of 3.6 and 22.83 kg/s because the "bottom gas" is the only type of gas conjectured to be a continuous flux (see details in Section 2.1.1 to 2.2.2). Only runs with T_{asc} closest to equilibrium temperature of 1069°C are kept.

3. Results

We systematically treated starting gas compositions cited in Table 1. They cover surface porosities between 10 to 70 vol.% and steps of 10 vol.% except the case with gas composition "top of the cycle" that was treated within a range of porosities of 2-70 vol.%. These gas compositions were then assembled in 10 scenarios listed in Table 2. Table A1, Figures A1 through A6 show the main results of the fitting procedure (porosity, velocity, rising time and radius blob/flux) and how the ascent temperatures compare with the equilibrium temperatures found by *Burgisser et al*. [in review].

Based on the evolution of porosity as a function of depth (equation 6), the minimum value of porosity is approximately 10^{-6} (Table A1, Figures A1a-A1e, A2a-A2e, A3a-A3e, A4a-A4e and A5a-A5e). This minimum occurs at various pressures and it results from the total amount of volatiles present at atmospheric pressure and thus of the surface porosity considered [*Burgisser et al*., in review]. Based on equation (6) we estimated the radius of the blob and we show the ascending temperature calculated for each blob accompanying the evolution of that radius as a function of depth, and the equilibrium temperature found by *Burgisser et al*. [in review] (Figures A1d-A1h, A2d-A2h, A3d-A3h, A4d-A4h and A5d-A5h). By using equation (11) we calculated the velocity for the blob/flux at each depth from the depth of starting vesiculation (Figures A1b-A1f, A2b-A2f, A3b-A3f, A4b-A4f and A5b-A5f). We integrated the velocity curves with equation (13) to obtain the rising time from that depth to the surface of the lake (Figures A1c-A1g, A2c-A2g, A3c-A3g, A4c-A4g and A5c-A5g).

In general, for a blob associated with the top/bottom of the cycle, the temperature of ascending melt is higher for a porosity of 10 vol.% than for a porosity of 70 vol.%. The lower the porosity, the larger the radius of the blob will be. The rising time of a blob is faster as the porosity decreases. We notice that blobs that would add 3.6 kg/s with either the composition of "top of the cycle" or "lake gas" rise with very low velocities (Figures A3b-A3f, A4b-A4f, respectively).

3.1. Reconciling geochemical and physical scenarios

Despite that every one of the above calculations matches the oscillation of 1 or 1.5 m for both gas composition and estimated flux of 19 and 23 kg/s, we are in the necessity of building scenarios, which are the result of the possible combinations for the cases presented in Table 2. These scenarios will respect these constraints:

(i) Equilibrium temperature falls within a range of blob/flow porosities.
(ii) Geometry of the plumbing system is limiting the diameter of a spherical blob(s)/flow.
(iii) Geochemical cyclical arrival between alternated (every 5 min) blobs reaching the surface of the lake every 10 minutes with "bottom" and "top" gas compositions. Each one of these blobs will carry to the surface 19 and 23 kg/s, respectively.
(iv) Geochemical cyclical arrival of simultaneous blobs reaching the surface of the lake with "bottom" and "top/lake gas" compositions. Each one of these blobs will carry to the surface 19 and 3.6 kg/s, every 5 and 10 minutes respectively.

(v) Steady flux (Poiseuille-type) of 19 kg/s with a composition of "bottom" will be accompanied by the intermittent arrival (every 10 minutes) of a blob with a composition of "lake gas" or "top" that will carry to the surface 3.6 kg/s.

(vi) Two blobs/flows cannot collide or occupy the same space; however they can be at the same depth if the size of the plumbing system allows it. Blobs don't interact, mix or merge, therefore, blobs of same composition and porosities will be separated above a "*detachment depth*" at which they behave independently or as isolated batches (i.e., when distance between blobs is larger than the blob radius). They can coexist above a "*generation depth*" if the geometry of the plumbing system allows it. Below "*generation depth*" our model finds its limits because our calculations treat individual blobs.

3.2. Selecting plausible scenarios

We will show all our results and we will describe how we created scenarios by combining the analyses cases given in Table 2. We will also show the path followed to select or discard scenarios in agreement with the above statements:

Scenario 1: The blobs that would add 19 and 23 kg/s with a composition of "bottom gas" and "top gas", respectively, have a close match of the equilibrium temperatures given by *Burgisser et al*. [in review] (Figure A1d-A1h). They have porosities between 60 and 70 vol.% (but both are closer to 70 vol.%) for explaining 1 m of lava lake oscillation (Table A1, cases 1-2). Those blobs have a time shift of 5 minutes in order to reproduce the time sequence called "Top of the cycle" (Figure 6a). In absence of a blob linked to a composition of "top gas" then it only releases what has been called "bottom gas" to reproduce the time sequence called "bottom of the cycle". Each blob has a diameter of 10 m when it ascends in the conduit (Figure 6b) and each one will reach a diameter of ~13 m at the surface of the lake (Table A1, Figure 6b). Each blob can perfectly be accommodated in a lake of elliptical shape as reported by *Oppenheimer et al.* [2009].

We selected this scenario because it represents the arrival of *same size alternated blobs with similar speeds* from a generation depth of 100-m (Figure 6b). This scenario indicates that a buoyant blob with a composition of "top gas" will accelerate as it nears surface (Figure A1b). From a depth of ~90 m, it will reach surface every 10 minutes to release 23 kg/s of gas

(Figure 6b) and will alternate with a blob with a composition of "bottom gas", corresponding to a blob porosity of 70 vol. %; Table A1 Figure A1e- A1g-A1h). This last blob will accelerate at a depth of ~70 m and reach the lake surface every 10 minutes, in order to release 19 kg/s to the atmosphere. The "detachment depth" of both types of blobs is around 225 m (Figure 6b). Blobs with "top gas" and "bottom gas" compositions will bring a total magma flux of ~195 m^3/s (2×10^5 kg/s) and 142 m^3/s (1.1×10^5 kg/s), respectively.

We tested the same scenario than above to explain a 1.5 m lake oscillation for similar blobs. Every blob closely matches the equilibrium temperatures given by *Burgisser et al*. [in review] (Figure A2d-A2h) when the porosities are between 30 and 40 vol.% (but closer to 30 vol.%) (Table A1, cases 3-4). However, the blobs would reach a diameter of ~18 m in the conduit and a diameter of ~20 m at surface (Table A1). Both diameters overcome the dimensions of a physical conduit and lake, unless we consider that the physical conduit has a larger diameter allowing the degassed magma to descend once it has released its gas. Nevertheless reasonable, this scenario was rejected.

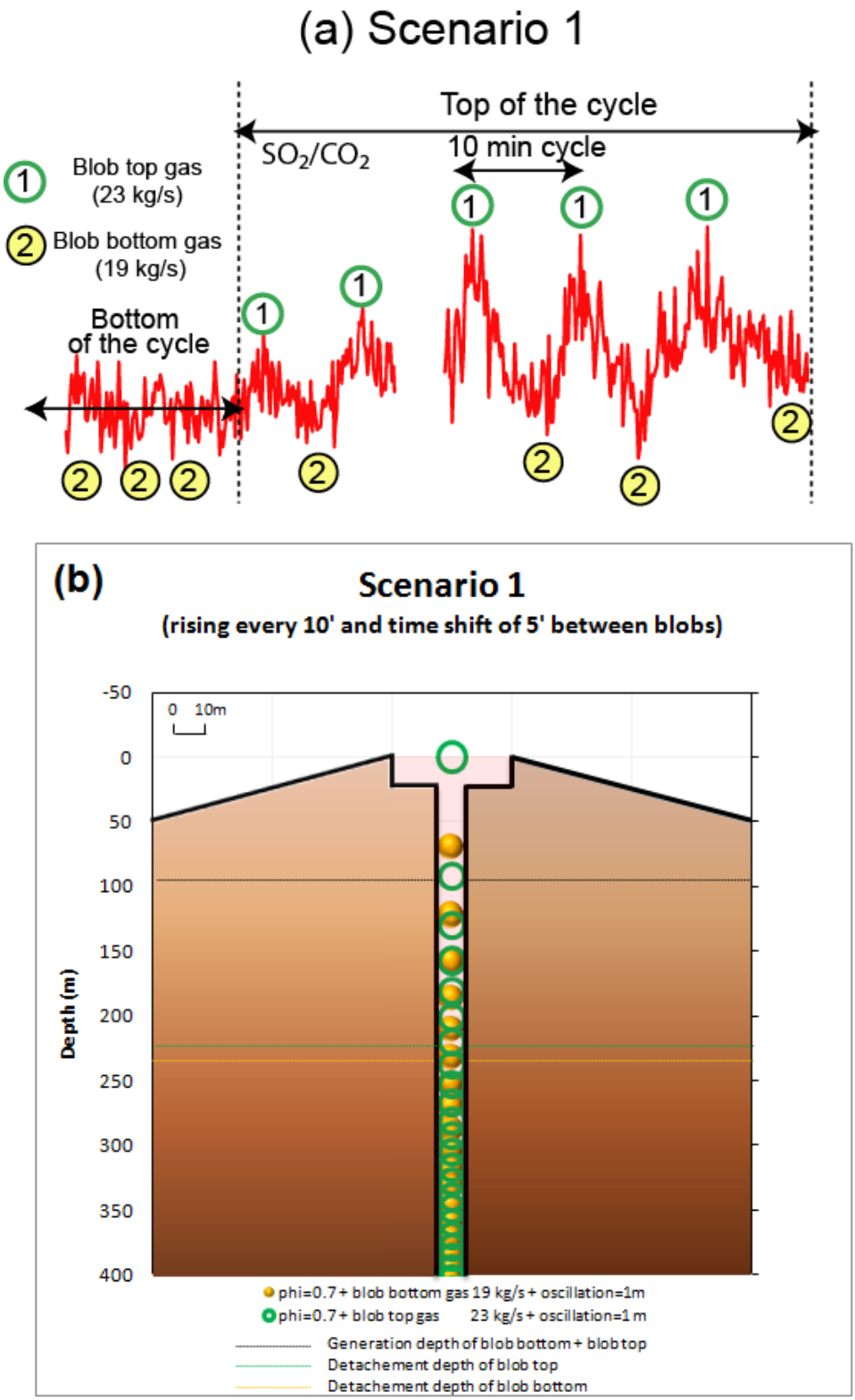

Figure 6. (a) Sketch of the geochemical cycle represented by the scenario 1. **(b)** Combination scenarios representing the rising time every 10 minutes of two intercalated blobs as a function of depth for the main compositions observed at Erebus. These scenarios are matching the gas flux observations of 19.22 ("bottom of the cycle") and 22.83 kg/s ("top of the cycle") for 1 m oscillation of the lake level.

Scenario 2: The blob that would add 3.6 kg/s with a composition of "top gas" explaining 1 m of lava lake oscillation closely matches the equilibrium temperatures given by *Burgisser et al*. [in review] for an initial porosity of 5 vol.% (Figure A3d, Table A1 case 5); however the same kind of blob explaining 1.5 m of lava lake oscillation would not satisfy the equilibrium temperature requirements (Figure A3h, Table A1 case 6). We have then rejected the creation of a scenario with this second kind of blob, but accepted the former one, which could reach the lake surface every 10 min. The blob with a composition of "bottom gas", as presented in the scenario 1 but reaching surface every 5 minutes, can release 19 kg/s (Table A1, case 1). Thus, when these two types of blobs reach surface and release their gases simultaneously, they would represent the intermittence between the maximum peaks of the "top of the cycle" (Figure 7a). In absence of a blob linked to a "top gas" then it only produces the release that has been called "bottom of the cycle". The blob with ~5 vol. % porosity that releases 3.6 kg/s would detach from a depth of ~25 m and would travel from there to the surface to reach a diameter of 32 m. The blob that releases 19 kg/s would have a diameter of 14 m (Figure 7b).

Our effort is to build a scenario in which *simultaneous blobs of different size* ascend. If the blobs are not subject to deformation due to the geometrical constraint, this scenario is only possible if both blobs coexist in a lake whose diameter widens to reach ~40 m between 70 and 20 m depth (Figure 7b); otherwise, the floor of the lake should be deeper than 20 m. Unless deformation of the blob providing a release of 3.6 kg/s is treated (and when it reaches surface at the same time than the blob releasing 19 kg/s), blobs should follow different paths up to surface after they have reached the bottom of the lake or eventually mix during its ascent. Therefore, this scenario is unlikely due to geometrical constraint and we discarded it. Should this "top gas" blob releasing 3.6 kg/s be associated to another type of flow geometry, such as core annular may respect the constraints; we test this configuration in the scenario 5.

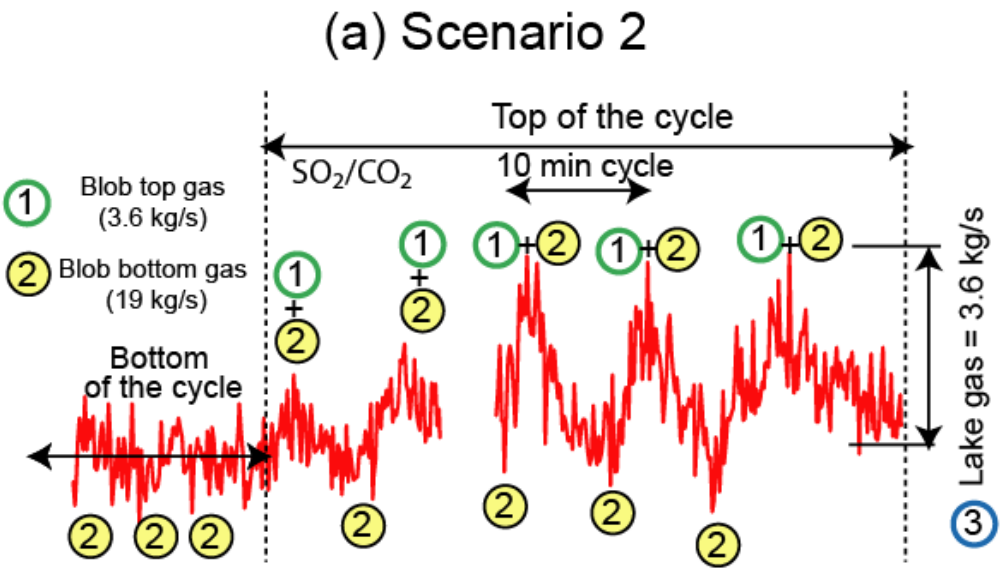

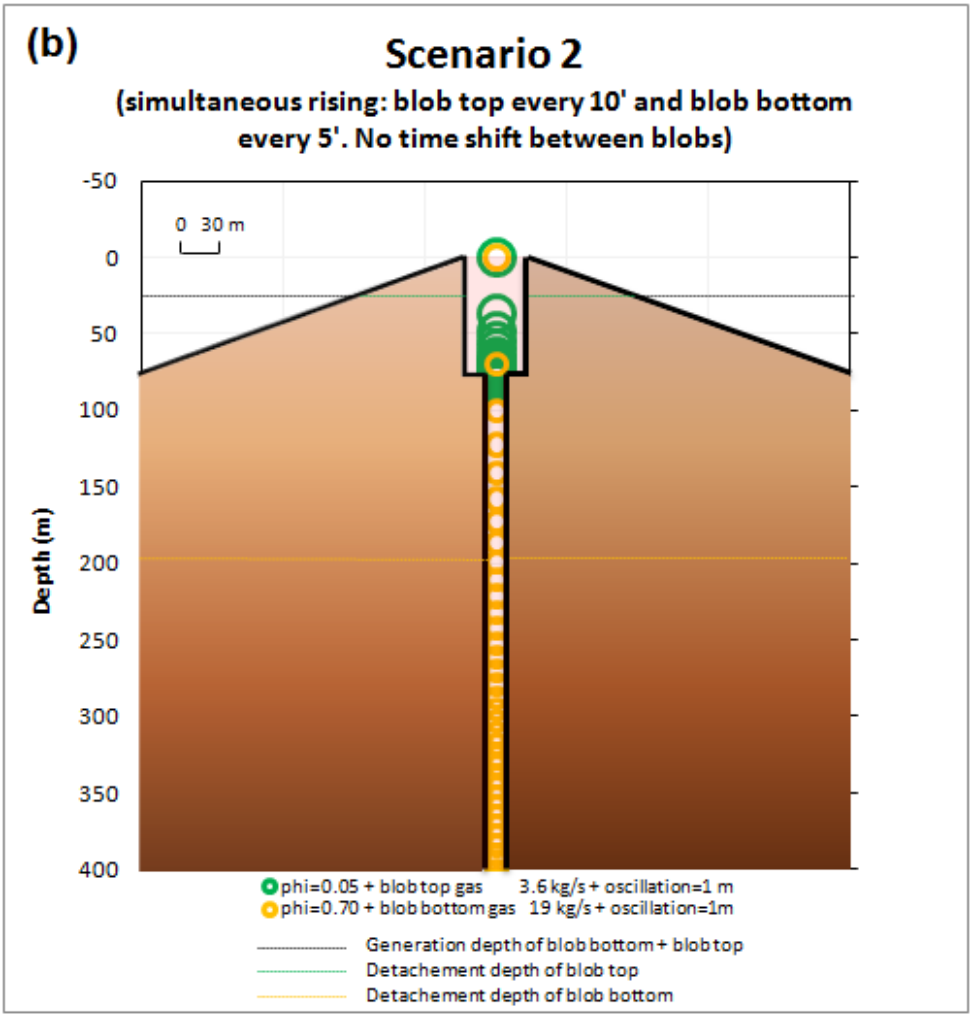

Figure 7. (a) Sketch of the geochemical cycle represented by the scenarios 2. **(b)** Combination scenarios representing the rising time every 10 minutes of two simultaneous blobs as a function of depth. These scenarios are matching the gas flux observations of 19.22 kg/s (taking a composition of the "bottom of the cycle") and 3.6 kg/s (with a composition of "top of the cycle"). Both kinds of blobs produce oscillation of the lake level of 1 m.

Scenario 3: A blob of 3.6 kg/s with porosities between 50 and 60 vol.% (but closer to 60%) and a composition of "lake gas" causing a 1-m oscillation would fit a ~10-m "conduit" diameter and closely match the equilibrium temperatures given by *Burgisser et al*. [in review] (Figure A4d, Table A1-case 7); however a blob with the same composition but causing an oscillation of 1.5 m is far to fit this conduit (Figure A4h, Table A1-case 8, 30-40 vol.%). We have then rejected the creation of a scenario with this second kind of blob, but accepted the former one, which could reach the lake surface every 10 min. The blob with a composition of "bottom gas" could also reach surface every 5 minutes to release 19 kg/s; it has the same characteristics as the one presented in scenario 1 and 2 (Table A1-case 1). Thus, when these both types of blobs reach surface and release their gases simultaneously, they would represent the intermittence between the maximum peaks of the "Top of the cycle" (Figure 8a). In absence of a blob linked to a "lake gas" then it only produces the release that has been called "bottom of the cycle". The blob that release 3.6 kg/s would detach from a depth of ~16 m and would travel from there to the surface to reach a diameter of 13 m. The blob that release 19 kg/s would have a diameter of 13 m and would detach from a depth of ~200 m (Figure 8b). Both kinds of blobs would fit the lake diameter of ~30-35 m reported by *Oppenheimer et al.* [2009]. However, our results below the lake floor are unlikely due to the geometrical constraints. Indeed, the vesiculation depth of the 3.6 kg/s blob (Table A1) is located deeper than the floor of the lake (~300 m; Table A1-case 7). The "conduit" diameter, as we have defined it, cannot accommodate both blobs side by side, they cannot overlap, go past or mix as long as they are in the conduit. Therefore, they would have to rise at similar velocities (as scenario 1), which is not the case. They could only coexist after they have reached the floor of the lake and could release their gas simultaneously. The blob "lake gas" would thus need to be generated in the conduit as a magma stream but blobs would only detach in the lake. We discard this scenario.

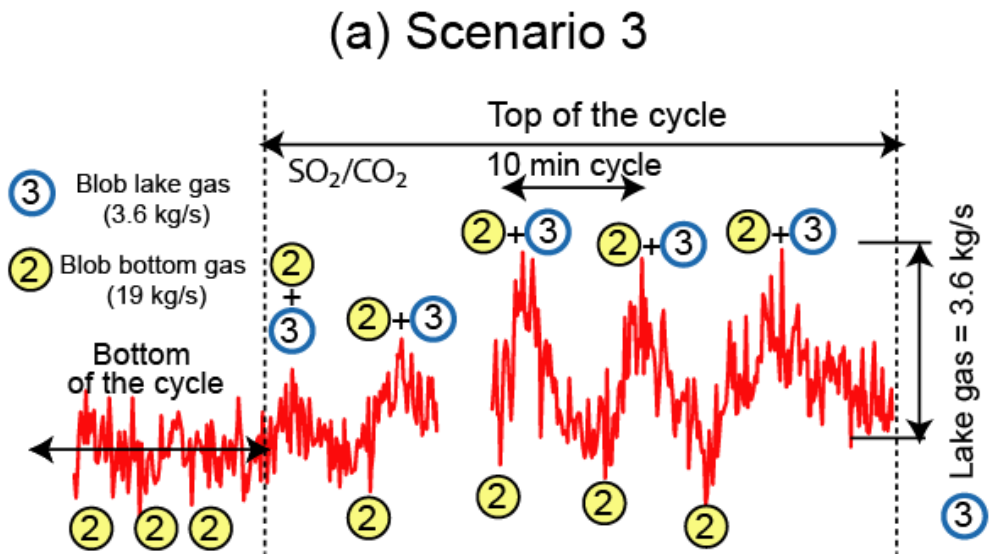

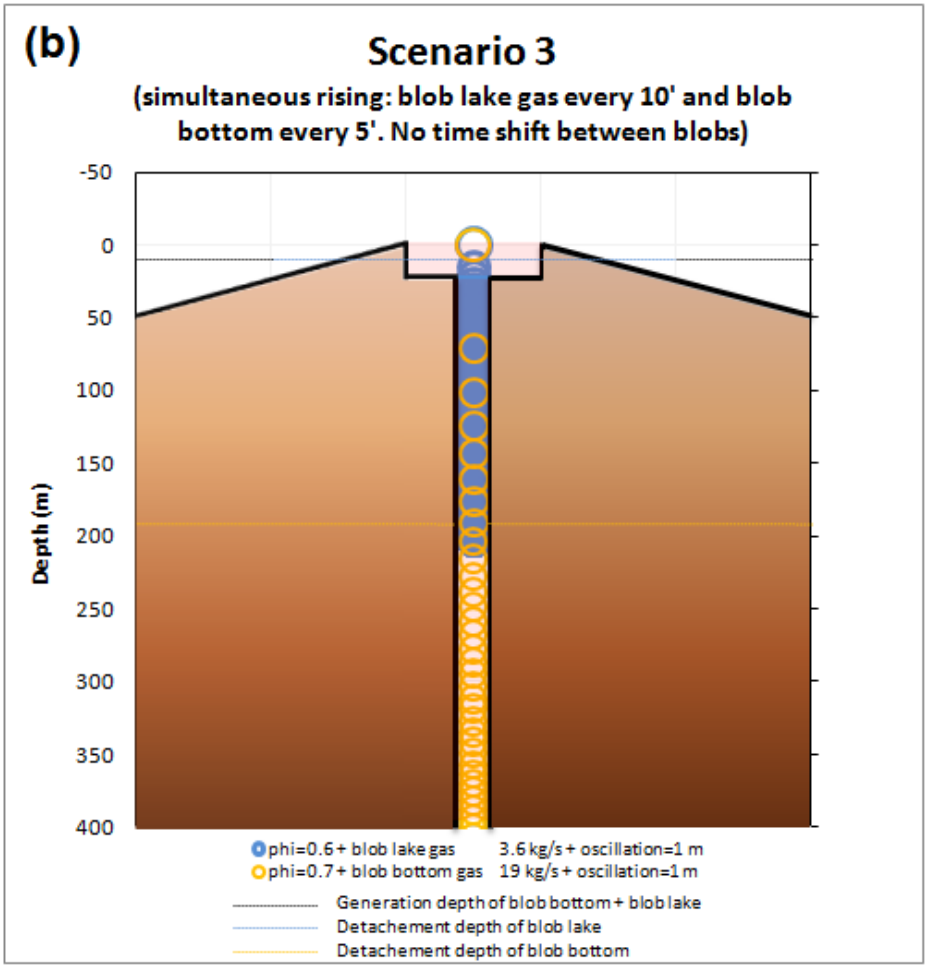

Figure 8. (a) Sketch of the geochemical cycle represented by the scenario 3. **(b)** Combination scenarios representing the rising time every 10 minutes of two simultaneous blobs as a function of depth. These scenarios are matching the gas flux of 19.22 kg/s (taking a composition of the "bottom of the cycle") and 3.6 kg/s (with a composition of "lake gas"). Both kinds of blobs produce 1 m oscillation of the lake level.

Scenario 4 and 5: We finally tested a Poiseuille-type flow with a "bottom gas" composition and releasing 19 kg/s combined with a blob of "lake gas" composition (scenario 4) and "top gas" composition (scenario 5) releasing 3.6 kg/s. These scenarios represent the intermittence between the maximum peaks of the "Top of the cycle" shown in Figure 9a. The blob with "top gas" and "lake gas" compositions are described in scenario 2 and 3, respectively.

A Poiseuille-type flow causing an oscillation of 1-m requires a porosity of 60 vol.% to match the equilibrium temperatures given by *Burgisser et al*. [in review] (Figure A5d, Table A1-case 9); its ascending radius would fit a 10-m "conduit" diameter. Since a flux with the same composition that would cause an oscillation of 1.5 m does not fit this conduit (Figure A5h, Table A1-case 10), we selected the flow causing an oscillation of 1-m. Such a Poiseuille flow requires a diameter of 14 m when it reaches the surface of the lake (Table A1), while the diameter of "lake gas" and "top gas" blobs would be of 14 and 32 m at surface, respectively (Table A1-cases 7 and 5). Combining a Poiseuille flow and a "lake gas" blob (scenario 4, Table A1-case7) is the only solution, as both would require almost the entire lake diameter to reach surface simultaneously. However, each one of these magma batches would have a diameter of 10 m when they ascend in the conduit (Figure 9b). The conduit diameter, the depth of the lake and the annular flow geometry cannot accommodate both blob and a continuous flux side by side nor allow them to mix. We thus discard this scenario. The scenario 5 combining Poiseuille flow and "top gas" blob (Table A1, case 5) would not respect this constraint either and was also discarded.

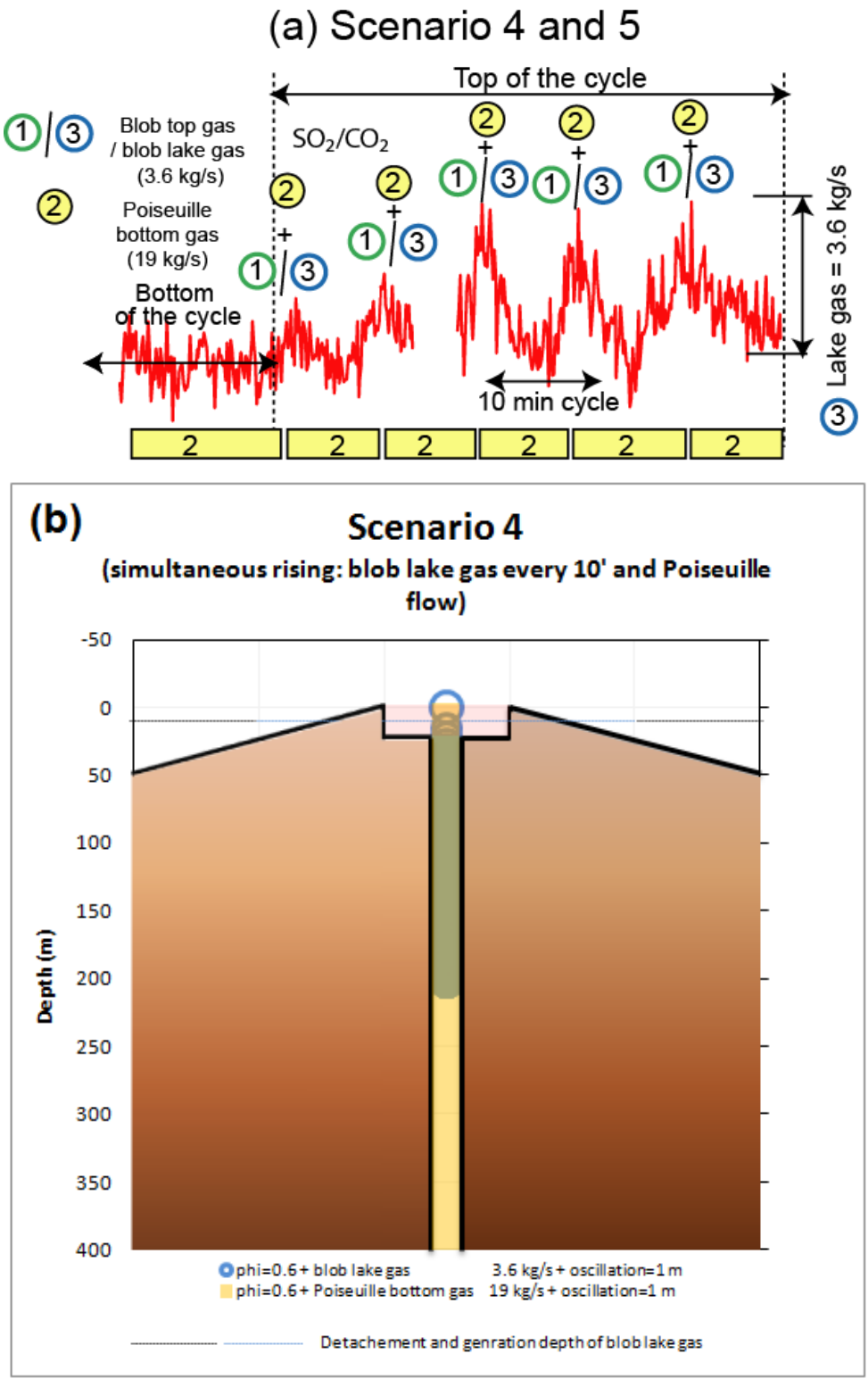

Figure 9. (a) Sketch of the geochemical cycle represented by the scenario 4, **(b)** Scenario representing the simultaneous rising of a Poiseuille flow and a blob as a function of depth matching the gas flux observations of 19.22 kg/s and 3.6 kg/s with a composition of "bottom of the cycle" and "lake gas", respectively. The two kinds of batches produce 1 m oscillation of the lake level (see details in the text).

3.3. Summary of results

Our results suggest that the temperature and porosity of the ascending magma are the main parameters controlling its rising. Magma ascent has been calculated considering (i) Stokes model approximation for a viscous and rigid sphere moving through a mobile surface and (ii) a Poiseuille flow. Both kinds of models were calculated individually (i.e., discretized in space and time). We have tested 5 scenarios in which the physics associated to the "bottom gas" composition was regarded as an individual "blob" and/or "continuous flux". This "bottom gas" represents the "bottom of the cycle" associated to a gas flux release of 19 kg/s. The "bottom gas" was intercalated with either a blob of "top gas" composition associated to a gas flux release of 23 kg/s (scenario 1) or a blob releasing 3.6 kg/s (with "lake gas" or "op gas" compositions) to bring the "bottom gas" flux to 23 kg/s (Scenario 2 to 5). The following table shows the main results of the blobs and continuous flux that produced individually oscillations of 1 m at the lake surface:

Table 3. Outputs of the fluid dynamical model before gas release for the scenarios treated in this study as the ones corresponding to the closest value of the equilibrium temperature indicated by *Burgisser et al*. [in review]. Notice that the batch with "bottom gas" composition is present in every one of the scenarios. In bold font is indicated the selected scenario.

Scenario #	Type of batch	Gas-Type	Vesiculation depth m	Porosity	Diameter m	Associated emitted gas flux kg/s
1	**Blob**	**Top gas**	**2108**	**0.7**	**13**	**22.83**
	Blob	**Bottom gas**	**3242**	**0.7**	**13**	**19.22**
2	Blob	Top gas	74	0.05	31	3.6
	Blob	Bottom gas	195.3	0.7	13	19.22
3	Blob	Lake gas	317	0.6	13.6	3.6
	Blob	Bottom gas	3242	0.7	13	19.22
4	Blob	Lake gas	317	0.6	13.6	3.6
	Poiseuille	Bottom gas	2326	0.6	13.6	19.22
5	Blob	Top gas	74	0.05	31	3.6
	Poiseuille	Bottom gas	2326	0.6	13.6	19.22

4. Discussion

According to the shape regime map of *Clift et al*. [1978] (Figure A6) the most likely geometry of a single bubble rising in a medium with properties of the magma of Erebus takes the shape of a sphere. This shape regime map is a function of dimensionless numbers such as the Reynolds number (equation 2) and:

Bond number:

$$Bo = \frac{(\rho_{desc} - \rho_{blob}) g \ 4 R_{blob}^2}{\sigma} \quad (18)$$

Morton number:

$$Mo = \frac{(\rho_{desc} - \rho_{blob}) g \mu_{desc}^4}{\sigma^3 \rho_{\mathrm{desc}}^2} \quad (19)$$

where σ is the surface tension between gas and melt. Blobs being bubbly melt, we can consider that σ represents the surface tension between melt and melt; its value is then 0, therefore $Bo = \infty$ and $Mo = \infty$. When the blobs porosity is higher than 70%, one can assume that they are only made of gas. Then $\sigma = 0.1$ N/m. Bo, Mo are thus $>10^{23}$ and $>10^{-1}$, respectively. Those values correspond to a blob of spherical shape. We then comfort ourselves that the results presented in this work correspond to that appropriated geometry.

Kazahaya et al. [1994], based on a double-pipe Poiseuille model, shows that the physical conduit radius can be inferred by the ratio of viscosities of ascending and descending magmas at the position of the boundary between up flow and downflow. Combining equations (13) and (14) from those authors, we have the following relationship:

$$\frac{\mu_{desc}}{\mu_{asc}} = \left(\frac{R_c}{R_a}\right)^4 - 1 - \frac{\left[\left(\frac{R_c}{R_a}\right)^2 - 1\right]^2}{\ln\left(\frac{R_c}{R_a}\right)} \quad (20)$$

where R_c is the conduit radius and R_a the ascending or core radius. We calculated the conduit radius by assuming $R_a = R_{blob}$.

Stevenson and Blake [1998] also indicates that conduit radius, R_c, can be inferred by a Poiseuille number, P_s, the terminal velocity of ascending magma, U_{asc} (in our case, we take $U_{asc} = U_{blob}$) and the $\Delta\rho$ (difference in density between the degassed and gas-rich magmas; in our case, we take $\Delta\rho = \rho_{blob} - \rho_{desc}$). The value of P_s is a function of μ_{desc}/μ_{asc} based on their experiments. In our model we always have that $1 < \mu_{desc}/\mu_{asc} < 12$. By combining equations (1) and (11b) from those authors the conduit radius is equal to:

$$R_c = \left\{ \frac{U_{asc}\ \mu_{desc}}{g\ \Delta\rho\ [0.020+0.041\ \log_{10}(\mu_{desc}/\mu_{asc})]} \right\}^{1/2} \quad (21)$$

Scenario #1 was selected among the five tested scenarios as the one satisfying best our assumptions. The other scenarios have their limitations below the "*generation depth*" because our physical model was conceived to treat individual batches. By using equations (20) and (21) we calculated the conduit diameter below the lake floor to be 20 and 24 m, respectively. Since our ratio μ_{desc}/μ_{asc} changes with depth, below the "*generation depth*" equations (20) and (21) yields that our batches can individually be fitted in a physical conduit of 20 and 21 m diameter, respectively. Should the lake have had a diameter of 40 m during the 1987/88 season then our result of a 20-m physical conduit diameter would be in agreement with *Dibble et al*. [2008] observation. Otherwise we expect that blobs can result of choking between ascending and descending currents.

We do not discard the possibility that further findings about the geometry of the physical conduit can add constraints that could play a role in "deforming" the spherical shape of the blob (especially for the discarded Scenario # 2). Besides, if the medium is considered as continuum, mixing of batches would be possible; for instance blobs of different size and composition (Scenario #2) could coexist and alter each other's properties (i.e., velocity, porosities, compositions), resulting in an hybrid blob. The same applies for the scenarios # 3-5 that have been discarded for incompatibility with our assumptions and might then be considered as "acceptable"; we left these configurations open to future studies.

Our selected scenario indicates that a water-rich (73 mol.%) and hot (1085°C) buoyant magma with a composition of "top gas" could vesiculate as deep as 2108 m. As the magma rises in the conduit, the pressure to which it is submitted decreases and leads to a sharp acceleration as it nears surface (Figure A1b). Individual blobs detach from the rising magma around 225 m, and from a depth of ~90 m they reach surface every 10 minutes to release 23 kg/s of gas (Figure 6b). They alternate with blobs with a composition of "bottom gas", which are slower, colder (1069°C), less water-rich (60 mol.%) and could have originated in the deeper part of the system (3242 m deep). These colder blobs detach also around 225 m and accelerate at a depth of ~70 m to reach the lake surface every 10 minutes and release 19 kg/s of gas to the atmosphere (Figure 6b). Blobs initiate deep below surface and their ascent lasts more than the time span separating two degassing events (Table A1-cases 1 and 2). Therefore, new blobs are already rising in sequence when a blob is released at surface and they are not initiated by the pressure drop caused by degassing and the change in level of the lake (Figure 10). The fluctuation of the lava lake level would be caused by the interaction of those batches of magma.

We thus interpreted the lava lake rising as follows; at depth, the magma containing dissolved gas rises by buoyancy. When the pressure has significantly decreased, gas starts to exsolve from the melt and the velocity increases. At time, it reaches a detachment depth and behaves as a differentiated blob whose velocity increases. When the blob reaches surface, the level of the lake increases under the extra supply of bubbly magma and the blob releases its gas to atmosphere while the degassed melt is spreading towards the edges of the lava lake (Figure 10a). The degassing rate decreases and the melt keeps spreading laterally as the whole surface tends to flatten (Figure 10b); the "fresh" melt overlaps the cooler and harder surface formed by the previous batches of magma. Other blobs, having formed at varying depth, are already on their way to surface, that they will reach periodically (Figure 10c) and the process repeats itself. The release of the gas at surface may enhance the formation of the blobs at their detachment depth, as the fluctuation of the pressure exerted by the column of magma in the lake and the conduit may be transmitted at such a shallow depth. Denser magma is drained back in the conduit and down to the magma chamber as lighter bubbly magma travels at counter-current in the same conduit. The denser magma, incompressible, may act as a viscous choke that will free the lighter magma at repetitive intervals, enhancing oscillations of the lava lake level.

The above process is similar to the one proposed by the experimental and theoretical model of *Witham et al*. [2006], in which the key element is that a bubble rich magma ascends in the conduit and drives up flow of liquid to the lake, without relating it to any geochemical process. When magma is bubble-poor (this would correspond to the stage represented in Figure 10c), it is dense and hence leads to a down flow. Through examination of the video, we observed that the batch arriving at surface generates a surging disturbance of ~14 m diameter (Figure 2a), which coincides with the diameter that we calculated for either a continuous flow or a blob in our model (Table 3).

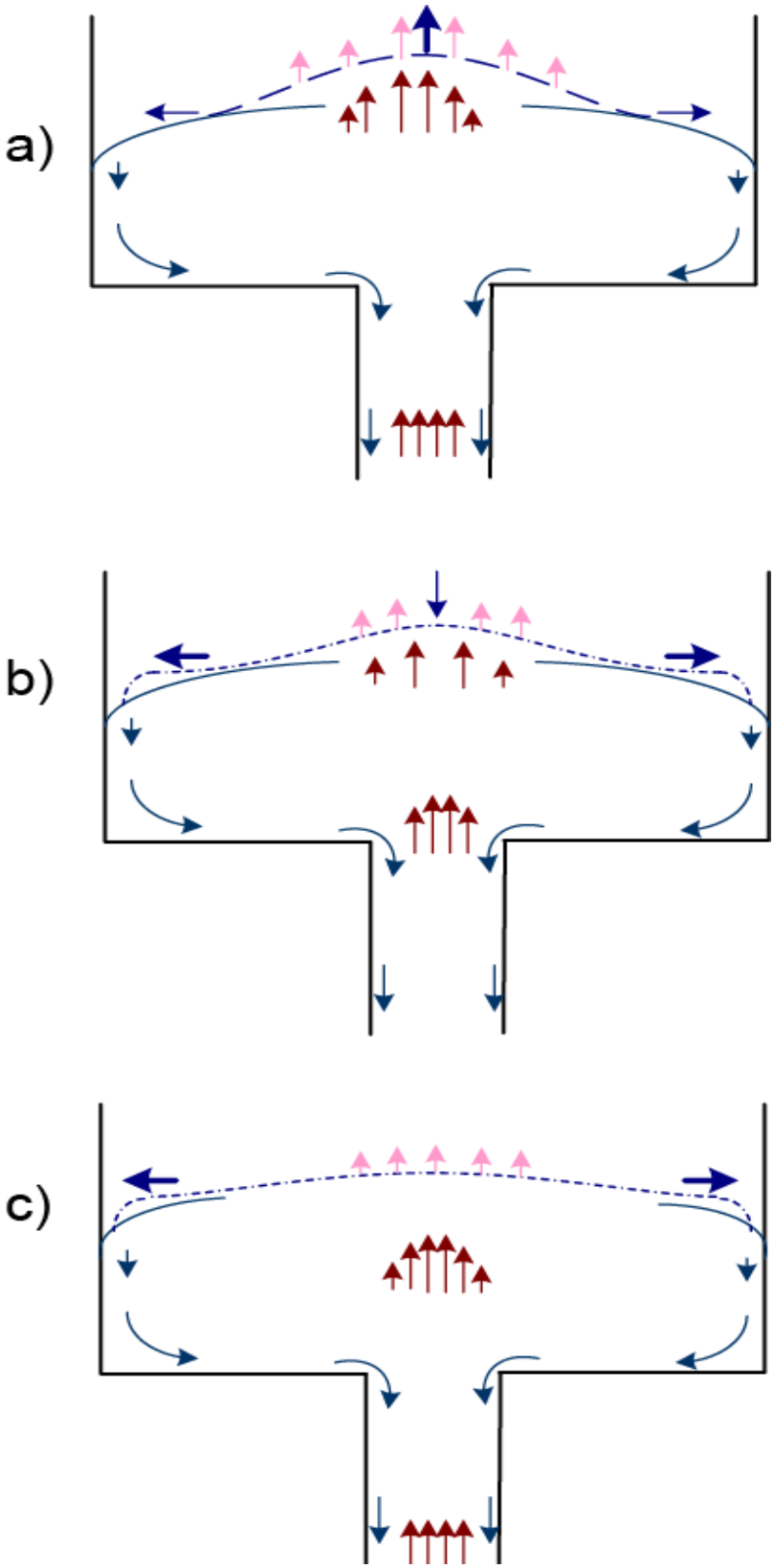

Figure 10. Cartoon of the periodic oscillations observed at Erebus when a bubble-rich mixture reaches the surface of the lake: (a) porous blob reaches and lifts the surface, releasing its gases, (b) degassed melt spreads radially and the surface flattens, releasing less gas as a next blob enters the bottom of the lake, (c) as the release is completed the denser magma sinks back to the system.

It would be valuable to test our model by taking field measurements: plotting the gas flux released by the two pulses and the associated variation of the level of the lake (for top and bottom of the cycles) versus time would be a great input. Each blob causing that geochemical sequence should reach surface alternately, while generating an oscillation of 1 m if our assumptions are right. For the lake to reach 1.5 m in height – while using the same modeled temperatures than the ones used to fit a 1 m oscillation - the calculated gas flux would be larger by 13 to 15 kg/s than the average fluxes mentioned in *Oppenheimer et al*. [2009] for the bottom and top of the cycle, respectively. This represents a variation of 40%. While this is outside the margin error of the 2004/2005 measurements, the fact that gas fluxes have never been measured simultaneously with the level fluctuations leaves the possibility of having the lake oscillating of 1.5 m while degassing ~32-38 kg/s. Alternatively, matching the release of 19 and 23 kg/s and an oscillation of 1.5 m would require a ΔT between upwelling and downwelling magma of 82°C and 85°C to be taken into account, for "bottom" and "top gas" compositions, respectively. Those blobs would have ~10 m and 14 m diameter in the conduit and at surface, respectively. Should a gas flux of 19 and 23 kg/s had been also measured in 2009, for a surface of the lake of 2500 m^2 and 1-m oscillation, the corresponding ΔT would have been of 125°C and 128°C for "bottom" and "top gas" compositions, respectively; those blobs would have ~14 m and 20 m diameter in the conduit and at surface, respectively, which means that deformation of the blob cannot be neglected.

It also would be valuable to differentiate and precisely track the temperature of the exposed incandescent magma, corresponding to the inner blob and that of its edge (e.g., Figure 2), as the level of the lava lake is rising. These temperatures are related with the ascent of the blob and the downwelling current, which would precisely back our assumptions of temperature contrast. Our estimations of magma flux (10^5 kg/s) are in the same order of magnitude than the value of 10^6 kg/s given by *Calkins* [2006] and our estimations of 10^5 kg/s presented in the next chapter using a different method.

Blobs rising from a same magma reach the surface with a differentiated volatile composition; the reason behind this variation could be a difference in bubble growth rate. Magma rising by buoyancy may be slowed down in its ascent if the geometry of roof of the magma chamber, located several hundred meters below surface, has a shape preventing a smooth funneling to the conduit. The further away from the vertical of the conduit, the longer it will take for

buoyant magma to eventually reach the entrance of the conduit. Therefore magma could be subject to a pressure drop whose gradient ΔP versus time would vary with its position in the chamber. The magma being exposed to a tiny ΔP during a long time will lead to a gas exsolution process different to that of a "rapid" magma. Consequently, if the decompression rate of some of the magma is differentiated by the geometry, bubble growth may also differ. Varying bubble growth rates would influence the amount of volatiles diffusing from the saturated melt to the bubbles. Gas composition would then be different whether it is released from a batch with a low or a fast bubbles growing rate. Besides, different bubble growth regimes will result in different porosities from one batch to another. Magma would rise up to the surface as blobs of different volatile composition and speed, due to their differentiated buoyancy in a degassed downwelling melt. These blobs could be assimilated as batches originated at different depths of the system.

5. Concluding remarks

Through our simple fluid dynamic model, we found that the temperature of ascending and descending magma currents is the key parameter to explain the cyclic behaviour of the lake linking the geochemistry and the physical oscillation.

By fixing several constraints such as magma volume causing the lava lake oscillation, ΔT for convective currents, measured gas fluxes, geometry of the lake and an ascending radius of magma close to that of the conduit diameter allowing to keep a sustained convection in Erebus [*Molina et al*., 2012], we found that for a same type of gas composition, the associated gas flux released at surface is lower if the vesiculation depth of magma batch is shallower (cases #2 and 5, Table A1). The ascent rate and the way magma detaches to generate isolated blobs depend on the gas composition (scenarios #1-5).

In particular, our results suggest that repetitive oscillations (1 m) of the lava lake level are caused by the intercalated ascent of two kinds of batches of magma originated from the shallower and deeper part of the magma system. Theses batches are differentiated by their chemical compositions and gas fluxes measured at the surface, their modeled temperature of ascending magma and velocity. The deeper batch (~3 km depth) has porosities of 70 vol.% at surface, is less water-rich gas (mol.% H_2O = 60), colder (1069°C) and is relatively slower

compared to a shallower blob (~2 km depth) with surface porosities of ~70 vol.% at surface, water-rich gas (mol.% H_2O = 73), hotter (1085°C) and faster. Every batch reach surface with a diameter of 13 m; which is highly consistent with the observation of videos showing spreading waves at surface.

We surmise that hotter and cooler batches would also explain the measurements of the higher and lower velocity speeds at surface of the lake, respectively. Besides, the amplitude of the oscillation for a given surface of the lake may be related to ΔT between ascending and descending currents. To a higher ΔT corresponds a larger amplitude of the height of oscillation. Moreover, as the area of the lake increases a larger ΔT would be required to generate a similar oscillation of 1-m.

References

Aster, R., S. Mah, P. Kyle, W. McIntosh, N. Dunbar, J. Johnson, M. Ruiz, and S. McNamara (2003), Very long period oscillations of Mount Erebus Volcano, *J. Geophys. Res.*, *108*(B11), 2522, doi:10.1029/2002JB002101.

Bower, L.A., Lee, T., (2010), Single bubble rising dynamics for moderate Reynolds number using Lattice Botlzmann Method, *Computers & Fluids.*, 39, 1191-1207, doi:10.1016/j.compfluid.2010.03.003.

Burgisser, A., Scaillet, B., Harshvardhan. (2008), Chemical patterns of erupting silicic magmas and their influence on the amount of degassing during ascent, J. Geophys. Res., 113, B12204, doi:10.1029/2008JB005680.

Burgisser, A, Oppenheimer, C., Aletti, M and Kyle, P.R. (in review), Backward tracking of gas chemistry measurements at Erebus volcano, *Geochem. Geophys. Geosyst*.

Calkins, J.A. (2006), Ground based thermal observations of two lava lakes at Mount Erebus Volcano, Antarctica in December 2004, M.S. Thesis, Dep. Earth and Env. Sci. New Mexico, Institute of Mining and Technology, Socorro, New Mexico, U.S.

Clift, R., Grace, J.R. and Webber, M., (1978), Bubbles, drops and particles. New Yrok: Academic Press.

Crowe, C., Sommerfeld, M., and Tsuji, Y., H (1997), Multiphase flows with droplets and particles, CRC Press.

Dibble, R. R., P. R. Kyle, and C. A. Rowe (2008), Video and seismic observations of Strombolian eruptions at Erebus volcano, Antarctica, *J. Volcanol. Geotherm. Res.*, *177*, 619–634, doi:10.1016/j.jvolgeores.2008.07.020.

Gerst, A., M. Hort and P.R Kyle (2008), 4D velocity of Strombolian eruptions and man-made explosions derived from multiple Doppler radar instruments, *J. Volcanol. Geotherm. Res.*, 177(3), 648-660, doi:10.1016/j.jvolgeores.2008.05.022.

Giordano, D., J. K. Russell, and D. B. Dingwell (2008), Viscosity of magmatic liquids: A model, *Earth Planet. Sci. Lett., 271*, 123–134, doi:10.1016/j.epsl.2008.03.038.

Harris, A. J. L., R. Wright and L.P. Flynn (1999), Remote monitoring of Mount Erebus Volcano, Antarctica, using Polar Orbiters: Progress and Prospects, *20*(15-16), 3051-3071, doi: 10.1080/014311699211615.

Kazahaya, K., Shinohara, H., Saito, G (1994), Excessive degassing of Izu-Oshima volcano: magma convection in a conduit, *Bull. Vol*, 56, 207-216.

Kelly, P. J., P. R. Kyle, N. W. Dunbar, and K. W. W. Sims (2008), Geochemistry and mineralogy of the phonolite lava lake, Erebus volcano, Antarctica: 1972–2004 and comparison with older lavas, *J. Volcanol. Geotherm. Res., 177*, 589–605, doi:10.1016/j.jvolgeores.2007.11.025.

Koyaguchi, T (1985), Magma mixing in a conduit, *J. Volcaol. Geotherm*. Res., 25, 365-369.

Krieger, I. M., and T. J. Dougherty (1959), A mechanism for non-Newtonian flow in suspensions of rigid spheres, *Trans. Soc. Rheol., 3*, 137–152.

Lamb, H (1945), Hydrodynamics. Cambridge University Press, Cambridge, 738 pp.

Mastin, L., and M. Ghiorso (2000), A numerical program for steady-state flow of magma-gas mixtures through vertical eruptive conduits, Open-File Report of the USGS, pp. 1-53.

McClelland, L., Simkin, T., Summers, M., Nielsen, E., and Stein, T. C., 1989, *Global Volcanism 1975–1985* (New Jersey: Prentice Hall).

Moggi, K (1958), Relations between the eruptions of various volcanoes and the deformations of the ground surfaces around them, Bull. Of Earthquake Res. Inst., vol. 36, 99-134.

Molina , I., A. Burgisser and C. Oppenheimer (2012), Numerical simulations of convection in crystal-bearing magmas: A case study of the magmatic system at Erebus, Antarctica, *J. Geophys. Res*., doi:10.1029/2011JB008760, in press.

Oppenheimer, C., A. S. Lomakina, P. R. Kyle, N. G. Kingsbury, M. Boichu (2009), Pulsatory magma supply to a phonolite lava lake, *Earth Planet. Sci. Lett*., 284, 392–398, doi:10.1016/j.epsl.2009.04.043.

Oppenheimer, C. et al, in prep, Pulse of a volcano measured by lava lake pressure gauge!

Shimozuru, C. (1978), Dynamics of magma in a volcanic conduit –Special Emphasis on Viscosity of Magma with Bubbles, *Bull Volcanol*., 41(4), 333–340.

Stevenson, D. S. and S. Blake (1998), Modeling the dynamics and thermodynamics of volcanic degassing, *Bull. Vol., 60*, 307–317.

Sweeney, D., P. R. Kyle and C. Oppenheimer (2008), Sulfur dioxide emissions and degassing behavior of Erebus volcano, Antarctica, *J. Volcanol. Geotherm. Res*., *177*, 725-733, doi: 10.1016/j.jvolgeores.2008.01.024.
Turcotte D. L., and G. Schubert (2002), *Geodynamics*, 2nd edition, Cambridge University Press, Cambridge.

Weinberg, R. F., and Y. Podladchikov (1994), Diapiric ascent of magmas through power law crust and mantle, *J. Geophys. Res.*, 99(B5), 9543–9559, doi:10.1029/93JB03461.

Witham, F., Woods, A.W., Gladstone, C., 2006. An analogue experiment model of depth fluctuations in lava lakes, Bull. Volcanol. 69, 51-56.

Witham, F., Llewellin, F., 2006. Stability of lava lakes, J. Volcanol. Geotherm. Res. 158, 321-332.

List of Appendix

Appendix A. General results and considerations of the fitting for each one of the cases considered in this study.

Table A1. Outputs of the fluid dynamical model before gas release (gas plus melt): 1-8 are the results for our "stokes approximation" and 9-10 are the results for our "Poiseuille approximation". $\boldsymbol{\phi}$ is porosity, $\boldsymbol{T_{asc}}$ and $\boldsymbol{T_{desc}}$ are ascending and descending temperatures, $\boldsymbol{\rho_{asc}}$ and $\boldsymbol{\rho_{desc}}$ are ascending and descending melt density, $\boldsymbol{R_{blob}}$ is radius of the blob or ascending magma in the case of a Poiseuille flow. Magma and volume fluxes ($\boldsymbol{Q_v}, \boldsymbol{Q_m}$) are reported for a period cycle. $\boldsymbol{Q_v}$ is volume flux defined as $\boldsymbol{Q_v} = Q_{mgas_{St}}/(\phi\rho_{gas})$ in the case of the "stokes approximation" or $\boldsymbol{Q_v} = Q_{mgas_P}/(\phi\rho_{gas})$ in the case of "Poiseuille approximation". $\boldsymbol{Q_m}$ is mass flux defined as $\boldsymbol{Q_m} = (Q_{mgas_{St}}/\phi\rho_{gas})\,\rho_{blob}$ in the case of the "stokes approximation" or $\boldsymbol{Q_m} = (Q_{mgas_P}/\phi\rho_{gas})\,\rho_{blob}$ in the case of "Poiseuille approximation". "Origin depth" is the depth at which vesiculation occurs, "Rising time" is the travel time from the vesiculation depth until surface of the lake and $\boldsymbol{Re}$ is Reynolds number. The symbol "*" indicates that it was not possible to fit the parameters of our model to the observed gas flux given by *Oppenheimer et al*. [2009]. Highlighted font shows the interval or the specific value for which our results enclose the equilibrium temperature given by *Burgisser et al*. [in review] for specific composition. Highlighted grey rows enhance the outputs of the main scenarios explained in this work.

Parameter	$\boldsymbol{\phi}$	$\boldsymbol{T_{asc}}$	$\boldsymbol{T_{desc}}$	$\boldsymbol{\rho_{asc}}$	$\boldsymbol{\rho_{desc}}$	$\boldsymbol{R_{blob}}$	$\boldsymbol{U_{blob}}$	$\boldsymbol{Re}$	$\boldsymbol{Q_v}$	$\boldsymbol{Q_m}$	***Origin depth***	***Rising time***
Type of fit/Units	***Dimension-less***	***°C***	***°C***	***kg/m³***	***kg/m³***	***m***	***m/s***	***Dimension-less***	***m³/s***	***Kg/s***	***m***	***min***
1. Bottom gas -blob of 19 kg/s and 1 m oscillation-	0.1	1155	1099	2449	2459	12.1	2.2	4.6	972.9	2.1×10^6	279	252
	0.2	1113	1057	2457	2468	9.9	1.7	1.3	509.7	1.0×10^6	535	1529
	0.3	1097	1041	2457	2468	8.7	1.5	0.7	341.3	6.0×10^5	842	6071
	0.4	1086	1030	2461	2473	7.8	1.3	0.4	252.3	3.8×10^5	1226	16095
	0.5	1078	1022	2463	2474	7.3	1.2	0.3	201.0	2.6×10^5	1687	23066
	0.6	**1072**	**1016**	**2464**	**2475**	**6.8**	**1.1**	**0.2**	**165.4**	$\mathbf{1.7 \times 10^5}$	**2326**	**43296**
	0.7	**1067**	**1011**	**2465**	**2474**	**6.5**	**1.1**	**0.2**	**142.0**	$\mathbf{1.1 \times 10^5}$	**3242**	**75950**
2. Top gas -blob of 23 kg/s and 1 m oscillation-	0.1	*	*	*	*	*	*	*	*	*	*	*
	0.2	1143	1087	2451	2463	9.9	2.4	3.3	720.2	1.4×10^6	324	655
	0.3	1119	1063	2455	2467	8.7	2.0	1.5	480.1	8.5×10^5	511	2202
	0.4	1105	1049	2457	2470	7.9	1.8	0.9	355.4	5.4×10^5	746	4467
	0.5	1096	1040	2459	2471	7.3	1.7	0.6	280.7	3.6×10^5	1058	13242
	0.6	**1089**	**1033**	**2460**	**2473**	**6.8**	**1.6**	**0.5**	**230.3**	$\mathbf{2.4 \times 10^5}$	**1484**	**21980**
	0.7	**1083**	**1027**	**2460**	**2473**	**6.5**	**1.5**	**0.4**	**195.3**	$\mathbf{1.6 \times 10^5}$	**2108**	**40141**
3. Bottom gas -blob	0.1	1110	1054	2457	2469	14.0	1.6	1.6	966.9	2.1×10^6	278	485
	0.2	1083	1027	2462	2474	11.3	1.3	0.6	506.7	1.0×10^6	534	2282
	0.3	**1069**	**1013**	**2464**	**2476**	**9.9**	**1.1**	**0.3**	**338.6**	$\mathbf{6.0 \times 10^5}$	**840**	**8595**

Parameter	ϕ	T_{asc}	T_{desc}	ρ_{asc}	ρ_{desc}	R_{blob}	U_{blob}	Re	Q_v	Q_m	Origin depth	Rising time
Type of fit/Units	Dimension-less	°C	°C	kg/m^3	kg/m^3	m	m/s	Dimension-less	m^3/s	Kg/s	m	min
of 19 kg/s and 1.5 m oscillation-	0.4	1060	1004	2466	2478	9.0	1.0	0.2	250.1	3.8×10^5	1224	22352
	0.5	1053	997	2467	2479	8.4	0.9	0.1	199.1	2.6×10^5	1684	31698
	0.6	1048	992	2468	2480	7.9	0.8	0.1	163.5	1.7×10^5	2322	59209
	0.7	1043	987	2469	2480	7.4	0.8	0.1	138.3	1.1×10^5	3234	103460
4. Top gas -blob of 23 kg/s and 1.5 m oscillation-	0.1	1151	1095	2450	2462	14.3	2.3	5.4	1470.2	3.3×10^6	155	127
	0.2	1103	1047	2458	2470	11.4	1.8	1.2	714.6	1.4×10^6	323	1155
	0.3	**1087**	**1031**	**2461**	**2473**	**10.0**	**1.5**	**0.7**	**476.2**	$\mathbf{8.5 \times 10^5}$	**510**	**3365**
	0.4	**1076**	**1020**	**2463**	**2475**	**9.0**	**1.4**	**0.4**	**352.2**	$\mathbf{5.4 \times 10^5}$	**745**	**6489**
	0.5	1069	1013	2464	2476	8.4	1.3	0.3	277.8	3.6×10^5	1056	18780
	0.6	1063	1007	2465	2477	7.8	1.2	0.2	227.6	2.4×10^5	1482	30761
	0.7	1058	1002	2466	2478	7.4	1.1	0.2	192.6	1.6×10^5	2103	55697
5. Top gas -blob of 3.6 kg/s and 1 m oscillation-	**0.02**	**1115**	**1059**	**2456**	**2468**	**21.5**	**0.9**	**1.6**	**1149.0**	$\mathbf{2.8 \times 10^6}$	**34**	**18**
	0.05	**1072**	**1016**	**2461**	**2475**	**15.9**	**0.5**	**0.2**	**395.3**	$\mathbf{9.3 \times 10^5}$	**81**	**346**
	0.1	1058	1002	2466	2478	12.7	0.4	0.1	229.6	5.2×10^5	155	1258
	0.2	1037	981	2469	2482	10.1	0.3	0.04	111.5	2.3×10^5	321	7061
	0.3	1026	970	2471	2483	8.8	0.2	0.02	74.1	1.3×10^5	508	18847
	0.4	1019	963	2473	2485	8.0	0.2	0.01	54.7	8.6×10^4	742	35007
	0.5	1013	957	2474	2486	7.4	0.2	0.01	43.0	5.7×10^4	1051	99538
	0.6	1008	952	2474	2487	6.9	0.2	0.01	35.0	3.8×10^4	1476	162146
	0.7	1004	948	2475	2487	6.5	0.2	0.01	29.6	2.5×10^4	2095	291492
6. Top gas -blob of 3.6 kg/s and 1.5 m oscillation-	0.1	1035	979	2470	2482	14.6	0.3	0.06	229.0	5.2×10^5	154	1687
	0.2	1016	960	2473	2485	11.6	0.3	0.02	111.2	2.3×10^5	321	9400
	0.3	1005	949	2475	2487	10.1	0.2	0.01	73.7	1.3×10^5	507	25071
	0.4	998	942	2476	2488	9.1	0.2	0.01	54.4	8.6×10^4	741	46596
	0.5	992	936	2477	2489	8.5	0.2	0.01	42.6	5.7×10^4	1050	132816
	0.6	988	932	2478	2490	7.9	0.2	0.01	34.8	3.8×10^4	1474	215424
	0.7	984	928	2479	2491	7.5	0.2	0.00	29.2	2.5×10^4	2092	389545
7. Lake gas -blob of	0.05	1085	1029	2461	2473	15.7	0.7	0.4	512.4	1.2×10^6	16	34
	0.1	1063	1007	2465	2467	12.4	0.5	0.2	2501.2	5.6×10^5	32	202
	0.2	1043	987	2468	2480	9.9	0.4	0.1	126.2	2.5×10^5	64	1075

Parameter	ϕ	T_{asc}	T_{desc}	ρ_{asc}	ρ_{desc}	R_{blob}	U_{blob}	Re	Q_v	Q_m	Origin depth	Rising time
Type of fit/Units	Dimension-less	°C	°C	kg/m^3	kg/m^3	m	m/s	Dimension-less	m^3/s	Kg/s	m	min
3.6 kg/s and 1 m oscillation-	0.3	1032	976	2470	2482	8.7	0.4	0.04	82.9	1.5×10^5	105	3722
	0.4	1024	968	2471	2484	7.9	0.3	0.02	61.8	9.5×10^4	155	9898
	0.5	**1018**	**962**	**2472**	**2485**	**7.3**	**0.3**	**0.02**	**48.7**	$\mathbf{6.3 \times 10^4}$	**223**	**20506**
	0.6	**1013**	**957**	**2473**	**2486**	**6.8**	**0.3**	**0.01**	**40.2**	$\mathbf{4.2 \times 10^4}$	**317**	**37622**
	0.7	1009	953	2474	2486	6.5	0.3	0.01	33.9	2.7×10^4	471	87729
8. Lake gas -blob of 3.6 kg/s and 1.5 m oscillation-	0.05	1060	1004	2465	2478	18.1	0.5	0.2	510.8	1.2×10^6	16	46
	0.1	1039	983	2469	2481	14.3	0.4	0.1	248.0	5.5×10^5	32	274
	0.2	1021	965	2472	2484	11.4	0.3	0.03	125.9	2.5×10^5	64	1438
	0.3	**1010**	**954**	**2474**	**2486**	**10.0**	**0.3**	**0.02**	**82.3**	$\mathbf{1.5 \times 10^5}$	**105**	**4964**
	0.4	**1003**	**947**	**2475**	**2487**	**9.0**	**0.2**	**0.01**	**61.4**	$\mathbf{9.5 \times 10^4}$	**155**	**13190**
	0.5	997	941	2476	2488	8.4	0.2	0.01	48.3	6.3×10^4	223	27392
	0.6	993	937	2477	2489	7.9	0.2	0.01	53.4	4.2×10^4	317	50175
	0.7	989	933	2477	2490	7.4	0.2	0.01	33.5	2.7×10^4	471	117288
9. Bottom gas - Poiseuille flow of 19 kg/s and 1 m oscillation-	0.1	1109	1053	2457	2469	12.2	1.3	1.1	594.7	1.3×10^6	278	648
	0.2	1092	1036	2460	2472	9.9	1.2	0.6	358.4	7.1×10^5	535	2457
	0.3	1082	1026	2462	2474	8.7	1.1	0.4	261.0	4.6×10^5	841	8383
	0.4	1076	1020	2463	2475	7.9	1.1	0.3	207.4	3.2×10^5	1226	20162
	0.5	1072	1016	2464	2475	7.3	1.1	0.2	175.9	2.3×10^5	1686	26778
	0.6	**1069**	**1013**	**2464**	**2476**	**6.8**	**1.0**	**0.2**	**153.8**	$\mathbf{1.6 \times 10^5}$	**2326**	**46911**
	0.7	1067	1011	2465	2476	6.5	1.0	0.2	137.9	1.1×10^5	3239	77234
10. Bottom gas - Poiseuille flow of 19 kg/s and 1.5 m oscillation-	0.1	1081	1025	2462	2474	14.1	1.0	0.5	606.3	1.3×10^6	278	923
	0.2	1064	1008	2465	2477	11.4	0.9	0.3	350.0	7.0×10^5	534	3510
	0.3	**1069**	**1013**	**2464**	**2476**	**9.9**	**1.1**	**0.3**	**338.6**	$\mathbf{6.0 \times 10^5}$	**840**	**8597**
	0.4	1049	993	2468	2479	9.0	0.8	0.1	196.7	3.0×10^5	1223	28946
	0.5	1053	997	2467	2479	8.4	0.9	0.1	199.1	2.6×10^5	1684	31698
	0.6	1043	987	2469	2480	7.9	0.8	0.1	144.2	1.5×10^5	2322	67631
	0.7	1040	984	2469	2481	7.4	0.7	0.1	128.8	1.0×10^5	3233	111467

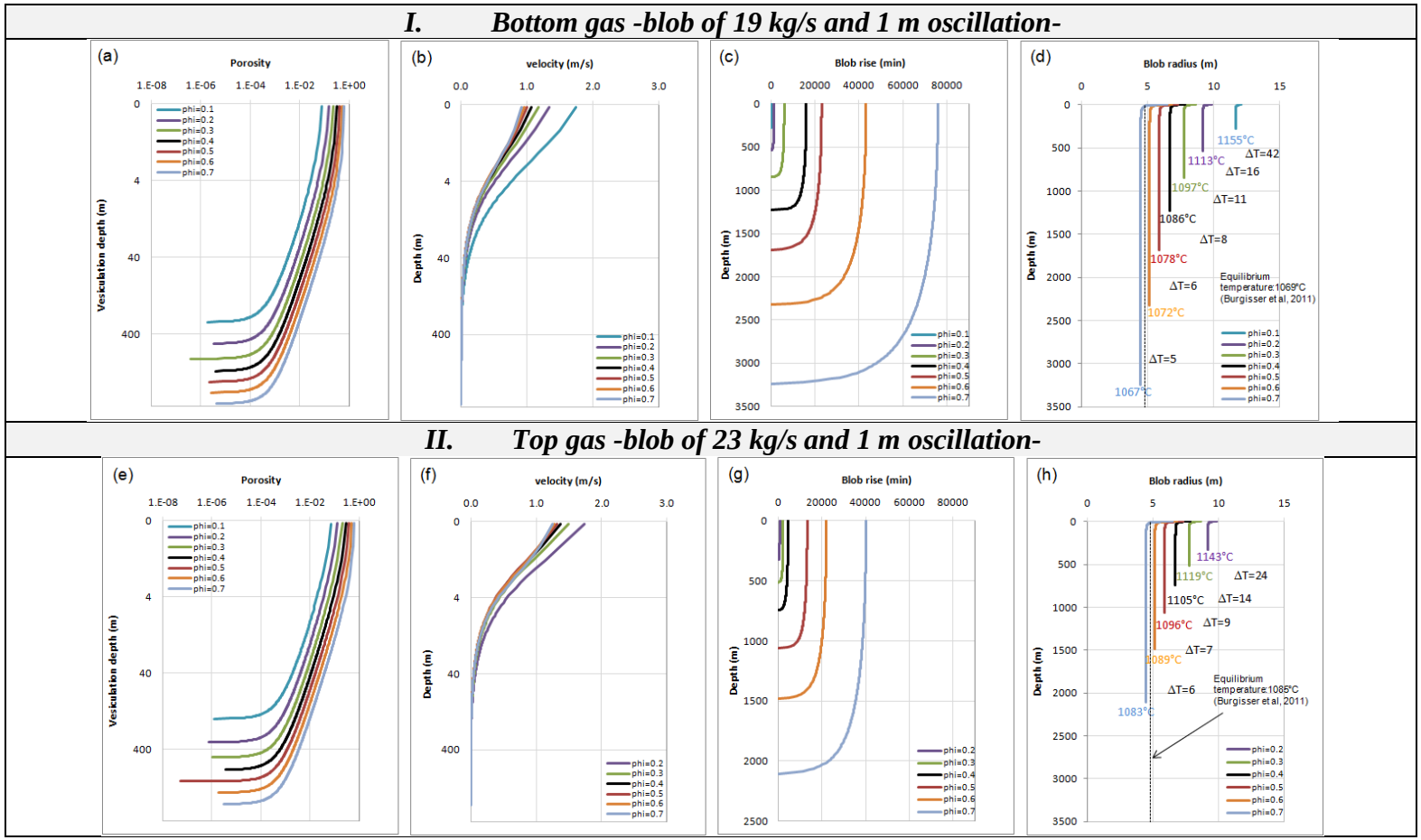

Figure A1. Variations of porosity, velocity, rising time and radius of blob as a function of depth for the main compositions observed at Erebus. Both are matching the gas flux observations of 19 and 23 kg/s for 1 m oscillation of the lake level.

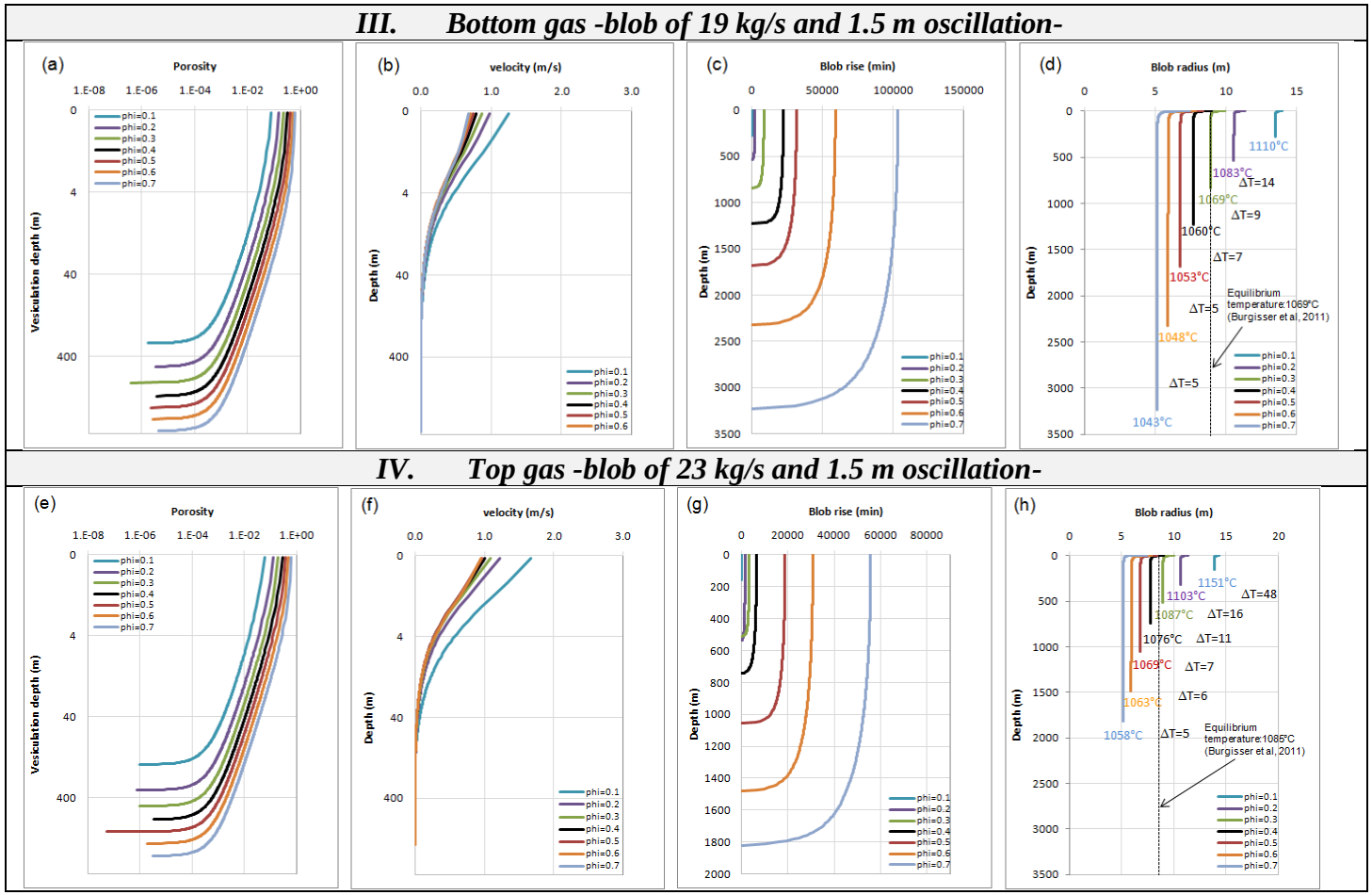

Figure A2. Variations of porosity, velocity, rising time and radius of blob as a function of depth for the main compositions observed at Erebus. Both are matching the gas flux observations of 19 and 23 kg/s for 1.5 m oscillation of the lake level.

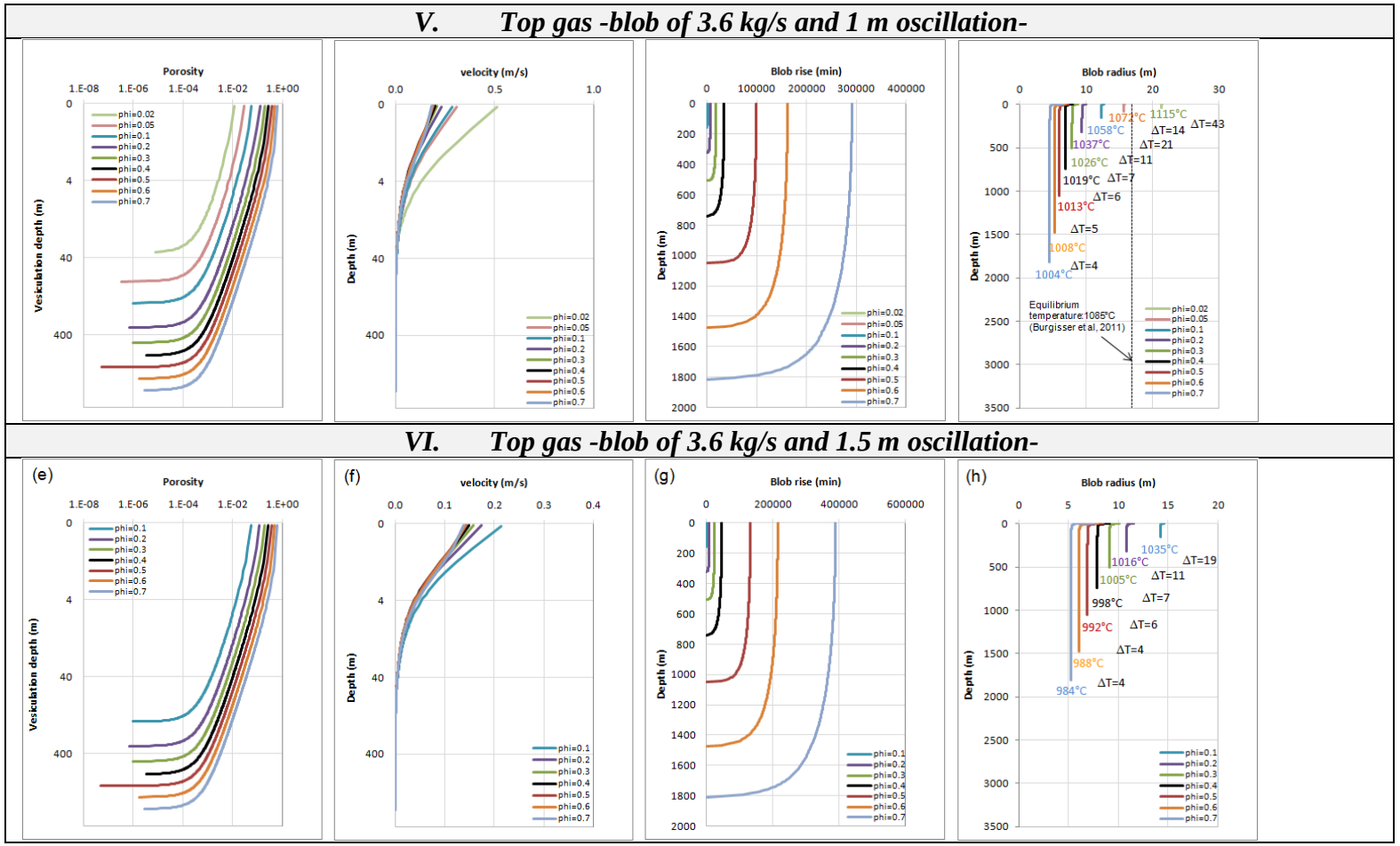

Figure A3. Variations of porosity, velocity, rising time and radius of blob as a function of depth for the main compositions observed at Erebus. Both are matching the gas flux observations of 3.6 kg/s for 1 m and 1.5 m oscillation of the lake level.

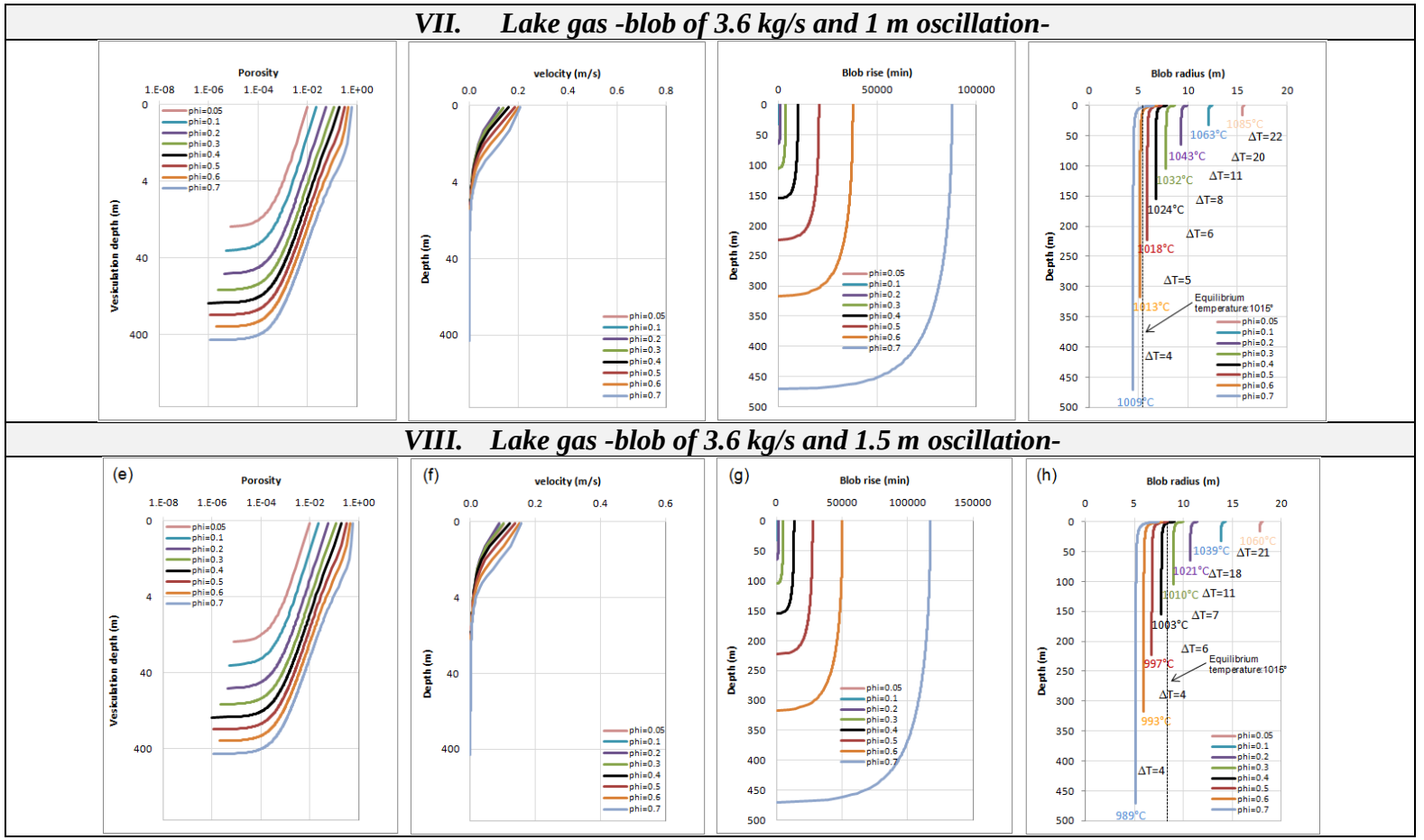

Figure A4. Variations of porosity, velocity, rising time and radius of blob as a function of depth for the main compositions observed at Erebus. Both are matching the gas flux observations of 4 kg/s for 1 m and 1.5 m oscillation of the lake level.

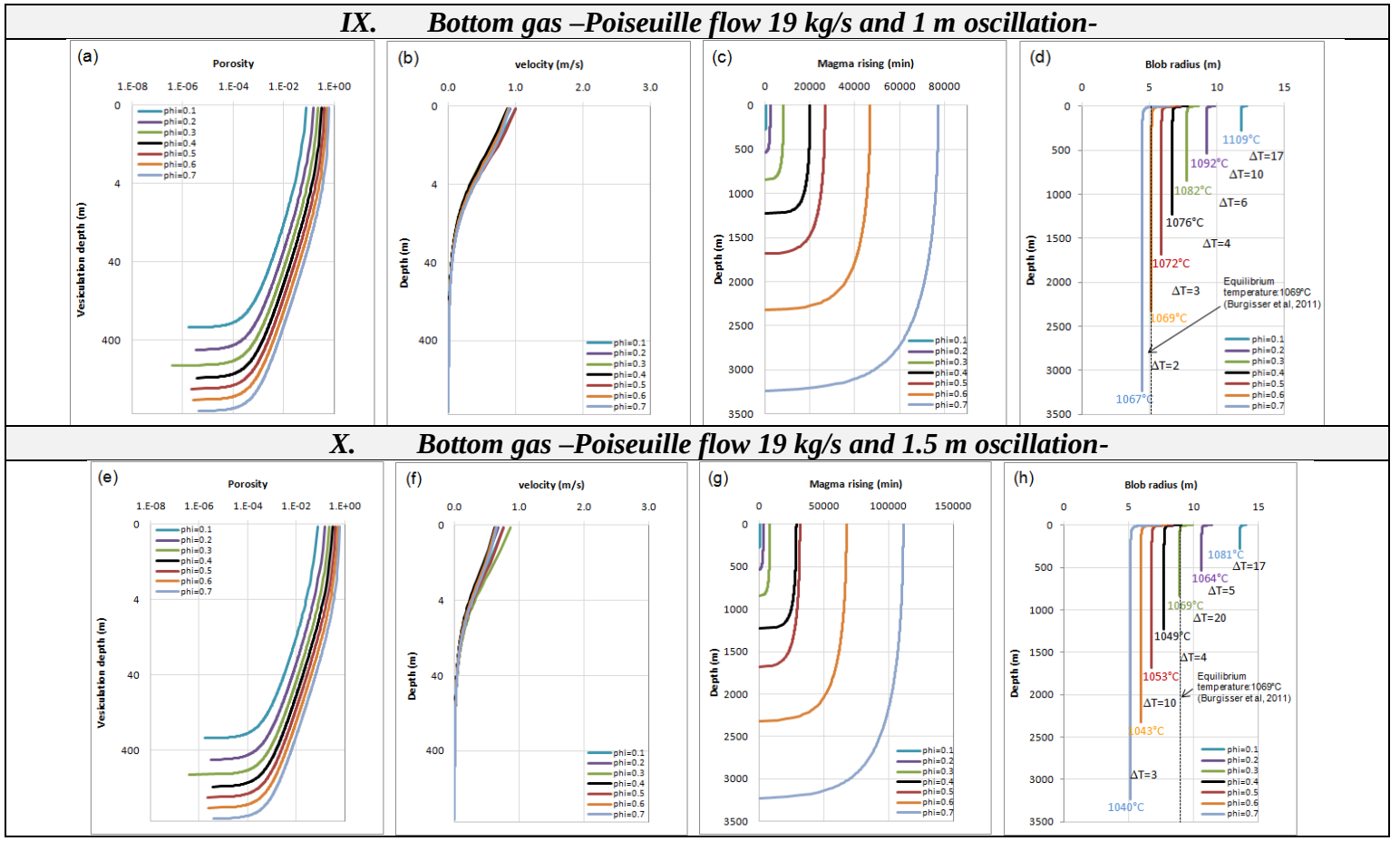

Figure A5. Variations of porosity, velocity, rising time and radius of blob as a function of depth for the main compositions observed at Erebus. Both are matching the gas flux observations of 19 kg/s for 1 m and 1.5 m oscillation of the lake level.

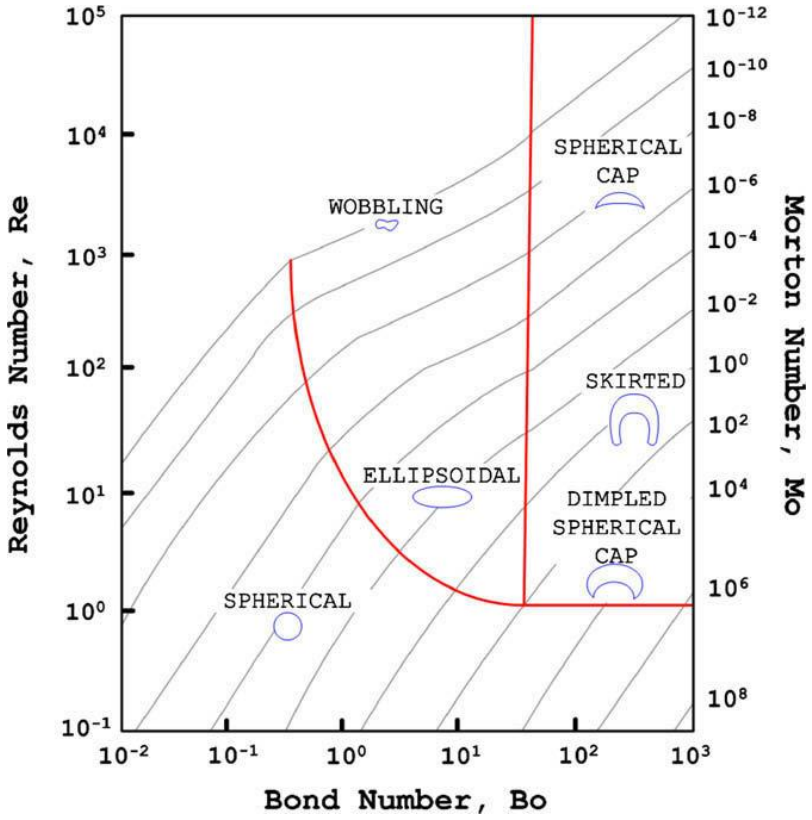

Figure A6. Shape regime map of *Clift et al*. [1978]. Erebus blobs would be outside of this mapped region, but belonging to the region of spherical shape.

Chapitre V

Physical models addressing level fluctuations of the lava lake at Erebus volcano, Antarctica: II. The role of the lake crust

Résumé

Les remarquables fluctuations du niveau du lac de lave du volcan Erebus, en Antarctique, ont été liées à des variations cycliques de la composition du panache de gaz. Nous considérons la surface du lac comme une croûte perméable se déformant sous la pression comme un écoulement de Bingham, montrant qu'une source peu profonde de gaz peut provoquer de telles fluctuations en ascendant dans un conduit au travers duquel percole un gaz généré en profondeur. L'épaisseur et la perméabilité de la croûte se formant en surface lorsque le magma se refroidit constituent des paramètres majeurs du processus de dégazage, car elles conditionnent la valeur de la porosité juste sous la surface. Nous montrons ensuite l'influence du diamètre du courant ascendant permettent à cette source peu profonde d'atteindre la surface avec un flux suffisant pour produire un dégazage dans des proportions en accord avec les observations.

Abstract

The remarkable fluctuations of the lava lake level at the Erebus volcano, Antarctica, have been linked to the cyclic variations of the gas plume composition. We consider the surface of the lake as a permeable crust deforming under pressure as a Bingham flow, showing how a batch of shallow source of gas can lead to such fluctuations when ascending in a conduit through which a deep-generated gas is percolating. The thickness and the permeability of the crust developing as the magma cools down constitute major parameters of the degassing process, because they condition the value of the porosity just below the surface. We then show the influence of the diameter of the ascending current allowing this shallow source to reach surface with a flux large enough to generate degassing in proportions consistent with the observations.

1. Introduction

Observations and measurements indicate that the surface of the Erebus lake periodically rises by 1 to 1.5 m and releases a flow of gas of 19.2 kg/s when it is at its lowest level up to 22.8 kg/s at its peak, before returning to its previous level [*Oppenheimer et al*., 2009 and *Oppenheimer et al.*, 2011, in prep., chapter IV]. The variation of gas composition have been reported to be in phase with surface velocities; if we assume that the rise of the level and the resulting oscillation causes the variation of the surface velocity, then the variation of the gas rates can be coupled with the change in level, as additional gas reaches surface. The average duration of a cycle is around 10 minutes and a new cycle resumes almost immediately.

We determine in this chapter how a continuous flow of gas-rich melt associated to a blob periodically reaching surface can generate an oscillation of the surface over a cycle of 10 minutes, while releasing 19.2 to 22.8 kg/s of gas through a permeable crust behaving as a Bingham fluid. At surface such a blob would generate a circular disturbance varying around 14 m in diameter (Figure 2a-2o, Chapter IV).

In this study, we consider that a continuous flow of magma ascends as a Poiseuille flow in the core of a concentric “pipe” while the degassed magma descends around this core without interfering with the ascending flow. This one is driven by the buoyancy due to the difference

in density between ascending and descending magma. Gas-rich blobs of magma periodically reach surface and disturb the equilibrium.

We consider here the surface of the lake as a mixture of melt, particles and gas that behaves as a Bingham fluid in a circular pipe, represented by the walls of the lake. However this surface is permeable and, under a threshold, the pressure below the surface is not sufficient to cause yielding and the surface of the lake remains still. An overpressure balances the atmospheric pressure, the weight of the surface and forces gas to escape at a rate of 19.2 kg/s, without applying a sufficient force to lift the surface. The gas-rich blobs are providing an additional amount of gas that increases the pressure below surface beyond this threshold. The force, proportional to the pressure and the area of the lake, lifts the surface while the resistance to the flow is proportional to the yield stress and the contact area at the circumference of the lake. As the pressure increases, the whole surface behaves as a piston.

The additional pressure is dissipated through the rising permeable surface and the gas rate increases. As the magma is degassed, the denser melt is circulated back in the conduit and the surface only is considered as "flowing"; therefore the thickness of the surface is considered as the length over which this flow develops. This same thickness is used to calculate the flow of gas through the permeable medium.

If we consider the variation of the flow rate between its lower and upper values as linear and identical for both increase and decrease of the pressure, we can calculate the mass of gas released during a full cycle. For different values of porosity, we evaluate the volume of melt associated to the volume of gas. We vary the thickness of the crust and the porosity of the magma just below the crust to reproduce the observations. The list of parameters used in this study is cited in Table 1.

Table 1. Parameter, symbols and units used in our modelling. Some variables are used as an input and an output simultaneouly because they are the result of the adjustement in agreement with other variables and/or observations.

Symbols			**Variable**		
Latin/Greek	**Value**	**Units**	**input**	**output**	**Parameter**
A	5.3				Constant accounting for interparticle cohesion
F_{dn}		kg m/ s^2			Down force
F_{up}		kg m/ s^2			Up force
g	9.81	m/s^2			Gravity acceleration

Symbols Latin/Greek	Value	Units	Variable input	Variable output	Parameter
h_{crust}	0.1–2.5	m	x		Crust thickness
H_{osc}		m		x	Height of oscillation
m_{gas}		Kg	x		Released mass of gas
M	0.027	kg/mol	x		Molar mass of gas
p	1				Constant reflecting response to shearing
ΔP		Pa	x	x	Overpressure below crust
$\overline{\Delta P}$		Pa		x	Average overpressure below crust
P_{atm}	6.50×10^4	Pa			Atmospheric pressure
P_{gas}		Pa	x		Confined pressure below crust
$\overline{P_{gas}}$		Pa		x	Average confined pressure below crust
P_{inc}		Pa	x		Pressure to initiate yielding
P_{step}		Pa	x	x	Pressure step
Q_{asc}		m^3/s		x	Volume flux of ascending magma
Q_{desc}		m^3/s		x	Volume flux of descending magma
Q_{gas}	19.2/22.8	kg/s	x	x	Rate of released gas
Q_{melt}		m^3/s		x	Flow rate of associated melt
r_a		m	x	x	Radius of core ascending fluid
$r_{(a+d)}$		m	x	x	Radius of ascending and descending fluid
r_y		m		x	Yield radius
R	8.3144	J/K mol			Perfect gas constant
R_c		m		x	Total radius of the conduit
R_{lake}	15.7	m			Lake radius
S_{lake}	770	m^2			Lake surface
t		s	x		time
t_{up}, t_{down}	300	s	x		Half of a cycle
T_m	1273	K			Magma temperature
U_{max}		m/s	x		Maximum ascending velocity
V_{gas}		m^3		x	Volume of confined gas
V_{melt}		m^3		x	Volume of associated melt
ρ		kg/m^3	x		Flow density
ρ_{gas}		kg/m^3	x		Gas density
ρ_a		kg/m^3	x		Density of ascending fluid
ρ_d		kg/m^3	x		Density of descending fluid
$\Delta\rho_{d-a}$		kg/m^3	x		Difference of density between ascending–descending fluids
τ		Pa	x		Shear force
τ_y		Pa	x		Yield strength
ϕ			x		Porosity
φ	0.30				Volume fraction of spheres in mixture
φ_c	0.25				Critical packing fraction of spheres in mixture
φ_m	0.85				Maximum packing fraction of spheres in mixture
k_1	2×10^{-10} –3×10^{-10}	m^2	x	x	Crust permeability (Darcian)
μ_a	$10^5/10^7$	Pa s	x		Viscosity of ascending magma / degasified layer
μ_d	10^5	Pa s	x		Descending fluid viscosity
μ_g	5.05×10^{-5}	Pa s			Gas viscosity

2. Permeability of the surface of the lake

The permeability is a measure of the resistance of a porous medium to allow a fluid to flow through it. The permeability to the gas of a porous cold crust at the top of the lake (degasified layer) is evaluated from the definition of Darcy's law. For a gas, since the volumetric flow rate varies with pressure, it is necessary to use either an integrated form of the Darcy's equation or an average value of the flow rate. Moreover, when the gas flows fast enough to generate turbulence, Darcy's law can only approximate the general equation of filtration, which has been expressed by *Forchheimer* [1901] as:

$$\overbrace{\overbrace{\frac{\Delta P}{L} = \frac{\mu}{k_1} v}^{Darcy\ law} + \frac{\rho}{k_2} v^2}^{Forchheimer\ law} \quad (1)$$

Where ΔP is the pressure difference along the porous medium, L is the length of the porous medium in direction of flow, k_1 and k_2 are the Darcian and inertial permeability coefficients, μ and ρ are the viscosity and density of the flowing fluid, and v is the filtration velocity of the gas through the porous medium.

The first term in RHS (right-hand side) equation (1) represents the viscous resistance to flow and the second term represents the kinetic effects (ρv^2) when the fluid velocities become higher. A criterion, used to distinguish between Darcy's and Forchheimer's forms, Reynolds number (*Re*) for a flowing gas through a porous medium is defined as:

$$Re = \frac{\rho_{gas} U_{gas} \theta}{\mu_g} \quad (2)$$

Where ρ_{gas} is the gas density, μ_g is the gas viscosity, θ is the pore diameter in the porous medium (taken here as the bubble radius) and U_{gas} is the gas velocity through this porous medium.

The bubble number density has been determined to be 10^{11} m^{-3} with a bubble radius ranging from 19×10^{-6} m to 566×10^{-6} m (Figure 1). This corresponds to 2.15×10^7 bubbles/m^2.

Considering that the gas is released over the whole area of the lake of 770 m^2, we calculate the number of bubbles reaching surface to be 1.65×10^{10}. The gas flux measurements of 19.22 and 22.83 kg/s corresponds to volumetric rates of 113.1 and 134.3 m^3/s, respectively. This represents a gas volumetric flux of 7.9×10^{-9} m^3/s and 6.7×10^{-9} m^3/s by bubble, with velocities ranging from 7×10^{-3} to 7 m/s. Using these values in equation (2) yield Reynolds numbers varying from 0.2 to 4.6. *Hassanizadeh and Gray* [1987] having determined that Darcy's flow can be considered as laminar if Reynolds number ranges between Re = 1 to 15, we can neglect Forchheimer's kinetic component.

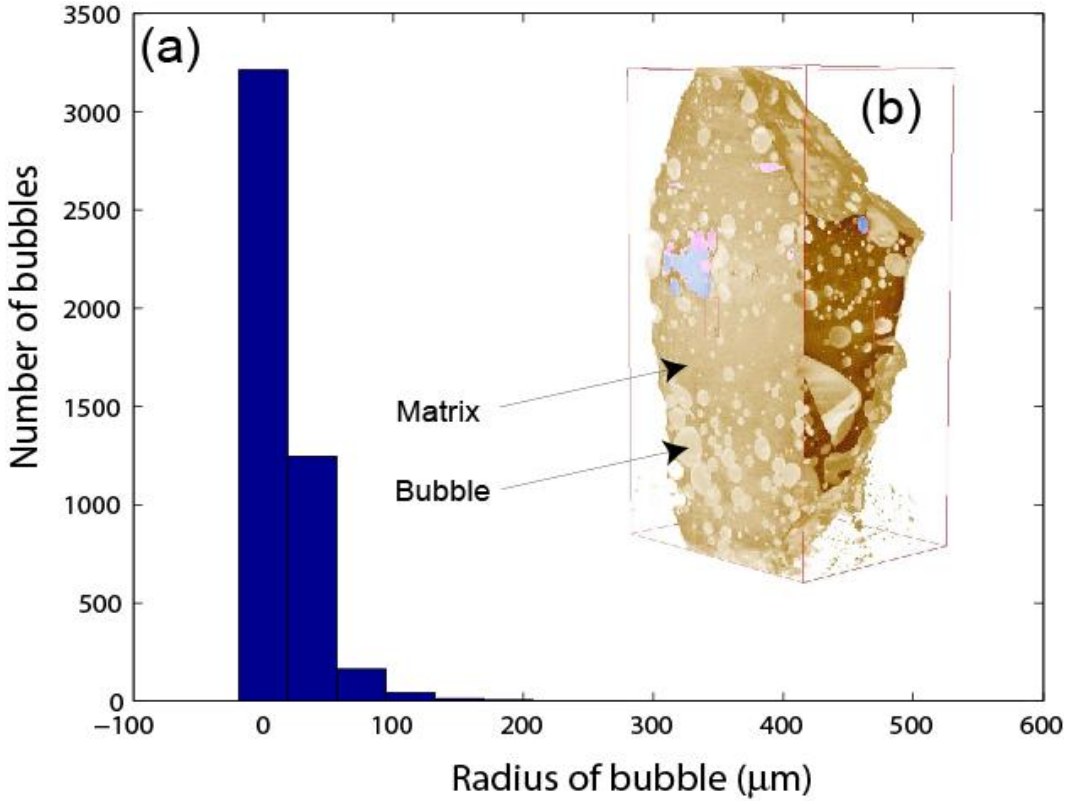

Figure 1. (a) Histogram of the radius distribution of bubbles for one bomb emitted by the lake, (b) Image of a tomography of one bomb ejected by Erebus. This sample yields a porosity of ~25 vol.% (image and data are courtesy of Ian Schipper).

The confining pressure below the surface crust layer being low, we consider that the gas passing through this layer behaves as an ideal gas. This is not a problem with the differential form of Darcy's law but - with finite difference approximation or when using the integrated form of Darcy's law - an average density must be used. This can be avoided by using the pressure squared as the dependent variable if the pressure is low enough for the ideal gas law

to be obeyed. Thus the version of equation (1) for a compressible ideal gas is expressed as follows (as *Rust and Cashman* [2004] and after neglecting the kinetic component):

$$\frac{P_{gas}^2 - P_{atm}^2}{2\,P_{atm}\,h_{crust}} = \frac{\mu_g}{k_1} U_{gas} \quad (3)$$

Where P_{gas} and P_{atm} are the gas pressure (confining) at the entrance (below the crust) and at the exit (atmospheric pressure) of the porous medium, respectively; h_{crust} is the thickness of the porous medium, μ_g is the fluid dynamic viscosity of the gas, U_{gas} is the filter velocity (volumetric flow rate per cross-sectional area) and k_1 the permeability of the layer to the gas.

From equation (3) we obtained a simple Darcian velocity for the gas U_{gas} which, multiplied by the gas density, $\rho_{gas} = (P_{atm}M)/(RT_m)$, and the surface of the lake, S_{lake}, allow us to estimate the mass rate, Q_{gas}, at atmospheric pressure:

$$Q_{gas} = \frac{P_{gas}^2 - P_{atm}^2}{2\,h_{crust}} \frac{k_1}{\mu_g} \frac{M}{R\,T_m} S_{lake} \quad (4)$$

3. Ascent velocity of the crust as a Bingham flow

The rigid crust is considered as a solid lid that moves up and down and its level fluctuates like a piston according to the overpressure that builds up underneath. The crust will start to move up only when the force exerted by the pressure (F_{up}) overcomes the force (F_{dn}) exerted by the atmosphere, its weight and the resistive shear force.

$$F_{dn} = (P_{atm} + P_{crust})S_{lake} \quad (5)$$

And

$$F_{up} = P_{gas}\,S_{lake} \quad (6)$$

Our assumptions are sketched in the Figure 2. At equilibrium, the friction exerced by the layer against the outer walls of the crater lake prevents the crust to move either upwards or downwards. When the level stands at its lowest, the force applied by the pressure below the

surface balances the atmospheric pressure, the lithostatic pressure of the layer and the friction of the layer at the edge of the lake; we define this period as the "*equilibrium of the lake*" (Figure 2a). This period of quiescence defines the baseline conditions for the gas flux, the pressure exerted by the gas below the surface and the level of the lake. Knowing the atmospheric conditions and the parameters defining the crust, we can estimate the pressure below this crust. The observations made by *Oppenheimer et al*. [2009] allow us to constrain it. Oppenheimer and co-authors measured a degassing rate of 19 kg/s when the lake stands at its lowest level. Combining equations (3) and (4), we calculate $P_{gas}^2 - P_{atm}^2$ and therefore the pressure below the crust. At equilibrium, the overpressure below the crust allows a constant degassing rate of 19.22 kg/s without being sufficient for the crust to move upwards. Therefore the force exerced by this overpressure corresponds to the friction at equilibrium, for which the ascent velocity of the crust is nil. Because the friction is almost entirely taken off, a slight increase of pressure below the crust is likely to lift the surface.

As additional gas reaches surface with the arrival of a "blob", the overpressure resulting from the gas expansion will increase the differential pressure across the crust and the upward force; so will the value of $P_{gas}^2 - P_{atm}^2$. The volume below the upper layer of the lake behaves as a buffer and would damper the downward motion of the surface as the gas flux drops below a rate of 19.2 kg/s; as the pressure increases, the resulting force overcomes the dynamic friction and the level starts rising; we define this period as "*disequilibrium of the lake*" (Figure 2b). We consider that thickness of the crust does not vary under pressure changes during one cycle; however the permeability has been adjusted for each value of the crust thickness, in order to solve the gas flux at equilibrium. This value of permeability remains constant throughout a cycle generated under a same value of crust thickness. We therefore expect the degassing rate to increase as per Darcy's law until the whole overpressure has been dissipated. The surface will then return to its previous value until another cycle resumes. Observations given by *Oppenheimer et al*. [2011, in prep] allow us to further constrain our model: we know that the level of the lake rises 1 to 1.5 m over a period of 300 s before it returns to its previous level over a same period of time and that the gas flux at the peak level has been measured at 22.83 kg/s. We calculate the magma current ascending as a Poiseuille flow in order to generate the 4 kg/s difference.

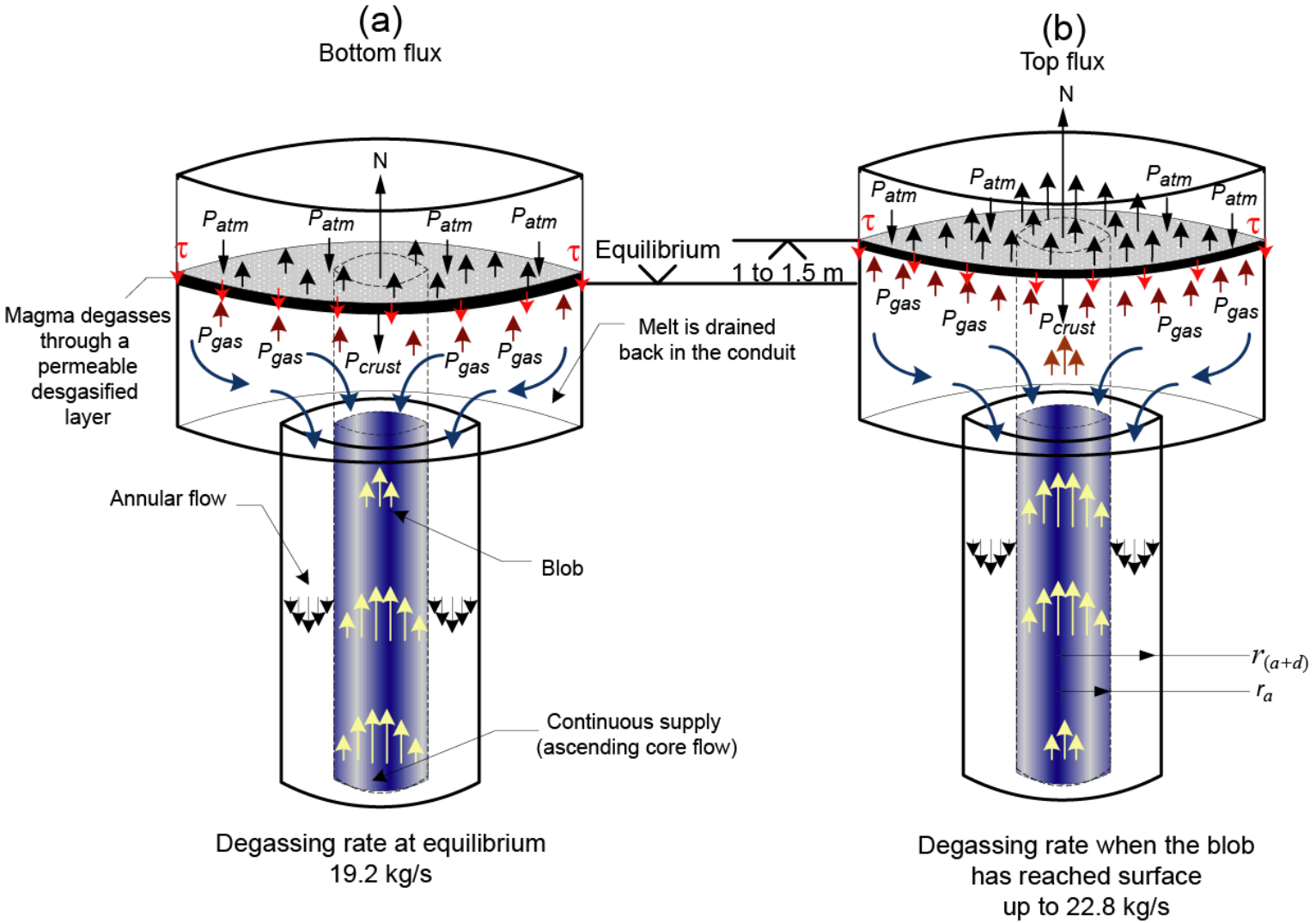

Figure 2. Cartoon representing the main forces of our system during two stages of activity in the lake: **(a)** "equilibrium of the lake system" and **(b)** "disequilibrium of the lake system".

At equilibrium, the overpressure ΔP below the crust is equal to P_{inc}, the minimum pressure sufficient to allow the degassing of 19.2 kg/s without being able to lift the crust yet (equation 7a). As soon as we increase the pressure below the crust (P_{gas}), the forces "F_{up}" and "F_{dn}" are no longer balanced by the shear force acting on the contact surface between the wall of the lake and the cold crust (equation 7b). The level starts to rise and the degassing rate increases. By adjusting the value of P_{step}, we obtain by regular increments (15 in total) a set of values of pressure below the crust; each value yields a new degassing rate covering the whole range 19.2 to 22.8 kg/s.

The force available to lift the crust will be :

$$F_{up-}\,F_{dn} = \begin{cases} \overbrace{\Delta P\,\pi\,R_{lake}^2}^{\text{Lift force}} = \overbrace{2\pi\,R_{lake}\,h_{crust}\,\tau_y}^{\text{Shear force}} & \text{if } \Delta P = P_{inc} \quad (7a) \\ \Delta P\,\pi\,r_y^2 = 2\pi\,r_y\,h_{crust}\,\tau_y & \text{if } \Delta P > P_{inc} \quad (7b) \end{cases}$$

Where the overpressure $\Delta P = P_{gas} - P_{atm} - P_{crust}$ if $\Delta P = P_{inc}$, and $\Delta P = P_{inc} + P_{step}$ if $\Delta P > P_{inc}$, R_{lake} is the radius of the lake, h_{crust} is the thickness of the crust, r_y is the yield radius and τ_y is the shear yield stress.

When $\Delta P > P_{inc}$, the yield radius, r_y, is thus:

$$r_y = 2\,\frac{h_{crust}\;\tau_y}{\Delta P} \qquad (8)$$

And the maximum velocity when $\Delta P > P_{inc}$ is be given by *Dixon* [2007]:

$$U_{max} = \frac{\Delta P\,(R_{lake} - r_y)^2}{4\mu_a h_{crust}} \qquad (9)$$

Where μ_a is the ascending fluid viscosity.

Hoover et al. [2001] and *Wildemuth and Williams* [1984] defined the yield stress τ_y of a mixture as:

$$\tau_y = A\left(\frac{\frac{\varphi}{\varphi_c}-1}{1-\frac{\varphi}{\varphi_m}}\right)^{\frac{1}{p}} \quad (10)$$

Where φ is the volume fraction of spheres (crystals) in the mixture; φ_c is the critical packing concentration at which the mixture can sustain external stress (zero-shear yield strenght) and φ_m is the maximum packing fraction (yield strength tends to infinity). *A* is a constant equal to 5.3 reflecting the interparticle cohesion and p is a constant reflecting the response of the aggregate to shearing; comprised between 0.5 and 2, we took a value of p = 1.

For values of φ = 0.3, φ_c = 0.25 and φ_m= 0.85, we obtained a value of τ_y = 1.64 Pa through equation (10). Since the thickness of the crust is unknown, we incremented it between 0.1 and 2.50 m by steps of 0.1 m. For each value of crust thickness, h_{crust} (e.g 0.1 m) and using equation (4), we determined the permeability of the crust, k_1, that solves our degassing rate at equilibrium conditions: at $\Delta P = P_{inc}$ and $Q_{gas} = 19.2$ kg/s. At this conditions, $P_g = P_{inc} + P_{atm} + P_{crust}$ and P_{inc} is obtained through equation (7a). $k_1 = 3.1 \times 10^{-10}$ m^2 and $P_g = 6.7 \times 10^4$ Pa were obtained by assuming R = 8.3144 J/K mol, T_m = 1273 K, M = 0.027 kg/mol, μ_g = 5.05×10^{-5} Pa s, P_{atm} = 6.5×10^4 Pa, R_{lake} = 15.7 m. In desequilibrium conditions, ΔP is obtained through equation (7b) and then $P_g = \Delta P + P_{atm} + P_{crust}$. By plugging P_g increment by increment and fixing R, T_m, M, μ_g, P_{atm} and $k_1 = 3.1 \times 10^{-10}$ m^2 in equation (4), we solved our degassing rate at disequilibrium conditions and obtained the value of Q_{gas} and the yield radius r_y at each value of the overpressure. We calculate then the maximum ascent velocity, U_{max} from equation (9). Under the initial equilibrium conditions, $r_y = R_{lake}$ and therefore $U_{max} = 0$ m/s. By multiplying the duration of a half of the cycle (5 min) by the average of the velocities resulting from the increase of the overpressure step by step, we obtain the height of the oscillation, H_{osc}, over this period. The calculation was repeated for the range of crust thicknesses defined above.

4. Gas pressure combined into an ideal gas law

Assuming that the pressure increases and decreases at identical rates, the mean mass of gas released during a full of cycle, m_{gas}, is defined as:

$$m_{gas} = \overbrace{(t_{up} + t_{down})\left(Q_{gas}{}_{t=t_{up}} - Q_{gas}{}_{t=0}\right)}^{\text{Gas associated to the magma batch (blob)}} + \overbrace{(t_{up} + t_{down})\left(Q_{gas}{}_{t=0}\right)}^{\text{Gas associated to the continous flow}} \quad (11)$$

Where Q at $t = 0$ is 19.22 kg/s and at $t = t_{up}$ is 22.83 kg/s.

However, we have set that the continuous flow of gas percolating through the conduit is not associated to melt contributing to the global melt budget. We look at determining which quantity of melt is associated to the gas released by the arrival of the blob; the second term in the RHS of equation (11) is not taken into account to calculate the volume of confined gas V_{gas}. Under pressure conditions, while ideal gas behavior is assumed, V_{gas} will be:

$$V_{gas} = \frac{m_{gas}\, R\, T_m}{M\, \overline{P_{gas}}} \quad (12)$$

Where the total average confining pressure below the crust, $\overline{P_{gas}}$, corresponds to the pressure exerted by the crust, P_{crust}, the atmosphere, P_{atm}, and the average overpressure, $\overline{\Delta P}$. The overpressure ΔP increases at every P_{step} , allowing the mass flux through the crust to increase from 19.2 to 22.8 kg/s.

The volume of melt associated to this gas volume, V_{gas}, will be:

$$V_{melt} = V_{gas}\left(\frac{1}{\phi} - 1\right) \quad (13)$$

Where ϕ is the porosity of the bubbly flow.

In a full cycle the flow rate of magma will be given by:

$$Q_{asc} = (V_{gas} + V_{melt})/(t_{up} + t_{down}) \quad (14)$$

As the whole volume of magma ascending in the core of the conduit reaches surface and degasses, the melt density increases and is drained back to the conduit as an annular flow; it does not contribute to the fluctuation of the level of the lake. The mass flux rate of the degassed melt being drained back to the conduit can thus be assumed to be the same that the ascending mass flux of melt. If we consider the depth in the conduit at which all the gas is dissolved in the melt, then $\phi = 0$ and the total volume of associated melt can be calculated through equation (13) over a 10 minute cycle.

5. Results

We varied the thickness of the crust from 0.05 to 2.5 m and calculated the released gas flux, Q_{gas}, from equation (4) under the conditions shown in equations (7a) and (7b). We then determined the height of the oscillation, H_{osc}. Results indicate how much pressure is required to generate an oscillation in the range of 1.09 and 1.42 m over a cycle of 10 minutes, while releasing 19.2 kg/s of gas at low lake level and 22.8 kg/s of gas at its peak level (Figure 3).

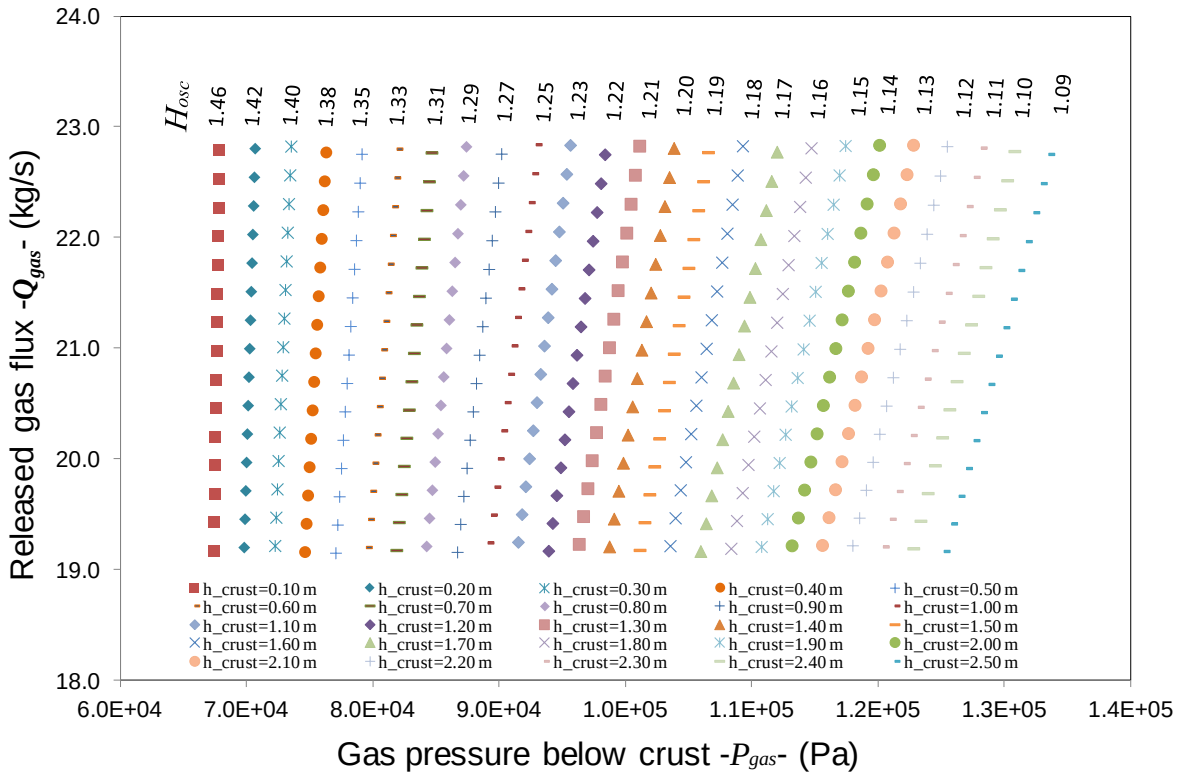

Figure 3. Released mass flux, Q_{gas}, at very P_{step}, through a crust of permeability varying from 3.01×10^{-10} m^2 to 2.16×10^{-10} m^2 as a function of the confined pressure, P_{gas}, for different thicknesses of the crust, h_{crust}. Q_{gas} is calculated through equation (4) and H_{osc} is obtained by multiplying the average crust velocity by a fixed time interval of 5 minutes

(details in the text). The yield radius, r_y varies from 15.7 m at 19.2 kg/s to 10^{-3} m at 22.8 kg/s.

We found that the arrival of a blob resulting in a mean overpressure $\overline{\Delta P}$ varying from 4.34×10^2 to 4.14×10^3 Pa (corresponding to a mean pressure below crust, $\overline{P_{gas}}$, between 7.03×10^4 Pa and 1.29×10^5 Pa) can generate an oscillation of the surface of 1.42 m to 1.09 m, respectively (Table 2) for a crust thickness varying between 0.2 and 2.5 m.

Table 2. Variation of the oscillation as a function of the crust thickness.

Crust thickness h_{crust} (m)	Mean overpressure $\overline{\Delta P}$ (Pa)	Permeability k_1 (m^2)	Oscillation height H_{osc} (m)
0.2	4.34×10^2	3.01×10^{-10}	1.42
0.4	8.40×10^2	2.90×10^{-10}	1.38
0.6	1.21×10^3	2.81×10^{-10}	1.33
0.8	1.58×10^3	2.72×10^{-10}	1.29
1	1.91×10^3	2.64×10^{-10}	1.25
1.2	2.23×10^3	2.55×10^{-10}	1.22
1.4	2.56×10^3	2.48×10^{-10}	1.20
1.6	2.87×10^3	2.41×10^{-10}	1.18
1.8	3.18×10^3	2.34×10^{-10}	1.16
2	3.47×10^3	2.28×10^{-10}	1.14
2.2	3.74×10^3	2.22×10^{-10}	1.12
2.4	4.00×10^3	2.16×10^{-10}	1.10
2.5	4.14×10^3	2.13×10^{-10}	1.09

As the thickness of the crust increases, the pressure required to release the gas in excess of 19.2 kg/s will be larger and the height reached by the level of the lake will be lower (Figure 3). This is due to the change in resistive shear force, to the larger force exerced by the weight of the crust and to the increased resistance of the permeable crust to allow gas passing through it. In absence of a new batch of magma rising to surface, the whole overpressure will progressively be dissipated and the confined pressure will eventually reach the one exerted by the crust. As the pressure below the crust decreases, so does the gas rate.

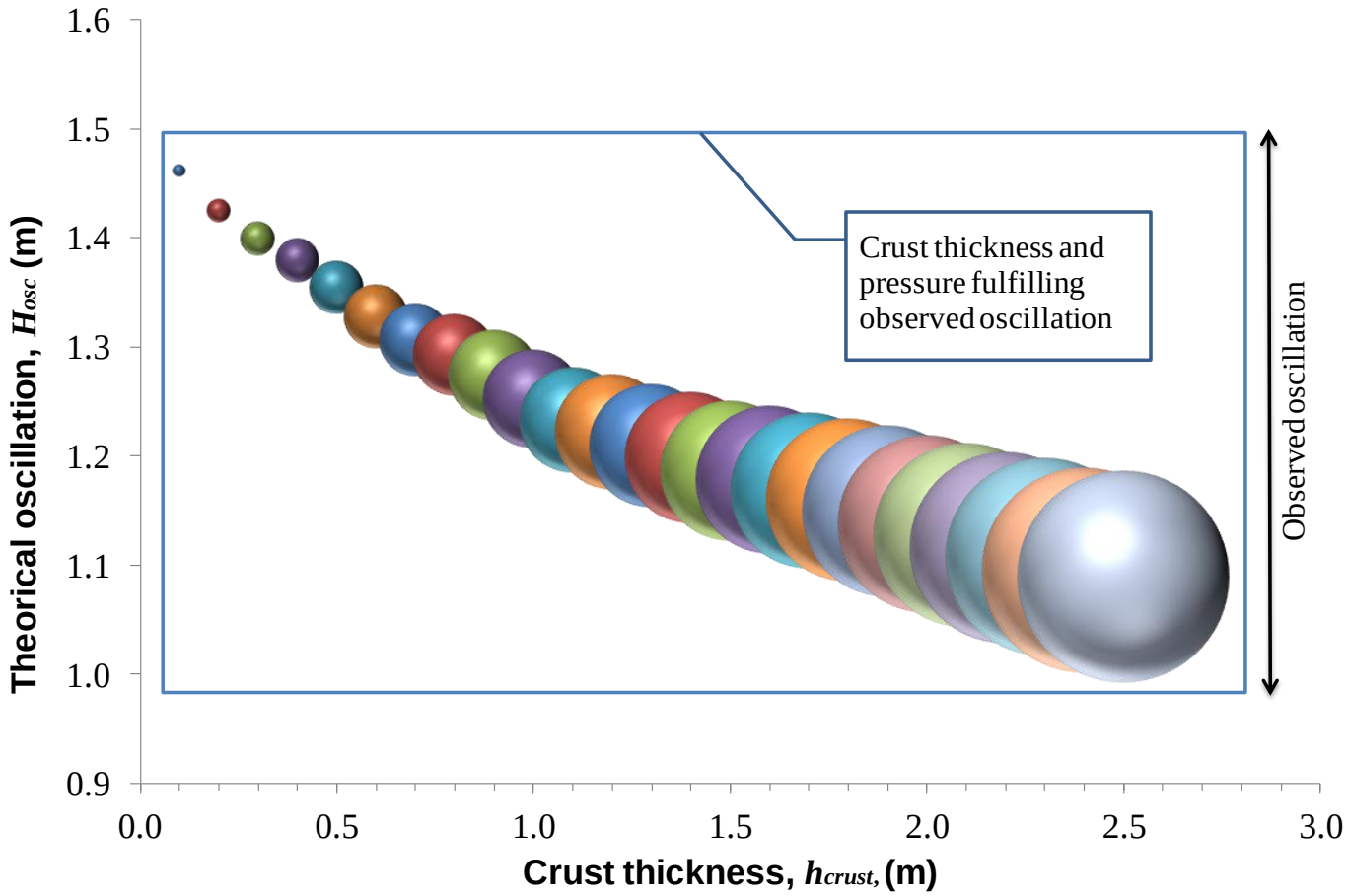

Figure 4. Variation of the level, H_{osc}, of the lake as a function of the thickness of the crust, h_{crust}, over half period (300 s). The size of the bubbles is proportional to the mean overpressure, $\overline{\Delta P}$, required to allow gas flowing to the crust and lift the surface over half a period of 5 minutes.

The volume occupied by the gas below the crust varies with the pressure required to overcome the resistance of the crust to the flow of gas. For any value of porosity and crust thickness, equation (12) to (13) give the volume of gas and associated melt and consequently the magma flux (equation (14)).

Table 3 lists the flux of magma (gas plus melt) required to release 3.6 kg/s of gas for different porosities and crust thicknesses.

Table 3. Variation of the flux of ascending magma for different thicknesses of the crust and at different porosities.

Crust Thickness h_{crust} (m)	Porosity ϕ							Oscillation Height H_{osc} (m)
	10%	20%	30%	40%	50%	60%	70%	
	Volume flow rate of magma Q_{asc} [(a)] (m^3/s)							
0.1	210	105	70	52	42	35	30	1.46
0.2	201	101	67	50	40	34	29	1.42
0.3	194	97	65	49	39	32	28	1.40
0.4	188	94	63	47	38	31	27	1.38
0.5	181	91	60	45	36	30	26	1.35
0.6	175	87	58	44	35	29	25	1.33
0.7	169	85	56	42	34	28	24	1.31
0.8	165	82	55	41	33	27	24	1.29
0.9	160	80	53	40	32	27	23	1.27
1.0	155	78	52	39	31	26	22	1.25
1.1	150	75	50	38	30	25	21	1.23
1.2	146	73	49	37	29	24	21	1.22
1.3	143	71	48	36	29	24	20	1.21
1.4	139	70	46	35	28	23	20	1.20
1.5	136	68	45	34	27	23	19	1.19
1.6	133	67	44	33	27	22	19	1.18
1.7	130	65	43	32	26	22	19	1.17
1.8	127	64	42	32	25	21	18	1.16
1.9	125	62	42	31	25	21	18	1.15
2	122	61	41	30	24	20	17	1.14
2.1	119	59	40	30	24	20	17	1.13
2.2	116	58	39	29	23	19	17	1.12
2.3	114	57	38	28	23	19	16	1.11
2.4	111	55	37	28	22	18	16	1.10
2.5	109	54	36	27	22	18	16	1.09

[(a)] Calculated through equation (14)

The thinner the crust, the lower the pressure required to flow the gas through the permeable medium and the higher the volume will be. On the contrary, for a thicker crust at a given

value of the porosity, a higher value of pressure is required for degassing to occur; the corresponding volume of magma decreases. The variation of Q_{asc} as a function of porosity (Table 3) follows power laws for each crust thickness, as illustrated in Figure 5, where we selected 4 examples.

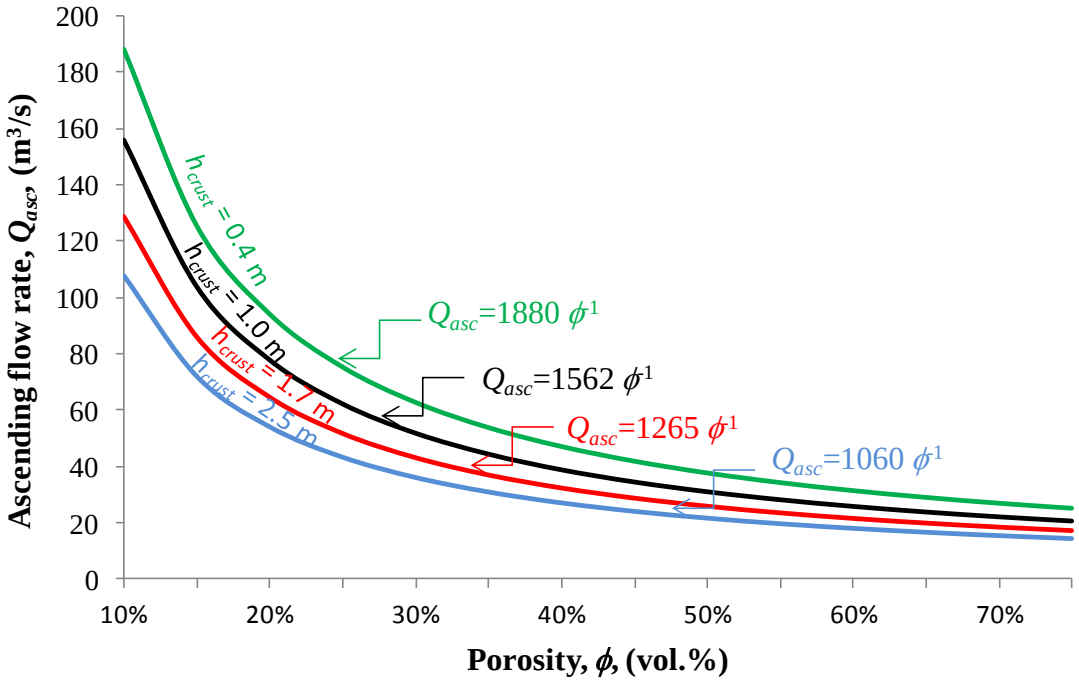

Figure 5 Variation of the ascending magma flux for different thicknesses of the crust and at different porosities, allowing a degassing rate of 3.6 kg/s.

Overall, Table 3 suggests that, for a crust thickness varying between 0.10 m and 2.5 m and a crust permeability varying between 3.01×10^{-10} and 2.13×10^{-10} m^2 (Figure 6), a magma of 10-70% porosity can release an increase of 3.6 kg/s of gas (the increment between the flow rate corresponding to a continuous degassing at 19.2 kg/s and the maximum 22.8 kg/s). The corresponding level increase varies from 1.46 m to 1.09 and the flow of magma from 210 m^3/s at 10% porosity to 16 m^3/s at 70% porosity.

To an oscillation of 1.25 m, for example, our model associates a crust thickness of 1 m, a mean overpressure of 1.91×10^3 and a permeability of 2.64×10^{-10} (Table 2). The flow rate of magma under these conditions varies from 155 to 22 m^3/s for porosities of 10% to 70%, respectively (Table 3).

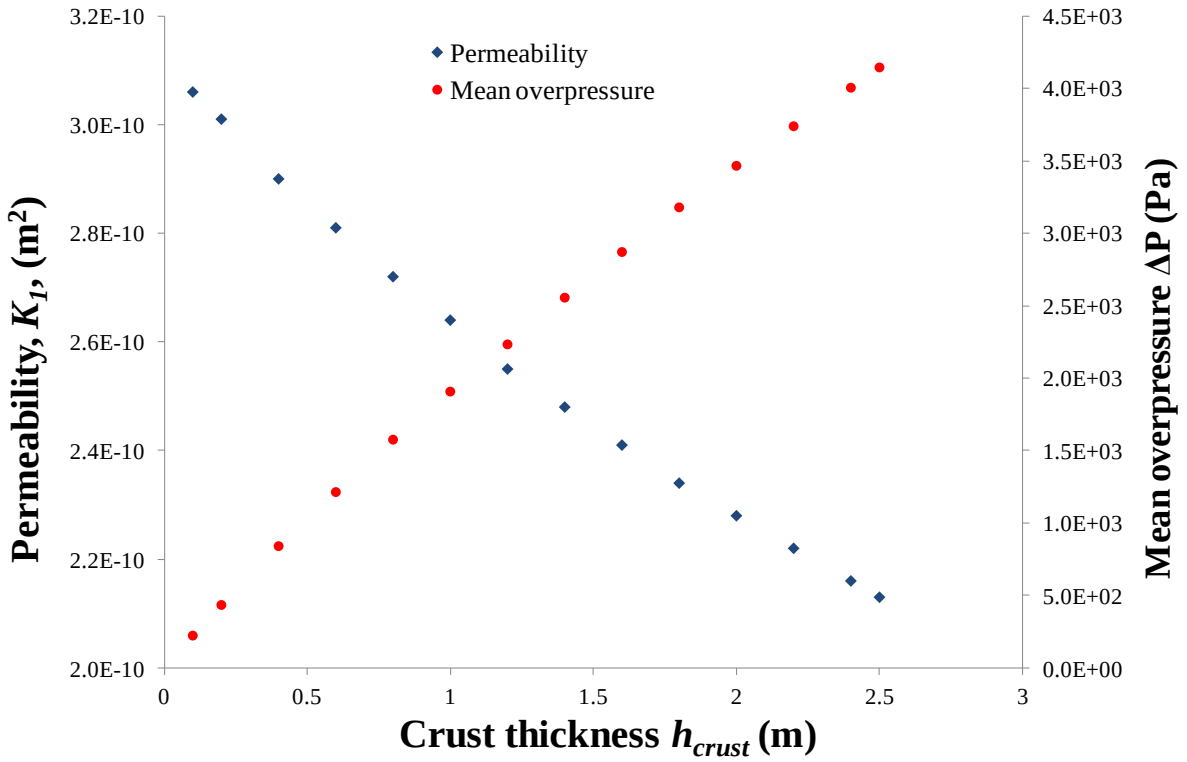

Figure 6. Relationship between the permeability of the crust and the overpressure required to degas up to 3.6 kg/s as a function of the thickness of the crust.

5.1. Constraints on porosity

Our aim is to investigate if a blob with a "top gas" composition, as we defined it in Chapter IV (Case 5-Table 2), can reach surface and degas at a rate matching observation in presence of a crust. In Chapter IV, we systematically treated starting gas compositions given by *Burgisser et al*. [in review] (Table 1 in Chapter IV) associated to a magma batch that ascends by buoyancy and is transported by convective currents with a ΔT of 56°C to release at surface 4, 19 and (or) 23 kg/s at surface. These compositions cover porosities between 10 to 70 vol.% and steps of 10 vol.% except the case with gas composition "Top gas" that was analyzed within a range of porosities of 2-70 vol.% (Figure 7a). Unlike in Chapter IV, in which we selected a particular case, we consider here all the outputs of density and viscosity as a function of depth for blobs porosities varying between 10-70 vol.% (Figure 7a-7c).

In this work, we have considered that the surface of the lake allows degassing as a permeable medium following Darcy's law while behaving as a Bingham flow, whereas the magma

ascends through the conduit as a Poiseuille flow in the core of a concentric pipe. The degassed magma descends outside this core without interfering with the ascending flow. The flow is driven by buoyancy due to the difference in density between ascending and descending magma. The flux of ascending magma has been expressed as *Lamb* [1959], p. 585 and *Kazahaya et al.* [1994]:

$$Q_{asc} = \frac{\pi \Delta\rho_{d-a}\, g\, r_a^4}{8\mu_a} \quad (15)$$

Where r_a is the radius of the inner ascending flow, μ_a is the viscosity of the ascending flow, $\Delta\rho_{d-a}$ is the density difference between ascending and descending flows and g is the gravity constant.

5.1.1. Method of solution

In Chapter IV, we calculated the ascending and descending densities and the viscosities as a function of depth as follows. The blob ascending densities are function of porosity ϕ (equation 4 from Chapter IV; Figure 7a) and were calculated as per equation 12 (from Chapter IV); we define it here as ρ_a (Figure 7b). The density of the descending magma around this blob (dry melt containing 30% of crystals) is a function of the descending temperature and we define it here as ρ_d (Figure 7b). The ascending and descending viscosities of the magma are a function of dissolved water fraction (0 wt.% of water in the case of descending) and a fixed 30 vol.% of crystals, ε_s, (equation 7 from Chaper IV) that we define here as μ_a and μ_d, respectively (Figure 7c). We then obtain $\Delta\rho_{d-a}$. The values of the parameters ρ_a, ρ_d, μ_a and μ_d used in this work result of the adjustement of ΔT and gas flux release of 3.6 kg/s for a blob with a composition "top gas" (Case 5-Table 2; Chapter IV).

In Chapter IV, the blobs were not constraint in their ascent and they were free to grow by expansion of the gas and buoyancy up to surface. However, if they rise in a conduit of limited size, the blobs are likely to be constrained and the ascending rate will be limited, as equation (15) suggests. If a blob, due to the presence of the crust, is not reaching surface, its ascending rate may not be sufficient to allow the observed degassing of 3.6 kg/s.

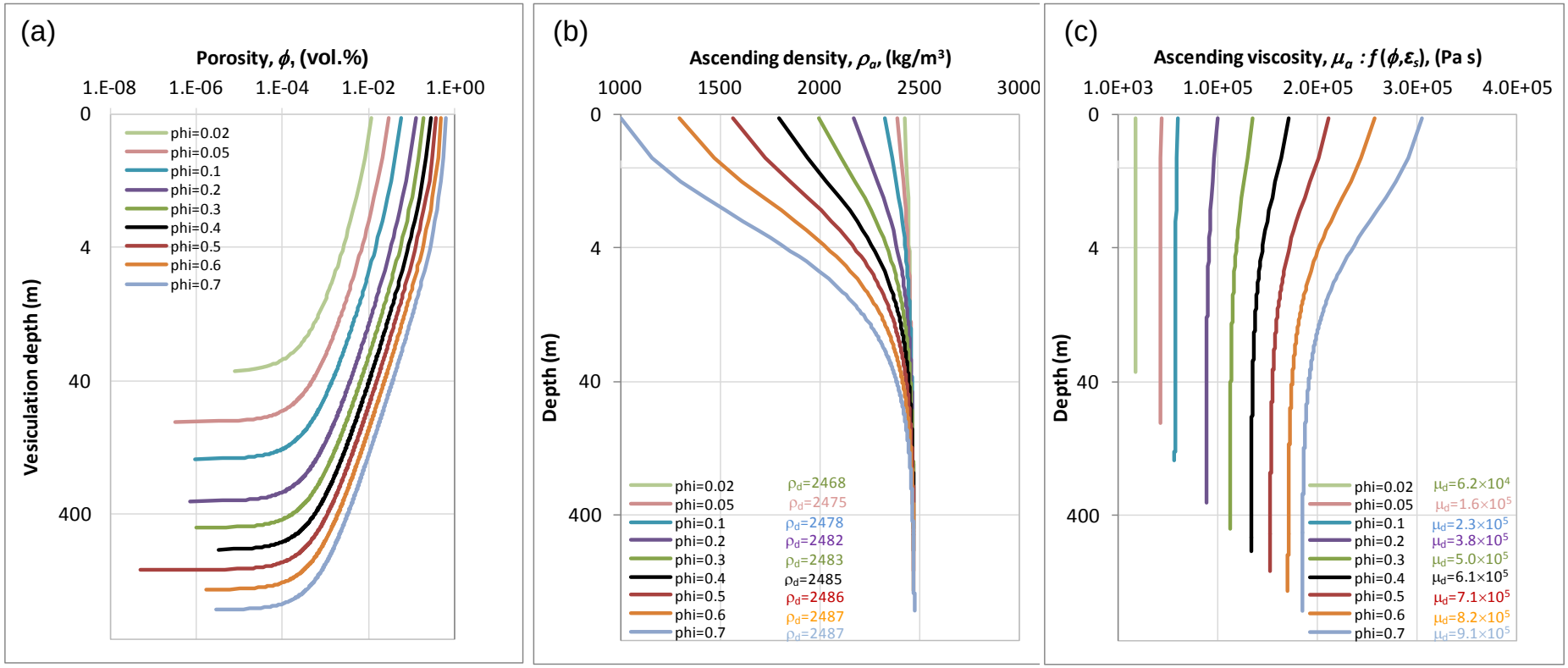

Figure 7. Parameters corresponding to the ascent of a blob with "Top gas" composition and degassing at a rate up to 4 kg/s for a ΔT of 56°C (case 5 from Chapter 4).

We know $\Delta\rho_{d-a}$, μ_a at any given depth (and as well porosity) and we vary the ascending magma radius, r_a, between 2.5 – 7.5 m with steps of 0.5 m (this maximum value of 7.5 m is suggested by the close observation of videos, Figure 2a, Chapter IV). We apply equation (15) and calculate the magma ascent rate, Q_{asc}, of blobs rising up to the lower face of the crust of thickness h_{crust}. As the crust prevents them to effectively reach surface, their maximum porosity, ϕ, will not be the nominal value for which they had been computed (the exact value of 10-70 vol.%), but the porosity at a depth ($\phi|_{z=h_{crust}}$) corresponding to the lower face of the crust.

Combining Darcy and the ideal gas laws explained in Section 4, we have quantified how much magma is required to degas 3.6 kg/s through any crust thickness between 0.1 and 2.5 m and for porosities varying from 10 to 70% (Table 3). We determined power laws of ascending flow rates as a function of porosity, ϕ, for crusts of 0.4, 1.0 and 1.7 m (Figure 6).

We can now determine under which conditions an ascending blob with a "top gas" composition is able to meet our requirements. In other words, we solve simultaneously a magma ascending rate Q_{asc} calculated through Poiseuille model and Darcy's law applied to a gas behaving as an ideal gas and flowing through a crust of thickness h_{crust}. The solution associates the porosity at depth, $\phi|_{z=h_{crust}}$, as follows:

$$\overbrace{Q_{asc}\left[r_a, \Delta\rho_{d-a}\left(\phi|_{z=h_{crust}}\right), \mu_a|_{z=h_{crust}}\right]}^{\text{Poiseuille model}} = \overbrace{Q_{asc}\left[\phi|_{z=h_{crust}}\right]}^{\text{Darcy-ideal gas law models}} \quad (16)$$

The solution of equation (16) is represented by the intersection of the curves given by the two models (Poiseuille and Garcy-ideal gas laws), as illustrated in Figures 8, 9 and 10.

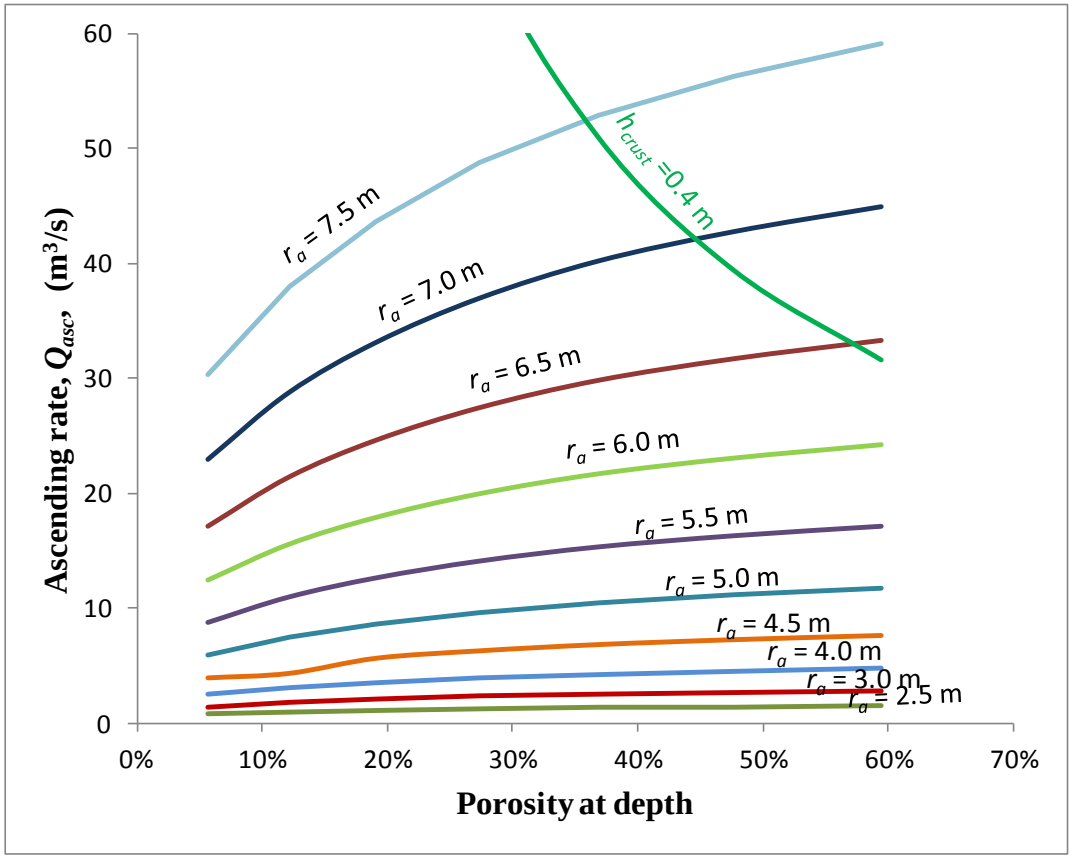

Figure 8. Ascending rate of magma for different values of blob porosities and radius of the ascending conduit for a crust of 0.4 m. Each blob of nominal porosity 10-70 vol.%, can ascend to surface, but the ascent rate will depend on the radius. The ascending flux corresponds to the intersection of the 10-70 vol.% lines parallel to the Y-axis with the radius curves. The line labelled "h_{crust} = 0.4 m" represents the ascending flux required to degas 3.6 kg/s at the respective porosities (See Figure 6 in Section 4).

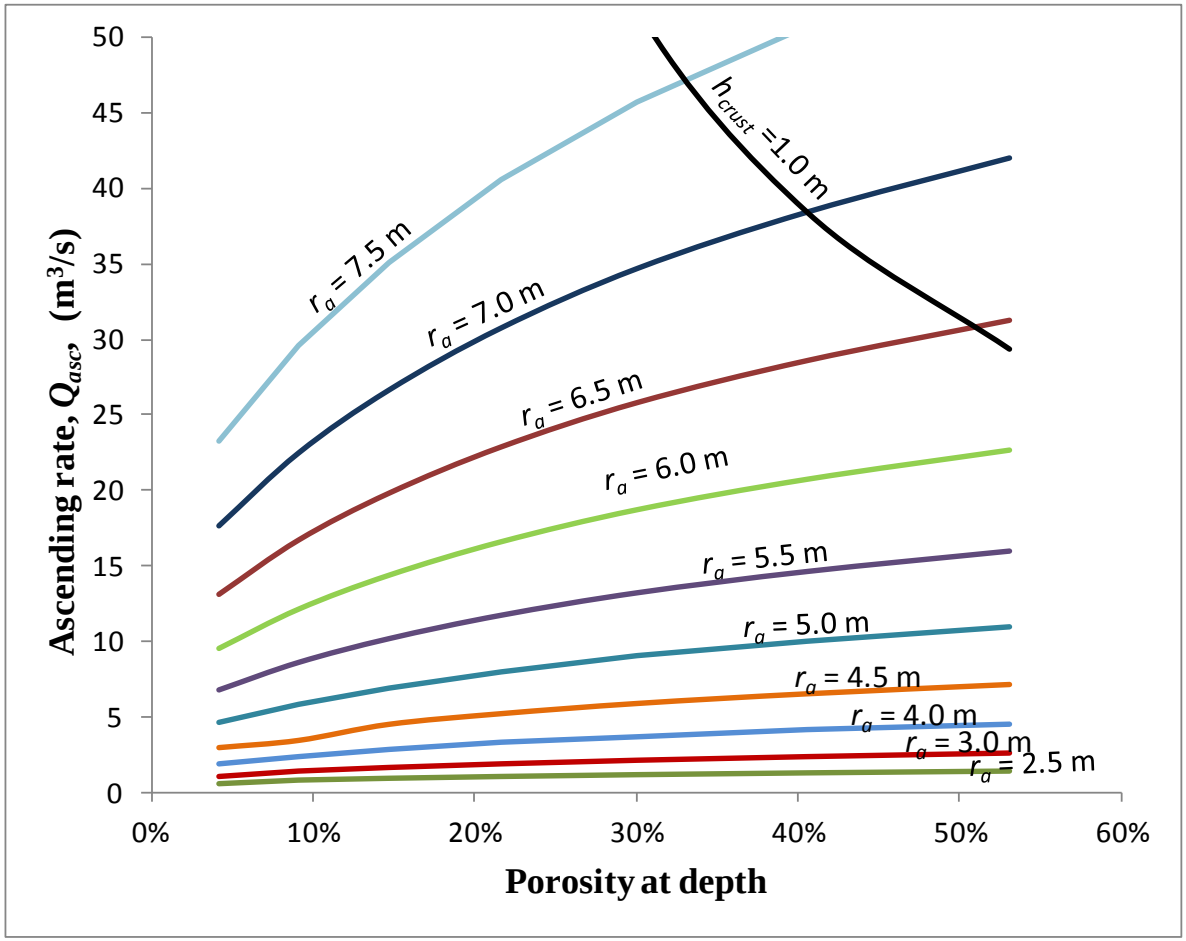

Figure 9. Ascending rate of magma for different values of blob porosities and radius of the ascending conduit for a crust of 1.0 m. Each blob of nominal porosity 10-70 vol.%, can ascend to surface, but the ascent rate will depend on the radius. The ascending flux corresponds to the intersection of the 10-70 vol.% lines parallel to the Y-axis with the radius curves. The line labelled "h_{crust} = 1.0 m" represents the ascending flux required to degas 3.6 kg/s at the respective porosities (See Figure 6 in Section 4).

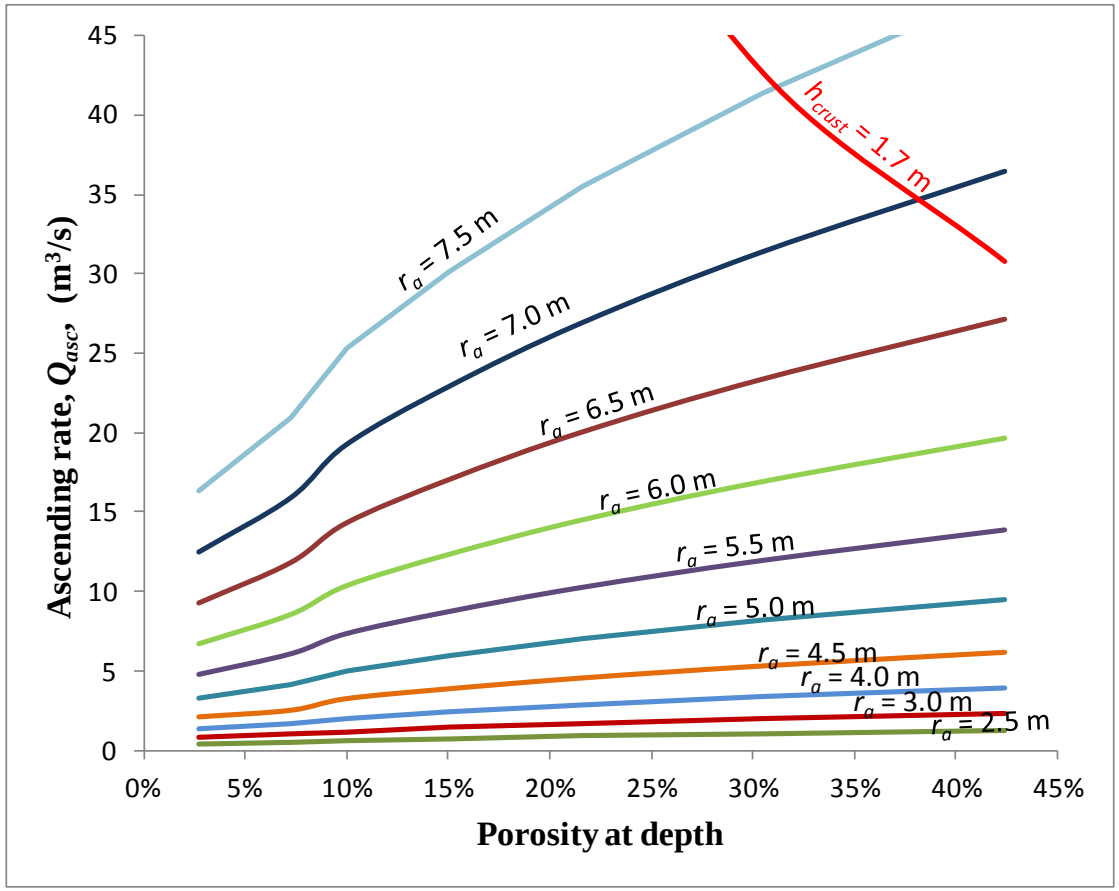

Figure 10. Ascending rate of magma for different values of blob porosities and radius of the ascending conduit for a crust of 1.7 m. Each blob of nominal porosity 10-70%, can ascend to surface, but the ascent rate will depend on the radius. The ascending flux corresponds to the intersection of the 10-70 vol.% lines parallel to the Y-axis with the radius curves. The line labelled "h_{crust} = 1.7 m" represents the ascending flux required to degas 3.6 kg/s at the respective porosities (See Figure 6 in Section 4).

Several criteriae of porosity and ascending radius respond simultaneously to our requirements. The following table compiles the solutions given by the intersection of the curves given by Figures 8, 9 and 10:

Table 4. Solution of porosity at depth for an ascending radius and magma flux for agiven crust thickness. NA means not applicable.

		Ascending radius, r_a, (m)		
		6.5	**7.0**	**7.5**
Crust thickness h_{crust}, (m)	**Porosity at depth**	**Ascending flux Q_{asc} (m^3/s)**		
0.4	36% 45% 57%	 33	 42	52.5
1.0	33% 41% 51%	 31	 38.5	47
1.7	31% 38% NA	 NA	 34.5	41.8

A set of solutions is represented by the line h_{crust} = 1.0 m. A blob of 33% porosity in a radius of 7.5 m and an ascending rate of 47 m^3/s will supply the required quantity of magma able to degas 3.6 kg/s, just like a blob of 41% porosity in a 7.0 m ascending radius supplying 38.5 m^3/s and a blob of 51% in 6.5 m-radius and 31 m^3/s. All the points in between the materialized radius diameter lines equally answer our requirement (Figure 9 and Table 5).

For h_{crust} = 1.7 m, the blob reach a porosity lower than the value they would reach at surface. The ascending flux is reduced and a larger conduit is required for the blob to ascend. A batch of 31% porosity can supply 41.8 m^3/s in a 7.5 m conduit radius. A blob of 38% porosity will be able to generate an additional degassing of 3.6 kg/s, providing 34.5 m^3/s of magma in a conduit of 7 m in radius (Figure 10 and Table 5).

For h_{crust} = 0.4 m, a blob of 36% porosity in a radius of 7.5 m and an ascending rate of 52.5 m^3/s will supply the required quantity of magma able to degas 3.6 kg/s, just like a blob of 45% porosity in a 7.0 m-radius conduit supplying 42 m^3/s and a blob of 57% in 6.5 m-radius and 33 m^3/s. Since the crust thickness conditions the pressure below the crust, the porosity of the magma below surface is higher than for the two previous cases (Figure 8 and Table 5).

6. Discussion

We have considered that the gas flow rate of 19.2 kg/s is percolating through the conduit as a continuous supply of "free gas", which therefore is generated deep in the magma chamber. In the calculations using the "top gas", we do not consider that a flux of melt is associated to this "bottom gas" degassing. The arrival of additional magma associated to the formation of a blob enhances convection at surface. When conditions are reached in the upper part of the conduit for this blob to form, it can only ascend at a sufficent rate if the conditions of buoyancy are met, resulting of the contrast between the density of the dry melt descending in the annular and that of the core. In absence of any other driving force, the ascent flow rate as defined in equation (15) is only sensitive to the value of $\Delta\rho_{d-a}$ and to the radius of the ascending core r_a. The presence of free gas in the conduit is likely to reduce considerably the density of the magma in the core of the conduit (Figure 11), slightly increasing Q_{asc}.

Several criteriae of porosity and ascending radius respond simultaneously to our requirements. Blobs with a "top gas" composition as defined in Chapter IV and of different porosities are able to reach surface with an ascending rate sufficient to release an additional 3.6 kg/s of gas. These conditions can be met even for large values of the crust thickness, provided that the conduit is large enough. However, we did not consider the additional pressure ΔP required for degassing through the crust. This pressure will not prevent the ascent of the blob as the crust physically does, but it is likely to keep more gas in solution. Therefore, for high values of the crust, the value of the porosity reached by the blob is over-evaluated.

If we consider a blob rising with a 41% porosity under a crust of 1 m, the rate of associated melt is 23 m^3/s. For a melt density of 2455 kg/m^3, this rate accounts for 5.6×10^5 kg/s. This is consistent with the magma flux of 3.45×10^6 kg/s estimated by *Calkins* [2006]. Over a duration of 300 s, this influx corresponds to a volume of 6900 m^3; distributed over a lake area of 770 m^2, this volume would represent a level increase of 9 m if our system was not in equilibrium. Therefore, the 23 m^3/s of melt are drained back in the annular conduit. Having considered the depth of the lake to be 20 m, the volume of the lake is 15400 m^3; a influx of 23 m^3/s yields a residence time of 11 min, close to the period of oscillation (10 min). The volume of a blob is then evacuated at a rate similar to that of the influx.

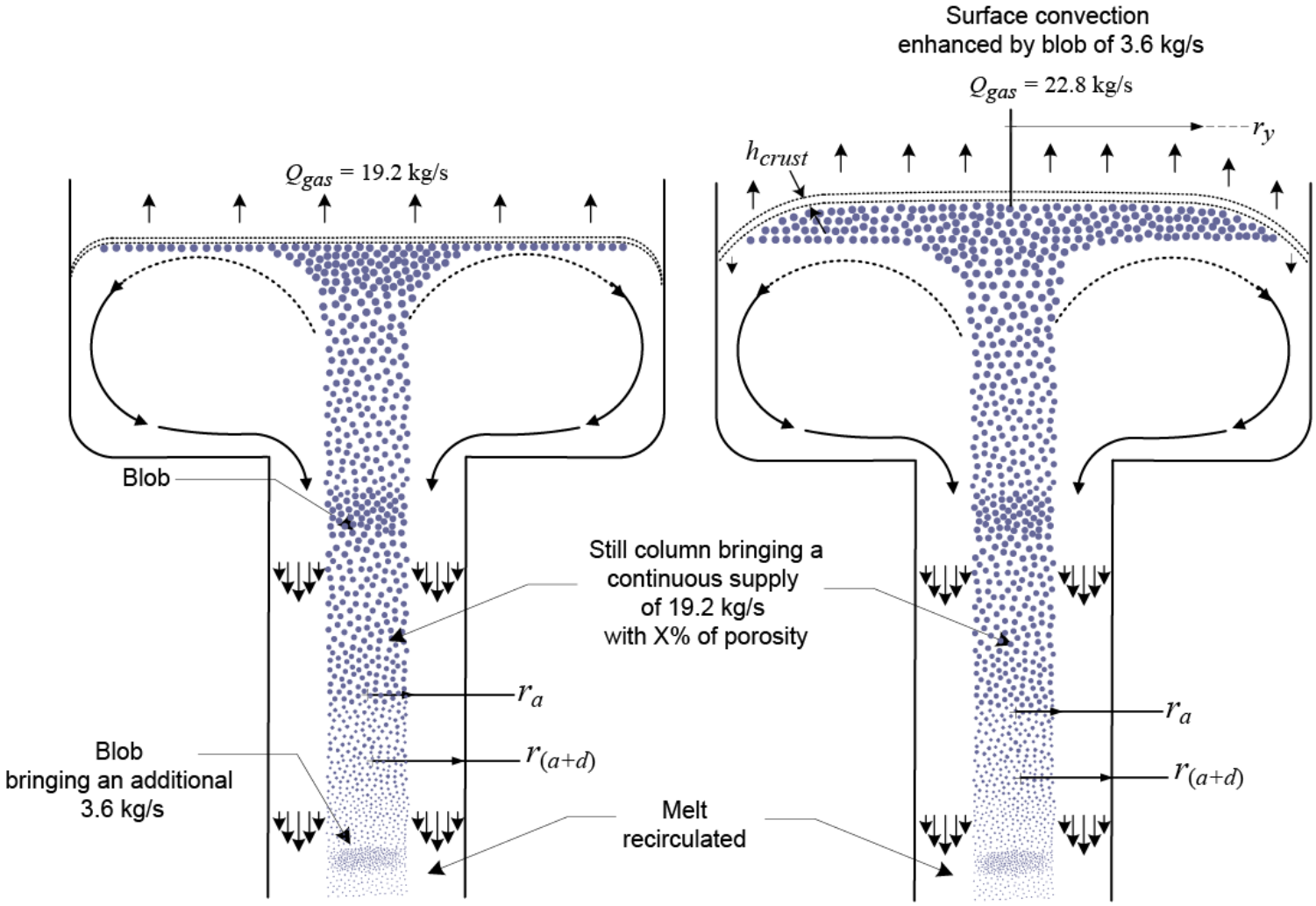

Figure 11. Cartoon representing the formation of a blob in a conduit whose porosity is enhanced by the ascent of continuous gas generated deep in the magma chamber.

We have considered bi-directionnal flows of gassy and degassed magma to be arranged in an annular manner in the conduit and in the lake (Figure 11). The volume flux of the descending magma Q_{desc} is expressed as follows (as *Lamb* [1959], p. 587 and *Kazahaya et al.* [1994]):

$$Q_{desc} = \frac{\pi \Delta \rho_{d-a}\, g\,)}{8\mu_d} \left\{ r_{(a+d)}^4 - r_a^4 - \frac{\left(r_{(a+d)}^2 - r_a^2\right)^2}{\ln \frac{r_{(a+d)}}{r_a}} \right\} \quad (17)$$

Where $r_{(a+d)}$ is the total radius of a conduit providing for both flows of dry descending melt and wet gassy ascending magma. Since no solids are ejected as surface, $Q_{desc} = Q_{asc}$. Combining equation (15) and (16), *Kazahaya et al.* [1994] have written:

$$\frac{\mu_d}{\mu_a} = f^4 - 1 - \frac{\left(f^2 - 1\right)^2}{\ln f} \quad (18)$$

Where $f = \frac{r_{(a+d)}}{r_a}$. Using values of viscosities of the descending and ascending magma for 40% porosity at surface (close to our 41%) to be μ_d = 6.07 × 10^5 and μ_a = 1.64 × 10^5, respectively (derived from Figure 7c at depth of 1 m) we find a ratio $\frac{\mu_d}{\mu_a} = 4.43$ wich solves equation (17) for a value of $f = 2.2$. *Stevenson and Blake* [1998] found that the relative radius of an ascending low-viscosity fluid injected in a denser and more viscous fluid $\left(\frac{1}{f}\right)$ varies between 0.53 and 0.64 over a broad range of viscosity contrast. The relative radius of our ascending core flow in the lake is of 0.46, in agreement with these authors' findings. If, rather than fixing the core radius, we set $r_{(a+d)} = 6$ m then the ascending core r_a = 2.76 m, too narrow to let a sufficient rate of magma reach surface and release 3.6 kg/s of gas. On the other hand if we fix, for example, $r_a = 7$ m, then $r_{(a+d)} = 15.2$ m. This value of $r_{(a+d)}$ at surface does not necessarily represents the radius of the conduit connecting the magma chamber to the lake, as the flux of the magma will be inferior at the connexion of the conduit with the lake than what it is below the crust. At surface, the magma ascends through an area of 154 m^2 and the melt descends through an area of 589 m^2. The 23 m^3/s of our example will sink at a rate of 3.9 × 10^{-2} m/s. For values of r_a of 6.5 and 7.5 m, the descend rate will be 4.5 × 10^{-2} and 3.4 × 10^{-2}, respectively (Table 6).

Table 5. Variation of the descending velocity of a fixed rate of dry melt as a function of the radius of the ascending core flow, r_a, and/or the total radius of ascending plus descending magma $r_{(a+d)}$ associated to a bubbly magma containing 40% porosity at surface.

Ascending radius r_a m	Total radius $r_{(a+d)}$ m	Core area S_a m^2	Total area $S_{(a+d)}$ m^2	Annular area S_a m^2	Descending rate m^3/s	Descending velocity m/s
6.5	14.3	133	641	508	23	4.5×10^{-2}
7	15.4	154	743	589	23	3.9×10^{-2}
7.5	16.5	177	853	676	23	3.4×10^{-2}

However, the overpressure below the crust will keep part of the volatiles in solution; the melt is recirculated down the conduit with a small amount of gas, whose fraction varies with the overpressure required to flow the gas through the permeable crust. Morevoer, if the residence time of 11 min is not sufficient for the blob to reach equilibrium by degassing as much as the overpressure allows, more gas will remain in solution. Consequently, we can consider an absolute and an effective porosity of the magma. If a 50% porosity blob reaches surface while 10% of the gas fraction is recirculated, the effective porosity – that contributing to the degassing - will be 40%. The descending magma will then have a density significantly lower than that of the dry melt, reducing the buoyancy and moreover the viscosity of the descending magma. We now consider our ascending and descending magmas with a top gas composition to have 50% and 10% porosity at surface respectively; the magma ascends in a same r_a= 7 m below a 1 m-thick crust. Their respective viscosity at a depth of 20 m (in the conduit) will be μ_d = 2.3 × 10^5 and μ_a = 1.58 × 10^5, respectively (data from Figure 7c). We obtain now $\frac{\mu_d}{\mu_a} = 1.44$ which solves equation (17) for a value of $f = 1.904$. In Chapter IV, we have calculated that, depending on the porosity of the blob, the value of the ascending radius increases by 0.4 to 2 m between the top of the conduit and the surface of the lake (Figure A3-Case 5 from Chapter IV). For a blob with 40% of porosity at surface the asceending radius changes by 1 m. A radius of 7 m at surface being only 6 m at the top of the conduit, we obtain a total radius $r_{(a+d)} =$ 11.4 m and the ratio $\frac{r_a}{r_{(a+d)}} = 0.53$ in good agreement with *Stevenson and Blake* [1998].

A relatively large range of radii and crust thicknesses falls in the envelope of solutions. Videos of the permanent activity of the volcano show that incandescent magma reaching

surface splits the crust over a large area, before it quickly heals; the thickness of the crust does not seem to be in the order of 2.5 m. We can then constrain our envelope of solutions by considering crusts thinner than 2 m. We have no physical mean of checking the diameter of the conduit; *Dibble et al*. [2008] reported direct observations made in the season of 1987/88 right after a massive ejection of solids emptied the lake; it allows somehow constraining the value of this diameter. They indicate that the conduit diameter would represent half of the initial diameter of the lake but no accurate information about the diameter of the lake itself has been reported for this specific period.

The incandescent magma reaches the surface of the lake over an area that, from the video, can hardly been related with accuracy to the diameter of the conduit underneath. However, the area submitted to a stronger convection when a blob reaches surface has a diameter varying between 10 and 15 m.

We can expect both ascending and descending magmas to interfere and partially mix when batches of fully (or partially) degassed descending magma sink in the conduit. Forcing an increasingly richer gas supply through a degassed magma flowing in opposite direction is likely to generate a sluggish flow that will in turn cause or enhance the fluctuation of the surface of the lake. *Huppert and Hallworth* [2007] studied such a buoyancy-driven exchange flow. They found that, when the viscosity contrast is high enough to prevent the fluids from mixing, the flow develops as an irregular column of upward moving fluid with varicose instabilities that can eventually break into discrete blobs. If the conduit does not have a radius of 11.4 m (~23 m in diameter) as suggested by our analysis, we can expect that magma mixing will take place in the conduit and consequently be at the origin of more complex convective patterns. A simple Poiseuille model may reach here its limits.

Gas bursting at surface before the lake has reached its highest level can release some of the confined pressure by a sudden drop of surface permeability (see Figure 2i in Chapter 4). The surface of the lake will then return to a lower level and therefore the amplitude of an oscillation can vary from one cycle to another. If the amount of released gas is large, enough pressure must accumulate for another cycle to resume. This explains why the surface level can remain still during 2 to 10 minutes between cycles, as reported by [*Oppenheimer et al.*, 2011, in prep.].

The surface of the lake has been reported as varying over time. The walls of the lake are therefore not perfectly vertical and the rising of the level in a funnel-shaped crater lake results in a decreasing ascent velocity as the volume spreads over a larger area. However we did not take this particularity into account to calculate the height of the oscillation, which thus may be slightly overestimated.

We have considered the pressure increase and the variation of the level as being linear in time. The pressure below the crust has to overcome the static friction, higher than the kinetic friction, before the level starts to move and this will cause a slight "delay" before the crust starts to rise. This delay reduces the time over which the level will rise and consequently minimizes the amplitude of the oscillation. However, the pressure that briefly accumulates below the crust to overcome the static friction will yield a higher value of initial velocity, minimizing the previous overestimation.

7. Conclusion

The level of the Erebus lava lake and the gas output fluctuate in phase over a period of 10 minutes. The level rises between 1 and 1.5 m before returning to its previous level, while the gas flux varies from 19.2 kg/s to 22.8 kg/s during enhanced convection. The gas composition is not the same when the gas flux is at its lowest than during the rising phase when the release rate reaches its peak.

We interpret the fluctuation of the level as the deformation of the surface under the form of a Bingham flow, resulting from the intermittent rise of a batch of magma in an otherwise steady flow of ascending gas in the core of the conduit, originated deep in the magma chamber. As the batch of magma originating at shallower depth ascends in the conduit and reaches surface, the overpressure results in an increase of the degassing rate and the rise of the surface once the friction has been overcome. Both the radius allowed for the magma to ascend and the density contrast between upwelling and descending magma must be large enough for the shallow batch of magma to ascend with a flow rate sufficient to supply the quantity of gas reported by observers.

Our model indicates that there is no unique combination of the parameters allowing simultaneously the observed rise of the level and degassing rates: thickness of the crust, porosity, permeability, crystal content, ascending magma radius and above all the diameter of

the conduit. If we consider the rise of a shallow-originated blob of magma with 40% porosity and a radius of 7 m reaching surface under a 1-m thick crust, the lake oscillates over 1.25 m in 10 minutes, while degassing up to 3.6 kg/s. The 23 m^3/s of associated melt have a residence time of 11 min and sink back at 3.9×10^{-2} m/s in the annular of 15.4 m radius (Table 5).

A sudden drainage of the lake has not been reported by observers, except when large gas slugs generate Strombolian explosions. It is then unlikely that large amounts of connected free gas be present below surface and therefore localized bursts of gas will have a limited impact on the oscillation. If a blob surfaces before the level has returned to its equilibrium, the healing crust in the area of strong convection will be thinner and less overpressure will be required for the level to resume rising. On the contrary, if bursting of a large amount of gas releases overpressure in excess, the delay before a new cycle resumes may lead to the formation of a thicker crust and the accumulation of melt in the lake. The progressive decrease of the gas flux reinforces our hypothesis that the magma reaches surface as a large homogenous mixture to release its gas through a permeable crust.

References

Burgisser, A, Oppenheimer, C., Aletti, M and Kyle, P.R. (in review), Backward tracking of gas chemistry measurements at Erebus volcano, *Geochem. Geophys. Geosyst*.

Calkins, J.A. (2006), Ground based thermal observations of two lava lakes at Mount Erebus Volcano, Antarctica in December 2004, M.S. Thesis, Dep. Earth and Env. Sci. New Mexico, Institute of Mining and Technology, Socorro, New Mexico, U.S.

Dixon, J. C. (2007), Appendix G: Bingham Flow: *The Shock Absorber Handbook*, edited by John Wiley & Sons, Ltd, pp. 398–400, doi: 10.1002/9780470516430.app7.

Forchheimer, P (1901), Wasserbewegung durch Boden, Z. Ver. Dtsch. Ing. 45, 1781-1788.

Hassanizadeh S.M. and W.G. Gray (1987), High velocity flow in Porous Media. Transport in Porous Media, 2, 521-531.

Huppert H. E. and M. A. Hallworth (2007), Bi-directional flows in constrained systems, *J. Fluid Mech., 578*, 95–112.

Hoover, S.R., Cashman, K.V., Manga, M., (2001). The yield strength of subliquidus basalts—experimental results, *J. Volcanol. Geotherm. Res.*, *107* (1–3), 1–18.

Kazahaya, K., Shinohara, H., Saito, G (1994), Excessive degassing of Izu-Oshima volcano: magma convection in a conduit, *Bull. Vol.*, 56, 207-216.

Lamb, H (1945), Hydrodynamics. Cambridge University Press, Cambridge, 738 pp.

Molina , I., A. Burgisser and C. Oppenheimer (2012), Numerical simulations of convection in crystal-bearing magmas: A case study of the magmatic system at Erebus, Antarctica, *J. Geophys. Res.*, doi:10.1029/2011JB008760, in press.

Oppenheimer, C., A. S. Lomakina, P. R. Kyle, N. G. Kingsbury, M. Boichu (2009), Pulsatory magma supply to a phonolite lava lake, *Earth Planet. Sci. Lett.*, 284, 392–398, doi:10.1016/j.epsl.2009.04.043.

Oppenheimer, C. et al, in prep, Pulse of a volcano measured by lava lake pressure gauge!

Rust, A.C. and Cashman, K.V. (2004), Permeability of vesicular silicic magma: inertial and hysteresis effects, *Earth Planet. Sci. Lett.*, 228 (1–2), 93-107, doi:10.1016/j.epsl.2004.09.025.

Stevenson, D. S. and S. Blake (1998), Modeling the dynamics and thermodynamics of volcanic degassing, *Bull. Vol., 60,* 307–317.

Wildemuth, C.R., Williams, M.C. (1984), Viscosity of suspensions modeled with a shear dependent maximum packing fraction, *Rheol. Acta*, *23*(6), 627–635, doi: 10.1007/BF01438803.

Conclusions générales

Nous avons étudié le caractère effusif du phénomène de dégazage permanent observé sur le volcan Erebus qui s'accompagne d'une variation cyclique de la composition des gaz et du niveau de son lac de cratère. Le cycle de vie des bulles de gaz dans un magma, depuis le stade de leur nucléation à des pressions et températures élevées jusqu'à leur émission à l'atmosphère, est difficile à simuler car il implique une ensemble de procédés extrêmement complexes. Nous avons donc procédé par étapes en simulant tout d'abord une convection en milieu fermé d'un mélange liquide-cristaux, qui s'est révélée insuffisante pour expliquer la vigueur de la convection observée in-situ. Une recharge permanente de la chambre magmatique contenant liquide et bulles permettait ensuite de reproduire un comportement pulsatile en milieu ouvert, se traduisant par des changements de vitesse en surface, dont les valeurs absolues ont augmenté substantiellement dans le lac et dans une moindre proportion à sa surface. L'introduction de deux batch de magma aux profondeurs de vésiculation différentes a permis de démontrer l'importance cruciale de la température et de la composition du gaz sur le comportement du lac de lave. Nous avons enfin montré combien les caractéristiques physiques de la surface du lac, telles que son épaisseur et sa perméabilité, contrôlent l'amplitude de la fluctuation de son niveau.

Nous montrons en **chapitre II** que le modèle numérique de dynamique des fluides que nous avons implémenté reproduit fidèlement les schémas de convection et les instabilités de Raleigh-Taylor observés et décrits par *Jaupart et Brandeis* [1986]. La vitesse à laquelle les panaches progressent vers le fond du système est en accord avec celle des modèles théoriques et leur différence avec celle observée au cours de l'expérience reste dans les limites de la précision des mesures. Les températures en fin de simulation sont également en accord avec celles de l'expérience. D'autre part, nous avons démontré que la simulation est applicable à un écoulement biphasique liquide-cristaux lorsque ces derniers se trouvent à une concentration proche de ou égale à leur valeur de compaction maximale.

L'application de notre modèle à un système magmatique simplifié ignorant la présence de

bulles et de cristaux (l'Erebus représenté par un lac de lave, un conduit et une chambre magmatique aux géométries peu complexes) montre qu'une activité convective en régime permanent est suffisante pour maintenir le magma au-dessus de sa température de transition vitreuse, à condition que le diamètre du conduit soit assez grand (10 m). Un conduit trop petit (4 m) entraîne l'isolation du lac car une instabilité visqueuse parvient à boucher l'entrée du conduit, perturbant l'ascension de fluide chaud, isolant le conduit et ralentissant le phénomène de convection dans tout le système. Les forces de flottabilité au bas du conduit sont alors insuffisantes pour entraîner les fluides vers la surface.

L'importance du diamètre du conduit sur les schémas de circulation a également été mise en évidence en présence de cristaux, dont la taille (5 cm) favorise la décantation. Leur prise en compte accélère la convection et améliore l'efficacité du transfert de chaleur entre la chambre magmatique et le lac de surface. Une simulation conduite sur une durée de 30 ans montre que le phénomène de convection est d'abord dominé par les forces thermiques, alors que les cristaux s'accumulent au fond de la chambre magmatique. La convection est ensuite plus dépendante de la décantation des cristaux dont certains demeurent en suspension, dans des proportions qui varient selon que le système est « fermé » ou « ouvert », et qui formeront un dépôt persistant atteignant une épaisseur de 10 m. Considérer notre simulation dans un système ouvert nous parait plus réaliste, car cela permet d'obtenir des vitesses de convection de surface ainsi qu'une fraction de cristaux en suspension plus élevées. Cependant ces valeurs simulées de vitesse et de contenu cristallin restent bien en deçà de celles mesurées sur l'Erebus. Notre simulation ne prenant pas en compte le dégazage permanent observé sur le volcan, nous en avons conclu que celui-ci joue un rôle majeur dans la génération et le maintien d'une convection vigoureuse, capable de limiter la décantation des cristaux et de provoquer le déplacement relativement rapide du magma en surface.

Nous avons montré en **chapitre III** comment sont initiées des impulsions successives de magma qui migrent dans le conduit vers la surface. Une période de relative inactivité d'une durée de ~500 secondes semble correspondre au développement d'un nouveau batch de magma dont l'ascension se traduit par des changements de vitesse en surface. Cette durée est en accord avec les variations de vitesse et de composition des gaz telles que les a documentées *Oppenheimer et al*. [2009], bien que les vitesses que nous avons calculées soient

de 2 à 3 ordres de grandeur plus petites. Des limitations de notre modèle nous sont donc apparues, suggérant la nécessité de varier les paramètres de perméabilité de la surface du lac et le taux de recharge continue en magma ainsi que de raffiner les paramètres numériques de la simulation, tels que tolérance, taille du maillage et facteurs de sous-relaxation des équations de mouvement.

Dans le **chapitre IV** nous montrons que la différence de température entre les courants de magma ascendant et descendant est le paramètre clé permettant d'expliquer le comportement cyclique du lac, mettant en relation les variations géochimiques et celle du niveau. En fixant plusieurs paramètres à l'origine de cette oscillation, nous avons également montré que, pour une même composition de gaz, il y a une corrélation entre la profondeur de vésiculation du magma et le flux de gaz associé : ce dernier est moindre lorsque la vésiculation se produit à faible profondeur. D'autre part, la vitesse d'ascension et la manière dont des blobs isolés se détachent dépendent de la composition du gaz.

Nos résultats suggèrent que les oscillations du niveau du lac proviennent de l'intercalation de deux sortes de batch de magma provenant de profondeurs distinctes, dont la composition chimique, les flux de surface, température et vitesse d'ascension diffèrent. Bien que leurs compositions soient différentes, ces batch ont un diamètre de l'ordre de 13 m, une valeur en accord avec les observations et les enregistrements vidéos dont nous disposons. Nous inférons que la différence de température entre les types de batch est à l'origine des variations geochimiques et de flux du gaz observées à la surface du lac, et que la différence de température entre courants ascendant et descendant peut faire varier l'amplitude de l'oscillation.

En **chapitre V**, nous avons considéré la surface du lac comme une croûte perméable se déformant comme un écoulement de Bingham sous l'influence d'un afflux de gaz, tel que nous l'avons défini en chapitre IV, généré à faible profondeur dans un conduit autrement alimenté de manière continue par un gaz d'origine plus profonde. En variant l'épaisseur de cette croûte sur une large plage, nous avons déterminé quelle pression piégée est requise pour maintenir le flux de gaz en surface tout en générant une hauteur d'oscillation du niveau du lac en accord avec les observations. Nous en avons déduit les flux de magma correspondant.

Un batch de magma capable d'entrainer un dégazage de 3.6 kg/s, tel qu'il est défini en chapitre IV et quelle que soit sa porosité, n'atteindra donc plus la surface mais restera piégé sous une hauteur égale à l'épaisseur du magma. Le flux de magma à cette profondeur est donc inférieur à ce qu'il aurait été si le batch avait atteint la surface. D'autre part, en chapitre IV, le batch de magma n'était pas contraint dans son ascension alors que son flux dépend du diamètre dans lequel il s'écoule et du contraste entre la densité du magma qui descend et de celle du magma qui monte (elle-même fonction de sa porosité). Nous avons déterminé qu'un tel batch de magma peut cependant entraîner un dégazage en accord avec les observations, sous une large plage d'épaisseur de croûte, à condition que le conduit soit assez large.

Ainsi, un batch de magma d'origine peu profonde et de 40% de porosité, atteignant la surface sous la forme d'un écoulement de 7 m de rayon sous une croûte d'un mètre d'épaisseur et de perméabilité 2.6×10^{-10}, entraine une oscillation de 1.25 m en 10 minutes. Une surpression sous la croûte de 3.81×10^{3} Pa est suffisante pour provoquer une augmentation du dégazage de 3.6 kg/s. Les 23 m^3 de magma associés à ce gaz auront un temps de résidence de 11 minutes et redescendront dans le conduit à une vitesse de 0.04 m/s. Le rayon du conduit requis pour un tel système est de 11.4 m. Les résultats et la méthodologie developés dans les **chapitres IV** et **V** sont complémentaires. Tous deux suggérent un rayon en surface du magma ascendant autour de 7 m, en accord avec les enregistrements vidéo, un débit de magma de 10^5 kg/s et un diamètre de conduit de 20 et 23 m. Si le lac avait un diamètre de 40 m au cours de la saison 1987/1988, alors ces resultats seraient en accord avec les observations directes. Si le conduit est plus petit, un mélange partiel entre les magmas circulant à contre-courant peut entraîner une vésiculation de l'écoulement central, ce qui provoquera à son tour une arrivée par à-coups du magma en surface. Ce scenario devie fortement d'un écoulement de Poiseuille classique, qui atteint sans doute ici ses limites. La modélisation numérique peut se révéler un outil majeur dans la résolution de ce type d'écoulement complexe.

Si le temps de résidence relativement court et la pression piégée sous la croûte maintiennent une quantité de gaz dissoute telle que le magma circulant dans le conduit est encore très poreux, le contraste de densité entre les magmas ascendant et descendant sera réduit. Une convection efficace ne sera assurée que si le diamètre du courant de magma ascendant est supérieur. La densité du magma descendant se trouvant également affectée, la profondeur

changera à laquelle le seuil de flottabilité nécessaire à l'ascension du blob est atteinte. Ce qui, à son tour, peut influer sur la nature des gaz libérés puisqu'il y a une corrélation entre leur composition et les profondeurs et températures auxquelles s'amorce l'exsolution.

Notre modèle indique qu'il n'y a pas de solution unique de combinaison des différents paramètres affectant le mouvement de la surface et le dégazage. Nous avons cependant déterminé un ensemble des critères de diamètre du courant de magma ascendant, de porosité et d'épaisseur de la croûte requis pour qu'un écoulement ascendant nous permette de reproduire les fluctuations observées, renforçant ainsi notre hypothèse que la surface se comporte comme un milieu perméable et déformable.

Le comportement effusif de l'Erebus est remarquable en ce sens que les conditions de pression et de température auxquelles le magma est soumis en profondeur semblent être proches de celles requises pour que les volatiles dissouts dans le magma exsolvent de manière continue. L'arrivée cyclique de gaz fait que la surface n'a pas le temps de se refroidir suffisamment pour qu'une croûte épaisse puisse se former. Le gaz piégé sous la surface est capable de soulever cette croûte et de la rompre, mais rarement de façon explosive car la pression ne peut s'y accumuler.

L'utilisation de lois de dynamique des fluides simples, telles que la loi de Stokes et de Poiseuille, auxquelles nous incorporons des paramètres propres à la dynamique des fluides volcaniques, nous a permis d'appréhender la complexité de ces écoulements et de déterminer quels axes nous devons explorer pour en améliorer la simulation. Cette approche innovante nous a permis d'analyser le comportement d'un batch de magma ascendant sous la forme d'un écoulement de Poiseuille en lui associant du gaz. Nous avons ainsi expliqué l'arrivée alternée de batch de compositions géochimiques différentes en raison de leurs profondeurs d'origine respectives. Nos résultats sont en accord avec les équilibres de température suggérés par le modèle d'Alain Burgisser et avec les fluctuations de débit, de composition et de niveau observées sur l'Erebus. Nous avons réduit avec succès la grande variété de solutions possibles en montrant l'importance de la géométrie du système magmatique, notamment le diamètre du conduit.

Notre modèle novateur peut être appliqué à d'autres systèmes volcaniques basaltiques et andésitiques lorsque l'on connait la composition du magma, des gaz relâchés et la géométrie

du système. Il peut aussi être transposé à d'autres volcans présentant à la fois une activité vulcanienne et strombolienne, tel que le volcan Tungurahua en Equateur. En 2006, alors que la croûte présente dans le cratère était suffisamment résistante pour contenir une pression élevée, une activité cyclique se traduisant par des explosions de type strombolien a culminé par une phase paroxysmale. Une activité vulcanienne a pu ensuite être observée pendant de nombreuses semaines, se traduisant par l'arrivée de batch de magma à intervalles réguliers [*Molina*, 2008].

Nous avons identifié plusieurs axes dans lesquels orienter nos recherches futures. Les bulles de gaz ont été considérées comme indépendantes les unes des autres et le phénomène de coalescence n'a pas été pris en compte. L'efficacité du dégazage lorsque le magma atteint la surface est mal connue ; en effet celui-ci est fonction de nombreux paramètres (p.e. viscosité du magma, tensions superficielles, taille des bulles, surpression). Le temps de résidence peut ne pas être suffisant pour assurer un dégazage aussi complet que les conditions de pression auxquelles il est exposé sous la croûte pourraient le permettre. Ceci nous permettra d'évaluer quelle fraction de gaz reste en solution lorsque le magma plus dense redescend dans le conduit. Un mélange des courants ascendant et descendant est susceptible de se produire et ce phénomène mal connu reste à étudier pour des vitesses, des mélanges biphasiques et des contrastes de viscosité tels que ceux que nous rencontrons dans un système magmatique. Cette connaissance nous permettra de mieux comprendre un éventuel phénomène de vésiculation. Mieux comprendre les phénomènes géochimiques et rhéologiques qui conditionnent le comportement effusif d'un écoulement dans un conduit ou une faille permettra sans doute de mieux connaître la transition à un régime explosif. C'est ce sur quoi nous nous proposons de travailler dans les prochaines années.

References

Jaupart, C., and G. Brandeis (1986), The stagnant bottom layer of convecting magma chambers, *Earth Planet. Sci. Lett*., *80*, 183–199, doi:10.1016/0012-821X(86)90032-4.

Molina, I. (2008), L'activité explosive du volcan Tungurahua (Equateur): Suivi des ondes acoustiques et sismiques pour analyser l'évolution temporelle de la source, *Rapport de Master –Spécialité Géophysique-*, IPGP, France.